NAVEED ANJUM

Hyperfine Structure of Spectral Lines of $^{143}Nd^{+}$, $^{145}Nd^{+}$, $^{139}La^{+}$, $^{141}Pr^{+}$ and $^{137}Ba^{+}$ Investigated by Collinear Laser Ion Beam Spectroscopy

DOCTORAL THESIS

For obtaining the academic degree of

Doktor der technischen Wissenschaften

Doctoral Programme of Technical Sciences
Technical Physics

Graz University of Technology

Supervisor:

Univ.-Prof. Dipl.-Ing. Dr.techn. Laurentius Windholz

Institute of Experimental Physics, Graz, Austria

November 2012

Deutsche Fassung:
Beschluss der Curricula-Kommission für Bachelor-, Master- und Diplomstudien vom 10.11.2008
Genehmigung des Senates am 1.12.2008

EIDESSTATTLICHE ERKLÄRUNG

Ich erkläre an Eides statt, dass ich die vorliegende Arbeit selbstständig verfasst, andere als die angegebenen Quellen/Hilfsmittel nicht benutzt, und die den benutzten Quellen wörtlich und inhaltlich entnommene Stellen als solche kenntlich gemacht habe.

Graz, am ....
(Unterschrift)

Englische Fassung:

STATUTORY DECLARATION

I declare that I have authored this thesis independently, that I have not used other than the declared sources / resources, and that I have explicitly marked all material which has been quoted either literally or by content from the used sources.

....
date (signature)

Dedicated

To

The most Kindhearted Person in my life

Muhammad Siddique . . . . . My Father

The most Beautiful Girl on this planet

Eshaal Naveed . . . . . My Daughter

&

The most Gorgeous Lady I ever met

Mariam Naveed . . . . . My Wife.

Acknowledgements

First and foremost, I offer my humble prayers to the God Almighty Who created this thought provoking universe, full of questions, riddles and mysteries that stimulate the curiosity and aesthetically compel us to explore its hidden meanings. Thanks to Allah almighty, Who blessed me with strength, courage and good health to achieve this goal.

I also present sincere praise and heartfelt obligations to the Holy Prophet Muhammad peace be upon him who is a inspiration for the humanity, irrespective of color, creed, cult or country.

I feel miserable to find appropriate words to pay deepest regards to my supervisor Prof. Dr. Laurentius Windholz, for his support, persistent guidance and continual help during my PhD. His motivation and encouraging attitude and ever vigilant technical support have always been a source of hope and inspiration for me during my research work.

Special thanks to Prof. Dr. Harry Hühnermann for his frequent visits from Marburg to Graz. I admire open heartedly his vast knowledge, technical skills and great attitude. His technical suggestions and moral values greatly helped me during my PhD.

I owe my sincere gratitude to Prof. W. E. Ernst, head of the Institute of Experimental Physics, Technical University Graz, for providing me an opportunity to carry out my research work. I wish to express my warm and sincere thanks to all the institute members, especially the people from electronic/machine workshop for their technical support, institute secretaries and computer administrator for their support in administrative matters and guidelines. I also warmly thanks Michaela Ellmeir for her help in translating thesis abstract from English to German.

I am thankful to my colleague Nadeem Akhtar for initial help, nice working atmosphere in the laboratory and encouragement. I am also thankful to all my Pakistani colleagues Imran Siddique, Syed Tanveer Iqbal, Muhammad Faisal, Shamim Khan and Nighat Pervez for their generous help, skilful guidance and healthy atmosphere. I would like to appreciate the role of all of Pakistani colleagues in Graz, especially Muddaser Abbas, for providing a very friendly environment and their support during my whole stay here in Graz. I am also thankful to all my friends in Pakistan for their best wishes and prayers.

The financial support from Higher Education Commission (HEC) Pakistan and study leave from the Optics Laboratories to carry out PhD studies is highly acknowledged with thanks.

Finally, I would like to thank my loving and caring parents and all family members (sisters, brothers and in-laws) for their encouragements and prayers. Their best wishes and consistent motivation helped me to focus on my goals. Especially the everlasting support and prayers of my father immensely contributed in my life. I am sorry from all my nieces and nephews to live many years away from all of you. I love all of you too much. At last but not least, I owe profound and heartiest thanks to my beloved wife, Mariam Naveed. This achievement would not be successful without her support. She always stood side by side with me in all matters of life and supported me through thick and thin. My deepest prayers for my daughter Eshaal Naveed. She is a gift from GOD for me during my PhD.

Naveed Anjum

Graz, Austria.

Declaration

This dissertation is submitted to the Institute of Experimental Physics, Graz University of Technology, Graz, Austria, in partial fulfillment of the requirement for the degree of Doctor of Technical Sciences.

The thesis is entitled:

Hyperfine Structure of Spectral Lines of $^{143}Nd^{+}$, $^{145}Nd^{+}$, $^{139}La^{+}$, $^{141}Pr^{+}$ and $^{137}Ba^{+}$ Investigated by Collinear Laser Ion Beam Spectroscopy

written by Naveed Anjum and has been approved by the Institute of Experimental Physics, Graz University of Technology, Graz, Austria.

The final copy of this thesis has been examined by the under signed authority, and find that both the content and the form meet acceptable presentation standards of scholarly work in the above mentioned discipline.

_____

Univ.-Prof. Dipl.-Ing. Dr.techn. Laurentius Windholz

Date _____

ABSTRACT

The Coulomb interaction between the positively charged nucleus and the electrons determines the radial probability density of electrons around the nucleus and define the energy levels. The electric interaction of electrons between themselves as well as among the magnetic moments associated with the electron spin and the electron's orbital angular momentum results in the fine structure energy levels. Atoms which have non-zero nuclear spin quantum number display an additional splitting of their fine structure energy levels. This splitting is caused by the electromagnetic interaction between the nuclear magnetic moment and electronic magnetic moment and is called hyperfine structure. Additional small shifts arise from deviation of the electric field of the nucleus from spherical symmetry. The magnetic dipole coupling constant *A* and the electric quadrupole coupling constant *B* are characteristic for each fine structure level.

Numerous aspects of current research in astrophysics demand improved data for individual as well as groups of lines in lanthanides. The effects of hyperfine structure are important because they can be larger than most other sources of uncertainties in the analysis of Doppler shift, speed of stars, elemental and isotopic abundances in stellar spectra. Therefore the precise knowledge of hyperfine structures is indispensable. The hyperfine structure can provide significant information concerning electronic properties and nuclear structure such as: nuclear ground state spin and electromagnetic moments. The electronic configuration of the lanthanides (elements with atomic number $Z = 57 - 71$) with minor exception is of the form [Xe] $4f^n$ (5d, 6s, 6p), where Xe is the xenon core and 'n' varies from 0 to 14. The exceptional properties of the lanthanides originate from the shielding of the 4*f* electrons from outer valence electrons and also due to the fact that binding energies of 4*f* electrons are comparable to the energies of 5*d* and 6*s* orbitals. These facts cause an extremely large number of energy levels originating from the $4f^n$ configuration result in the tremendous complex spectra of the lanthanides.

In this research work the hyperfine structures of spectral lines of barium (Ba) and three lanthanides elements; praseodymium (Pr), lanthanum (La) and neodymium (Nd) have been investigated. The hyperfine splitting factors *A* and *B* of the involved levels have been determined with high accuracy and the data are compared with other published results.

This research work is divided in four parts. In the 1^{st} part, the hyperfine structures of the spectral lines of the singly ionized praseodymium (Pr II) are investigated by three different laser

spectroscopic techniques; laser induced fluorescence (LIF) spectroscopy, inter-modulated saturation spectroscopy and collinear laser ion beam spectroscopy (CLIBS). The LIF and inter-modulated saturation studies are performed with a liquid nitrogen cooled hollow cathode discharge lamp whereas the CLIBS measurements are carried out using a Johnson type surface ion source. The 2nd part is concerned with the a control-check of the Marburg mass separator (MARS-II), as it was shifted from the University of Marburg, Germany, to Graz University of Technology in 2002. The check is performed using a well known spectral line 5853.67 Å of the odd isotope of singly ionized barium (^{137}Ba II). In the 3rd part of this work the hyperfine structure of spectral lines of lanthanum-139 ions (^{139}La II) is investigated. The 4th part is devoted to the investigation of the hyperfine structure of spectral lines of two odd isotopes of singly ionized neodymium (^{143}Nd II and ^{145}Nd II) and the determination of the coupling constants *A* and *B* of the involved levels. To determine the hyperfine anomaly the ratios of the magnetic dipole constants, i.e A_{143}/A_{145}, and the electric quadrupole constants B_{143}/B_{145} of the corresponding levels are also calculated.

The last three parts of this research project are executed using the high resolution, Doppler reduced method of CLIBS. In CLIBS technique the ions are accelerated by applying a high potential difference (~ 20 kV). Due to the accelerating cooling (kinematic compression) the spread in velocities in the direction of the flight is reduced several times, hence the Doppler width is reduced. The accelerated ion beam is mass separated by an 80° magnet and an isotopically pure ion beam is obtained in the interaction chambers where it interacts with light. A tunable ring dye laser of bandwidth less than 1 MHz, pumped by an Ar^+ laser beam is used as the excitation source and the dyes Rhodamine 6G and Sulforhodamine B are used to cover the wavelength region of 5700 - 6400 Å. For LIF and inter-modulated saturation spectroscopy the laser frequency is stabilized on the internal reference cavity of the dye laser and laser frequency is scanned whereas in the case of the CLIBS measurements the laser frequency is locked on the frequency of one of the components of the hyperfine structure under investigation and the post-acceleration voltage is scanned to record the hyperfine structure. The photon counting method is applied to record the hyperfine structure and a fit program is used to determine the coupling constants *A* and *B*.

During this research project altogether 149 fine structure energy levels have been investigated by laser excitation of 137 spectral lines. Various levels have been investigated for the first time and

the coupling constants of numerous levels have been improved. Most of the spectral lines were well separated from each other but in some cases blend structures are also recorded. The comparison of the three spectroscopic methods revealed that CLIBS is the much superior technique to reduce the Doppler broadening and for the accurate determination of hyperfine coupling constants.

Abstrakt

Die Coulomb-Wechselwirkung zwischen dem positiv geladenen Kern und den Elektronen bestimmt die radiale Wahrscheinlichkeitsdichte der Elektronen um den Kern und definiert somit die Energieniveaus. Die elektrische Wechselwirkung der Elektronen untereinander und zusätzlich die Wechselwirkung zwischen den mit dem Elektronenspin und dem Bahndrehimpuls verbundenen magnetischen Momenten ergeben die Feinstrukturniveaus. Atome, die eine von Null verschiedene Kernspinquantenzahl besitzen, zeigen eine zusätzliche Aufspaltung der Feinstrukturniveaus. Diese Aufspaltung wird verursacht durch die elektromagnetische Wechselwirkung zwischen dem magnetischen Moment des Kerns und dem magnetischen Moment der Elektronenhülle und wird als Hyperfeinstruktur bezeichnet. Zusätzliche kleine Verschiebungen entstehen durch die Abweichung des elektrischen Feldes des Kerns von der sphärischen Symmetrie. Die magnetische Dipolkopplungskonstante A und die elektrische Quadrupolkopplungskonstante B sind charakteristisch für jedes Feinstrukturniveau.

Zahlreiche Aspekte der aktuellen Forschung in der Astrophysik erfordern verbesserte Daten sowohl für einzelne, als auch für Gruppen von Linien der Lanthanoide. Der Einfluß der Hyperfeinstruktur ist wichtig, denn dieser kann größer sein als die meisten anderen Unsicherheitsquellen in der Analyse der Dopplerverschiebung zur Bestimmung der Geschwindigkeit von Sternen sowie der Element- und Isotopenhäufigkeit in Sternspektren. Daher ist die genaue Kenntnis der Hyperfeinstruktur unverzichtbar. Die Hyperfeinstruktur liefert außerdem wesentliche Informationen über die Elektronenhülle und Aufbau des Kerns wie z.B. Grundzustandsspin des Kerns und seine elektromagnetischen Momente. Die Elektronenkonfiguration der Lanthanoide (Elemente mit einer Kernladungszahl Z=57-71) hat mit geringeren Ausnahmen die Form [Xe] $4f^n$(5d, 6s, 6p)], wobei [Xe] die Konfiguration von Xenon ist und ‚n' zwischen 0 und 14 variiert. Die bemerkenswerten Eigenschaften der Lanthanoide stammen von der Abschirmung der 4f-Elektronen durch äußere Valenzelektronen und auch von der Tatsache, daß die Bindungsenergien der 4f-Elektronen vergleichbar sind zu den Energien der 5d- und 6s-Elektronen. Diese Tatsachen bewirken eine extrem große Anzahl von Energieniveaus der 4f-Konfigurationen und ergeben die enorm komplexen Spektren der Lanthanoide.

In dieser Forschungsarbeit wurde die Hyperfeinstruktur von Spektrallinien des Bariums (Ba) und von drei Elementen der Lanthanoide - Praseodym (Pr), Lanthan (La) und Neodym (Nd) -

untersucht. Die Koeffizienten der Hyperfeinaufspaltung A und B der beteiligten Niveaus wurden mit hoher Genauigkeit bestimmt und die Daten werden mit anderen veröffentlichen Ergebnissen verglichen.

Diese Forschungsarbeit ist in vier Teile gegliedert. Im ersten Teil wird die Hyperfeinstruktur einiger Spektrallinien von einfach ionisiertem Praseodym (Pr II) mittels drei verschiedener Laserspektroskopietechniken: Laserinduzierter Fluoreszenzspektroskopie (LIF), intermodulierter Sättigungsspektroskopie und Kollinearer Laser - Ionenstrahl - Spektroskopie (CLIBS) untersucht. Die Untersuchungen mit LIF und mit der intermodulierten Sättigungsspektroskopie wurden mit einer Flüssigstickstoff-gekühlten Hohlkathodenentladungslampe durchgeführt, während die CLIBS-Messungen mit einer Ionenquelle vom Typ Johnson durchgeführt wurden. Der zweite Teil befaßt sich mit der Kontroll-Überprüfung des Marburger Massentrenners (MARS-II), welcher von der Universität in Marburg/Lahn, Deutschland, zur Technischen Universität in Graz im Jahr 2002 überstellt wurde. Die Überprüfung wird durchgeführt unter Verwendung der gut bekannten Spektrallinie 5853.67 Å des ungeraden Isotops des einfach ionisierten Bariums (^{137}Ba II). Im dritten Teil dieser Arbeit wird die Hyperfeinstruktur von Spektrallinien des Lanthan-139 Ions (^{139}La II) untersucht. Der vierte Teil widmet sich der Untersuchung der Hyperfeinstruktur einiger Spektrallinien von zwei ungeraden Isotopen des einfach ionisierten Neodyms (^{143}Nd II und ^{145}Nd II) und der Bestimmung der Kopplungskonstanten A und B der beteiligten Niveaus. Um die Hyperfeinstruktur-Anomalie zu bestimmen, wurden die Verhältnisse der magnetischen Dipolkonstanten, d.h. A_{143}/A_{145}, und der elektrischen Quadrupolkonstanten B_{143}/B_{145} der entsprechenden Niveaus berechnet.

Die letzten drei Teile dieses Forschungsprojekts werden unter Verwendung der hochauflösenden, Doppler-reduzierten Methode CLIBS durchgeführt. Bei der CLIBS-Methode werden die Ionen durch eine angelegte hohe Potentialdifferenz (~20 kV) beschleunigt. Aufgrund der Beschleunigungskühlung (kinematische Kompression) wird die Geschwindigkeitsverteilung in Flugrichtung stark reduziert und infolgedessen die Dopplerbreite verringert. Der beschleunigte Ionenstrahl wird durch einen 80° Magneten der Ionen-Masse entsprechend aufgetrennt und dadurch wird ein isotopenreiner Ionenstrahl erzeugt, der in der Wechselwirkungskammer mit Licht wechselwirkt. Ein durchstimmbarer Farbstoff-Ringlaser mit einer Bandbreite kleiner als 1 MHz, gepumpt von einem Ar^+-Laser als Anregungsquelle und betrieben mit den Farbstoffen Rhodamine 6G und Sulforhodamine B wird verwendet, um den Wellenlängenbereich von 5700 –

6400 A abzudecken. Für LIF und die intermodulierte Sättigungsspektroskopie wird die Laserfrequenz auf den internen Referenzresonator des Farbstofflasers stabilisiert und die Laserfrequenz wird durchgestimmt, wohingegen im Fall der CLIBS Messungen die Laserfrequenz auf die Frequenz einer der zu untersuchenden Hyperfeinstrukturkomponenten stabilisiert ist und die Nachbeschleunigungsspannung verstimmt wird um die Hyperfeinstruktur aufzunehmen. Die Photonenzählmethode wird angewendet um die Hyperfeinstruktur aufzunehmen und ein Fit-Programm wird verwendet um die Kopplungskonstanten A und B zu bestimmen.

Während dieses Forschungsprojekts wurden insgesamt 149 Feinstrukturniveaus durch die Laseranregung von 137 Spektrallinien untersucht. Für mehrere Niveaus wurden zum ersten Mal die Kopplungskonstanten bestimmt und für zahlreiche Niveaus wurde die Genauigkeit verbessert. Die meisten Spektrallinien waren gut von einander getrennt, aber in einigen Fällen wurden auch Blend-Strukturen aufgenommen. Der Vergleich der drei spektroskopischen Methoden ergab, daß CLIBS die deutlich überlegene Methode ist, um die Dopplerverbreiterung zu reduzieren und die Hyperfeinkopplungskonstanten genau zu bestimmen.

Table of Contents

1 INTRODUCTION

1.1 The Development of Spectroscopy

The appearance of multicolored arc of visible light after rain showers evoked the people for thousands of years. This phenomena of rainbow effect remained an unexplained curiosity until 1666 when Sir Isaac Newton tackled the problem by studying the nature of light [1]. Newton showed that white light from the sun could be dispersed into a continuous series of colors which he called as spectrum. He used a small aperture to define a beam of light, a lens system to collimate it, a glass prism to disperse light and a screen to display the resulting spectrum. The first spectroscope of Newton fulfills all the major requirements of a modern spectroscopic instrument. William Wollaston [2] and Fraunhofer [3] observed the dark absorption lines of the sun light. The French astronomer P.J.C Janssen [4] observed a new yellow line in the solar spectrum with help of a spectroscope and later it was attributed a new element called as helium (Gk. Helios, meaning "the sun"). Thus with the help of spectroscopy an element was discovered in another part of the solar system before it was detected on earth.

Now the concept of spectroscopy is regarded as any interaction with radiative energy as a function of its wavelength or frequency. Newton's simple experiments on light marked the beginning of the science of spectroscopy and the explanation of discreet absorption and emission light quanta gave birth to most revolutionary branch of physics called Quantum Mechanics. The key experiments which brought a paradigm shift in science from classical to quantum physics are Max Planck's explanation of blackbody radiation, Einstein' explanation of the photoelectric effect and Niels Bohr' explanation of atomic structure and spectra.

The invention of the laser in 1960, development of modern techniques of high resolution spectroscopy, availability of more sophisticated spectroscopic instruments and better understanding of atomic and molecular structures had attracted several thousands of researchers around the globe in last few decades. Spectroscopy has a very special position in physics, chemistry and in science in general. It can provide accurate answers to some of the most

searching questions, particularly those with reference to atomic and molecular structure. The modern techniques of spectroscopy have a vital role in chemical analysis and in investigation of composition of planets, comets, stars and the interstellar medium.

1.2 **Applications of Laser Spectroscopy**

The relevance of laser spectroscopy for numerous applications in physics, chemistry, biology, or to environmental studies and technical problems has rapidly gained massive significance. Here only few selected applications are mentioned. For more details and comprehensive understanding the review articles [5-6] and references given therein can be consulted.

Laser spectroscopy has become an indispensible tool in many fields of chemistry to collect vital information. It is used in analytical chemistry for ultrasensitive detection of small concentration of pollutants, trace element and short-lived intermediate species in chemical reactions. The formation and defragmentation of molecules during a collision can be directly viewed in time-resolved spectroscopy with ultra short laser pulses (femtosecond lasers). Many other characteristics of laser spectroscopy in chemistry can be found in references [7-8].

The applications of laser spectroscopy in biological systems are mostly based on the absorption of laser photons, which bring the system into a non equilibrium state. The time evolution of the relaxation processes that bring the system back to thermal equilibrium are measured by laser spectroscopy. The structure of biological molecules has been successfully determined by the combination of laser induced fluorescence (LIF) and Raman spectroscopy. Fast dynamical processes like isomerization during the photosynthesis or the formation of the antenna molecules during the first steps of the visual process can be studied by time-resolved spectroscopy.

Medical applications of laser spectroscopy are enormous and it has benefitted the mankind in many diverse disciplines. The majority of the applications are based on the high laser output power which can be focused into a small volume. The strong dependence of the absorption coefficient of the living tissues on the wavelength allows selection of the penetration depth of the laser beam by selecting the suitable laser wavelength. Some of the laser spectroscopy applications are heterodyne measurement of ear drums, cancer diagnostics and therapy with the hemato-porphyrin derivative (HPD) technique ,laser induced thermotherapy of brain cancer and fetal oxygen monitoring [9].

Many sophisticated techniques of laser spectroscopy have been successfully employed for understanding of our environment, like the earth atmosphere, the water resources and the soil. The spectroscopic techniques like, direct absorption measurement, resonance two-photon ionization, photoacoustic detection, laser induced fluorescence techniques , spontaneous Raman scattering, and many other sensitive methods of laser spectroscopy have been applied to various environmental problems.

Mainly the laser spectroscopy is related to the research in the field of basic sciences. But with passage of time progress has been made and now laser spectroscopy is quite capable to solve some interesting technical problems and offer some graceful solutions. It is being used in investigations and optimizations of flames, combustion processes in fossile power stations, in car or in steel plants, measurement of flow velocities and turbulences in aerodynamic and hydrodynamic [10].

1.3 **The Development of Ion Beam Spectroscopy**

The discovery of anode rays was made by Julius Plucker when he passed an electric current though a vacuum tube in 1858 [11]. At the end of the 19^{th} century it was realized that these rays are fast moving charged particles called electrons. A few years later in a similar experiment like Plucker, Wilhelm Wien [12] observed one additional beam in an evacuated discharge tube which was travelling in opposite direction as of anode rays. This additional beam was produced by interaction of cathode rays with gas molecules in the discharge tube. These new rays were also deflected by electric and magnetic field but in opposite direction as that of electrons and it was concluded that these rays are positively charged particles. Later on J.J. Thomson thoroughly investigated the properties of positive rays and in 1912 he was able to make a positive ray analyzer, now called as mass spectrograph [13]. In this mass analyzer a beam of positive ions was passed though parallel electric and magnetic fields and the deflected beam was projected onto a photographic plate. The measurement of deflection was carried out through the mass-to-charge ratio (m/e) of the positive ions. Thomson recorded the first mass spectrum by specific m/e ratio of different ions.

Thomson's mass spectrograph was very sensitive and it could measure the residual air in the discharge tubes, traces of water vapors and even the mercury from the pumping system. The credit of two important discoveries goes to Thomson, first the discovery of electron and seconds

the discovery of isotopes. Thomson discovered the two most abundant naturally occurring isotopes of neon. The modern mass spectrometers can have very high resolution and are used in various disciplines of science like measurement of bond energies, tracer experiments in biology and medicine and dating of geological samples.

The spectroscopic studies of ions are relatively difficult to perform mainly due to two reasons. The first problem originates from the low densities of ions which can be produced in high vacuum environment of ion beams or discharge cells. At atmospheric pressure the density of a gas is ~ 10^{19} cm^{-3} whereas the typically densities of ions are in the range of 10^{4} -10^{8} cm^{-3} during experiments. The low densities of ions forced to use highly sensitive detection system. The second problem arises from the high reactivity of ions. The remedy to such a problem is to creating ions continuously (as in gas discharge) or by constantly producing and isolating ions (as in ion beams or in ion traps).

The study of ions had been discussed in literature under the following four headings: discharge spectroscopy, photoelectron spectroscopy, ion beam spectroscopy and ion-trap spectroscopy [14]. In ion beam spectroscopy, the ions are continuously produced in an ion source and are accelerated to high energies by applying potential difference and are injected into a high vacuum chamber. The high vacuum environment (~ 10^{6} mbar) minimizes the collisions and helps to maintain the initial state of the population while a mass selector can be used to select isotope or species of interest. The collimated ion beam interacts with laser beam and their interaction is observed through a suitable detection mechanism.

1.4 **The Development of Collinear Laser Ion Beam Spectroscopy (CLIBS)**

The laser was invented in 1960 [15] and the first experiment on laser-ion-beam interaction was performed in 1965 by J L Hall and coworkers at JILA [16]. In 1970, Lineberger and Woodward first time used tunable laser radiations in their experiments [17]. Andrä in 1973 introduced a new method for precision lifetime measurements in fast moving atoms [18] and in 1974 he suggested laser induced quantum beat method in fast ion beams [19]. The real beginning of Collinear laser ion beam spectroscopy (CLIBS) is attributed to S.L. Kaufman [20] who in 1976 proposed a method to achieve high resolution in fast beams. His method was based on the velocity bunching

effect and he suggested that a resolution of few MHz can be achieved at optical frequencies. In the same year Wing et al [21] applied Doppler tuning in ion-beam-laser resonance method to observe the vibration-rotational spectrum of the hydrogen molecular ion HD^+. Dufay and coworkers [22] initiated in-flight Lamb-dip technique to measure hyperfine (hf) structures in different Ba^+ isotopic beams. They used a commercial 350-keV heavy-ion accelerator and a fixed-frequency Ar^+ laser at 454 nm wavelengths. To record the hf structure the Doppler tuning was performed and a post acceleration voltage was used. In the beginning of 1977 Meier et al [23] showed with help of high resolution laser induced spectroscopy that metastable ions are very suitable for optical experiments in fast ion beams. The metastable Xe^+ ions were excited by a tunable dye laser at wavelength of 605 nm and green fluorescence light (λ= 529 nm) was recorded. Later in the same year C. Höhle et al. [24] performed high resolution spectroscopy on fast Ba^+ ion beams and determined the isotopic shift as well as hyperfine dipole and quadrupole splitting factors *A* and *B.* Both the experiments were performed on the Marburg separator MARS II at the Philipps University Marburg, Germany. Rosner et al [25-26] introduced the laser radio-frequency double resonance method in 1976, which can reduce the resolution up to the order of few kHz, a factor of 10^3 more as compared to classical CLIBS. In 1989 by using this method Berrah-Mansour et al. [27] measured the hf structure of the metastable $3d^2$ configuration in Sc II with high precision and proved that this method can improve the earlier results by more than a factor of 150.

In collinear laser ion beam laser spectroscopy (CLIBS) the ions are produced in an ion source. The large thermal spread in velocity distribution of ions in ion source results in a very high Doppler broadened line width (~ 1GHz). To reduce the Doppler broadening a high acceleration voltage is applied which through kinematic compression reduces the line width to the range of 40 - 60 MHz. After passing through a magnet a mass selected ion beam interact collinearly (or anti collinearly) with laser beam and the resulting fluorescence is recorded with a photomultiplier tube and photon counter. Doppler scanning is performed to record the hyperfine structure. In Doppler scanning a post acceleration (or deceleration) voltage is applied along the beam direction and the laser frequency is kept fixed. More details of CLIBS and its advantages and applications will be discussed in chapters 8 and 9.

The MARburg Separator (MARS –II) at the Marburg University had contributed a lot in the investigations of spectroscopic properties of various elements and in the period of 1976 – 1996 it

had produced nearly 60 publications [23-24, 28-30]. In 2002 this machine was transported to the Institute of Experimental Physics, Technical University Graz, Austria and for the last couple of years it is operational again and has been used for spectroscopic measurements. Various other groups around the world like in Canada [31-33], Sweden [34-35], Japan [36], China [37-39] and IRIS (Investigation of Radioactive Isotopes in Synchrocyclotron) in Russia [40] have contributed significantly in the field of collinear laser ion beam laser spectroscopy.

1.5 **An Overview of the Thesis**

This research thesis is virtually divided into two parts. First part (chapter 1 - 6) is mainly related to the literature survey, some fundamental aspects of hyperfine structure and various laser spectroscopic methods. The second part of the thesis (chapter 7 - 11) is concerned with the spectroscopic techniques used in this work, their experimental setups, results and discussions and conclusions. Chapter wise summary is given in next paragraphs.

In chapter 1, the initial development in spectroscopy, applications of laser spectroscopy, ion beam spectroscopy and collinear laser ion beam spectroscopy (CLIBS) were discussed. Chapter 2 is mainly related to the review work concerning the lanthanum, praseodymium and neodymium. Some basics of atomic structure are presented in chapter 3 while chapter 4 is related to discussions about the hyperfine structure. The 5^{th} chapter is related to the spectral line broadening mechanisms in spectroscopy while different laser spectroscopic techniques are mentioned in chapter 6.

In chapter 7 the experimental setup of inter-modulated laser induced fluorescence spectroscopy is discussed and hyperfine structure of the spectral lines of singly ionized praseodymium (Pr II) is compared with three spectroscopic techniques. The detail theoretical discussion about CLIBS is given in chapter 8 while the experimental setup of CLIBS and it various parts are explained in chapter 9. The experimental investigations with the help of CLIBS of various elements like singly ionized barium, lanthanum and neodymium and are discussed in chapter 10. Finally the chapter 11 is devoted to the conclusions.

2 LITERATURE SURVEY

This chapter is devoted to the literature survey of the lanthanum (La), praseodymium (Pr) and neodymium (Nd). First a short overview of the lanthanide and their importance with respect the spectroscopic investigation is given. Then the physical and chemical properties in addition to the experimental investigations of the neutral as well as La II, Pr II and Nd II are summarized.

2.1 An Overview of Lanthanides

The lanthanides are a group of elements with atomic number $Z = 57 – 71$, i.e. from lanthanum to lutetium. They are known as lanthanides because the lighter elements in the series are chemically similar to lanthanum. Lanthanides possess the common feature of xenon (Xe) structure with two or more outer electrons. These fifteen elements ($Z = 57 - 71$) along with chemically similar elements scandium and yttrium are also called rare-earth elements. The electronic structure of the lanthanide elements, with minor exceptions is [Xe] $4f^n$ (5d, 6s, 6p) and in their compounds in most cases the general configuration of ions is [Xe]$4f^N$. The exceptional properties of the lanthanides originate from the shielding of the 4*f* electrons from outer valence electrons and also due to the fact that binding energies of 4*f* electrons are comparable to the energies of 5*d* and 6*s* orbitals [41]. These considerations and the fact that an extremely large number of quantum states originate from the $4f^N$ configuration results in generally tremendously complex spectra of lanthanides ions.

The study of the lanthanide elements in astrophysics started with the invention of spectroscopy during the latter half of the 19^{th} century [42]. Lanthanide elements were detected in stellar spectra as early as 1913 [43]. Abundances of heavy elements in stars provide vital information about nuclear processes occurring in the stellar interiors and the mixing processes that bring them to the observable surface [44]. Lanthanide elements found in chemically peculiar (CP) stars of the upper main sequence, metal-deficient stars of the galactic halo and in the sun are of particular current interest [45-46]. Relatively large lanthanide abundances have been discovered in many galactic halo stars. These are among the oldest stars in our galaxy and have great importance in understanding neutron-capture nucleosynthesis in novae and supernovae and transport of mass

between the stellar interior and the photosphere [47]. Many aspects of current research in CP stars demands improved data for individual as well as group of lines in lanthanides. The atomic properties of lanthanides are not only fundamental for astrophysics but these are also essential in the design of the commercial high intensity discharge lamps [48] and in the use of their spectra to explore the crystalline structure of divalent and trivalent crystal salts. The study of oscillator strengths and lifetime of the levels of lanthanides atoms and ions are also vital for the development of gas lasers in which lanthanides are used as an active medium. The data on the radiative constants of lanthanides are also imperative for exploration of the plasma in thermonuclear devices, where lanthanides are present as impurities. The rising attraction in radiative constants and other spectroscopic parameters of lanthanides atoms and ions is due to their significance in astrophysical exploration, such as [49]:

- Determination of lanthanides in the sun.
- Examination of the processes taking place in the stellar atmosphere.
- Understanding the origin of sun and other stars.
- Theoretical authentication of nucleosynthesis of chemical elements in astral matter.

There is an increasing demand in astrophysical community for accurate spectroscopic data i.e. hyperfine structure, isotope shift, radiative life time, oscillator strength, branching fraction, wavelength and radiative transition rate of rare-earth ions [46]. Modeling the atmospheric structure requires reliable abundance estimation.

The importance of hyperfine structure and isotope shift (IS) was first highlighted by Abt [50]. Now it is well known fact that hyperfine structure can have large effects on stellar absorption line profile and the abundances of the elements deduced from stellar spectra. The effects of hyperfine structure are important because they can be larger than most other sources of uncertainties in the analysis [51]. Thus for accurate determination of abundances in stellar spectra the precise knowledge of hyperfine structure is indispensable.

In this research work the hyperfine structure of spectral lines of barium and three lanthanides elements; lanthanum, praseodymium and neodymium has been investigated by the method of collinear laser ion beam spectroscopy in the wavelength region of dyes Rhodamine 6G and Sulforhodamine B. The magnetic dipole coupling constants A and the electric quadrupole coupling constant B of the involved levels of Ba II, La II, Pr II and Nd II have been determined

with high accuracy and the data are also compared with literature values. For neodymium two odd isotopes ^{143}Nd and ^{145} Nd are studied and for comparison in addition to CLIBS the inter-modulated saturation spectroscopy of Pr II has also been performed. The barium isotope, ^{137}Ba II is used for the control-check of the MARS-II.

2.2 Lanthanum (La): An Element

Lanthanum is the first element of the lanthanides series, which any way take their name from it, due to similar chemical properties. Lanthanum differs from other lanthanides because its ground state configuration contains no 4*f* electrons which is a specific feature of all other lanthanides. The name lanthanum is due to the Greek word lanthaneia, which means "hidden". A Swedish chemist, Carl Gustav Mosander, discovered lanthanum in 1839. Lanthanum is a soft, malleable, silvery white metal and can easily oxidize. A cubic centimeter sample of lanthanum will completely oxidize within a year. Lanthanum is the most strongly basic of all the trivalent lanthanides and this property attracted the Mosander to isolate and purify the salts of this element. The major production of lanthanum (more than 25 %) comes from the ores of monazite (Ce, La, Th, Nd, Y)PO_4, and bastnaesite (Ce, La, Y)CO_3F, through an ion exchange process. The composition of lanthanum in earth's crust is nearly 0.0018%.

Lanthanum has two natural isotopes, a stable isotope ^{139}La and a radioactive isotope ^{138}La. The natural abundance of ^{139}La is 99.91% and that of ^{138}La is 0.01%. Altogether lanthanum have 38 radioisotopes with ^{138}La being the most stable one with a half-life of 1.05×10^{11} years and the half life of ^{137}La is 60,000 years. Most of the remaining radioactive isotopes have half-lives less than 24 hours [52]. Some of the chemical and physical properties of La are listed in Table 2.1.

Table 2.1: *Some of the physical and chemical properties of lanthanum [53]*

Symbol	La	Color	silvery white
Atomic number (Z)	57	Crystal structure	hexagonal
Mass number (A)	138.90547	Thermal conductivity	13.4 W/m-K
Melting point	920 °C, 1688 °F	1st Ionization energy	538.1 kJ/mol
Boiling point	3464 °C, 6267 °F	Electron-negativity	1.10 (Pauling scale)
Density	6.162 g/cm^3 @ 300 K	Oxidation states	3, 2 (strongly basic oxide)
Nuclear spin *I* (^{139}La)	7/2	Atomic radius	187 pm
Nuclear magnetic moment μ_I (^{139}La)	2.7830455 (9) μ_N	Electric quadrupole moment Q (^{139}La)	0.20 barn

Lanthanum consists of a central xenon (Xe) core with three outer electrons which can take part in interactions. The ground state electronic configuration of La I is; $1s^2\ 2s^2\ 2p^6\ 3s^2\ 3p^6\ 3d^{10}\ 4s^2 4p^6\ 4d^{10}\ 5s^2\ 5p^6)\ 5d^1\ 6s^2\ ^2D_{3/2}$ and for La II is; $1s^2\ 2s^2\ 2p^6\ 3s^2\ 3p^6\ 3d^{10}\ 4s^2 4p^6\ 4d^{10}\ 5s^2\ 5p^6)\ 5d^2\ ^3F_2$. Due to an odd number of protons Z = 57, the ground state nuclear spin of all the isotopes of lanthanum is non-zero i.e. for ^{139}La, I = 7/2 and ^{138}La, I = 5 etc. The presence of three electrons which can take part in interaction and relatively larger value of nuclear spin *I*, the atomic spectra of ^{139}La is quit dense and complicated. Although a significant spectroscopic work had already done on Lanthanum but still there is room for more investigations and improvement of the results.

Uses of Lanthanum:

- Lanthanum hexaboride (LaB_6) has a low work function and very high electron emissivity.
- The luminance and the lifetime of LaB_6cathodes are 10-15 times better than tungsten. LaB_6 is used in electron microscope, microwave tubes, electron beam welding, X-ray tubes, electron lithography and free electron lasers [54].
- LaB_6 is a superconductor at temperature of 0.45 K [55].
- Lanthanum fluoride (LaF_3) is a vital constituent of a heavy fluoride glass named ZBLAN. This glass has higher transmittance in the infrared range and is thus used for fiber-optical communication systems [56].
- Carbon arc lights are produces from lanthanum which are used in motion picture industry for projector lights and studio lightning.
- Lanthanum is used in steel to improve its malleability and ductility.
- Lanthanum introduces special refractive properties in glass and is used in expensive camera lenses.
- Lanthanum is also used to make flint for lighters.
- Lanthanum is used for cracking catalyst as hydrocarbons in oil refineries.
- As alloys, lanthanide is used in fuel cells and batteries.
- As a medicine it is used for treating higher blood phosphate levels in patients who are on dialysis due to kidney disease.

Lanthanum has a moderate level of toxicity and should be handled with care.

2.3 Spectroscopic Studies of Lanthanum: An Experimental Review of La I and La II Spectral Lines

Rybar in 1911 [57] published the measurements of Zeeman effect in lanthanum spectra but he was not able to explain most of the complex patterns. Popow [58] in 1914, from the observation of Zeeman effect find six La lines consisting of triplet P and triplet D terms. In 1914 Paulson [59] published a list of constant differences occurring between wave number related to La spark lines. In 1927 A.S. King and E. Carter [60] investigated the temperature behavior of many spectral lines of La in an electric furnace. Meggers in 1927 published two papers about the discovery of new energy levels in ionic as well as in neutral lanthanum. In first paper he classified about 110 spectral lines of La^{+} which resulted in 22 new energy levels [61] and in second paper he presented 48 energy level for neutral La and combination of these energy level accounted for 130 spectral lines [62]. Anderson in 1934 investigated the hyperfine structures of 25 lines of La I and determined the absolute overall widths of each member of the $5d^26s^4F$ levels and computed the nuclear g-factor and magnetic moment [63]. In 1957 Ting [64] measured the hyperfine structure of ^{139}La in the ground level $5d6s^2\ ^2D$ by the atomic-beam magnetic resonance method and determined the magnetic dipole interaction constants *A* and the quadrupole interaction constants *B* of the involved levels. Ahmed et.al [65] recorded the Fourier transform spectrum of lanthanum in the energy range 3500 - 14500 cm^{-1}, classified the even configurations $(5d + 6s)^3$ and determined the magnetic hyperfine constants of 29 even levels. W. Fischer [66] in 1972 investigated the hyperfine structure of two lines of highly enriched ^{138}La isotope by means of optical interference spectroscopy and determined of the nuclear electric quadrupole moment. In 1970s Childs and Goodman performed a number of experiments to study the hyperfine structure of ^{139}La using atomic beam laser spectroscopy and resolved closely spaced doublet spectral lines [67-68]. In 1980 Höhle and coworkers [28] measured the hyperfine structure of the ^{139}La II line, $5d^2\ ^3F \rightarrow 5d4f\ ^3F_4^0$ at λ = 579.8 nm, by means of collinear laser ion beam spectroscopy and not only observed $\Delta F = 0, \pm 1$ hyperfine transitions but also observed $\Delta F = \pm 2$ transitions. The interpretation of $\Delta F = \pm 2$ transitions as well as their relative line strengths was explained on the basis of a three-quantum process. The same group in 1981 [69] used the high resolution technique of CLIBS and measured the hyperfine structure constants of all the $5d^2$ and 5d6s levels in ^{139}La. In 1988 Childs [70] used the atomic-beam laser-rf double-resonance method to measure precisely the dipole and quadrupole hyperfine structure constants of 11 levels of the $5d^26s$

configuration and four levels of the $5d^3$ configuration of ^{139}La . The results were compared with multi-configuration Dirac-Fock (MCDF) ab initio calculations. In 1990 Caiyan et.al [71] used the techniques of Doppler-free intermodulated fluorescence, Doppler-limited laser-induced fluorescence and optogalvanic spectroscopy in a homemade hollow-cathode discharge tube to investigate the hyperfine structure coupling constants of La I.

Maoscheng et.al Guang-Wu Li et.al and Ma Hong (2000-2002) [38, 72-73] applied the method of CLIBS and determined the hyperfine coupling constants of many spectral lines of singly ionized lanthanum. Derkatch and coworkers in 2002 [41] investigated experimentally as well as theoretically the life time of metastable levels in La II and found that experimental results are in good agreement with the relativistic Hartree-Fock calculations including core polarization. Schef et.al in 2006 [74] used the laser and radio-frequency double resonance (LRDR) technique in a collinear geometry and recorded the hyperfine structure of the 5d 6s b^1D_2 level in La II. The accuracy of their results was more than 100 times better previous published results. Furmann and coworkers (2007-2010) [75-79] applied the techniques of laser induced fluorescence and optogalvanic spectroscopy in a hollow cathode discharge and investigated numerous energy levels in neutral as well as singly ionized lanthanum. The group classified many energy levels in La I and La II and determined the hyperfine coupling constants for these levels. Majority of the investigated levels were reported first time. Dembczyński et.al [80] applied the quantitative method to determine two-body contributions to the fine and the hyperfine structure, resulting from the excitations from electronic closed shells to open shells and from open shells to empty shells. On the basis of experimental data available, he analyzed the configuration $(5d+6s)^3$ in lanthanum atom. In 2010 Nighat et al. [81] performed LIF spectroscopy in hollow cathode discharge on free La atoms and ions. She investigated more than 150 spectral lines and determined hyperfine coupling constants of 99 energy levels of La I and 28 energy levels of La II. To obtain the desired laser wavelengths she used the dyes Coumarin 102, Coumarin 30 and Rhodamine 700 nm a single mode ring dye laser. N. Anjum et al. [82] in 2011 investigated five lines of La II using the method of CLIBS and determined the hyperfine coupling constants of eight energy levels. Recently Güzelçimen and coworkers [83] has applied the method of LIF and optogalvanic spectroscopy and has classified 176 spectral lines of La I. In these investigations magnetic dipole hyperfine structure constants *A* for 73 upper levels has been determined out of which the coupling constants *A* for 18 levels are reported for the first time.

2.4 **Praseodymium (Pr): An Element**

A Swedish scientist C.G. Mosander in 1841 discovered an oxide which was named as “didymium”. In 1885 the Austrian chemist Baron Carl Auer von Welsbach separated didymium into two elements Praseodymium (Pr) and Neodymium (Nd). The name praseodymium originated from the Greek words "*prasios didymos"* meaning "*green twin*". The rare-earth element praseodymium is the 3rd element of the lanthanides series with atomic number Z = 59 and atomic weight A = 140.9076 a.m.u. The metallic Pr is a soft, silvery, malleable and ductile martial. Its oxidation rate is somewhat less than lanthanum, neodymium, cerium or europium, but it does develop a green oxide coating when exposed to air. Like lanthanum, praseodymium is also primarily obtained from Monazite sand through an ion exchange process. Some of the chemical and physical properties of Pr are listed in Table 2.2.

Table 2.2:Some of the physical and chemical properties of praseodymium [53]

symbol	Pr	Color	silvery white
Atomic number	59	Crystal structure	hexagonal
Standard atomic weight	140.90765	Thermal conductivity	12.5 W/m-K
Melting point	935 °C, 1715 °F	1st Ionization energy	527 kJ/mol
Boiling point	3520 °C, 6368 °F	Electron-negativity	1.13 (Pauling scale)
Density	6.77 g/cm^3 @ 300 K	Oxidation states	4, 3, 2 (mildly basic oxide)
Nuclear spin I	5/2	Atomic radius	182 pm
Nuclear magnetic moment μ_I	4.2754 (5) μ_N	Electric quadrupole moment Q	-0.066 barn

Praseodymium has only one stable natural isotope $^{141}Pr_{59}$ (100% natural abundance) whereas 38 radioisotopes of Pr have been characterized. The most stable radioisotope is ^{143}Pr with half-life of 13.57 days and the half-life of ^{142}Pr is 19.12 hours. The half-lives of all the remaining radioisotopes are less than 6 hours and most of them have half-lives of seconds [52].

Like other elements of the lanthanides group, praseodymium also consists of a central xenon core with five outer electrons which can take part in interactions. The ground state configuration of Pr I is ($1s^2\ 2s^2\ 2p^6\ 3s^2\ 3p^6\ 3d^{10}\ 4s^2 4p^6\ 4d^{10}\ 5s^2\ 5p^6$) $4f^3 6s^2$ ($^4I°_{9/2}$) and of Pr II it is ($1s^2\ 2s^2\ 2p^6\ 3s^2\ 3p^6\ 3d^{10}\ 4s^2 4p^6\ 4d^{10}\ 5s^2\ 5p^6$) $4f^3$($^4I°_{9/2}$) 6s (9/2,1/2)°$_4$. The nuclear spin quantum number I of ^{141}Pr is

5/2 and magnetic moment μ_I is 4.2754 μ_N. The presence of five electrons in Pr I and four electrons in case of Pr II in an open 4*f* shell configuration the spectrum of praseodymium is extremely complex with very large number of lines.

Uses of Praseodymium:

- Praseodymium is being used to make an alloy named as "Misch metal" which is used to make cigarette lighters.
- Praseodymium along with magnesium is used to make high strength metal alloys that are being specially used for manufacturing aircraft engines [84].
- Due to the excellent refractory properties the oxides of praseodymium are a part of the core material of carbon arc lights which are popularly used in movie industry for the purpose of projection and studio lighting.
- Praseodymium salts along with a few other substances are used to add an intense yellow color in the manufacturing of glasses and enamels.
- Praseodymium is also used as a colorant in the making a special type of glass named didymium glass which is used for making welder's and glass blower's goggles [53].
- Usually, neodymium is used in high strength magnets but sometimes to reduce the cost, neodymium is replaced by praseodymium.
- Silicate crystals doped with praseodymium ions have been used to slow a light pulse down to a few hundred meters per second [12].
- A strong magneto-caloric effect produced in praseodymium nickel alloy ($PrNi_5$) has allowed to approach within one thousands of a degree of absolute zero.[13]
- Praseodymium doped fluoride glass is used as a single mode fiber optical amplifier [14].
- A colored stone made from praseodymium and synthetic cubic zirconia gives yellowish green color which is used for making jewelry.

Generally the toxicity of praseodymium is mild to moderate. However, inhalation of its dust or fumes could be hazardous for health. Therefore suitable safety measures are necessary to handle it for commercial uses.

2.5 Spectroscopic Studies of Praseodymium: An Experimental Review of Pr I and Pr II Spectral Lines

The first study of the hyperfine structure of Pr was made by A. S. King in 1928 [85]. He observed the spectra in an electric furnace and gave reliable wavelengths measurement and observed 1018 lines for Pr I and Pr II in the wavelength region 3111 - 6828 Å. White in 1929 [86] studied 173 spectral lines of Pr II in the wavelength range 3920 - 4860Å and from his investigations he discovered the spin quantum number I = 5/2 of the nucleus of the praseodymium atom. Rosen and coworkers in 1941 [87] investigated the Zeeman effect of Pr lines in the region 2400 - 7100 Å. Baker and Bleaney in 1955 [88] determined the hyperfine structure constants of many energy levels of Pr II. In 1962, Amado et al. [89] used atomic beam magnetic resonance method to investigate the hyperfine structure of the short living (19 hours) isotope (Pr^{142}) of praseodymium and determined its splitting factor, nuclear spin, electric quadrupole and magnetic dipole hyperfine constants, nuclear moment and quadrupole moment. In 1965 Reader and Sugar [90] found the nuclear moment of Pr^{141} by using Goudsmit-Fermi-Segrè formula. J F Wyart et al. [91] used Racah's method to improve the energies of the energy levels of configuration $4f^N(5d + 6s)$ for Pr II and Pr III. Ginibre [92-94] used the method of high resolution Fourier transform (FT) spectroscopy to investigate to the spectrum of Pr II in the wave number range of 2783 - 27920 cm^{-1}. She classified a large number of unidentified lines and improved the energies values of many known levels. In 1987 M. N. Reddy and G. N. Rao [28] classified 121 spectral line of Pr I and Pr II by using laser optogalvanic spectroscopy in a hollow cathode discharge lamp. Childs and Goodman [95] with the help of laser-rf double-resonance method classified many lines of Pr II in the wavelength range of 5746 – 6148 Å. In 1982, Macfarlane et al. [96] improved the value of nuclear magnetic moment of Pr^{141} μ_N = 4.2754(5) by two orders of magnitude.

H Iimura et al. [97] investigated the hyperfine structure of Pr II by using the high resolution method of collinear laser ion beam spectroscopy and measured the magnetic dipole and electric quadrupole constants for many levels. In 1996, Kuwamoto et al. [98] used the method of laser-atomic beam fluorescence spectroscopy to investigate hf structure of Pr I spectral lines in the wavelength range of 5440 - 5960 Å. They measured the coupling constants for 57 levels, found 18 new transitions and determined the energies and electronic total angular momentum for 11 levels. Maosheng et al and Rivest et al in the years 2000 and 2002 [99-100] investigated the hf

structure of many spectral lines of singly ionized Pr by the methods of CLIBS and determined the electric quadrupole and magnetic dipole coupling constants of the involved levels. The investigations of B Furmann et al. [101] contributed a lot for the hyperfine structure measurements of neutral and singly ionized praseodymium. They used the method of laser induced fluorescence spectroscopy in a hollow cathode discharge and discovered 57 new levels for Pr I and 45 new levels for Pr II and determined the magnetic dipole and the electric quadrupole constant of the investigated levels. In 2007, R. Li et al. [102] measured the oscillator strengths of many levels of Pr II levels by the method of fast-ion-beam laser-induced-fluorescence. In 2010, S Oppel et al. [103] used the Pr I spectral lines in the IR region to stabilized a diode laser within the frequency of 1.4(1) MHz for an average time of 0.2 seconds. N.Anjum et al. [104] measured accurately the hyperfine coupling constants of singly ionized praseodymium by using the method of CLIBS and compared the results with literature values. B Gamper et al. [105] in 2011, recorded a highly resolved Fourier transform spectrum of the Pr I and Pr II and classified more than 1200 lines and discovered 24 new Pr I levels. In 2011 K. Shamim et al. and T. I. Syed et al. [35, 36] used the method of laser induced fluorescence spectroscopy in a hollow cathode discharge lamp and discovered nearly 94 new levels and classified more than 500 spectral lines of Pr I. Recently N. Akhtar and L. Windholz [106] have used the Fourier transform spectrum to improved the energy values for 227 known fine structure levels of singly ionized praseodymium.

2.6 **Neodymium (Nd): An Element**

Neodymium (Nd) is the 4^{th} element of the lanthanides group. As mentioned in one of previous sections the Austrian chemist Baron Carl Auer von Welsbach separated it from didymium in 1885. Neodymium is a bright silvery-yellow lustrous metal. It is very reactive and quickly blemishes in air and the coated surface formed do not protect the metal from further oxidation. Therefore it must be stored away from contact with air i.e. in a light mineral oil or under inert gasses.

Neodymium does not exist in nature as the free element. It is produced from monazite and bastnaesite that contain small amounts of all the rare earth metals. China, United States, Brazil, India, Sri Lanka, and Australia are the leading countries for mining of neodymium. The reserves of neodymium are estimated about eight million tones. Although neodymium belongs to the rare earth elements but it is not rare at all. In the earth crust its abundance is ~ 38 mg/kg, which is the

second highest among rare-earth elements after cerium. Nd exists in two allotropic forms; double hexagonal structure transforms to a body-centered cubic structure at temperature about 863 °C. Some of the chemical and physical properties of La are listed in Table 2.3

Naturally occurring neodymium is a mixture of five stable isotopes, ^{142}Nd, ^{143}Nd, ^{145}Nd, ^{146}Nd and ^{148}Nd and two radioisotopes, ^{144}Nd and ^{150}Nd. The natural abundance of naturally occurring isotopes according to increasing mass is 27.2%, 12.2%, 8.3% , 17.2% and 5.7% while the abundance of two radioisotopes is 23.8% and 5.6%, respectively [52]. Up to now thirty- three radioisotopes of neodymium have been characterized. The half-life of the two naturally occurring radioisotopes are 2.29×10^{15} years (alpha decay) for ^{144}Nd and for ^{150}Nd 7×10^{18} years (double beta decay). The half-lives of all the remaining radioactive isotopes are less than 11 days and the majority of them have half-lives less than 70 seconds.

Table 2.3: Some of the physical and chemical properties of neodymium [53].

Symbol	Nd	Color	silvery white
Atomic number	60	Crystal structure	hexagonal
Standard atomic weight	144.242(3)	Thermal conductivity	16.5 W/m-K
Melting point	1024 °C, 1875 °F	1st Ionization energy	533.1 kJ/mol
Boiling point	3074 °C, 5565 °F	Electron-negativity	1.14 (Pauling scale)
Density	7.01 g/cm3 @ 300 K	Oxidation states	3, 2 (mildly basic oxide)
Nuclear spin I (^{143}Nd)	7/2	Atomic radius	181 pm
Nuclear magnetic moment μ_I (^{143}Nd)	-1.065(5) μN	Electric quadrupole moment Q (^{143}Nd)	-0.63(6) barn

Like lanthanum and praseodymium, neodymium also has a central xenon core but with six outer electrons which can take part in interactions. The ground state configuration of Nd I is ($1s^2$ $2s^2$ $2p^6$ $3s^2$ $3p^6$ $3d^{10}$ $4s^2$$4p^6$ $4d^{10}$ $5s^2$ $5p^6$) $4f^4$ $6s^2$ ($^5I_4$) and of Nd II it is ($1s^2$ $2s^2$ $2p^6$ $3s^2$ $3p^6$ $3d^{10}$ $4s^2$$4p^6$ $4d^{10}$ $5s^2$ $5p^6$) $4f^3$($^5I_4$) $4f^4$ $6s$ $^6I_{7/2}$. Due to even number of protons Z = 60 only two odd isotopes (^{143}Nd and ^{145}Nd) have nuclear spin quantum number I = 7/2 while for the five even isotopes the nuclear spin quantum number is zero. A hyperfine splitting of a fine structure level is observed only if the nuclear spin quantum number is non-zero. The magnetic dipole moment of ^{143}Nd is μ_I = -1.065(5) and the electric quadrupole moment Q = -0.63(6) barn [107]. The presence of six electrons in valence shell which can take part in interaction, due to open 4*f* shell configuration,

occurrence of seven stable isotopes and due to relatively larger value of nuclear spin quantum number, the spectra of neodymium is tremendously complex with very large number of lines.

Neodymium has been found and studied in many CP stars like the HD 101065 [108], the Am star β Aur [109] and the HgMn star HR 7775 [110]. As a stable nuclear species, Nd is also useful for estimating the age of the Galactic halo [111]. The Th:Nd (Thorium: Neodymium) abundance ratio in G-dwarf stars have been measured to estimate the age of galaxy [112].

Uses of Neodymium:

- Neodymium compounds were first commercially used as glass dyes in 1927 and for a long time they lingered in glass industry.
- Neodymium-Samarium dating is useful for determining the age relationship of the rocks.
- Due the unusually large specific heat capacity at liquid-helium temperatures neodymium is useful in cryocoolers.
- The magnets made form neodymium ($Nd_2Fe_{14}B$) are the strongest permanent known magnets. A Nd magnet of a few grams can hold a thousand times its own weight. These magnets are commonly used in products such as microphones, professional loudspeakers, in-ear headphones, and computer hard disks, where low magnet mass or volume, or strong magnetic fields are required.
- Larger neodymium magnets are used in high power versus weight electric motors (for examples in hybrid cars) and generators (for example aircraft and wind turbine electric generators).
- Neodymium is also used in rare-view mirrors of vehicles to diminish the glare at night.
- Neodymium glass is used in incandescent light bulbs. It blocks the yellow light in bulbs and provides white light which is more like sunlight.
- Neodymium is helpful in predicting the size and strength of volcanic eruption. The composition of neodymium isotopes in lava is related to size of volcanic eruption. By determining the isotopic concentration in lava the prediction of coming eruption can be made and the residents can be warned according to the intensity of lava eruption.
- Neodymium is also used with various other substrate crystals, such as yttrium aluminum garnet, in the Nd:YAG laser. The Nd:YAG laser is one of the most commonly used solid-state lasers.

- Neodymium-doped crystals (typically Nd:YVO_4) generate high-powered infrared laser beams which are converted to green laser light in commercial diode-pumped solid-state (DPSS) hand-held lasers and laser pointers.
- The High Energy Laser Embodying Neodymium (HELEN) i-terawatt neodymium-glass laser installed at UK Atomic Weapons Establishment (AWE), can create plasmas of around10^6 K. It is used to acquire data for modeling the density, temperature and pressure inside warheads [113].
- Neodymium has low to moderate toxicity level. Neodymium dust and salts are very irritating to the eyes and skin. Therefore suitable safety measures are necessary to handle it for extensive uses.

2.7 Spectroscopic Studies of Neodymium: An Experimental Review of Nd I and Nd II Spectral Lines

The first spectroscopic study of neodymium was performed in 1933 by A.S. King [114] in an electric furnace and gave reliable wavelengths measurement and observed of 276 lines. The first preliminary measurements of Zeeman effect in Nd were reported by H.J. Vliet [115] who in 1939 investigated 263 spectral lines. In 1942 Albertson et al [116] measured the first spark spectrum of Nd II and classified 367 lines arising from 30 lower and 57 upper levels. The first report on the isotope shift in neodymium spectrum belongs to Klinkenberg [117], who in 1945 observed 60 Nd I spectral lines with resolved or nearly resolved isotope structure. For Nd I, the first energy levels were found a few years later by Ph Schuurmans [118]. The nuclear spins of ^{143}Nd and ^{145}Nd were first measured by Bleaney and Scoil in 1950 [119] by using paramagnetic resonance technique and their results were confirmed by Murakawa and Ross [120] by optical hyperfine structure measurements. Bleaney et al. in 1954 [121] and Halford et al. in 1958 [122] estimated the quadrupole moments of ^{143}Nd and ^{145}Nd isotopes. The isotope shift in singly ionized neodymium was first time measured by Nöldeke in 1955 [123]. He measured the transition of the types $4f^4 6p–4f^4 6s$ and $4f^4 6p–4f^4 5d$ in the wavelength region 4012 – 5320 Å. Hassan and Klinkenberg [124] in 1963 investigated a detailed spectrum of neodymium. They classified 555 lines of Nd I in an electrode-less discharge tube, reported Zeeman effect measurements for 110 spectral lines observed in the hollow cathode operating in the weak magnetic field and also discussed the isotope shift measured by various authors. In the same year Spalding [125]

measured the hf structure and nuclear moments of ^{143}Nd and ^{145}Nd by using atomic-beam resonance method. In 1971, Blaise et al [126] investigated the spectra of Nd I and Nd II in the wavelength range 2450 - 40500 Å, emitted by an electrode-less discharge tube. They measured nearly 25000 wavelengths by means of a computer and from Zeeman patterns of strongest lines classified about 1500 energy levels. Childs and Goodman [127] in 1972, investigated the hyperfine structure of ^{143}Nd and ^{145}Nd isotopes by using the atomic beam resonance method. Later Childs [128] used the more accurate method of atomic beam laser-rf double resonance to study the hyperfine structure of high angular moment states in ^{143}Nd I and ^{145}Nd I. In 1981, Van Leeuwen et al [129] use crossed laser atomic beam and actively stabilized C.W ring laser to investigate the hyperfine structure and isotope shift in 9 spectral lines of Nd I. Subsequently isotope shifts in Nd I and Nd II had been investigated for hundreds of lines in many different kinds of experiments (Fabry-Perot spectroscopy, Fourier transform spectroscopy) by various groups [123-124, 130-134]. The first study of optical isotopic shift in Nd II by collinear laser ion beam spectroscopy was reported by Lu Fuquan et al [135] in 1991. In their investigations they measured the optical isotope shifts in the $4f^{4}5d^{6}6K_{9/2} - (23537)^{0}_{9/2}$ transition and deduced the changes in mean-square nuclear charge radii among the isotopes with mass numbers 142-150. Later Hongliang [136-138], Macfarlane [139] and Rosner [33] also used the method of CLIBS to determine the isotope shift of neodymium for various spectral lines. The incomplete data on spectral line classifications up to 1960 was a major barrier to determine the accurate values of oscillator strength and radiative life time of atomic and ionic excited states of rare-earth elements. The first measurement of lifetime of singly ionized neodymium was carried out by Andersen and coworkers in 1975 [140]. They applied the beam foil method and determined the life time of four Nd II levels. In 1980, Marek and Stahnake [141] measure the lifetime of 18 Nd I levels in the energy range 16000 – 25000 cm^{-1} by using the delayed-coincidence method with pulsed laser excitation. Two year later Gorshkov et al [142] measured the lifetime of 38 levels of Nd I and 11 energy levels of Nd II in the energy range of 17000 – 26000 cm^{-1}. They used the method of delayed-coincidence but crossing atomic and pulse electron beams were used for excitations. Ward et al [143-144] incorporated the laser ion beam technique using intracavity excitation and measured the lifetime of 24 Nd II levels. Faquan and Wei [145-146] applied the time-resolved technique of collinear laser ion beam laser spectroscopy to determine the radiative lifetime of singly ionized neodymium. Pinciue et al. [44] and Scholl et al. [147] applied CLIBS and two variants of beam-laser techniques and determined altogether the radiative lifetime of 48 levels of

Nd II and 33 levels of Pr II. The energies of the upper levels were less than 30000 cm^{-1} and lifetime were in the range of 7-170 ns. The largest-scale laboratory study (to date) of Nd II transition probabilities using modern methods was performed by Hartog et al. in 2003 [148]. They measured radiative lifetimes for 168 odd-parity levels of Nd II using laser-induced fluorescence. The lifetimes were combined with branching fractions measured using Fourier-transform spectrometry to determine transition probabilities for over 700 lines of Nd II.

Although very large numbers of research reports are available in literature in which CLIBS has been used to study several different spectroscopic parameters of Nd II, like isotopes shifts [33, 138] branching fractions and oscillator strengths [149] etc, surprisingly only two papers are available in literature using CLIBS to study hf structure and magnetic dipole and electric quadrupole coupling constants *A* and *B* of Nd II. The first study was performed by Maosheng et al [99]. Seven spectral lines in the range 570-583 nm involving 10 fine structure energy levels were presented. The second such study was reported by Rosner et al [33] in which 110 transitions in Nd II in the wavelength range 418 - 465 nm are presented. The lower states of these transitions includes the ground state and 10 metastable even-parity states with energies up to 5986 cm^{-1} and 64 odd-parity upper states with energies up to 29434 cm^{-1}.

Recently N. Anjum et al. have investigated more than 100 spectral lines of two odd isotopes of singly ionized neodymium ($^{143}Nd^{+}$ and $^{145}Nd^{+}$) by high resolution technique of collinear laser ion beam spectroscopy. One journal publication [150] is ready to be submitted in which CLIBS is used to determine the hyperfine structure constants of 6 metastable even-parity lower levels and 19 odd-parity upper levels of $^{143}Nd^{+}$. The magnetic dipole interaction constants *A* and the electric quadrupole interaction constants *B* were determined with high accuracy. For some levels the hf interaction constants were measured for the first time using CLIBS. At least two more journal publications are expected in coming months.

3 A SHORT REVIEW OF ATOMIC STRUCTURE

The idea of "atom" goes back to the time of Democritus (around 460 B.C) when scientists believed that all matter is made of smallest, indivisible particles called as an atom (atom meaning not divisible). The silence of nearly 2000 years about the nature of the matter was broken by John Dalton in 1802, when he presented his atomic theory. In his theory he claimed that the matter is made of extremely small particles called as atoms which cannot be subdivided, created or destroyed. The atoms of a particular element are identical in all properties like mass and size whereas the atoms of the different elements are different. In a chemical reaction the atoms are combined, separated or rearranged and in a chemical compound the atoms of different elements are grouped together in simple whole numbers. Gustav Kirchhoff and Robert Bunsen [151] in 1859 observed that the atoms can only absorb or emit light of certain discrete wavelengths. These wavelengths which are characteristics of each element are called as the absorption or emission spectra of the elements. In 1869, the Russian chemist Dmitri Mendeleev created the first version of the periodic table of elements based on the similar properties and predicted the properties of elements yet to discovered. In 1897, the English physicist J.J. Thomson discovered the electron and proposed a model for the structure of the atom. Later on the detailed spectral study of the simplest atom, the hydrogen atom, was carried out by Lyman, Paschen, Brackett and Pfund.

In the modern era of spectroscopy and for the true understanding of the atomic structures, the knowledge of the theory of quantum mechanics is indispensable. Quantum mechanics is the most unified theory of atomic physics which is mainly attributed to Schrödinger but the work of de Broglie, Heisenberg, Dirac and many others is also equally important. However, quantum mechanics came into being due to direct or indirect growth of the earlier theories. Max Planck's idea of energy packets called as "quanta", Rutherford's nuclear model of an atom and Bohr's assumption of fixed energy orbits set the foundation of the true understanding of the atomic structure. Although the semi-classical theory of Bohr was not able to describe truly the full

features of even the simplest one-electron atom but it provided an atomic model which can be easily visualized as the pictorial concept at the back of mind.

The physical systems coupled with atomic physics consist of neutral atoms, ions and molecules in addition to more modern "artificial atoms" such as quantum dots. The interaction of applied fields such as the magnetic, electric, oscillating or static determines the structures of these systems. These interactions control the system through applied fields or on the other hand use matter to control the electromagnetic fields. Thus the true understanding of the atomic physics is essentially required to study interaction of electromagnetic radiations with matter.

3.1 **Schrödinger Equation for One-Electron Systems**

The one-electron systems are simplest atoms to be studied quantum mechanically and consist of elements in which one electron exists in valance orbit. Hydrogen is the first element of this category in which one electron moves under the influence of the spherical symmetric Coulomb potential of one proton. The other one electron systems (like hydrogen) are in ionic form, He^{+}, Li^{++}, Be^{+++}, etc in which the valance orbit has one electron but the nucleus more than one proton. The Schrödinger equation can be solved exactly only for one electron systems and for the solution of other atoms or molecules (multi-electron systems) some approximations have to be made.

The potential energy '*V(r)*' of an electron of charge '-e' moving in the Coulomb field of the nucleus of charge '+Ze' at distance of 'r' is given by

$$V(r) = -\frac{Ze}{4\pi\varepsilon_o\, r}\,. \qquad 3.1$$

For a better understanding of the spectrum of hydrogen and other one electron systems we apply the time independent Schrödinger equation.

$$\hat{H}\psi(r,\vartheta,\varphi) = E\psi(r,\vartheta,\varphi)\,. \qquad 3.2$$

Here $\psi(r,\vartheta,\varphi)$ is the wave function or eigenvalue function and the equation is called as eigenvalue equation. The Hamiltonian $\widehat{H}$ is the total energy operator for a one electron system and is given by

$$\widehat{H} = -\frac{\hbar^2}{2m}\nabla^2 + V(r)\,. \qquad 3.3$$

where '∇^2' is the Laplacian operator, *V(r)* is the potential energy and 'm' is the reduced mass and are respectively given by

$$\nabla^2 = \frac{\partial^2}{\partial x^2}+\frac{\partial^2}{\partial y^2}+\frac{\partial^2}{\partial z^2}.$$

$$V(r) = -\frac{Ze}{4\pi\varepsilon_o\, r}.$$

$$m = \frac{m_e\, M}{m_e+M}.$$

$m_e =$ mass of an electron

$M =$ mass of nucleus

The probability of finding the electron at a point in space around the nucleus defined by the co-ordinates (r,ϑ,φ) is given by

$$\psi\psi^* = |\psi|^2.$$

The total energy operator Hamiltonian $(\widehat{H})$ operates on the wave function (ψ) and gives the energy eigenvalue *E* and the eigenfunction. If for one eigenvalue of energy more than one eigenfunctions exists then the eigenvalue *E* is called as degenerate.

When the Laplacian operator '∇^2'is expressed in spherical polar co-ordinates then the wave function $\psi(r,\vartheta,\varphi)$ can be separated into a spherical radial function *R(r)* and a angular function *Y(*ϑ,φ*)* given by

$$\psi(r,\vartheta,\varphi) = R(r)Y(\vartheta,\varphi) \qquad 3.4$$

The Schrödinger equation can now be written in set of two equations in form of radial part and angular part.

$$\left(-\frac{\partial^2}{r\partial r^2}r + \frac{l(l+1)}{r^2} + \frac{Ze^2}{r}\right)R(r) = ER(r). \qquad 3.5$$

$$\widehat{L^2}Y(\vartheta,\varphi) = l(l+1)Y(\vartheta,\varphi)\,. \qquad 3.6$$

where L^2 is the total orbital angular momentum operator. The equation 3.6 can further be separated into ϑ and φ. The solution of Schrödinger equation is given by

$$E_n = -\frac{me^4}{2\hbar^2(4\pi\varepsilon_o)^2}\frac{Z^2}{n^2}\,. \qquad 3.7$$

In above equation *n* is called as the principle quantum number and it defines the energy of the state and it can have integer values like 1, 2, 3, 4 ..... In equation 3.6, *l* is the orbital angular quantum number and can have values $l \leq n-1$, i.e. 0, 1, 2, 3, 4……. corresponding to s, p, d, f, g ….. orbitals. The solution of equation 3.6 with angular part φ gives magnetic quantum number m_l, which can have values *+l, l-1, ...,0,.....-l+1, -l.*

The spinning motion of electrons causes the spin-orbit interaction which results in the fine structure energy levels. In case of the hydrogen like atoms, the total wave function of an atom in terms of orbitals wave function $\psi(r,\vartheta,\varphi)$ and spin wave function $\chi(m_s)$ is given by

$$\boldsymbol{\psi} = \psi_{nlsm_lm_s}(r,\vartheta,\varphi\, m_s) = R_{nl}(r)Y_{lml}(\vartheta,\varphi)\chi(m_s)\,. \qquad 3.8$$

In equation 3.8, *n, l, s* are the principle, orbital and spin quantum numbers, respectively. Whereas m_l is the projection of *l* and m_s is the projection of *s* with reference to the z-axis.

3.2 **Many Electron Systems**

With the increasing number of electrons around the nucleus the system becomes more and more complex due to the interactions between the electrons themselves. Thus the Hamiltonian of the whole system has to be modified and some correction terms are introduced to visualize a more realistic picture of the allowed energies. The modified Hamiltonian for N-electron system can be written as

$$\widehat{H} = \sum_{j,i=1}^{N}\left(-\frac{\hbar^2}{2m}\nabla_j^2 + V(r_i)\right) + \ correction\ terms\ . \qquad 3.9$$

In above expression the correction terms are also called as the fine structure corrections and are mainly due to the electron-electron interactions, nucleus-electrons interactions, interactions between the spin and orbital motion of electrons. These interactions introduce perturbations in the kinetic as well potential energies of the electrons. Now the total Hamiltonian can be written in the form given below

$$H = H_o + H_{ee} + H_r + H_D + H_{SO}\ . \qquad 3.10$$

where

$H_o \equiv$ core Hamiltonian $\sum_{j,i=1}^{N}\left(-\frac{\hbar^2}{2m}\nabla_j^2 + V(r_i)\right)$ and represent the electrons-nucleus electrostatic interaction

$H_{ee} \equiv$ Hamiltonian represents the electron-electrons repulsive interactions

$H_r \equiv$ Hamiltonian represents the relativistic term

$H_D \equiv$ Darwin Hamiltonian

$H_{SO} \equiv$ Hamiltonian represents spin-orbit electrons interactions.

3.2.1 **Electron-electron Interaction (H_{ee})**

The energy operator for electron-electron repulsive interaction is given by

$$H_{ee} = \sum_{i<j}\frac{Ze^2}{r_{ij}}\ . \qquad 3.11$$

where r_{ij} is the mean distance between a pair of electrons. The solution of equations 3.11 gives the interaction energy among the pair electrons and is given by

$$E_{ee} = \langle\psi(1)\psi(2)\left|\frac{Ze^2}{r_{ij}}\right|\psi(1)\psi(2)\rangle\ . \qquad 3.12$$

The above equation can be further solved in form of Coulomb or direct integral and exchange integral. The Coulomb integral gives the interaction energy due to the distribution of electrons whereas the exchange integral gives the energy between the pairs of electrons.

3.2.2 The Relativistic Term (H_r)

The relativistic energy is given in the form

$$E = \sqrt{(m^2c^2)^2 + (pc)^2}$$

$$= m^2c^4 + \frac{p^2}{2m} - \frac{p^4}{8m^3c^2} + \ldots.$$

In above expression the third term is the first order relativistic correction energy and is of the order of 0.1 cm^{-1}.

$$H_r = \frac{p^4}{8m^3c^2} . \qquad 3.13$$

3.2.3 The Darwin Term (H_D)

The physical origin of the Darwin term is a phenomenon in Dirac theory called as "zitterbewegung" (in German) i.e. "trembling motion" in which the electron does not move smoothly but instead go through tremendously fast small scale fluctuations which forces the electron to see a smeared out Coulomb potential of the nucleus. The Darwin term acts only at the origin and therefore is non-zero only for s states (l = 0 states). It causes a shift of less than 0.1 cm^{-1} and is given by

$$H_D = \left(\frac{e\hbar^2}{8m^2c^2}\right) \nabla \cdot E \ . \qquad 3.14$$

3.2.4 The Lamb Shift

Another phenomenon like Darwin term shifts the s-state energy higher than p-state and is called Lamb shift. According to Dirac, the energies of $2S_{1/2}$ and $2P_{1/2}$ states should be equal for hydrogen but the state $2S_{1/2}$ lies higher than $2P_{1/2}$ state and there is a difference of 0.0034 cm^{-1} in

the energies of the two states. This energy difference was measured by Lamb and Rutherford and is called as the Lamb shift. Quantum electrodynamics theory (QED) explains this effect on the basis that the ground state of the electromagnetic field is not zero but it undergoes vacuum fluctuations that interact with the electron. For hydrogen-like ions this shift in energy is proportional to Z^4.

3.2.5 Spin-orbit Interaction (H_{SO})

The spin-orbit interaction describes a weak magnetic coupling between the spin and the orbital motion of electron(s) i.e. the interaction between the intrinsic magnetic field generated by spinning electron and the magnetic field generated by orbiting electron around the nucleus. This interaction mechanism separates the energy of internal states of the atom on the basis of spin-aligned and spin-antialigned. The splitting of energy levels into further levels governed by spin-orbit interaction is called as the fine structure energy levels. The fine structure energy levels are separated in the energy range of 10-1000 cm^{-1}. The existence of fine structure was one of the first proofs of the spinning motion of electrons. The Hamiltonian H_{SO} for multi-electron system is given by

$$H_{SO} = \xi(r)\vec{L}\cdot\vec{S}\,. \qquad 3.15$$

where $\vec{L} = \sum \vec{l_i}$ and $\vec{S} = \sum \vec{s_i}$ are the total orbital angular momentum and the total spin angular momentum of the electrons, respectively and $\xi(r)$ is the fine structure splitting factor. It depends on electronic configuration of $\vec{L}$ and $\vec{S}$ and its expectation value is given by

$$<\xi(r)> \propto <\psi\left|\frac{1}{r^3}\right|\psi>\ . \qquad 3.16$$

The total angular momentum $\vec{J}$ is given by

$$\vec{J} = \vec{L} + \vec{S}\,. \qquad 3.17$$

Taking scalar product of equation 3.17 with $\vec{J}$, rearranging it for $\vec{L}\cdot\vec{S}$ and inserting it in equation 3.15, gives

$$H_{SO} = \xi(r)\frac{(J^2 - L^2 - S^2)}{2} . \qquad 3.18$$

And the splitting energy is given by

$$\Delta E_{SO} = <\psi\xi(r)\frac{(J^2 - L^2 - S^2)}{2}\psi> . \qquad 3.19$$

$$\Delta E_{SO} = <\psi\xi(r)> \frac{1}{2}[J(J+1) - L(L+1) - S(S+1)] . \qquad 3.20$$

- The selection rules for dipole transitions are; $\Delta J = 0, \pm 1$.
- For $\xi(r) > 0$, the fine structure multiplets are normal and for $\xi(r) < 0$, the fine structure multiplets are inverted.
- The width of splitting between $L + S$ and $L - S$, for $L > S$ is $< \xi(r) > 2S(2L + 1)$ and for $S > L$, is $< \xi(r) > 2L(2S + 1)$.
- The total angular momentum quantum number J can have values $|L - S|$, $|L - S| + 1, \ldots \ldots \ldots L + S - 1$, $L + S$.
- Each term splits into $(2L+1)$ if $L < S$ or into $(2S+1)$ energy levels if $S < L$.

The separation of energy in adjacent fine structure components is given by

$$\Delta E(J) = E(J) - E(J-1) = <\xi(r)> J . \qquad 3.21$$

This is known as the Landé interval rule and it states that the interval between successive energy levels is proportional to the larger of the two J values involved. The energy difference does not depend on the orientation of total angular momentum J i.e. it does not depends on M_j.

Thus we have,

$$\sum_{|L-S| \le (L+S)} (2J+1)\Delta E_J = 0 . \qquad 3.22$$

The center of gravity (the mean value of the energy multiplets) coincides with the unsplitted energy and is given by

$$< E > = \frac{\sum_J (2J+1)\, E_J}{\sum_J (2J+1)} \, . \qquad 3.23$$

As the energy contribution of Darwin and relativistic terms are very small as compared to other correction terns, thus the Hamiltonian for the N-electrons can be written as

$$H \approx H_o + H_1 + H_2 \, . \qquad 3.24$$

In the above relation H_1 stands for electron-electron interaction and H_2 stands for spin-orbit interaction and depends on the atomic number *Z*. In heavy atoms (large Z values) the spin-orbit interaction is dominant as compared to the electron-electron interaction thus H_1 can be treated as the perturbation while for lighter atoms electron-electron interaction is dominant as compared to the spin-orbit interaction therefore H_2 is treated as the perturbation.

3.3 **Coupling of Angular Momenta**

In multi-electron systems where several electrons are normally present in partially filled subshells, the spin angular momenta and the orbital angular momenta can organize in different ways to provide different values of the total angular momentum. This coupling of the individual angular momenta is basically classified on the basis of the dominance of the spin-orbit interaction or electrostatic Coulomb interaction between the electrons. Two frequently used coupling schemes are LS-coupling and jj-coupling.

3.3.1 **LS-Coupling**

The LS-coupling or Russell-Saunders coupling [152] is normally used when the electrostatic interaction between electrons is dominant over the spin-orbit interaction. This coupling scheme is normally used for lighter atoms (generally Z < 30) and is dominant in low lying state of the atoms. In this coupling scheme the individual spin angular momenta (s_i) of electrons are combined together to get total spin angular momentum quantum number $\vec{S}$ and similarly the orbital angular momenta (l_i) of individual electrons are combined together to get total angular momentum quantum number $\vec{L}$. The vector sum of $\vec{S}$ and $\vec{L}$ gives the total orbital angular momentum of the atomic system $\vec{J}$ i.e.

$$\vec{S} = \sum_i \vec{s_i} \text{ and } \vec{L} = \sum_i \vec{l_i}$$

$$\Rightarrow \qquad \vec{J} = \vec{L} + \vec{S}$$

And their magnitudes is given by

$$|\vec{S}| = \sqrt{S(S+1)}\,\hbar \quad \text{and} \quad |\vec{L}| = \sqrt{L(L+1)}\,\hbar\,.$$

$$|\vec{J}| = \sqrt{J(J+1)}\,\hbar\,.$$

The possible $\vec{J}$values lie in the range $|L+S|, \ldots\ldots\ldots\ldots\ldots |L-S|$.

An electronic state is represented in the form $n^{2S+1}L_J$. Where 2S+1 is the multiplicity (*M*) of the state and the latter *L* represents the state and is given by

$L \equiv$ 0, 1, 2, 3, 4, 5, …..

S, *P*, *D*, *F*, *G*, *H*, …..

Examples

The energy state 3^3P_1 corresponds to n = 3, *S* = 1, *L* = 1, *J* = 1

The energy state $4^2D_{3/2}$ corresponds to n = 4, *S* = 1/2, *L* = 2, *J* = 3/2

3.3.2 **jj-Coupling**

In jj-coupling scheme the spin-orbit interaction is dominant over the electrostatic interaction between the electrons. This coupling scheme is effective for heavier atoms and is stronger for high lying states. In jj-coupling scheme $\vec{l_i}$ and $\vec{s_i}$ of the individual electrons are initially coupled to form the resultant angular momentum $\vec{j_i}$

$$\vec{j_i} = \vec{l_i} + \vec{s_i}\,.$$

The angular momentum $\vec{j_i}$ of different electrons now coupled together to form total angular momentum $\vec{J}$ of the atom.

$$\vec{J} = \sum_i \vec{j_i}\,.$$

The possible J values lie in the range

$$\left|\sum_i \vec{J}_i\right|_{\text{Max}}, \left|\sum_i \vec{J}_i\right|_{\text{Max}} - 1, \ldots\ldots\ldots\ldots \left|\sum_i \vec{J}_i\right|_{\text{Min}}$$

In this coupling mechanism an electronic state is represented by $(j_1, j_2)_J$. As an example for a d-electron $J = 1, 2$ and $j = 3/2, 5/2$, $j_1 = 1/2$, $j_2 = 3/2$, the state is $(1/2, 3/2)_1$ and $(1/2, 3/2)_2$.

Practically for most of the atoms, an intermediate coupling scheme which is neither pure LS-coupling nor jj-coupling is applied.

3.4 **Central Field Approximation**

In multi-electron atoms, the repulsive electron-electron interaction and attractive electron-nucleus interaction are rather very large and it is not feasible to solve Schrödinger equation either analytically or numerically. Hartree and Fock developed an approximation method called as the central field approximation to deal with this problem. This method is based on the assumption that all interactions whether attractive or repulsive are equivalent to an effective field (central field) and any arbitrary electron moves in this effective potential $U(r)$. The effective potential is considered as isotropic function (independent of ϑ and φ) and depends only on the radial distance r from the electron under consideration.

4 ELEMENTS OF HYPERFINE STRUCTURE

The Coulomb interaction between the positively charged nucleus and the electrons determines the radial probability density of electrons around the nucleus. The interaction of electrons between themselves as well as among the magnetic moments associated with the electron spin and the electron's orbital angular momentum results in the fine structure energy levels. As in an atom the electrons moves under the influence of the field generated by the nucleus, the spectral energy distribution of an atom depends upon the nuclear charge number. Atoms which have non-zero nuclear spin quantum number display an additional splitting of their fine structure energy levels. This splitting is caused by the electromagnetic interaction between the nuclear magnetic moment and electronic magnetic moment and is called hyperfine (hf) structure. The name hyperfine is due to the fact that hyperfine interaction energy is three orders of magnitude smaller than the fine structure energy (hf splitting is of the order of 0.001 to 1 cm^{-1}). This large difference in energy is due to the mass ratio of electrons and protons. Although generally the hf splitting is smaller than the fine structure splitting, in some cases they are not "hyperfine" small but could be even be greater than the fine structure splitting. This large splitting is due to the mutual interaction of electrons [153]. The interaction among the total nuclear spin quantum number I and electronic angular momentum quantum number J of electron results in new total angular momentum quantum number F for an atom and is given by

$$\vec{F} = \vec{I} + \vec{J}$$

The value of I and J determines the number of levels into which a hyperfine level splits. For $J \leq I$ a fine structure level splits into $(2J+1)$ hyperfine structure components and for $J > I$ a fine structure level splits into $(2I+1)$ hyperfine structure components. The magnetic dipole interaction constants A, the electric quadrupole interaction constants B and the total angular momentum J of the combining energy levels are the characteristics of the hyperfine structure of a spectral line and determine the splitting of the hyperfine pattern of a spectral line.

The nuclear spin quantum number *I* is the resultant of spin and angular momenta of nucleons (with some exceptions as for tantalum-180 (^{180}Ta): I = 9) and it can be integral or half integral.

The first observation of hyperfine structure in optical spectra was made at the end of 19th century independently by A. Michelson (1891), and by Ch. Fabry and A. Perot (1897) [5]. In order to explain the hyperfine splitting, W. Pauli, in1924, proposed that the atomic nucleus possesses intrinsic angular momentum [154]. The importance of hyperfine structure and isotope shift in solar spectrum was first highlighted by Abt [50]. Now it's well known that hyperfine structure can have large effects on stellar absorption line profile and the abundances of the elements deduced from stellar spectra. The effects of hyperfine structure are important because they can be larger than most other sources of uncertainties in the analysis [51]. Thus for accurate determination of abundances in stellar spectra the precise knowledge of hyperfine structure is indispensable. The hyperfine structure can provide significant information concerning electronic properties and nuclear structure such as: nuclear ground state spin and electromagnetic moments [119, 125]. Theoretical calculations and combination of accurate spectroscopic constants can lead to the determination of quadrupole moments [14].

Although the hyperfine effects are concerned with very small shifts in energies these effects have a great importance in explanation of atomic physics to astrophysics. For example, the 21 cm famous line of hydrogen (frequency ≈1420.4 MHz) produced as a radiative transition between the two hyperfine levels has an immense significance in radio astronomy. The modern atomic clocks are based on the hyperfine transition of heavy alkali atoms. The massive reproducibility of these transitions led to define second in term of the hyperfine transition of cesium-133 (^{133}Cs). Now the second is defined as the duration of 9192631770 periods of radiation corresponding to the transition between two hyperfine levels of ground state ^{133}Cs atom.

The existence of the electric and magnetic fields inside the nucleus of an atom is due to the localized charges and current distributions. These fields can disintegrate into multipole fields which results in the creation of multipole moments. The Coulomb electrostatic field which defines the overall structure of an atom and drives the electrons to move in their orbits around the nucleus results in the formation of an electric monopole (the first of multipole moment). The higher order multipole moments usually having small energy association are referred as the hyperfine effects.

Not all multipole fields that can exist classically are permissible in the case of a nucleus and there are two rules for the existence of multipole moments of the nucleus. The first rule states that a 2^k-pole can exist only if $k \leq I$ and the second rule states that even magnetic 2^k-pole and odd electric 2^k-pole do not exist due to parity violation. Usually in atomic physics two lowest multipole with $k = 1$ and $k = 2$ are important whereas the higher multipole are considered more significant in nuclear physics. The magnetic dipole interaction corresponds to $k = 1$ and the electric quadrupole interaction corresponds to $k = 2$. The interaction of magnetic dipole moment and electromagnetic moment of electrons results in further splitting of fine structure energy levels (hyperfine structure). The magnetic dipole interaction constant A defines the width of splitting of a fine structure energy level. The interaction of electric quadrupole moment and electromagnetic moment of electrons results only in shift of the hyperfine structure levels. This shift is some time referred as the electric hyperfine structure and defined by a constant recognized as the electric quadrupole interaction constant B.

4.1 **Magnetic Dipole-Dipole Interaction**

The interaction between the magnetic dipoles of the nucleus and the electrons is called as a dipole-dipole interaction and results in the splitting of fine structure energy levels into hyperfine energy levels. Due to spherical charge distribution of S states the dipole-dipole interaction is zero and this interaction contributes only for states with $L \geq 1$. The nuclear magnetic moment μ_I associated with nuclear spin angular momentum I is given by

$$\mu_I = g_i \mu_N I \qquad 4.1$$

Where g_i is called nuclear Landé factor or nuclear g-factor and μ_N is known as the nuclear magneton. In terms of Bohr's magneton μ_B, the nuclear magneton is given by

$$\mu_I = {}^{\mu_B}/_{1836}$$

$$= 5.0508 \times 10^{-27} \quad J/T \,. \qquad 4.2$$

The magnitude of $\vec{I}$ is

$$\left|\vec{I}\right| = \sqrt{I(1+I)}\,\hbar\,.$$

The interaction nuclear magnetic moment μ_N and intrinsic magnetic field $\vec{B}$ associated with the spin and orbital motion of the electrons results in a small energy perturbation of atom which is given by following Hamiltonian

$$\hat{H}_\mu = -\vec{\mu}_N \cdot \vec{B}\,. \qquad 4.3$$

The intrinsic magnetic field $\vec{B}$ of electrons is proportional to total angular momentum $\vec{J}$

$$\vec{B} \propto \vec{J}$$

Thus

$$\hat{H}_\mu \propto -\vec{I}\cdot\vec{J}$$

$$\hat{H}_\mu = A\,\vec{I}\cdot\vec{J}\,. \qquad 4.4$$

In above equation '*A*' is the magnetic dipole interaction constant. It depends on nuclear and magnetic quantities and determines the width of splitting of a fine structure energy level.

The interaction energy is given by

$$E_\mu = <\psi(\mathrm{r},\vartheta,\varphi)\left|\hat{H}_\mu\right|\psi(\mathrm{r},\vartheta,\varphi)>$$

$$E_\mu = <\psi(r,\vartheta,\varphi)\left|\,A\,\vec{I}\cdot\vec{J}\right|\psi(r,\vartheta,\varphi)>\,. \qquad 4.5$$

As

$$\vec{F} = \vec{I} + \vec{J}$$

$$\vec{F}\cdot\vec{F} = (\vec{I}+\vec{J})\cdot(\vec{I}+\vec{J})$$

$$F^2 = I^2 + J^2 + 2(\vec{I}\cdot\vec{J})$$

$$(\vec{I}\cdot\vec{J}) = \frac{F^2 - I^2 - J^2}{2}\,. \qquad 4.6$$

Thus the solution of equation (4.5) gives

$$E_\mu = \frac{A}{2}\left[F(F+1) - I(I+1) - J(J+1)\right]. \qquad 4.7$$

For simplicity we can write

$$E_\mu = \frac{AC}{2}. \qquad 4.8$$

where

$$C = \left[F(F+1) - I(I+1) - J(J+1)\right]. \qquad 4.9$$

Like fine structure level the Landé interval rule is also valid for magnetic hyperfine splitting. Thus the energy difference between the consecutive hyperfine levels is given by

$$\Delta E_\mu(F, F-1) = E_\mu(F) - E_\mu(F-1)$$

The solution of above equation gives

$$\Delta E_\mu(F, F-1) = AF. \qquad 4.10$$

The constant '*A*' is a function of '*J'* and is given by

$$A(J) = \frac{\mu_I < \vec{B} >}{I\,J}.$$

$$A(J) = \frac{\mu_I < \vec{B} >}{1836\,J}. \qquad 4.11$$

4.1.1 Properties of Magnetic Hyperfine Multiplets

- For transition between two different hyperfine multiplets, the selection rules for electric dipole transition are $\Delta F = 0, \pm 1$ and transition $F = 0 \rightarrow F = 0$ is forbidden.
- The spacing between two neighboring hyperfine levels is proportional to the larger value of *F* of the levels involved.

- The possible values of F can be $|I-J|, |I-J|+1, \ldots\ldots\ldots, I+J-1, I+J$.
- The number of hyperfine components is equal to $2I+1$ if $J > I$ or $2J+1$ if $I \geq J$.
- The total width of splitting (ΔW) between the levels $J+1$ and $|J-1|$ depends upon the values of I and J and are given by

$$\Delta W = AI(2J+1) \text{ for } J \geq I$$

$$\Delta W = AI(2I+1) \text{ for } I \geq J$$

- Equation 4.11 shows that for a fixed value of $|\vec{B}|$, the value of the magnetic dipole coupling constant A is maximum for minimum value of J. The possible minimum value of J = ½ which corresponds to an unpaired s electron. Thus the width of splitting is largest for an unpaired s electron.

The hyperfine multiplets are said to be normal if $A > 0$ and are called as inverted if $A < 0$. In case of normal multiplets, the levels with largest F values correspond to highest energy and in case of inverted multiplets the levels with largest F values correspond to the minimum energy.

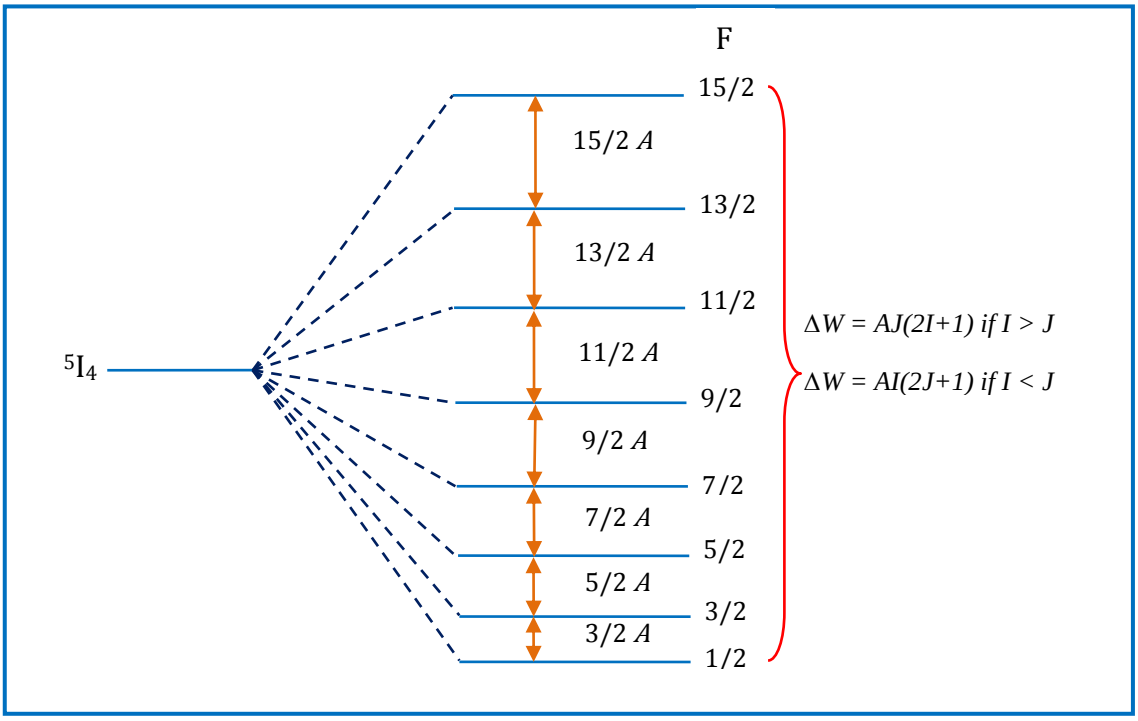

Figure 4.1: Ground state splitting of neodymium into 8 hyperfine levels.

4.2 **Electric Quadrupole Interaction**

Although the existence of electric quadrupole moment of nucleus was suggested by Murakawa [155] when he observed anomalies in the hyperfine structure of iodine the first solid proof of the existence of nuclear quadrupole moment was provided by Schüler and Schmidt [156] when they explained the deviation of Landé interval rule in the hyperfine structure of two isotopes of europium. The electric quadrupole moment 'Q' is an important parameter of the nucleus which determines the shape of the ellipsoid of nuclear charge distribution. The nucleus has spherical charge symmetry for Q = 0 whereas a non-zero quadrupole moment indicates that the charge distribution is not spherically symmetric. Conventionally the value of Q is taken to be positive if the ellipsoid is prolate and negative if it is oblate. In prolate configuration (Q > 0) the nuclear charge distribution is elongated in the direction of nuclear spin quantum number *I* and in oblate configuration (Q < 0) the nuclear charge distribution is elongated normally to the direction of *I*. The electric quadrupole moment of nucleus is measured in unit of barn and 1 barn is equivalent to 10^{-24} cm^2.

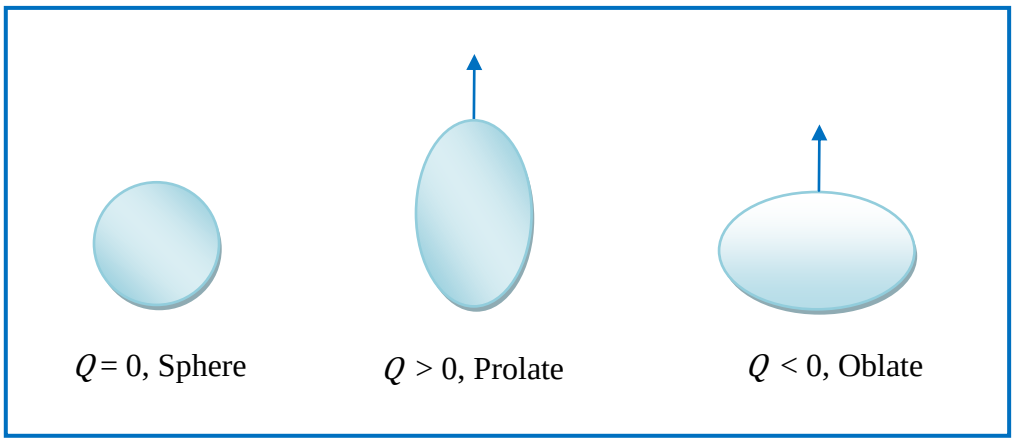

Figure 4.1: Charge distribution of nuclei for different values of Quadrupole moments.

The electric quadrupole hyperfine structure is the interaction between the electric quadrupole moment of the nucleus and the electrostatic potential caused by the spin and orbital motion of the electrons at the nucleus. The energy shift due to electric quadrupole interaction is given by

$$E_Q = \frac{B}{4}\left[\frac{\frac{3}{2}C(C+1) - 2I(I+1)J(J+1)}{I(2I-1)J(2J-1)}\right]. \qquad 4.12$$

where

$$B = eQ\left[\frac{\partial^2 V}{\partial z^2}\right]$$

$$C = F(F+1) - I(I+1) - J(J+1)$$

B = electric quadrupole hyperfine constant or electric quadrupole coupling constant

V = electrostatic potential caused by all electrons at the nucleus.

while I, J and F have their usual meanings.

From equation 4.12, the following remarks can be made;

- B is zero for $J = ½$ and $I < 1$.
- B is zero for atoms containing even number of neutrons and even number of protons.
- Electron charge distribution is spherical for 'S' electrons, therefore $\frac{\partial^2 V}{\partial Z^2} = 0$. Thus for 'S' electrons the electric quadrupole coupling constant 'B' is also zero.

The combination of magnetic dipole interaction and electric quadrupole interaction gives the total splitting of the hyperfine structure i.e.

$$\Delta E_{hfs} = E_\mu + E_Q$$

$$\Delta E_{hfs} = \frac{AC}{2} + \frac{B}{4}\left[\frac{\frac{3}{2}C(C+1) - 2I(I+1)J(J+1)}{I(2I-1)J(2J-1)}\right]. \qquad 4.13$$

In above equation although magnetic dipole interaction constant $A(J)$ and electric quadrupole interaction constant $B(J)$ both are function of J but their dependence on total angular momentum quantum number F is not equivalent. The magnetic dipole constant is responsible for further splitting of the fine structure levels into the hyperfine levels whereas electric quadrupole constant is responsible for the shifting of the hyperfine levels. This shifting of the hyperfine levels results in the violation of Landé interval rule and it becomes more and more prominent when the numerical value of B becomes comparable to the magnitude of the hyperfine coupling constant A.

4.3 **Experimental Investigation of Hyperfine Constants**

As mentioned previously that equation 4.13 is the sum of magnetic dipole and electric quadrupole coupling constants. The total interaction energy can be written as

$$\Delta E_{hfs} = \alpha\, A(J) + \beta B(J)\,. \qquad 4.14$$

In above equation α and β are called Casimir factors and are function of *F*, J and *I*.

$$\alpha = \frac{C}{2} = \frac{1}{2}[F(F+1) - I(I+1) - J(J+1)]. \qquad 4.15$$

$$\beta = \frac{1}{4}\left[\frac{\frac{3}{2}C(C+1) - 2I(I+1)J(J+1)}{I(2I-1)J(2J-1)}\right]. \qquad 4.16$$

The selection rules for allowed transitions among two different hyperfine levels of two different fine structure levels are:

- $\Delta F = 0, \pm 1$
- $\Delta J = 0, \pm 1$
- $F = 0 \;\rightarrow F = 0$ transition is not allowed.
- Parities of the involved levels must be different.

For spectral line each allowed transition is referred as the component of the hyperfine structure pattern and these components can be determined by the following formula.

$$\upsilon = \upsilon_c + \alpha_o(F_o, J_o, I_o)A_o + \beta_o(F_o, J_o, I_o)B_o - \alpha_u(F_u, J_u, I_u)A_u - \beta_u(F_u, J_u, I_u)B_u. \qquad 4.17$$

In above equation υ_c is the center of gravity of the transition and corresponds to the energy difference of the involved fine structure levels. The center of gravity of hyperfine multiplets is not affected by the magnetic dipole and electric quadrupole splitting. $A_o$and B_o are the hyperfine constants of the upper level whereas $A_u$and B_u are the hyperfine constants of the lower level

involved in the transition. The hyperfine coupling constants are characteristics of hyperfine levels and be determined by solving the equation 4.17 by least square method.

The Line Intensity

The relative intensities of the hyperfine components can be calculated by the following famous relation

$$I(F_o \rightarrow F_u) = \frac{(2F_o + 1) \cdot (2F_u + 1)}{2I + 1} \begin{Bmatrix} J_o & F_o & I \\ F_u & J_u & 1 \end{Bmatrix}^2 . \qquad 4.18$$

where J_o, J_u and F_o, F_u are the total orbital angular momentums and total atomic angular momentums of the upper and lower levels respectively. The term in the curly brackets is called as the 6j-symbol. The above formula is suitable only for weak interactions among the neighboring fine structure levels. The components $\Delta F = \Delta J$ i.e. for which F and J are oriented in the same direction are called strongest components or diagonal components. The strength or the line intensities of the diagonal components increases with increasing F values. The hyperfine components corresponding to $\Delta F \neq \Delta J$ are called weaker components or off-diagonal components.

5 BROADENING AND PROFILES OF SPECTRAL LINES

The spectral transitions are not infinitesimally narrow and have characteristics line shapes and spectral widths. The phenomena which contribute in the spectral line width are; finite lifetime of the excited state, arbitrary motion of the atoms/molecules and collisions between neighboring particles. These broadening mechanisms are respectively referred as the natural broadening, Doppler broadening and collisional broadening. Line broadening can be homogeneous or inhomogeneous. If the absorption or emission probability of radiations for all atoms/molecules in a discharge cell is isotropic, it is called homogeneous broadening and if it is anisotropic, the broadening is called inhomogeneous. Natural broadening and pressure broadening are examples of homogeneous broadenings whereas Doppler broadening is an example of inhomogeneous broadening. The line broadening also depends upon the apparatus used for the measurement of wavelength and line profiles or for the sensitive detection of the radiations. The basic components of all the spectrograph are; prisms, grating or interferometers. Here we will exclude the discussion about the instrumental broadenings.

For accurate intensity and wavelength measurement the understanding of spectral lines profiles and the distribution of intensity around the central frequency υ_o is necessary. The line profile is defined as the spectral distribution function $I(\upsilon)$ of the absorbed or emitted radiation in the vicinity of central frequency υ_o and is shown in the figure 5.1. The spectral line width is always determined by its full width half maximum (FWHM) and is simply called as the line width or half width of spectral line. The line width is determined by the frequency interval $\delta\upsilon = |\upsilon_2 - \upsilon_1|$, between the $\upsilon_1$and $\upsilon_2$for which $(\upsilon_1) = I(\upsilon_2) = I(\upsilon_o)/2$. The spectral region inside the half width is known as the kernel of the line and the regions outside the line width are known as the line wings (Figure 5.1). Some line profiles have broad core and small wings while others have a narrow core and broad wings. The former line shape is called Gaussian line profile and the later is called Lorentzian line profile (Figure 5.2).

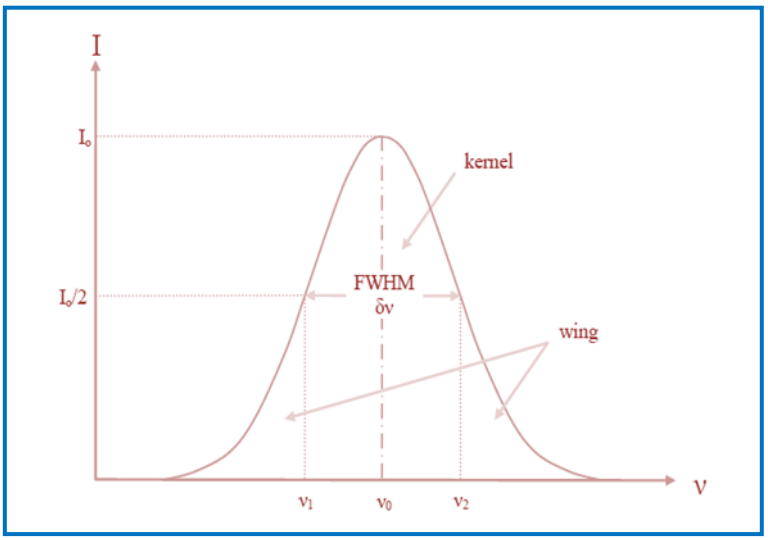

Figure 5.1: The spectral line profile.

5.1 **Natural Broadening**

Heisenberg's uncertainty principle in time and energy form is $\Delta t_i \Delta E_i \cong \hbar$. According to this principle any given atomic energy level i does not have an absolutely defined energy E_i but is somewhat a superposition of possible energy states spread around E_i. Consequently, transitions of electrons taking place between any two energy states do not reflect an exact particular energy difference. In other words, absorption of photons does not occur at a particular precise, unique wavelength/frequency but over a specific range. This type of broadening process is called natural broadening and the line width is called natural line width. It is originated from the life time (τ_i) of the state and is given by

$$\Delta E_i = {}^{\hbar}/_{\tau_i}$$

and in frequency term,

$$\Delta\omega_i = \frac{1}{\tau_i} \qquad 5.1$$

i.e. the reciprocal of the mean life time of the state gives the spread in energy or in frequency (natural broadening) of the state. The life time for the metastable states or ground states is relatively long (infinitively long for ground state) which support to neglect $\Delta\omega_i$ in most cases.

For a dipole allowed transitions between any two states $E_i \rightarrow E_f$ having mean life times τ_i and τ_f respectively, the natural line width of the spectral line is given by

$$\Delta\omega_n = \frac{1}{\tau_i} + \frac{1}{\tau_f} . \qquad 5.2$$

The excited states life times are of the order of 10^{-6} to 10^{-9} seconds, thus the corresponding line widths are in the range of 0.1 to 100 MHz. The natural broadened profile function of a spectral line is given by

$$I(\upsilon) = I_o \frac{\frac{1}{4\pi\tau}}{(\upsilon - \upsilon_o)^2 + (\frac{1}{4\pi\tau})^2} . \qquad 5.3$$

where I_o is the maximum intensity and υ_o is the resonance frequency. The intensity function $I(\upsilon)$ represents a Lorentzian line shape. The natural broadening is very small as compared to other types of spectral line broadening mechanisms and it is not possible to observe it without special high resolution spectroscopic techniques. The natural boarding is homogeneous type broadening.

5.2 **Doppler Broadening**

One of the most important spectral line broadening mechanism in gases at low pressure is the Doppler broadening. It is caused by the random thermal motion of atoms/molecules. Different velocities of atoms or molecules cause a different shift (Doppler shift) in the absorption or emission line profile of the elements and the mutual effect of these shifts results in the broadening of the line profile. The atom or molecules moving with velocity υ_x will absorb/emit the light of frequency given by

$$\upsilon = \upsilon_o \left(1 \pm \frac{\upsilon_x}{c}\right). \qquad 5.4$$

where υ_o is the resonant frequency and c is the velocity of light. The " $\pm$ " sign indicates whether the atom/molecules are moving towards or away from the incident radiation. The Doppler broadened spectral line has a Gaussian line profile and it is inhomogeneous type broadening. The Doppler line width for the centre frequency of υ_o is given by

$$\delta\upsilon_D = 7.16 \times 10^{-7}\, \upsilon_o \sqrt{T/M} . \qquad 5.5$$

where $\delta\upsilon_D$ is the Doppler width, *T* is the temperature in Kelvin and *M* is the molar mass of the element under consideration. Following remarks can be readily made from the above equation.

- The Doppler width is directly proportional to the central frequency of absorption or emission of a spectral line so the Doppler width is greater in the UV and visible frequency ranges as compared to IR frequency.
- The Doppler width is directly proportional to the atomic mass with the relation $\frac{1}{\sqrt{M}}$, thus the heavy elements have smaller Doppler width.
- The Doppler width and temperature is also directly proportional according to following relation, $\delta\upsilon_D \propto \sqrt{T}$. Therefore the Doppler width reduces by decreasing the gas temperature i.e. cooling of discharge cell with liquid nitrogen can significantly decrease the Doppler width.

Generally the natural line width is completely shrouded by much larger Doppler width and sub-Doppler methods of laser spectroscopy are essentially required to reduce the Doppler broadening. Some methods of sub-Doppler spectroscopy are discussed in next chapter and two methods, collinear laser ion beam spectroscopy and inter-modulated saturation spectroscopy, are used in this work for spectroscopic investigations.

5.3 **Collisional (Pressure) Broadening**

This broadening mechanism prevails at rather high densities (pressure) of the gas atoms/molecules and occurs due the interaction between the neighboring atoms. The presence of the neighbouring atoms effects the position of the atomic energy levels particularly if the neighbours are charged particles like ions or electrons. This energy shift depends on the electronic structure of the interacting particles, on the mutual distance of two particles and also on the specific energy levels. If the interaction between the two neighbours is attractive then the shift in energy is negative and is positive when the interaction is repulsive.

An atom in the excited state can decay to the ground either by spontaneous emission or by an impact with the other atoms. In the later case the life time of the excited state is shortened and as a result the line is broadened. At high enough pressure the collision rate is also high which stimulates the broadening and the broadening mechanism is named as the collisional broadening or pressure broadening. The collisional broadening predominantly takes place in gas discharges

and plasmas due to the long range Coulomb interaction between charged particles. The core of collisional broadening is the elastic and inelastic interaction between the atoms and ions. In the elastic interactions the fluorescence intensity remains constant but a shift in frequency occurs which changes the phase of the oscillator. On the other hand the fluorescence intensity decreases in the inelastic collisions.

The collisional broadening can be classified on the basis of collisions as Lorentz broadening and Holtzmark broadening. If the collisions take place between different kinds of atoms the broadening is called Lorentz broadening and is called Holtzmark broadening if the collisions occur between the same kinds of atoms. Like natural broadening the collisional broadening is a homogeneous broadening and has a Lorentzian line profile but it has comparatively larger width as compared to natural broadening.

The collisional broadening can be minimized by maximizing the mean free path of the atoms/molecules i.e. by sustaining very low pressure in the vapors/discharge cells. The information regarding the collisions in the gas/plasma can be collected by varying the pressure and monitoring the resulting changes in the line width.

5.4 **Stark Broadening**

At higher densities when the collisions between ions and electrons are prominent an additional broadening mechanism can play a role in escalating the spectral line widths. The source of this broadening is the strong electric field between ions and electrons and is called the Stark broadening in the honor of J. Stark who observed this effect in 1913. An electric field splits a level into *J+1* sublevels. The weak lines are considerably affected by Stark broadening because the electric field spread the spectral lines over a substantial distances and it becomes hard to observe these lines against background. Doppler broadening is the governing factor at high temperatures and low plasma densities whereas the Stark broadening is prominent at high densities and low temperatures. But in overall picture of temperature and density the Doppler broadenings are dominant.

5.5 **Saturation Broadening**

The line width can also broaden when a strong resonant radiation field interacts with atoms/molecules and the phenomenon is called as saturation broadening or power broadening. At high enough resonant laser intensities the rate of excitation becomes greater than the de-excitation rate and as a result the lower state population decreases i.e. causing the saturation of the transitions. The saturation effect is dominant at the center of the transition and diminishes as the laser frequency shifts away from the core. At the central laser frequency, the fluorescence signal and the laser intensity are not proportional to each other whereas at the wings of the laser intensity (low intensity) they are proportional and the result is line broadening. For the homogeneous line profile the saturation broadening has a Lorentzian line shape and for the inhomogeneous line profile the saturation broadening cause a Gaussian line shape.

5.6 **Self-absorption Broadening**

The fluorescence light emitted through a de-excitation process can be re-absorbed by an atom or molecule present in the specimen. As the absorption is maximum at the line center than at wings thus at the central frequency the intensity of the emission line decreases more. Thus self-absorption broadens the spectral line and is called as the self-absorption broadening.

5.7 **Time of Flight Broadening**

For the Doppler free transition the line width can be broadened if the interaction time (time of flight) of radiation field with atoms/molecules is shorter as compared to the excited state life time of the state. In this case the line width depends on the interaction time instead of the spontaneous life time of the state. This broadening mechanism is prominent in case of transverse atomic laser beam spectroscopy where the interaction time could be less than 10^{-9} sec and resulting in line broadening of few GHz. This type of broadening can be reduced either by decreasing the velocity of the atoms/molecules or by increasing the diameter of the laser beam.

5.8 **Combined Line Profile**

The various broadening mechanisms discussed in the preceding sections are present up to some extent in most of the experiments although their contribution can be changed by changing the

experimental conditions and techniques. For example to trim down the pressure broadening the pressure is decreased, to minimize the Doppler broadening the temperature is decreased or a suitable sub-Doppler spectroscopic technique is applied and similarly the saturation broadening can be avoided by choosing a weak laser intensity. But as whole it is not completely feasible to isolate a spectral line from all broadening effects. Thus a spectral line is normally consisted of as the convolution of various broadening processes i.e.

$$I(\upsilon) = I_N(\upsilon) \cdot I_S(\upsilon) \cdot I_{TOF}(\upsilon) \cdot I_D(\upsilon) \cdot I_P(\upsilon) \cdot \cdot \qquad 5.6$$

where

$I(\upsilon) \equiv$ Resultant/total broadening

$I_S(\upsilon) \equiv$ Saturation broadening

$I_D(\upsilon) \equiv$ Doppler broadening

$I_P(\upsilon) \equiv$ Pressure broadening

$I_{TOF}(\upsilon) \equiv$Time of flight broadening

.

.

.

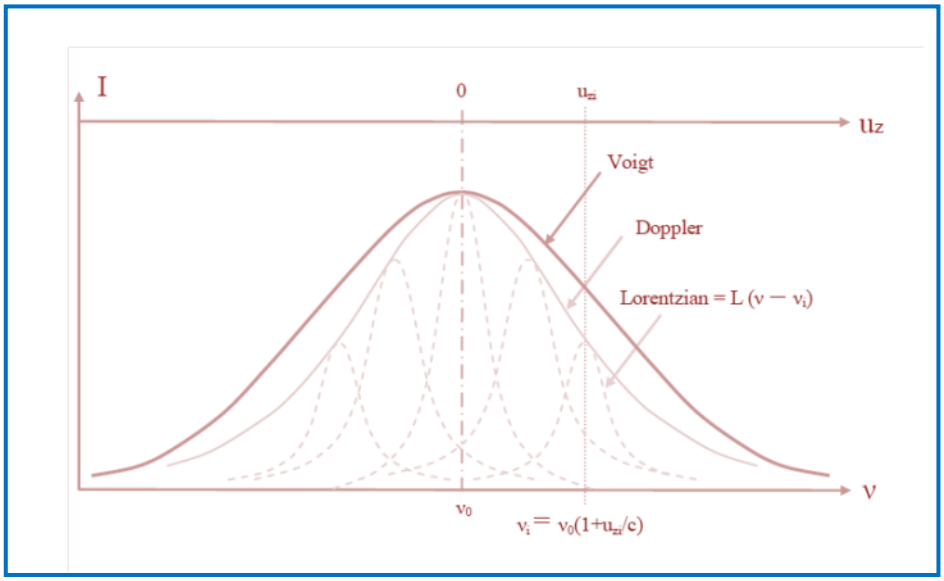

Figure 5.2: Voigt profile as a convolution of Gaussian and Lorentzian line profiles with different velocity groups u_{z_i}.

The resultant or total line broadening is neither Gaussian nor Lorentzian because the line profiles of all the broadening processes are not the same. Doppler broadening has a Gaussian line profile whereas natural broadening and collisional broadening both have Lorentzian line profile. On the other hand the line profile of saturation broadening may be Gaussian or Lorentzian. Therefore the line profile of resultant broadening is the convolution of the Gaussian and Lorentzian functions and is called as the Voigt line profile.

$$I_V(\upsilon) = I_G(\upsilon) \cdot I_L(\upsilon). \qquad 5.7$$

where

$I_V(\upsilon) \equiv$ Voigt profile

$I_G(\upsilon) \equiv$ Gaussian profile

$I_L(\upsilon) \equiv$ Lorentzian profile

We applied three different spectroscopic techniques in this work and find an enormous change in the line widths. The laser induced fluorescence spectroscopy and inter-modulated saturation spectroscopy performed on praseodymium in a hollow cathode discharge cell cooled by liquid nitrogen resulted in line widths of the order of ~ 800 MHz and ~200 MHz respectively. Whereas the line widths in the range of 40 - 70 MHz were recorded for neodymium, lanthanum and praseodymium by using the sub- Doppler technique of collinear laser ion beam spectroscopy.

6 LASER SPECTROSCOPY

The invention of lasers brought phenomenal changes in all sphere of human life. Generally all the areas of scientific disciplines have benefitted from lasers but the contribution in the field of atomic and molecular physics is beyond any comparison. The uses of lasers as light sources have completely renovated the field of spectroscopy. Several new methods of high resolution spectroscopy are developed and the precision of old spectroscopic techniques are redefined. There are numerous advantages of lasers over the conventional light sources. Some of the selected parameters which make them superior over the conventional light sources are listed below:

- A laser beam is highly monochromatic light source.
- A laser beam is highly collimated light.
- The spectral power density of a laser beam is extremely high.
- The coherence length of a laser beam can be very large.
- Much higher spectral resolution can be achieved when a laser is used as a light source.

There are three major components of a laser system; an optical cavity called the optical resonator, a laser gain medium (also called active laser medium) and a pump source to excite the atoms/molecules in the gain medium.

The optical resonator consists of at least two mirrors between which the light bounces back and forth. To define the optical modes and in consequence the laser beam one or more mirrors are curved. The reflectivity of lasers mirrors is typically ~ 99.9%. However one of the end mirrors, called output coupler, is partially reflective so that a portion of the light is transmitted. The gain medium in the resonator amplifies light and thus compensates for the losses through the output coupler and other sources. Lasers are classified by the type of gain medium they use (gas lasers, solid-state lasers, dye lasers, semiconductor lasers, etc.). The gain medium is used for population inversion and stimulated emission processes. In a continuous wave (CW) laser, the gain in the laser gain medium and the losses from the output coupler plus other losses are in equilibrium.

Since the amplification process maintains the phase and direction of the light, the laser output is highly directional and coherent. To achieve population inversion in a gain medium some pumping process is required, which lifts the gain medium into the required energy state. Typical pumping processes are electrical current in a gas or semiconductor laser or optical pumping in a solid-state or dye laser. Optical pumping is usually achieved either by flash lamps or by another laser.

Organic dyes are used as the gain medium in dye lasers. The wide gain spectrum of available dyes allows these lasers to be highly tunable. Although the gain medium in tunable lasers are mainly in liquid form but narrow-line-width tunable laser emission has also been demonstrated in solid-state dye gain media [157]. A numerical comparison between a conventional light source (RF discharge) and single mode cw dye laser is given in Table 6.1

Table 6.1: Comparison between a conventional light source and single mode cw dye laser [158]

	RF discharge lamp	cw sinle mode dye laser
Line width	1000 MHz	1 MHz
Power within a useful solid angle	10^{-2} W	10^{-1} W
Power density per unit frequency	10^{-6} W/(cm^2 MHz)	10^{3} W/(cm^2 MHz)
Irradiated area (depends on focusing)	10^{2} cm^2	10^{-4} cm^2
Total output of a line	10^{-1} W	10^{-1} W

6.1 **Ring Dye Laser**

The laser system in our experimental setup consists of a ring dye laser having a bandwidth of less than 1 MHz, pumped by an Ar^+ laser. A mechanical layout and position of various components of the ring dye laser are shown in Figure 6.1. For a good mechanical strength and stability all components (mechanical or optical) are mounted directly or indirectly to a two inch Invar bar. The coefficient of thermal expansion for Invar is very low and it can passively stabilize the cavity length of less than 1 micron / degree centigrade. In 1966, Sorokin et al [159] and Schäfer et al. [160] discovered independently laser action in organic dyes. Now several hundreds of dyes are available which can be used as a laser media. One of the most frequently used laser dyes is Rhodamine 6G, dissolved in ethylene glycol.

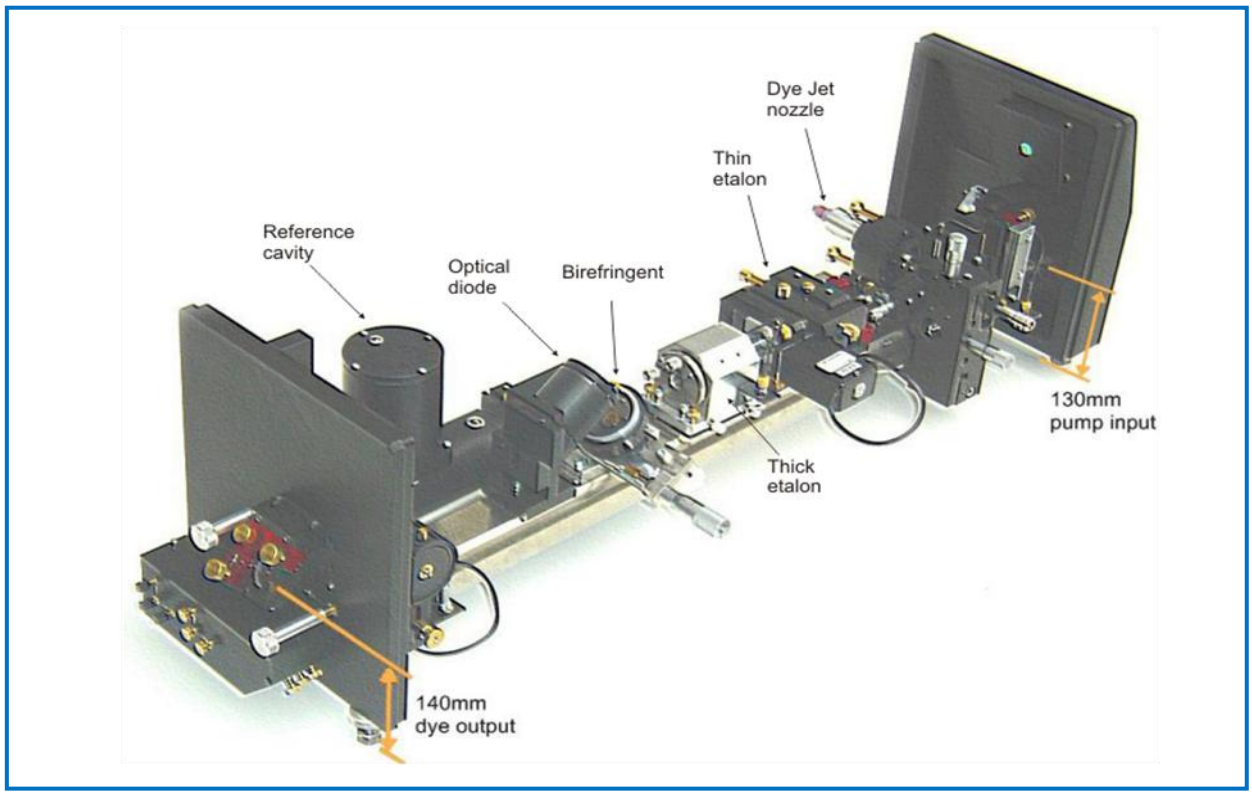

Figure 6.1 A view of real cw ring dye laser [161].

The general energy level structure of organic dye is shown in Figure 6.2. When the dye solution is irradiated by the pumping laser (Ar^+ laser in our case), some of the dye molecules are excited from the singlet ground state band S_0 to the higher excited state band S_1. The excited molecules decay very quickly (~ 10^{-12} s) through radiation-less transition to the lowest level of the excited state S_1. From this state the dye molecules can jump through unwanted radiation-less route to the triplet state T_1 or can decay to the sublevels of ground S_0 through induced emission in time interval of ~ 10^{-9} s. The transition from S_1 to S_0 determines the laser frequency. These ro-vibronic levels are strongly collisional broadened due to the interaction between the dye and the solvent molecules. This results in continuous emission spectra of dye molecules rather than discrete, and thus offer an extended range of continuous tunable laser wavelength [158].

The triplet state T_1 not only makes it difficult to achieve population inversion between the states S_0 and S_1 but it also favors the transition from triplet state T_1 to higher triplet state T_2, through absorptions of the radiations. This unwanted phenomenon can be avoided if the state T_1 is eliminated from the resonator in time scale less than the life time of the state T_1. This is achieved by circulating the dye solution with high enough speed to reduce the time of flight of dye through the active region.

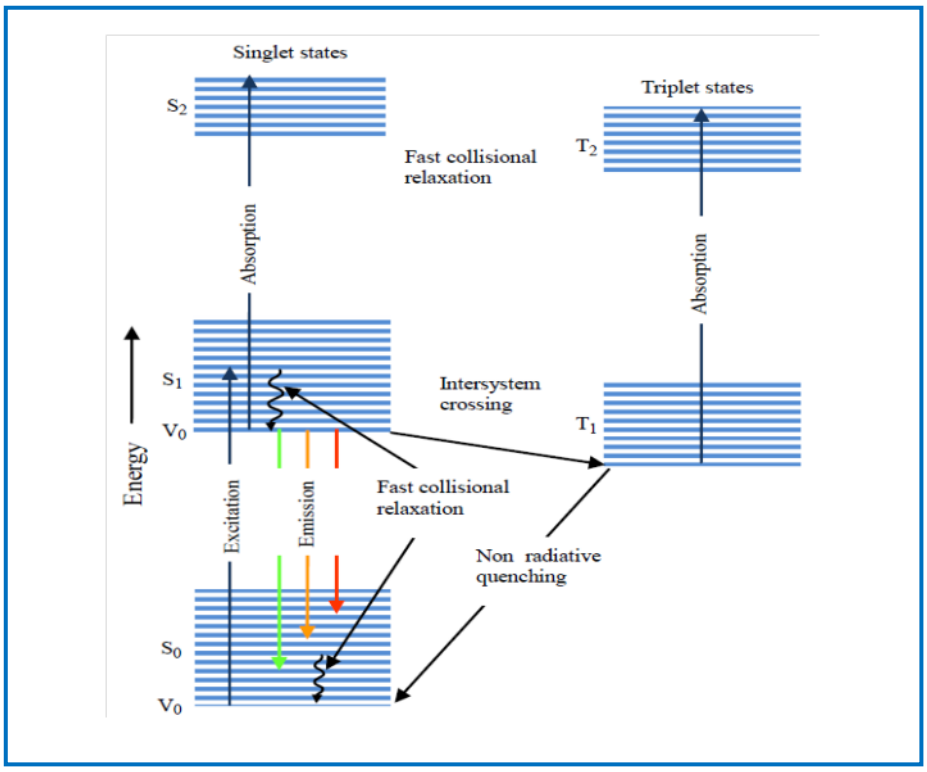

Figure 6.2: *Schematic energy level diagram of a dye molecule [162].*

A schematic of optical arrangements of the ring dye laser is shown in Figure 6.1. The pumping mirror Mp focuses the intense laser beam from pumping laser (Ar^+ laser) on to the dye jet. A smooth stream of dye flows through the dye nozzle at high pressure and the dye jet is slanted at Brewster angle to minimize the reflection losses. The dye molecules excited by absorption of pumping laser light decay spontaneously and emit symmetrical fluorescence in all directions in space. The lower folding mirror M1, the upper folding mirror M3, the output coupler M4 and the tweeter mirror M2 form a closed resonator. When the fluorescence light form a closed path an induced emission occurs and two laser beams travel in opposite directions starting from the dye jet. To increase the laser output power and smooth operation of the laser one of the laser beams is suppressed and amplification of light is achieved only in one direction. For this purpose an optical diode in combination with a quartz plate is introduced in the laser cavity. The optical diode is an arrangement of Faraday rotator and a Brewster angled rhomb surrounded by a permanent magnet. The combination of optical diode and a thin quartz plate introduce fewer losses for laser light in one direction but more losses for laser light moving in opposite direction. Thus amplification of laser circulating in only one direction is achieved. The large cavity length offers an enormous amount of standing waves which can with stand in the laser cavity.

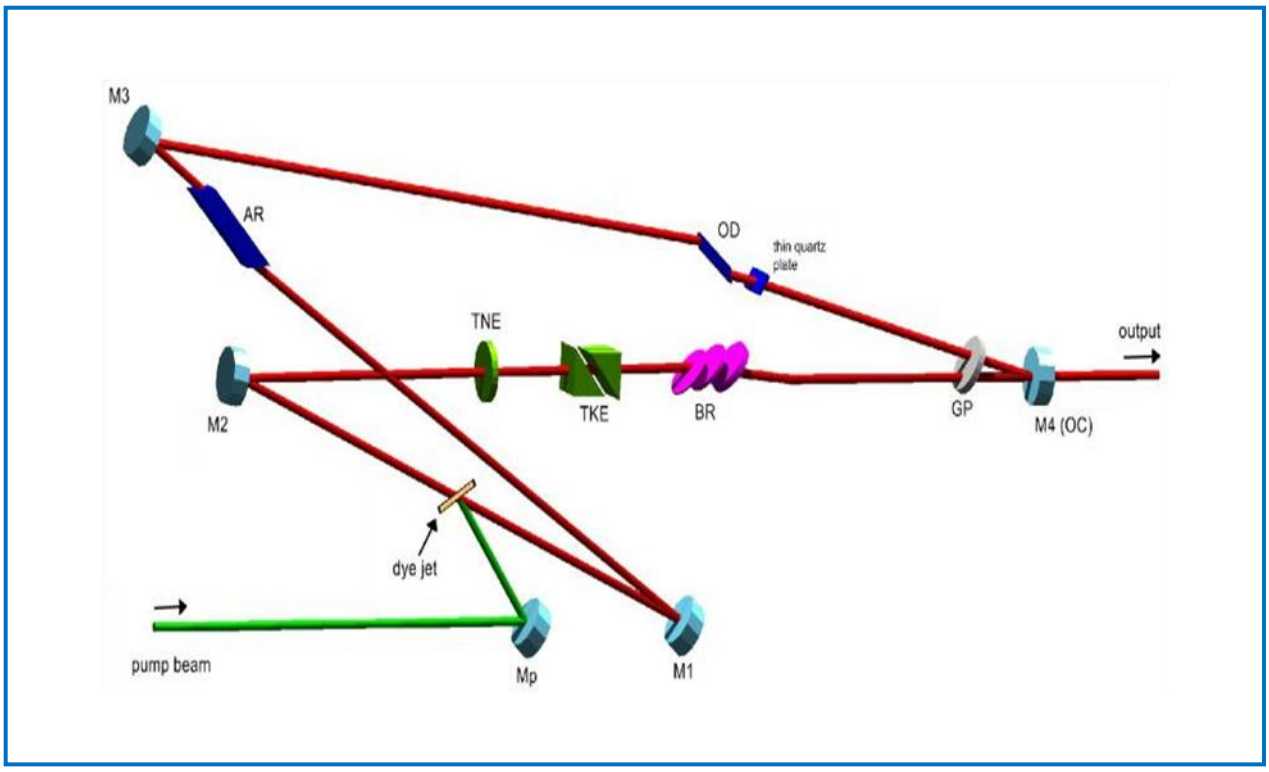

Figure 6.3: Optical arrangements of ring dye laser [161] .

Mp = pump mirror, M1 = lower folding mirror, AR = Astigmatism compensation rhomb, M2 upper folding mirror, OD = Optical diode, GP = Galvo plate, M4 = Output coupler, BR = Birefringent, TKE = Thick etalon, TNE = Thin etalon, M2 = Tweeter mirror (mounted on PZT).

Thus a massive number of longitudinal modes exist in the laser light. To select a single mode laser operation several wavelength selecting elements are introduced in the laser cavity.

The first wavelength selecting element is a birefringent filter. It is a Lyot type filter and consists of three parallel quartz plates; each successive plate has thickness of four times the previous one and mounted at Brewster angle. The free spectral range (FRS) of birefringent is normally of the order of THz and depends upon the thickness of the plates. Further selection of the laser wavelength is made through two etalons; the thin etalon and the thick etalon. The thin etalon is a 0.5 mm thick quartz plate and is mounted nearly perpendicularly to the incidence. Its FSR is ~ 200 GHz and transmission more than 80 %. The thick etalon has a thickness of 10 mm, FSR 14 GHz and transmission of ~ 80 %. It is a prism shaped etalon and is mounted on piezo-electric-transducer (PZT), normal to the laser beam axis.

These three frequency selective elements are not only used for single mode laser operation but the combination of these also defines the scanning mechanism of the laser. The Brewster angled

tuning plate called as the Galvo plate is used for the continuous change of the cavity length and frequency shift of the selected mode. The Brewster plate is mounted on a small Galvo-drive so that tuning can be controlled with an applied voltage. To get rid of the frequency fluctuations due to the thermal instabilities, turbulences and micro bubbles in dye jet, pressure and refractive index variations etc. the laser is actively stabilized to an external confocal reference cavity. The detail of the reference cavity and locking mechanism is given in operating manual of dye laser [161]. A side locking technique in which the laser is locked to one side of the transmission signal is used to stabilize the laser frequency. The error signal from the reference cavity is divided into low and high frequency parts. The low frequency instabilities are compensated by the Galvo plate while the high frequency fluctuations are controlled by the tweeter mirror.

The transmission curves of the birefringent, thin and thick etalons are drawn in Figure 6.4. When the laser is properly locked and the transmission curves of all these elements are aligned to identical wavelength a single mode laser with a bandwidth of less than 1 MHz can be achieved. The scanning range of dye laser used in our laboratory is 30 GHz.

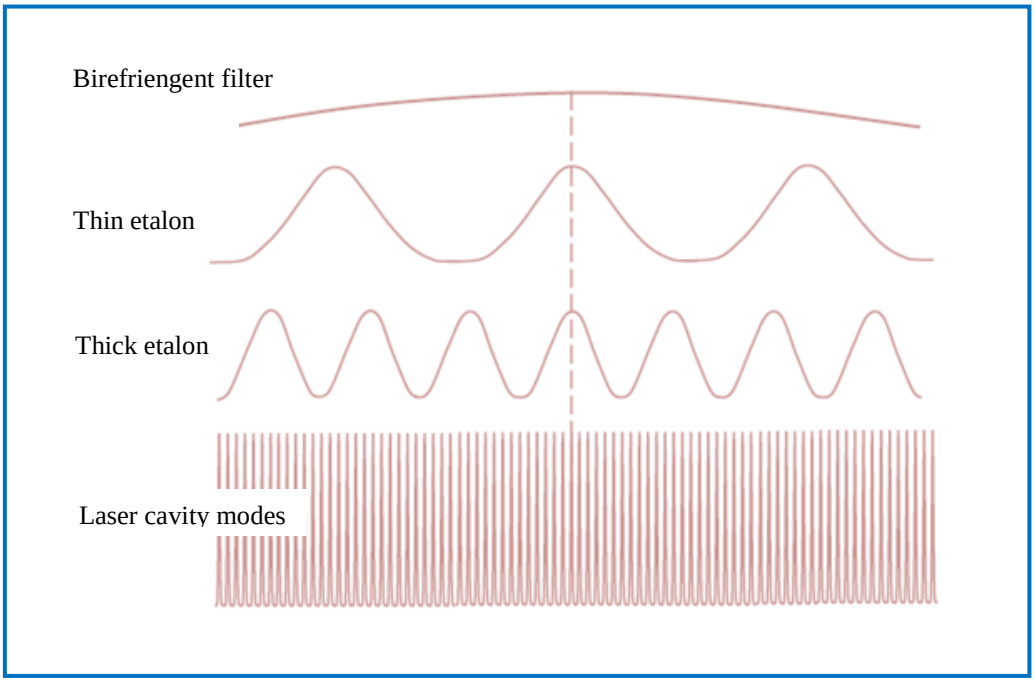

Figure 6.4: Transmission curves of mode selecting elements.

6.2 **Laser Spectroscopy**

The roots of spectroscopy originated from the Newton's famous experiments on the dispersion of white light into a range of colors. Now the concept of spectroscopy is regarded as any interaction with radiative energy as a function of its wavelength or frequency. Spectroscopy is basically an experimental subject and is mainly related with the absorption, emission or scattering of electromagnetic radiation by atom or molecules. Spectroscopy is a very vast field and it has been further expended by the invention of the laser in 1960. The development of wide range and sophisticated tunable lasers in 1970's brought a gigantic acceleration in the field of spectroscopy. The new methods of high resolution spectroscopy are developed and the precision of old spectroscopic techniques are redefined.

There are numerous ways/types in which laser spectroscopy can be classified but on a very broad spectrum and on basis of spectral resolution laser spectroscopy can be divided in two main categories. Doppler broadened or Doppler limited laser spectroscopy and Doppler-free or sub-Doppler or Doppler reduced laser spectroscopy.

6.2.1 **Doppler Limited Laser Spectroscopy**

The spectral resolution depends upon the spectroscopic techniques as well as on the spectroscopic instruments but generally in Doppler limited laser spectroscopy the spectral resolution is not very high and in most cases the line width of the optical transitions is many times larger than natural line widths. The main source of very large Doppler widths is thermal motion of the atoms/molecules. The spectroscopic techniques like laser induced fluorescence spectroscopy, optogalvanic spectroscopy, cavity ring down spectroscopy, absorption spectroscopy, photoacoustic spectroscopy, etc. are the examples of Doppler limited laser spectroscopy. In the following discussion only laser induced fluorescence spectroscopy and optogalvanic spectroscopy are presented.

6.2.1.1 Laser Induced Fluorescence Spectroscopy

The laser induced fluorescence (LIF) is a process in which atoms or ions (i.e. the plasma in a hollow cathode gas discharge lamp) are excited to higher electronic energy states through absorption of a suitable laser frequency and subsequently the excited energy states decay to the lower energy states through several processes and fluorescence is one of them. The emission

spectrum provides information for qualitative as well as quantitative analysis. In general, the fluorescence intensity is a function of the species concentration (number density) and the gas temperature and pressure. The fluorescence signal also linearly depends on the intensity and the absorption cross-section of the laser beam. By virtue of the fact that the energy states of atoms or molecules are quantized, the spectral absorption regions are also quantized. But in case of large molecules the spacing of the discrete transitions may be sufficiently small (the number of transitions sufficiently great) that discrete absorption regions are not good enough resolved and instead of discrete absorption lines only absorption bands are observed. Typically, fluorescence occurs at wavelengths greater than or equal to the laser wavelength. The emitted fluorescence is incoherent and is mostly unpolarized due to collisions. A sophisticated experimental setup used for LIF spectroscopy at Institute of Experimental Physics, Technical University Graz is shown in Figure 6.5. The plasma in the hollow cathode discharge lamp is irradiated by a suitable laser frequency. For phase sensitive detection the laser intensity is chopped with a mechanical chopper and the modulated frequency is fed into a lock- in-amplifier as reference signal. A grating monochromatic and a photomultiplier serves as a selection and detection mechanism of LIF signal.

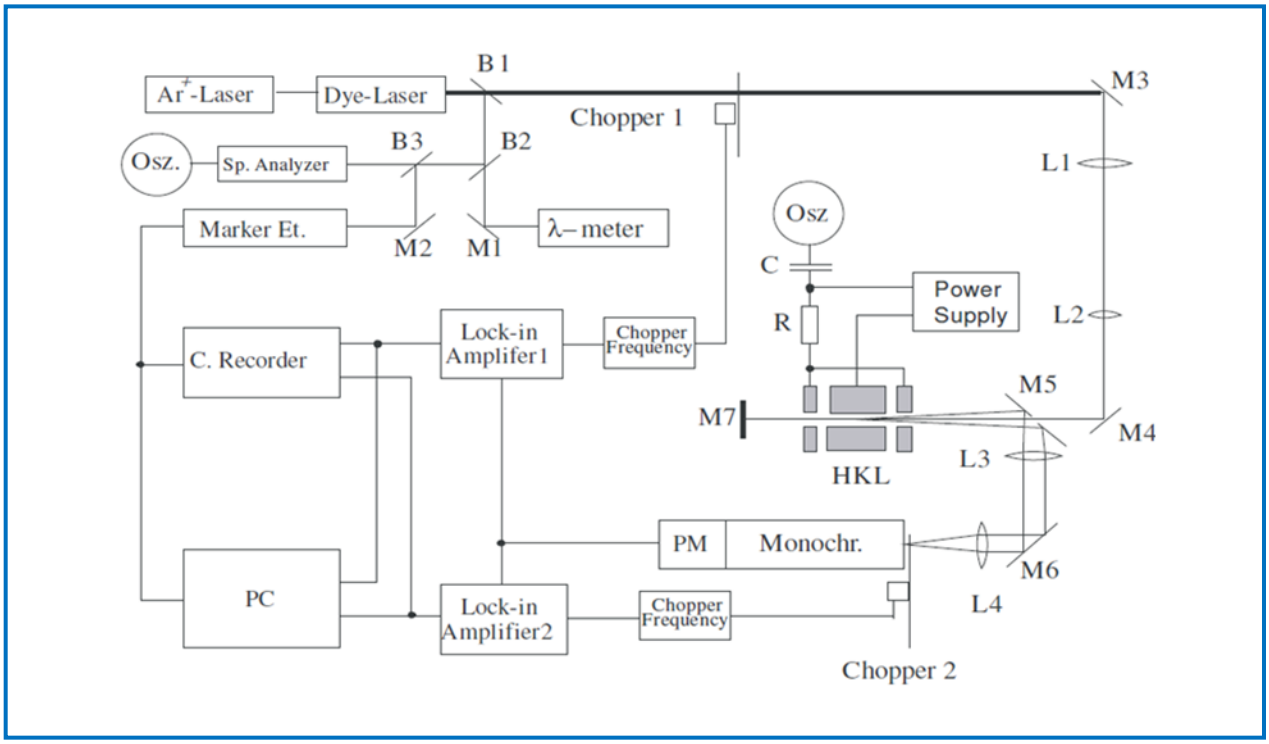

Figure 6.5: A Schematic of experimental setup of LIF spectroscopy [163].

The observed fluorescence lines can be categorized into three types.

Positive Fluorescence

A schematic of LIF signals is depicted in Figure 6.6. The excitations take place from lower level E_2 to the upper level E_3 at resonance laser wavelength λ_{23}. The upper level E_3 can decay to the lower levels E_4 and E_5 by emitting fluorescence signal of wavelength λ_{34} and λ_{35} respectively. When laser intensity is modulated through a mechanical chopper and the LIF signal is recorded through a phase sensitive detection technique, the maximum LIF signal is observed when the modulation frequency and LIF signal are in phase. In view of the fact that LIF signal increases when laser is on, is called a positive phase or positive signal.

Negative Fluorescence

Now consider a situation in which a lower level involved in a transition is lying higher than other lower levels. In this case the former lower level can decay to further lower levels by emitting LIF signal. This is possible when the laser frequency is in resonance for transition E_2 to E_3, some of the atoms in energy state E_2 can decay to the energy state E_1 by emitting a fluorescence signal λ_{12}. In this case the population of the state E_2 decreases when the laser is on and the observed fluorescence is 180°out of phase as compared to positive fluorescence and as a result this kind of fluorescence signal is called negative fluorescence.

Impact or collisional coupling

In densely populated environment there is possibility that two or more energy levels in excited states can lie very close to one another. In this case due to collision atoms can transfer their energy to other closely lying energy levels. This non-radiative energy transfer is called impact or collisional coupling. After the impact coupling the atoms decay to suitable lower levels through emission of fluorescence light. In Figure 6.6 the impact coupling takes place between the closely lying energy levels E_3 and E_6 and the energy level E_6 decay to energy level E_7 through emission of fluorescence light λ_{67}. Population transfer is equally possible between equal energy lower levels e.g. E_2 and E_8. It is important to note that in all three types of fluorescence mentioned above, the observed hyperfine structure is generated through transition between the states E_2 and E_3.

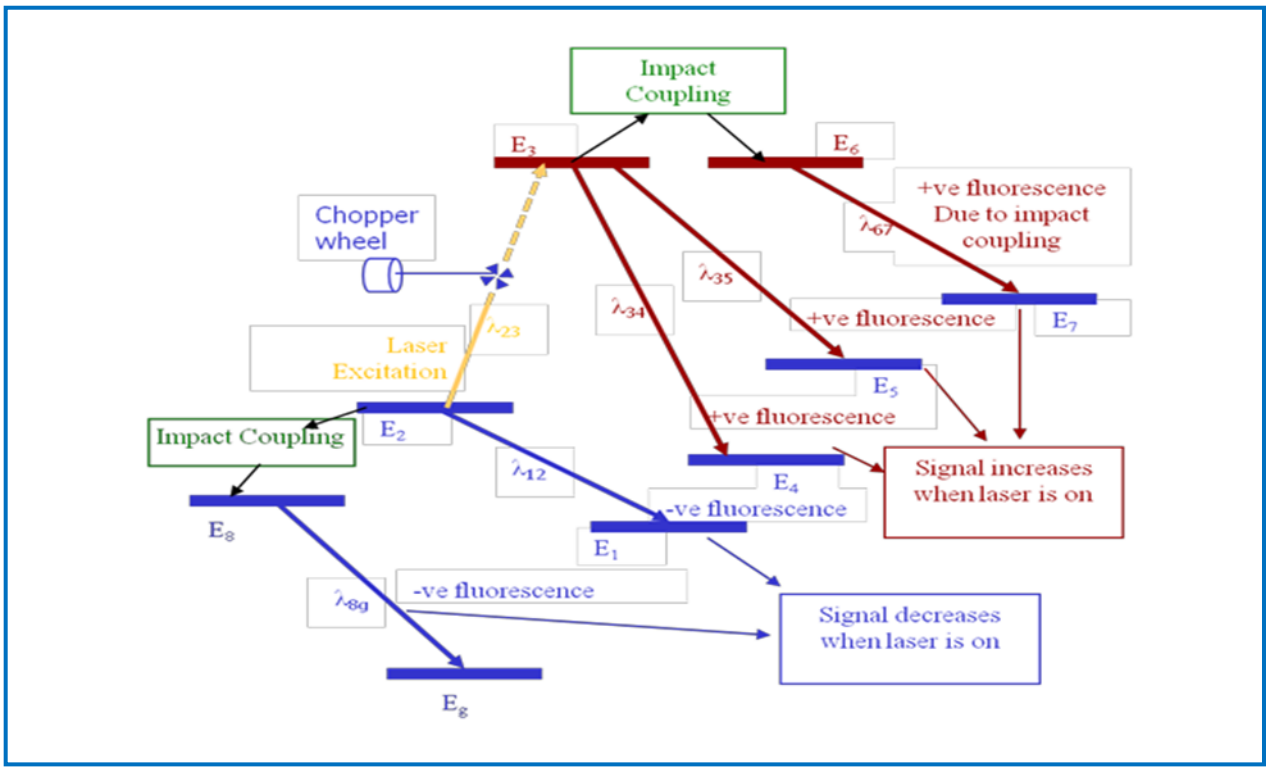

Figure 6.6: Pictorial representation of laser induced fluorescence signals [163].

Advantages and Applications of LIF Spectroscopy

Some selected advantages and applications of LIF spectroscopy are listed below:

- LIF is one of the efficient ways to analyze blended structures. In a blend situation, for a narrow laser frequency scan more than one closely spaced energy levels are excited simultaneously (all lines involved in transition have same center of gravity wavelength). The hyperfine structure of each line and identification of the energy levels can be made by observing the individual fluorescence channels corresponding to different upper levels.
- In LIF method, the signal to noise ratio is very high due to phase sensitive detection.
- The dependence of excited state population on temperature, offers a way to measure the temperature using LIF technique.
- By measuring the Doppler shift of the transition along the laser beam propagation axis the velocity of the atom / molecules can be measured.
- A careful analysis of pressure-dependent transition broadening can provide information about the pressure inside the discharge cell.

6.2.1.2 Optogalvanic Spectroscopy

Optogalvanic spectroscopy is a form of absorption spectroscopy in which the induced changes in the electrical properties of atoms/ions (plasma in gas discharge) are observed. Optogalvanic effect was realized in 1928 by Penning [164] in neon gas discharge cell. In optogalvanic spectroscopy a self-sustained gas discharge is illuminated by a resonant radiation with an atomic or molecular transition of the elements and changes in the electrical conductivity of the discharge are observed.

An experimental setup for optogalvanic spectroscopy is shown in Figure 6.7. A hollow cathode discharge cell is irradiated with a dye laser beam. When the laser frequency is tuned to the optical transition frequency of atomic/ionic levels a population density of lower and upper levels changes. Consequently the electrical conductivity of the gas discharge changes due to the change in the plasma density. The change in the current ΔI is measured across the ballast resistor R as a voltage change $\Delta V = R\Delta I$. To improve signal to noise ratio a phase sensitive detection system can be employed.

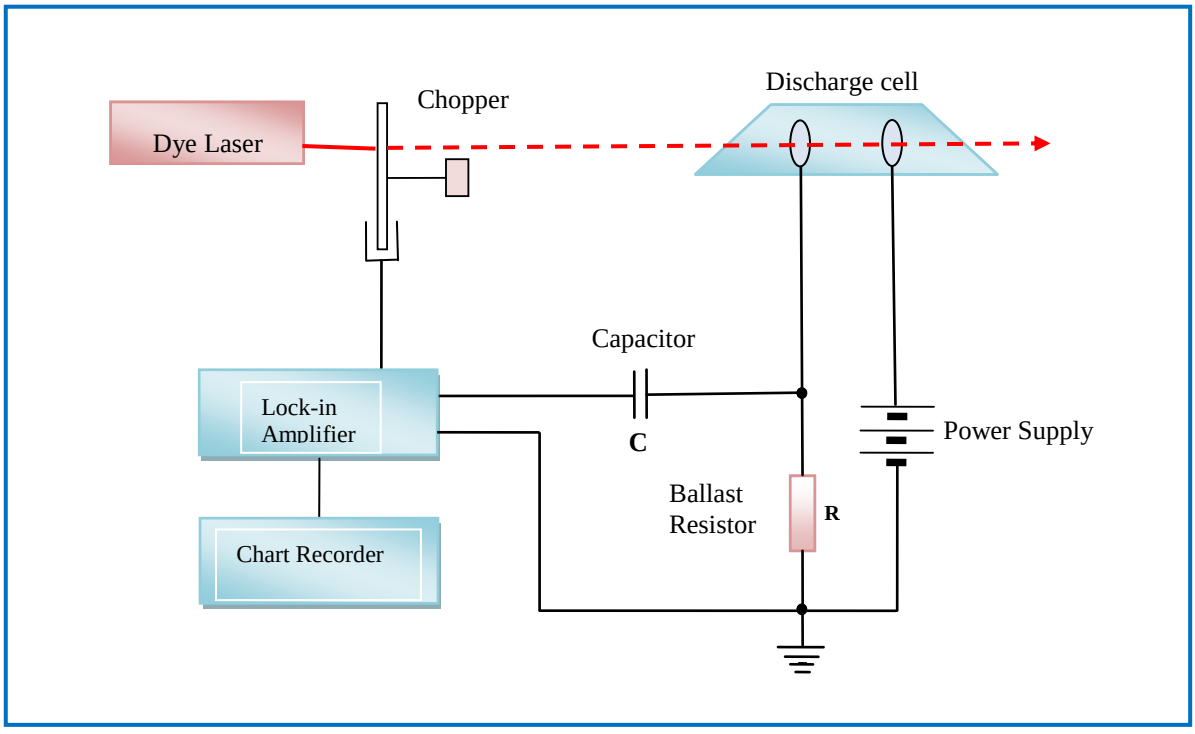

Figure 6.7: A schematic of Experimental setup for optogalvanic spectroscopy.

Optogalvanic diagnostics are applicable over an extremely broad range of discharge conditions. Different processes dominate in the various discharge regimes so optogalvanic detection is a

versatile tool and has provided many new insights. In high pressure regime the super-elastic processes are dominant, electron collisional mixing prevail in the normal glow and in the Townsend regime (low pressure discharge region) the fundamental ionization mechanisms take control.

In optogalvanic spectroscopy there is no need of monochromator and photomultiplier tube because the discharge also acts a detector. A good stability of the discharge is required throughout the recording because minor instabilities of discharge can produce large noise in the output signal.

The dominant processes which contribute to ionization of an atom are listed below:

At low pressure the direct ionization is dominant and is given;

$$A + e^- \rightarrow A^+ + 2e^-$$

Collisional ionization by metastable atoms takes place at normal discharge pressure;

$$A^* + B^* \rightarrow A^+ + B + e^-$$

Direct photo-ionization by electromagnetic radiation;

$$A + h\nu \rightarrow A^+ + e^-$$

Two steps or multistep ionization process (normally occurs in higher excited states);

$$A + e^- \rightarrow A^*$$
$$A^* + e^- \rightarrow A^+ + 2e^-$$

The excitation and ionization mechanisms in gas discharge, plasma and flame [165] can be explored by simple optogalvanic spectroscopy. It has been applied to the measurement of the pressure broadening and frequency shift in the negative glow region of a hollow cathode discharge [166] This technique has wide range applications in atomic structure studies, laser wavelength control-check, intensity and frequency stabilization of lasers and analytical chemistry [167] Optogalvanic double-resonance spectroscopy provides another method of state-selective spectroscopy in plasma [168].

6.2.2 **Doppler-Free (Sub-Doppler) Laser Spectroscopy**

The higher resolutions abilities of a spectroscopic method are a demanding subject for better understanding of the complex optical spectra of various atomic/ionic transitions. Single mode lasers systems with sufficiently narrow line width and sophisticated methods of Doppler width reduction are necessary to completely resolve the intricate spectral lines. In the following debate few methods of Doppler-free (Doppler reduced) spectroscopy like, two photon spectroscopy, saturation spectroscopy and collimated atomic beam spectroscopy are discussed. While a detail discussion and experimental investigation about intermodulated saturation spectroscopy and collinear laser ion beam spectroscopy (CLIBS) will be presented in chapters 7-10.

6.2.2.1 Two Photon Laser Spectroscopy

In two-photon laser spectroscopy an atom/molecule can be excited from one state (usually the ground state) to a higher energy electronic state by simultaneous absorption of two photons either from two different lasers or two photons from the same laser. The energy difference between the involved lower and upper states of the molecule is equal to the sum of the energies of the two photons. Two-photon transitions are several orders of magnitude weaker than allowed one photon transitions. It is a nonlinear optical process and the strength of absorption depends on the square of the light intensity. Thus for the observation of two-photon transitions lasers with sufficiently high intensities are required. Although two-photon absorption phenomenon was predicted in 1931 by Maria Goeppert-Mayer [169] but it was experimental observed in 1961 with the invention of the laser [170].

A schematic representation of two-photon absorption process is shown in Figure 6.8. An atom in ground state (E_i) absorbs a photon of energy $h\omega_1$and makes a transition to intermediate excited state E_m. Absorption of another photon of energy $h\omega_2$ can lift the atom to further high lying excited state of energy E_f. If an atom moves with velocity υ (in laboratory frame of reference), the laser frequency ω is Doppler shifted (in moving atom frame of reference) to $\omega' = \omega - k.\upsilon$. The resonance condition of two-photon simultaneous absorption is

$$\frac{(E_f - E_i)}{h} = (\omega_2 + \omega_1) - \upsilon\,(k_2 + k_1). \qquad 6.1$$

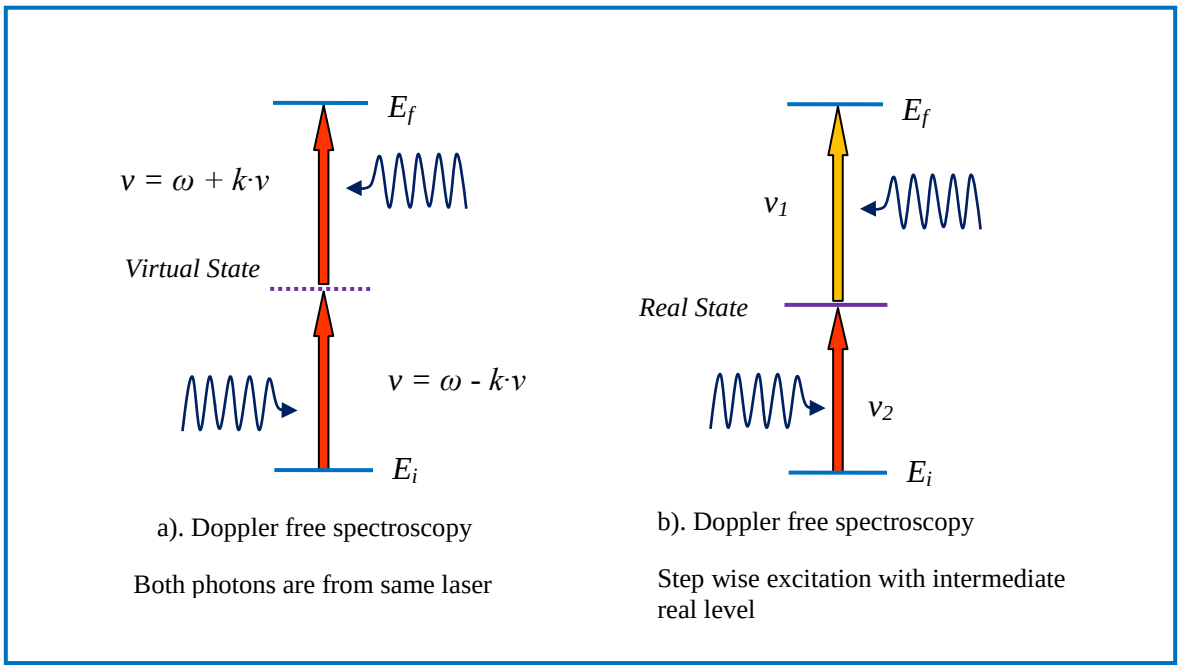

Figure 6.8: Two-photon absorption mechanism.

If two photos from same laser are absorbed in opposite direction i.e. $\overrightarrow{k_1} = -\overrightarrow{k_2}$ then the Doppler shift from two-photon absorption is completely cancelled out and all atoms regardless of their velocities absorb the same laser frequency $\omega_2 + \omega_1 = 2\omega$. Thus all atoms irrespective of their velocities contribute to the two-photon absorption, which is now Doppler-free.

The signal recorded by two-photon laser spectroscopy is shown in Figure 6.9. The narrow peak is produced due to the absorption of two same frequency photons propagating in opposite direction and the Doppler broadened background originate from absorption of two same frequency photons moving in same direction. Thus for photons approaching with opposite *k* vectors the Doppler width is cancelled and a Doppler-free signal is obtained but the Doppler width is added (becomes twice as compared to single photon absorption) when parallel *k* vectors photons are absorbed. Figure 6.8 (b) is also a form of two-photon Doppler free absorption but in this case the intermediate state is a real state and also two-photons are absorbed from two different lasers frequencies. The interaction probability of two opposite *k* vectors photons is twice as compared to parallel *I* vectors photons. That is way the intensity of narrow peak signal is much higher than Doppler broadened background.

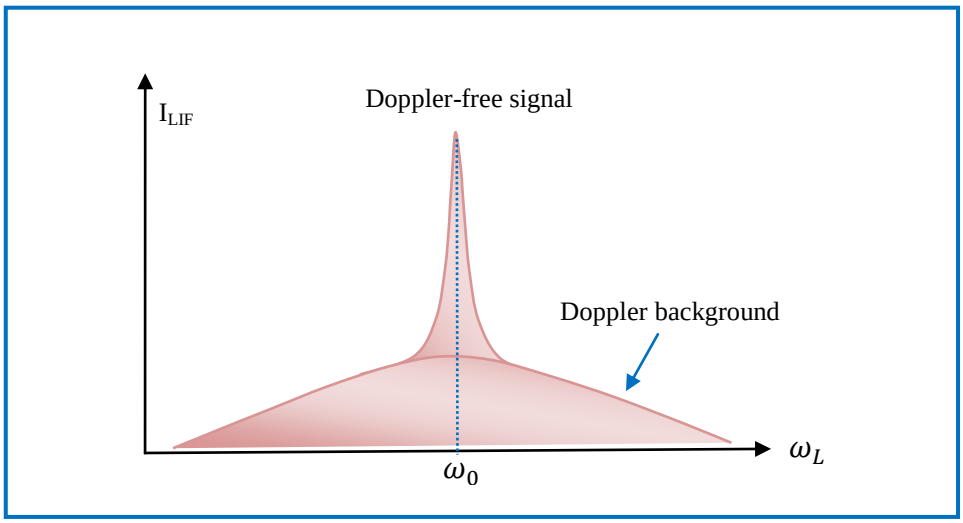

Figure 6.9: Two-photon Doppler free and Doppler broadened line profiles

- Doppler-free two photon absorption is independent of atomic/molecular velocities.
- The optical transition rules for two-photon are $\Delta L = 0$ and $\Delta L = \pm 2$.

6.2.2.2 Saturation Laser Spectroscopy

The underlying principle of Doppler-free saturation spectroscopy is based on velocity selective saturation of Doppler broadened atomic/molecular transitions. This spectroscopic technique is also called Lamb dip spectroscopy because the spectral line width is equivalent to the width of the Lamb dip.

When a vapor cell with Maxwell ions velocity distribution profile is irradiated by an intense monochromatic tunable laser beam and the laser frequency is tuned to the resonance frequency of a particular transition, the laser saturates a particular velocity group, let say v_z. Within the velocity interval dv_z the population density $N_1(v_z)dv_z$ of the lower level decreases due to the saturation effect and as a result the population density of the upper level $N_2(v_z)dv_z$ increases with reference to the lower level (Figure 6.10). This velocity selective minimum in Maxwell velocity distribution is called Bennet hole [171]. Now if another laser beam of same frequency and intensity is irradiated on the vapor cell from opposite direction, another Bennet hole is burnt in the Maxwell population distribution $\Delta N(-v_z)$ at velocity component $-v_z$. Normally the intensity of the laser beam is distributed in two equal parts which are irradiated on the vapor cell from opposite directions. At the centre of transition frequency ω_0, a dip (Lamb dip) is observed in the Doppler broadened absorption profile. At this frequency both laser beams interact with same

velocity group i.e. $v_z = 0$ (perpendicular to both laser beams). This velocity group experiences double laser intensity as compared to other velocity groups and the saturation effect for this group is greater. The experimental setup and details discussion about saturation spectroscopy can be found in ref. [10].

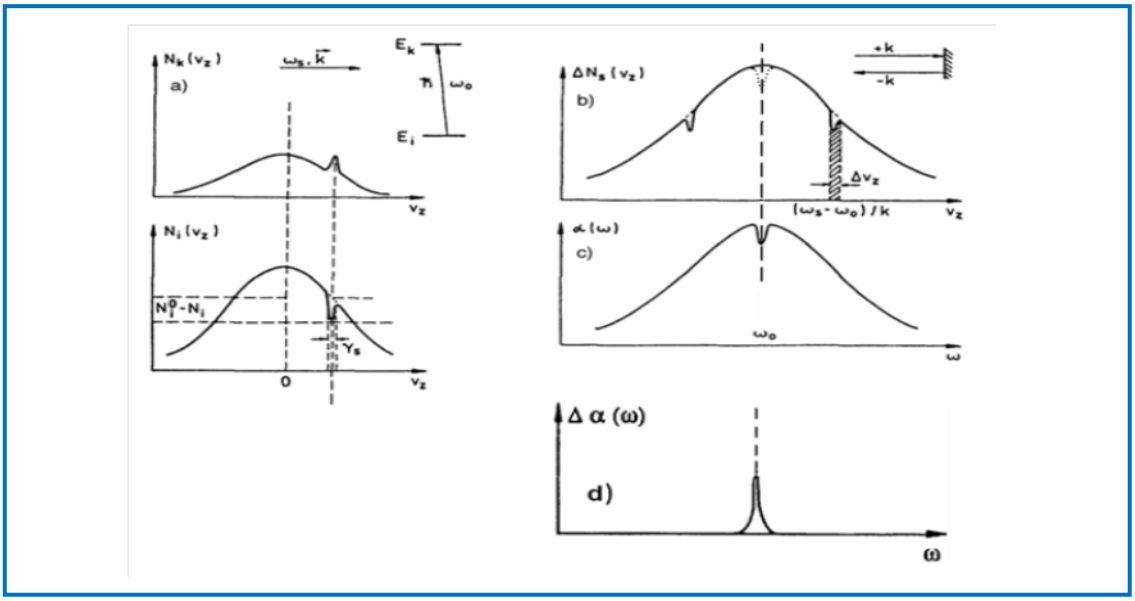

Figure 6.10: Velocity-selective saturation. (a) Bennet hole and dip when laser beam has $\omega \neq \omega_0$; Bennet holes produced by the two counter propagating laser beams for $\omega \neq \omega_0$ and for $\omega = \omega_0$ (dotted curve); (c) Lamb dip in the absorption profile $\alpha(\omega)$; (d) Lamb dip signal at the laser beams modulation frequencies f_1+f_2 [this figure is taken from "Laser spectroscopy" by W. Demtöder].

6.2.2.3 Collimated Atomic Beam Laser Spectroscopy

This is another method of high resolution spectroscopy in which the Doppler width of spectral lines is reduced by narrowing the transversal velocity spread in the atomic/molecular beam. An experimental layout for realization of collimated atomic beam laser spectroscopy is shown in Figure 6.11. Atoms/molecules effusing with high velocities from the reservoir (oven) through a small hole are collimated by inserting few slits in the beam path and a single mode laser beam is irradiated perpendicularly to the atomic/molecular beam. The collimation ratio C (C = s/d) defines the reduction of the Doppler width. For normal Doppler broadening Δv_D inside the oven and collimation ration C, the reduced Doppler width, $(\Delta v_D)_{res}$, is given by equation 6.1.

$$(\Delta v_D)_{res} = \frac{\Delta v_D}{C\sqrt{2}}. \qquad 6.2$$

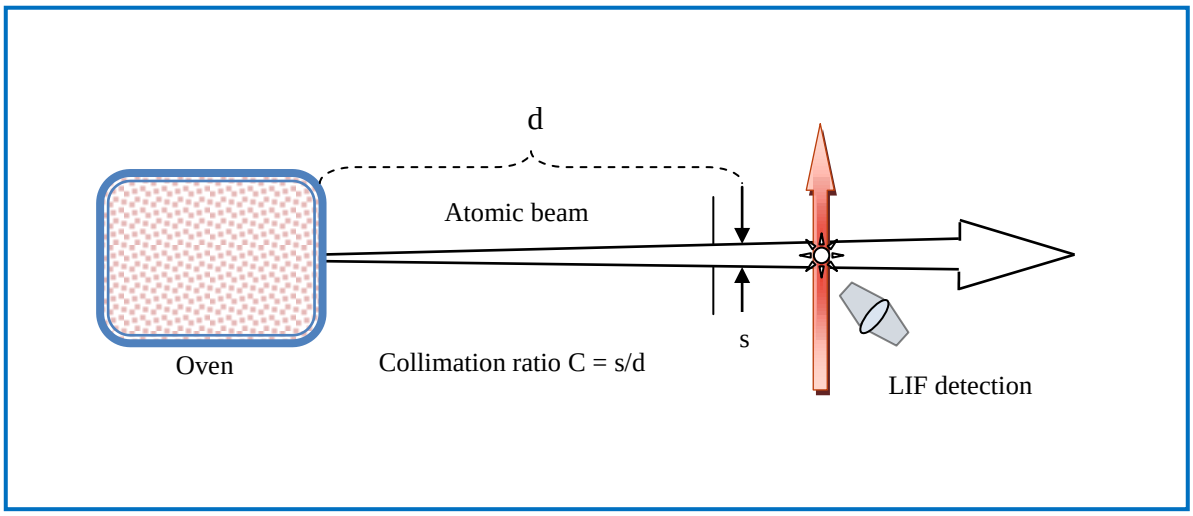

Figure 6.11: Experimental layout of collimated atomic beam laser spectroscopy.

Main features of atomic beam spectroscopy:

- Atomic beam spectroscopy is essentially possible for almost all the elements.
- The collisional effects in comparison to discharge cells are substantially low.
- By using high collimation ratios and sustainably low laser powers the spectral resolution in the range of natural line width of spectral lines can be reached.
- Due to very small interaction length and isotropic emission of fluorescence light at solid angle of 4 π radians, weak transitions are not feasible to investigate.
- This method is feasible to investigate only ground state or low lying excited states transitions which can be populated in the oven.

7 INTER-MODULATED LIF SPECTROSCOPY of Pr II LINES and COMPARISON of THREE SPECTROSCOPIC METHODS

The techniques of saturation spectroscopy were discussed in chapter 6. The methods of saturation spectroscopy are considered as sub-Doppler (Doppler reduced) or sometimes Doppler-free laser spectroscopy. Inter-modulated laser induced fluorescence spectroscopy or Lamb dip spectroscopy is one of the techniques of laser spectroscopy which can significantly reduce the Doppler broadening effects. This chapter is dedicated to the experimental investigations of the hyperfine structure of singly ionized praseodymium (Pr II) using the method of inter-modulated laser induced fluorescence spectroscopy and the results will be compared to the Doppler limited and collinear laser ion beam spectroscopy (CLIBS). As discussed in the previous chapter a high intensity laser beam is divided in two counter-propagating laser beams of nearly equal intensities which interact with the zero velocity groups of ions. One laser beam (pump laser) when interact with ionic cloud of Pr II, it burns a hole in the Maxwell velocity distribution curve of the lower levels of spectral line and when the counter propagating laser beam (probe laser) interacts with same velocity group (already excited ions by pump laser), a Lamb dip is observed in the absorption spectrum. The pump and probe laser beams are chopped at two different frequencies f_1 and f_2 respectively and the phase sensitive fluorescence signal is observed by a lock-in amplifier at sum or difference of the two frequencies i.e. $f_1 \pm f_2$. To make a comparison between the different spectroscopic techniques (Doppler limited, Lamb dip and CLIBS) several spectral lines of Pr II were recorded in three ways. In this chapter inter-modulated laser induced fluorescence spectroscopy will be discussed and a comparison will be made with Doppler limited laser spectroscopy and CLIBS.

7.1 **Experimental Setup**

Roughly speaking the experimental setup for the inter-modulated laser induced fluorescence spectroscopy can be divided into three main parts:

- A laser as an excitation light source.
- A hollow cathode discharge lamp as the source of free atom and ions.
- Detection and measurement of laser induced signals (LIF).

The excitation light source in this experiment is a tunable cw ring dye laser pumped by an $Argon^{+}$ laser or by a solid state diode pumped, frequency doubled, Nd:Vandate Nd:YVO_4 laser (Verdi V-18). The dye Rhodamine 6G is employed to get the desired laser wavelength.

To get free atoms and ions a hollow-cathode discharge lamp (HCL) is used. Praseodymium in the form of a hollow cylinder of length 19 mm and inner diameter 3 mm is fixed inside a hollow copper cathode. On both sides of the cathode two aluminum anodes are integrated and to avoid any contact between the anodes and cathode ceramic holders are used (Figure 7.1). The cathode and anodes are separated by a distance of ca. 0.75 mm. All the components are assembled inside a glass tube collinearly. Both sides of the glass tube are closed by two circular quartz plates. For more details about the fabrication and specification of the hollow cathode the literature given in references [172-174] can be consulted.

To perform saturation spectroscopy argon gas is used as the working gas in the hollow cathode and to obtain a good signal to noise ratio the pressure of argon gas is maintained in the range of 0.02 to 0.2 mbar and the discharge current ~ 60 mA. The sputtering of the cathode material (Pr) takes place when accelerated ions of argon strike the cathode. The collisions between the Pr atoms and argon gas create a Pr and Ar atoms not only in ground states but also in high lying excited states. In this way various Pr I, Pr II, Ar I and Ar II states are populated and a number of spectral lines can be investigated. Generally the Doppler width of spectral lines in the hollow cathode is very large (~ 1GHz) and to reduce it to the range of 600 - 700 MHz the hollow cathode is cooled with liquid nitrogen.

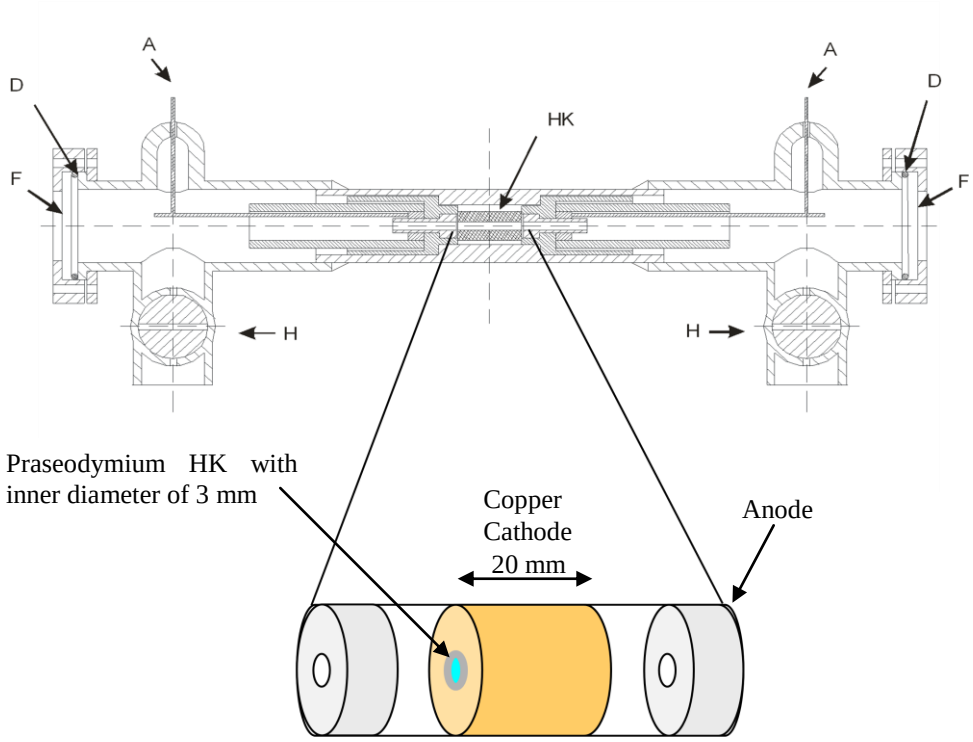

Figure 7.1: Cross sectional view of a hollow cathode discharge lamp. HK = hollow cathode, A = anode, F = quartz windows, D= O-rings, H= glass stop cocks [172-174].

The experimental setup used for inter-modulated laser induced fluorescence spectroscopy is basically the same as it was discussed in chapter 6 (6.2.1.1). But some modifications were necessary to perform saturation spectroscopy and the modified experimental setup is given in Figure 7.2. The laser system in this setup consists of a ring dye laser (Coherent Model 899-21) having a bandwidth of less than 1 MHz, pumped by an Ar^+ laser (Coherent Innova 200). The beam splitter BS1 splits the dye laser beam into two parts, a relatively weaker laser beam (~10 %) and a stronger laser beam (~90 %). The weaker laser beam is further divided by beam splinters BS2 and BS3 and guided by the mirrors M2 and M3 towards a λ-meter (wave meter), a spectrum analyzer and a marker etalon. The marker etalon is a temperature stabilized Fabry-Perot interferometer and is used to generate equidistant frequency marks. The stronger laser beam is guided by the mirror M4 to pass through a telescope formed by the lenses L1 and L2. The telescope collimates the laser beam and irradiates the Pr-Ar cloud in the hollow cathode uniformly. The mirror M5 deflects the laser beam to a 50-50 beam splitter BS4 which splits the laser beam into two equal intensities laser beams (pump and probe beams). A mechanical chopper is used to chop the pump beam and probe beam with frequencies f_1 and f_2, respectively.

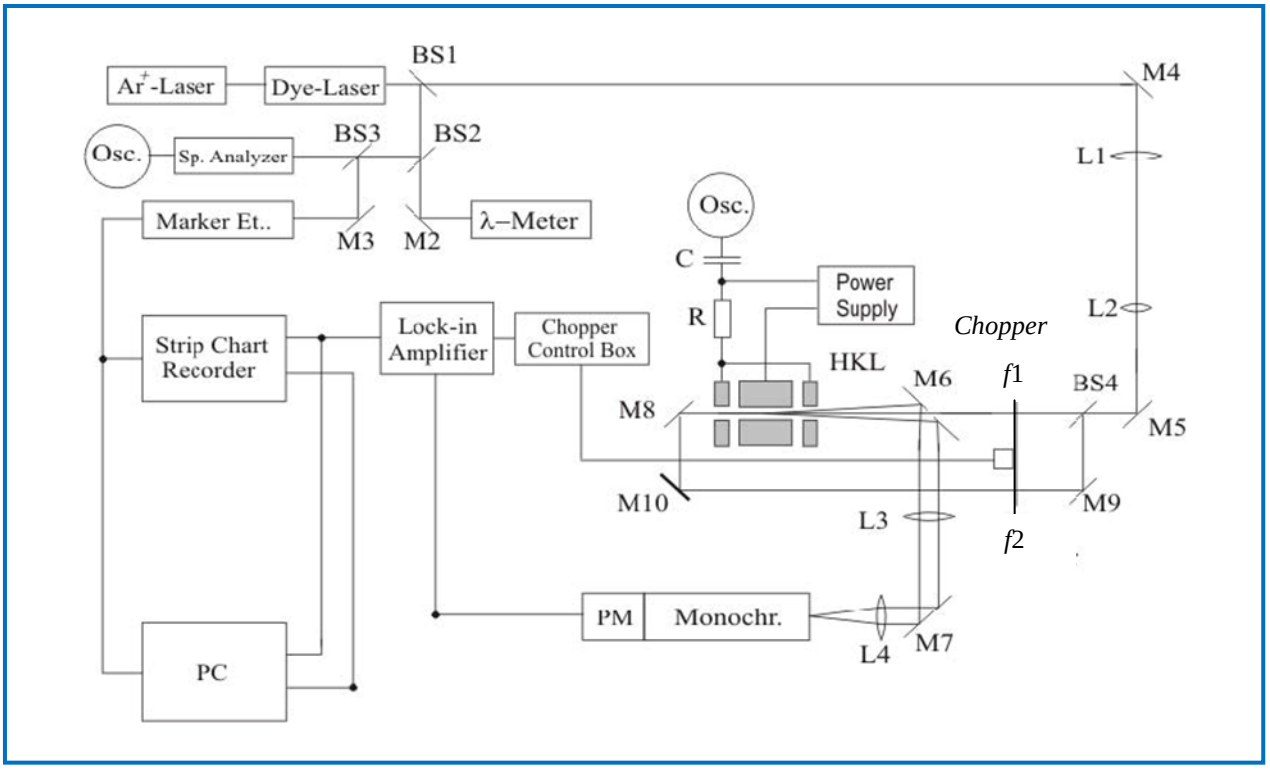

Figure 7.2: An experimental setup for inter-modulated laser induced fluorescence spectroscopy. HKL: hollow cathode lamp, BS1…BS4: beam splitters, L1….L4: lenses, C: capacitor, R: resistance, Osc: oscilloscope, PM: photomultiplier tube, PC: computer

The pump beam is directly shined into the hollow cathode while the probe laser beam is diverted into the hollow cathode from opposite direction with the help of mirrors M9, M10 and M8.

The pump and probe laser beams interact with the Pr-Ar plasma in the hollow cathode and if the laser frequency is in resonance with the difference of energies of the upper and lower levels i.e. $\Delta E = h\nu$, the atom/ions are excited from lower level to excited level. The decay of the excited level into some lower levels results in the laser induced fluorescence (LIF). The LIF signal is guided by the mirrors M6 and M7 and focused by the lenses L3 and L4 into a grating monochromator of 1200 lines/mm (JOBIN YVON HR 640). A photomultiplier tube (Hamamatsu R955) installed at the exits slit of the monochromator is used for the detection of LIF signal. The signal from the photomultiplier tube is fed into the lock-in amplifier for phase sensitive detection. The phase sensitive detection frequency of the lock-in amplifier is set to sum or difference of the frequencies of the pump and probe laser beams i.e. $f_1 + f_2$ or $f_1 - f_2$. The signals from the marker etalon and the lock-in amplifier are documented simultaneously on a chart recorder and in a computer for further analysis.

To create saturation effects usually a high laser power is required. In this work to perform saturation spectroscopy and to investigate the hyperfine structure of the spectral lines of Pr II a dye laser power in the range of 300-700 mW is used. The power of the ring dye laser is measured at the output coupler. For observation of Lamb dips normally the intensity of the laser beam is distributed in two equal parts which are irradiated on the vapor cell from opposite directions. At the centre of transition frequency ω_0, a dip (Lamb dip) is observed in the Doppler broadened absorption profile. At this frequency both laser beams interact with same velocity group i.e. $v = 0$ (perpendicular to both laser beams). This velocity group experiences double laser intensity as compared to other velocity groups and the saturation take place (for details see chapter 6).

Lamb dips are observed at the center of the Doppler broadened hyperfine components when pump and probe laser beams are chopped with the same frequency as publicized in Figure 7.3a. By chopping the pump and the probe laser beams at two different frequencies (f_1 and f_2) and recording the fluorescence signal through lock-in amplifier results in the Doppler broadened background removed inter-modulated laser induced fluorescence signals of the hyperfine structure under consideration as shown in Figure 7.3b. The mechanical chopper consists of a rotating metal disc with two concentric rows of different number of holes. The chopping frequencies used for the pump and probe laser beams are f_1 = 92 Hz and f_2 =138 Hz.

Before recording the hyperfine structure the most intense and suitable fluorescence signal is searched within the working limitations of the monochromator and photomultiplier tube. This is done by tuning the laser frequency to the strongest hyperfine component and searching for the strongest LIF signal by scanning the transmission wavelength of the monochromator. Once best suitable LIF signal is selected the laser frequency is scanned over the whole hyperfine structure.

It is observed that the Doppler width in case of inter-modulated laser induced fluorescence spectroscopy is almost 3 times less as compared to the Doppler limited spectroscopy. That is the reason why the scanning speed of laser frequency is kept very slow. It is also noted that by increasing the time constant of the lock-in amplifier to 100 msec the signal can be enhanced. To determine the frequency spacing accurately a marker etalon of a free spectral range (FSR) of 367.6 MHz is used. The equidistant frequency spacing marked by the marker etalon is also shown in Figure 7.3. For further analysis of the data the computer programs “data viewer”, “simulation” and “fitter” are used. For comparison the hyperfine structure of spectral lines of Pr II using

Doppler limited spectroscopy are also recorded. For this purpose the experimental set up mentioned in section 6.2.1.1 is employed. The results of Doppler limited spectroscopy, inter-modulated laser induced fluorescence spectroscopy and collinear laser ion beam laser spectroscopies are compared at the end of this chapter.

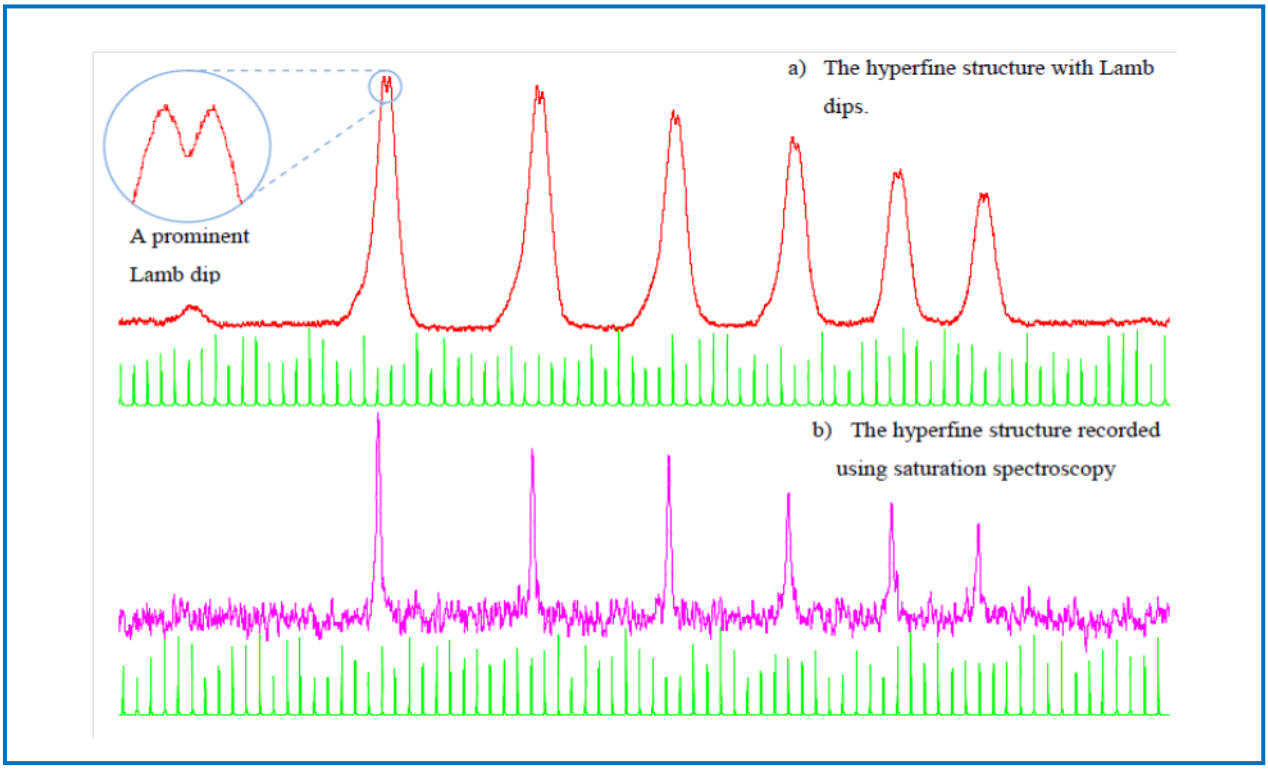

*Figure 7.3: *The hyperfine structure of the Pr spectral line. a) Lamb dips are observed when pump and probe laser have same chopping frequency. b) The Doppler broadened background is eliminated when chopping frequency of pump and probe laser beams are different [162].*

*The work on Lamb dip, inter-modulated laser induced florescence and Doppler limited laser spectroscopy was performed with the help of other colleagues in our group.

7.2 Analysis of Recorded Hyperfine Structure

For a complete understanding of a recorded hyperfine structure of a spectral line and for the classification of the levels and for the determination of the hyperfine coupling constants and other parameters a comprehensive analysis of spectrum is required. The computers programs; “data viewer”, “simulation program” and “fitter program” are used for the further analysis of the recorded hyperfine structure. In the following paragraphs only brief descriptions of these programs are given.

7.2.1 **Data Viewer**

For the graphical representation of the recorded hyperfine structure the computer program called as the “data viewer” is used.

Features of this program are:

- It makes easy to select a best recorded file of a hyperfine structure for data analysis.
- It generates input “mes” file for fitter program.
- The conversion from wavelength to wave number and vice versa can be made.
- The center of gravity of a fluorescence line can be estimated with the help of this program.
- For correction of background a linear or a spline function can be used and maximum 50 data points can be selected to minimize the irregular background.

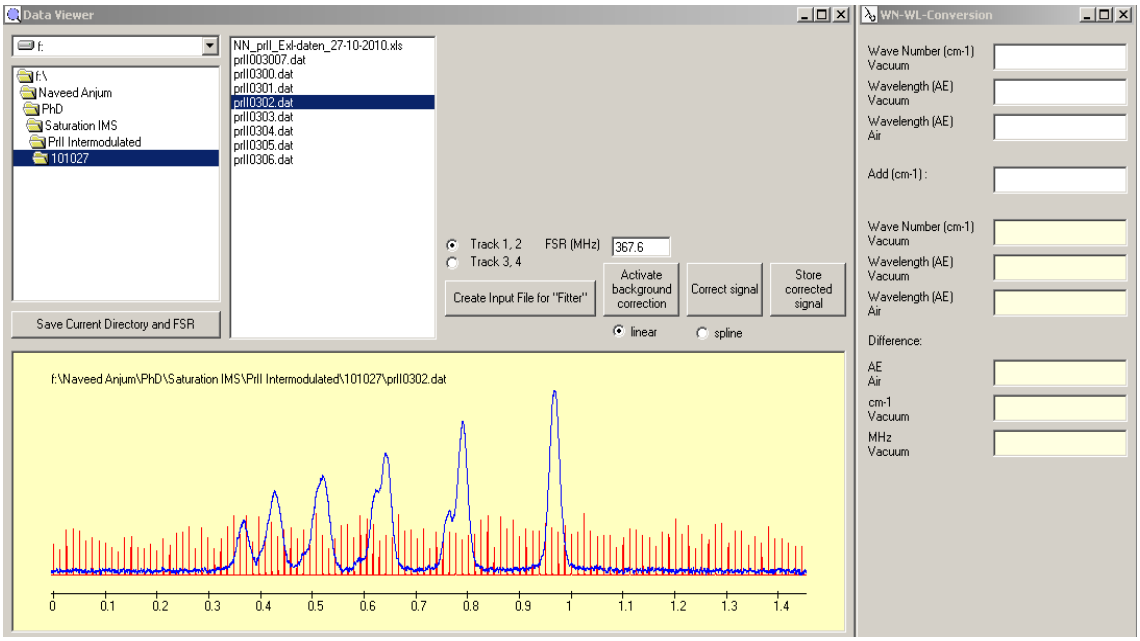

*Figure 7.4**:** Data viewer displaying the hyperfine structure of the Pr II line λ=5790.16. The lower window shows the measure hfs (file Pr II 0302) and collimation marks (367.6 MHz) are signal from marker etalon. The window on right side is conversion of wavelength/wave number in air to wavelength/wave number in vacuum and vise versa.*

7.2.2 **Simulation Program**

The hyperfine structure of a classified or unclassified line can be simulated with the help of the simulation program. This program is the part of the classification program and can be opened in the classification program or directly from main window by calling the program “HfsSim5”. The

program can be used in two ways. If the hyperfine structure data as the value of the nuclear quantum number *I*, total angular momentum quantum number (J_o, J_u) and the hyperfine coupling constants (A_o, B_o, A_u, B_u) of the upper and lower levels of the spectral line are known and stored in database, the program loads these data. Otherwise assumed input values of J_o, J_u A_o, B_o, A_u, and B_u are inserted (right window figure 7.5). These data are used to calculate the hyperfine structure of the upper and lower levels, the position of the centre of gravity and relative transition energies. On the upper part of the left window (figure 7.5) these values are displayed. By further assuming the line width a simulated hyperfine structure curve is calculated (left window, middle) and compared with the experimental curve. In figure 7.5 both curves agree well with each other (only the assumed line width is obviously too small). For a suitable estimation of the input parameters for the "Fitter Program" the simulation program provides a solid foundation of hypothetical hyperfine structure to be matched with the experimentally recorded linearized hyperfine structure. It can be used to calculate the accurate center of gravity of a line by overlapping of the hyperfine structures of this line from FT spectrum and suggested by classification program. Figure 7.5 displays the matching of simulated curve with the experimentally recorded linearized hyperfine structure for the unclassified line at λ = 5815.287 Å.

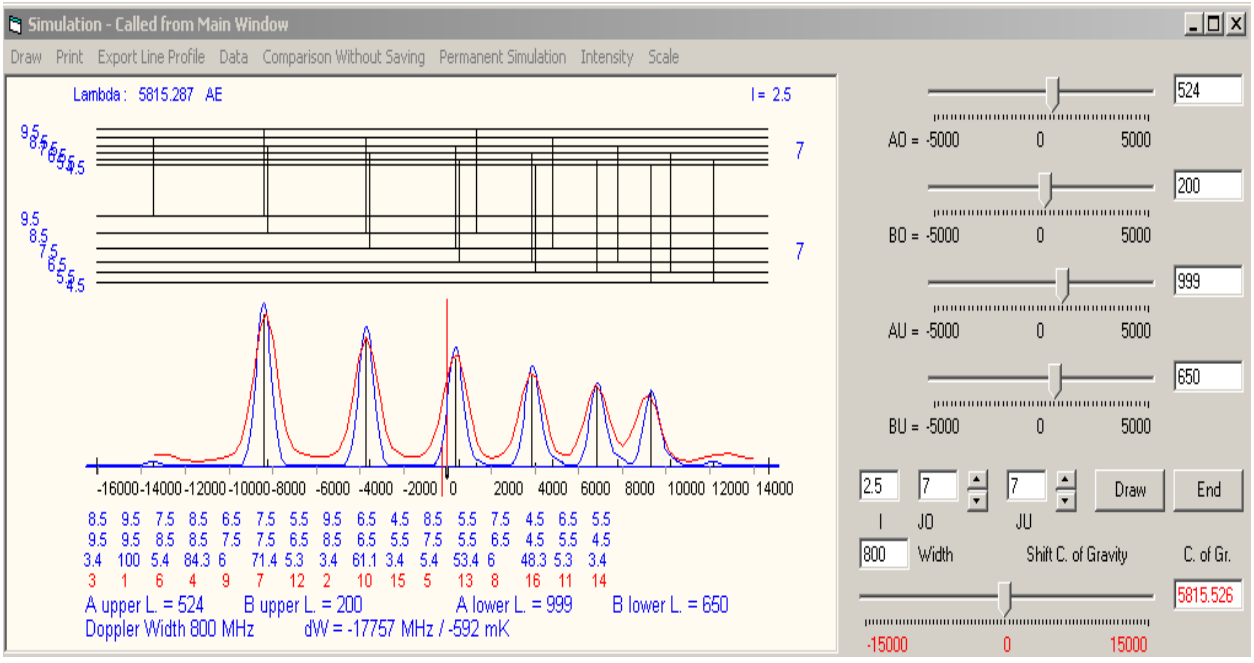

Figure 7.5: Simulation of the line λ = 5815.287 Å and its hyperfine structure taken from experimentally recorded linearized file for unclassified line.

7.2.3 **Fitter Program**

The experimentally recorded hyperfine structure of a spectral line is further analyzed with the help of a fit program called as the "Fitter Program". This program was developed in 1984 by T. Quiering [175] under supervision of Prof. G. H. Guthöhrlein (University of Bundeswehr Hamburg, Germany). The program uses the least squares criteria for fitting the recorded hyperfine structure and calculates the hyperfine coupling constants *A* and *B*, the line width of the spectral line and the center of gravity of the recorded hyperfine structure. The method of least square (Gauss-Newton method) is an iteration process and is based on the minimization of the sum of the squares of the deviation of the points from the experimentally recorded and calculated curves. While recording the hyperfine structure the laser frequency is scanned as a function of time, but this scanning mechanism is not absolutely linear. For linearization the recorded hyperfine structure is converted to the intensity versus the linear frequency scale. In linearization process the intensity distribution I(t) (intensity as a function of time) is converted into intensity distribution I(v) (intensity as a function of frequency) and this is done with the help of equidistant frequency-signals recorded simultaneously with the LIF signal. For linearization the start wavelength value of the laser scan and the FSR of the marker etalon are provided as the input parameters to the data file. The fitter program calculates the position of the hyperfine components using the expression given below

$$\upsilon = \upsilon_c + \alpha_o(F_o, J_o, I_o)A_o + \beta_o(F_o, J_o, I_o)B_o - \alpha_u(F_u, J_u, I_u)A_u - \beta_u(F_u, J_u, I_u)B_u. \qquad 7.1$$

Where υ_c is the center of gravity of the spectral line and α_o, β_o, α_u, β_u are the Casimir factors and A_o, B_o, A_u, B_u are the hyperfine coupling constants for the upper and lower levels respectively (see section 4.3). The intensity of each component is determined by applying the 6j-symbol formula (equation 4.18). The input parameters like the number of isotopes, nuclear spin quantum number (*I*) angular momenta of coupling levels (Ju and Jo), frequency position of the strongest hyperfine component, hyperfine coupling constants (*A, B*) of combining levels, spectral width of components (hwb), and suitable model function (such as Gaussian, Lorentzian or Voigt line profile) etc are fed in the input file (*.ein) of the fitter program. The fitter program uses the least squares method and determines the set of data points by minimizing squared error sum (ESS) given by the following formula.

$$ESS = \sum_{k=1}^{n} [I_v(k) - I_v(V_k, \vec{a})]^2 . \qquad 7.2$$

Where $I_v(k)$ is the measured intensity on a particular frequency position V_k, $I_v(V_k, \vec{a})$ is the calculated intensity related to point V_k and $\vec{a}$ is the corresponding set of fit parameters .

The fitter program performs several iterations and after each run the old data points are replaced with new calculated one. After a number of iterations based on ESS the program reaches the best fit values of the structure under investigation. Depending upon the circumstances some input parameters can be fixed. For example if the hyperfine coupling constants of any of the involved level are already known then these parameters are kept as constant and only the values of the remaining parameters are calculated. This is done by simply replacing the digit '1' with '0' in the corresponding place of the parameter (14^{th} line in fitter program).

Explanation of some commands of fitter:

- Rechnen ---- Linearisieren, is used for linearization.
- Rechnen---- Fitten, is applied to start fitting process.
- Ansicht----- Eingabedatei, is used to view input file.
- Ansicht----- Ausgabedatei, is used to view output file.
- Grafik ----- Unlinearisterte, Messung is used to view unlinearized file.
- Grafik---- Linearistierte Messung, is used to display linearized file.
- Grafik---- Startsituation, is used to view start situation of fitting.
- Grafik----Bestsituation, is to display best fitted structure.
- Rechnen ----Eingabedatei übernehmen, is used to select best fit parameter as input file.

Input file (*.ein)


```
91 0.001 10          // Fitverfahren (klassisch 1, Einzellinien 2)
1          // Anzahl der Isotope
3.5 // Jo
3.5    // Ju
3.5          // I
1    // Haeufigkeit
0.0  // Offsetfrequenz
1 2365     // lage der hoechsten Komponente

-248  -70  -227  200  //Ao,Bo,Au,Bu

1172.8 1172.8    // Untergrund
3          // Modellfunktion (Gauss)
40       // HWB1.0
0.8   //
1 1 1 1 1 1 1    // Steuerparameter: Ao, Bo, Au, Bu, nus, hwbG,

1 0            // Steuerparameter Untergrund
NE           // Cross-Over Resonanzen
JA           // Intensitaeten im th. Verh. koppeln ?
4 1    // deltaF = deltaJ = 0
7 1    // deltaF = deltaJ = 0
10 1    // deltaF = deltaJ = 0
13 1    // deltaF = deltaJ = 0
16 1    // deltaF = deltaJ = 0
19 1    // deltaF = deltaJ = 0

2 1    // deltaF = +1
5 1    // deltaF = +1
8 1    // deltaF = +1
11 1    // deltaF = +1
14 1    // deltaF = +1
17 1    // deltaF = +1
20 1    // deltaF = +1

3 1    // deltaF = -1
6 1    // deltaF = -1
9 1    // deltaF = -1
12 1    // deltaF = -1
15 1    // deltaF = -1
18 1    // deltaF = -1
21 1    // deltaF = -1
```

output file (*.aus)

```
Summe der Intens. =     620.319

rel. Schwerpunkt =    2824.780 MHz
abs. Schwerpunkt =    5141.482 1/cm
Vakuumwellenlänge =   19449.644 A
Luftwellenlänge   =   19444.334 A



Profilfunktion:   Mischfunktion  (eta : Lorentzanteil)

Iso |  HWB/MHz   | 1-eta |   eta
----+-----------+-------+-------
  1 |  599.80    | 1.000 | 0.000


Hyperfeinstrukturkonstanten :

 Isotop  1 :    I = 7/2   Jo = 7/2   Ju = 7/2

              Ao =  -243.97 MHz     Au =  -211.57 MHz
              Bo =   669.71 MHz     Bu =   319.57 MHz

Untergrund        =     367.01

Fehlerquadratsumme  = 6966485.805930
Intervall-Guete     =       1.43
Guete               =       1.43

Iterationsverlauf:
-------------------------------------------------------------------------
Iteration   Guete         FQS        Marq-Steps     Pen-Summe
-------------------------------------------------------------------------
    0       0.9990     349264905.6       0           0.0
    1       0.2296     234414576.0       2           0.0
    2       1.3780       9164534.8       0           0.0
    3       1.3150       8446723.5       1           0.0
    4       1.3871       7796156.1       3           0.0
    5       1.3946       7737091.6       2           0.0
    6       1.4191       7538211.5       0           0.0
    7       1.4730       7133597.8       0           0.0
    8       1.4094       7023857.9       0           0.0
    9       1.4217       6970959.5       2           0.0
   10       1.4251       6966485.8       1           0.0
```

```
NE          // Intensitaeten mit bel. Verh. koppeln ?
NE          // Hyperfeinkonstanten koppeln ?
NE          // Halbwertsbreite/Kurvenformparameter koppeln ?
NE          // Abs. Isotopieverschiebung vorgeben ?
NE          // Rel. Isotopieverschiebung vorgeben ?
NE          // Abs. Abstaende vorgeben
NE          // Rel. Abstaende vorgeben
NE          // Intensitaeten zusammenfassen ?
NE          // Intensitaeten vorgeben ?
Ne          // Fitintervalle vorgeben ?
```

```
Endergebnis  ( 10.te Iteration)       Fitverfahren 1

Startwellenlänge in A          :   19450.00
Startwellenzahl in 1/cm        :    5141.388

Fluoreszenzwellenlänge in A    :       0.00
Fluoreszenzwellenzahl in 1/cm  :       1.#IO

Anzahl der Datenpunkte         :     623
Anzahl der Isotope/Einzellinien :      1
Anzahl der Parameter           :      9

Eichfaktor                     :   8.000000000 MHz

Alle Isotope: Lagen und Häufigkeiten (errechnet aus den Intens.)

Iso |  Lage/MHz   | abs.Lage*cm | Intensitaet  |  Hfk.th.  | Hfk.fit | Hfit/Hth.
----+------------+-------------+--------------+-----------+---------+----------
 1 |   2824.78   |  5141.482   |   620.32     | 100.00    | 100.00  |  1.000

Isotope mit Kernspin :

Isotop   1 :       I = 7/2   Jo = 7/2   Ju = 7/2

 Nr | Fo  ->  Fu  |  Lage/MHz  |Intensitaet |rel. Int. |Ifit/Ith.| Flaeche
----+-------------+------------+------------+----------+---------+--------
  2 |   7 ->    6 | 1171.34    |   16.15    | 0.125000 | 1.00    |0.000e+000
  5 |   6 ->    5 | 1355.32    |   25.85    | 0.200000 | 1.00    |0.000e+000
  8 |   5 ->    4 | 1660.36    |   30.00    | 0.232143 | 1.00    |0.000e+000
 11 |   4 ->    3 | 2037.06    |   29.54    | 0.228571 | 1.00    |0.000e+000
 14 |   3 ->    2 | 2443.18    |   25.39    | 0.196429 | 1.00    |0.000e+000
  1 |   7 ->    7 | 2515.39    |  129.23    | 1.000000 | 1.00    |0.000e+000
  4 |   6 ->    6 | 2592.14    |   84.00    | 0.650000 | 1.00    |0.000e+000
  7 |   5 ->    5 | 2750.83    |   50.77    | 0.392857 | 1.00    |0.000e+000
 17 |   2 ->    1 | 2843.61    |   18.46    | 0.142857 | 1.00    |0.000e+000
 10 |   4 ->    4 | 2948.57    |   27.69    | 0.214286 | 1.00    |0.000e+000
 13 |   3 ->    3 | 3149.64    |   12.92    | 0.100000 | 1.00    |0.000e+000
 20 |   1 ->    0 | 3210.38    |    9.69    | 0.075000 | 1.00    |0.000e+000
 16 |   2 ->    2 | 3325.45    |    4.62    | 0.035714 | 1.00    |0.000e+000
 19 |   1 ->    1 | 3454.56    |    0.92    | 0.007143 | 1.00    |0.000e+000
 21 |   0 ->    1 | 3766.88    |    9.69    | 0.075000 | 1.00    |0.000e+000
  3 |   6 ->    7 | 3936.19    |   16.15    | 0.125000 | 1.00    |0.000e+000
 18 |   1 ->    2 | 3936.40    |   18.46    | 0.142857 | 1.00    |0.000e+000
  6 |   5 ->    6 | 3987.65    |   25.85    | 0.200000 | 1.00    |0.000e+000
 15 |   2 ->    3 | 4031.90    |   25.39    | 0.196429 | 1.00    |0.000e+000
  9 |   4 ->    5 | 4039.04    |   30.00    | 0.232143 | 1.00    |0.000e+000
 12 |   3 ->    4 | 4061.14    |   29.54    | 0.228571 | 1.00    |0.000e+000
```

```
NE          // Guetenintervall vorgeben?
1.0         // Skalierungsfaktor
NE          // Flaechennormierung
NE          // Penalty-Funktionen
```

```
0 0 0 0   100 500  500 //
100  0      //
0.1         //
```

The fitter program also allows using multiline fitting. In multi line fitting the hyperfine structure of two or more than two lines can be fitted simultaneously. The multiline spectrum arises due to the presence of more than one spectral lines very close to each other and is normally recorded in a single laser scan. In the fitter program multi-isotopes fitting is also possible. In this case the spectral lines of more than one isotope are recorded together. Some multiline recordings will be discussed in chapter 10.

7.3 Comparison between Doppler Limited, Inter-modulated Saturation Spectroscopy and CLIBS

The experimental investigations of the hyperfine structure carried out in this work are divided into four parts. In the first part a comparative study of singly ionized praseodymium (Pr II) is performed using three different techniques of laser spectroscopy i.e. Doppler limited laser spectroscopy, inter-modulated laser induced fluorescence spectroscopy or Lamb dip spectroscopy and CLIBS. The second part is concerned with the readjustment and checking of the Marburg mass separator MARS-II, as it was shifted from the University of Marburg Germany to Graz University of Technology in 2002. In third part the investigation of hyperfine structure of spectral lines of lanthanum (La II) and two odd isotopes of neodymium (^{143}Nd II and ^{145}Nd II) is performed by the method of CLIBS. In fourth part the ratios of magnetic dipole constants i.e A_{143}/A_{145} and electric quadrupole constants B_{143}/B_{145} of the two odd isotopes of neodymium are determined.

These spectroscopic techniques have a large difference in their spectral resolutions. The line widths of spectral lines recorded by Doppler limited spectroscopy are of the order of 600 – 700 MHz and in case of inter-modulated laser induced fluorescence spectroscopy the line widths are reduced almost three times (~ 200 MHz) whereas the high resolution technique of CLIBS can drastically reduce the spectral line width to the range of 40 – 70 MHz. The hyperfine coupling constants determined by three methods are compared in Table 7.1.

In this section the first part of the work is presented in the form of the comparison of spectral resolution of three techniques of laser spectroscopy and their ability to accurately determine the magnetic dipole coupling constant *A* and electric quadrupole coupling constant *B.* The last three parts will be presented in chapter 10.

7.3.1 The Hyperfine Structure of the Pr II Spectral Line 5815.17 Å

The hyperfine structure of the spectral line 5815.17Å recorded by the Doppler limited spectroscopy, inter-modulated fluorescence spectroscopy and by CLIBS is shown the figures 7.6(a), 7.6(b) and 7.6(c) respectively. The energy level diagram is given in figure 7.7(a) while a close comparison of the hyperfine structure recorded by three laser techniques is given in figure 7.7(b).

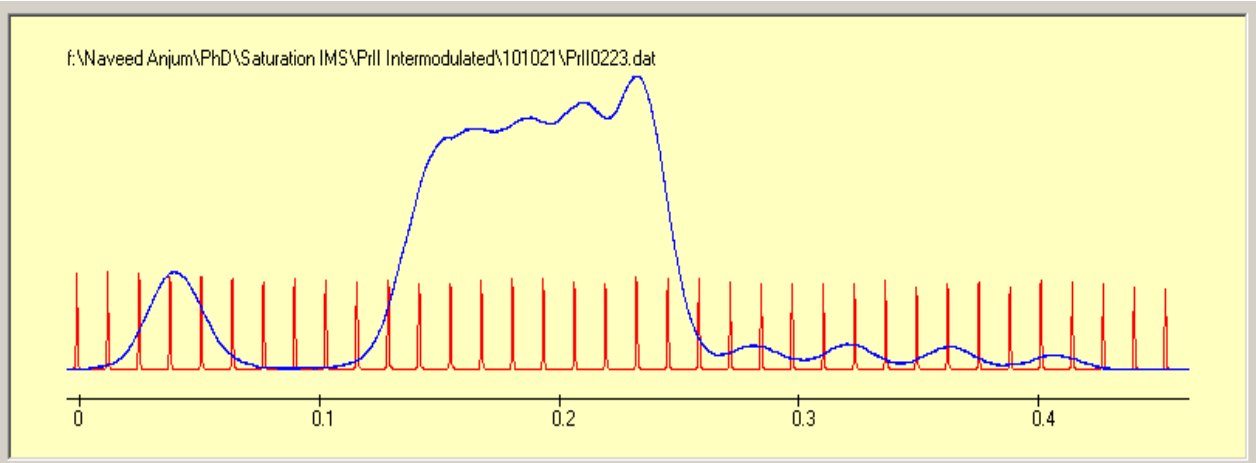

Figure 7.6(a): The hyperfine structure of Pr II spectral line 5815.17 Å recorded using Doppler limited spectroscopy

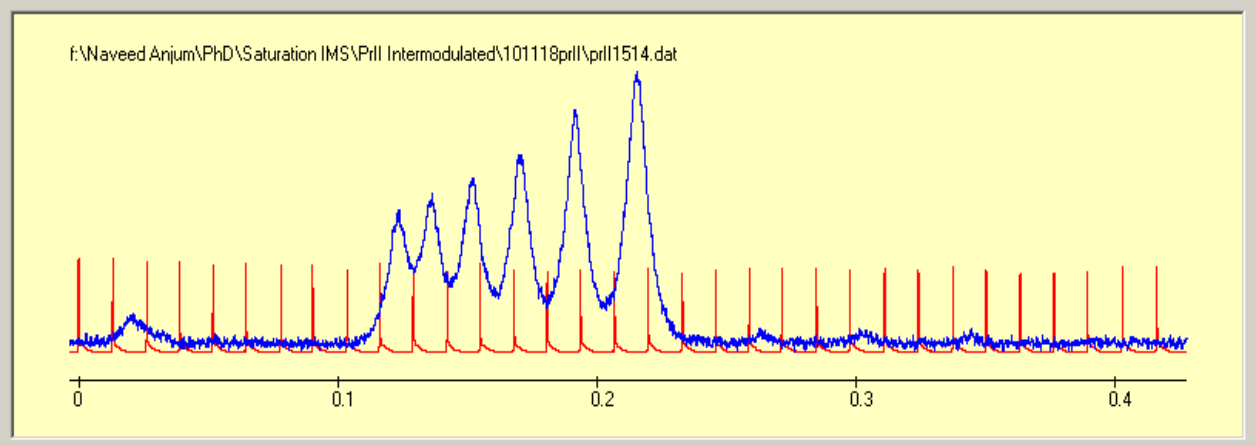

Figure 7.6(b): The hyperfine structure of Pr II spectral line 5815.17 Å recorded using Inter-modulated spectroscopy

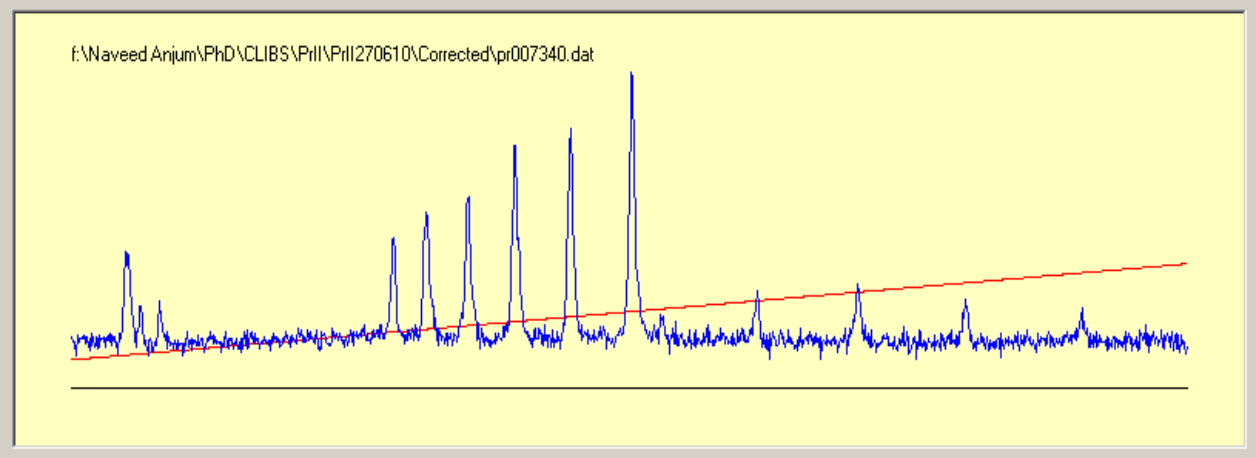

Figure 7.6(c): The hyperfine structure of Pr II spectral line 5815.17 Å recorded using CLIBS

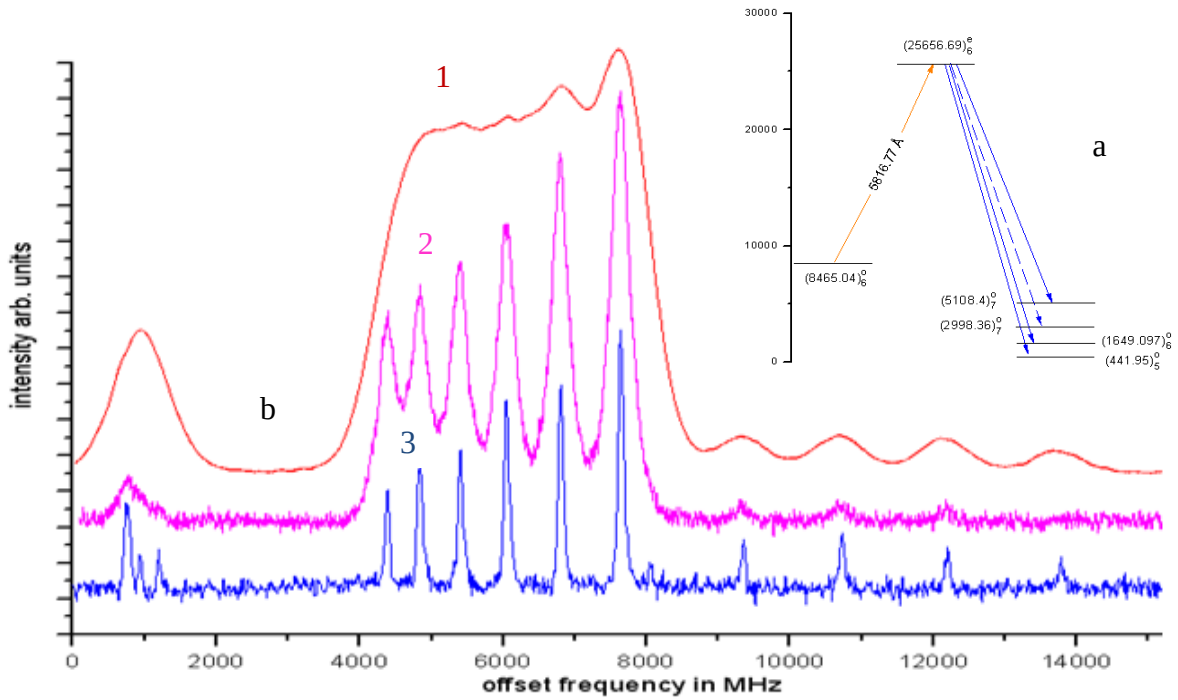

Figure 7.7: *The Hyperfine Structure of Pr II Spectral Line 5815.17 Å, a) Energy level diagram, b) Comparison of the hyperfine structure recorded by three laser techniques, 1) Doppler limited, 2) Inter-modulated, 3) CLIBS*

The spectral line 5815.17Å shown in Figure 7.7 is the result of the transition from the upper level $^{5}I_{6}$ ($\sigma = 25656.69\ cm^{-1}$) to lower level $^{3}I^{\circ}_{6}$ ($\sigma = 8465.04\ cm^{-1}$) .The figure 'a' shows the energy level diagram and the figure 'b' shows the hyperfine structure recorded by three different spectroscopic techniques. The red curve (1), the pink curve (2) and the blue curve (3) are recorded by the Doppler limited, inter-modulated saturation spectroscopy and CLIBS respectively. The Doppler limited measurements were taken at a buffer gas pressure of 0.2 mbar and the laser power was ~ 200 mW. To observe the saturation effects in the case of inter-modulated saturation spectroscopy a relative high laser power of the order of ~ 600 mW and a gas pressure 0.15 mbar was used. In both cases the strongest LIF signal was recorded which corresponds to monochromator transmission wavelength 3964 Å and the recordings were made with the liquid nitrogen cooled hollow cathode discharge lamps (figure 7.1). The CLIBS structure was recorded at a nominal laser power of ~ 90 mW and the fluorescence signals in the transmission maximum of the BG-12 filter and photomultiplier tube (XP 2020) i.e. in the range of 3500 - 4800 Å. In the cases of Doppler limited and inter-modulated saturation spectroscopy the laser was locked to the internal reference cavity of the dye laser whereas in the case of CLIBS the dye laser was locked on one of the hyperfine component under investigation (details of the locking scheme are discussed in chapter 9).

Figure 7.7 shows clearly that the Doppler limited spectroscopy was not capable to resolve the diagonal (stronger) and off-diagonal (weaker) hyperfine components. Although in case of inter-modulated saturation spectroscopy the diagonal components are completely resolved, the off-diagonal components are still not clearly resolved and the intensities of off-diagonal components are almost 40% less than the theoretical predicted values. Only the high resolution technique of CLIBS is quite capable to completely resolve the diagonal as well as off-diagonal hyperfine components and the intensities of the experimental recordings are in good agreement with theoretically predicted values. The line width of nearly 630 MHz and 215 MHz was obtained with Doppler limited spectroscopy and inter-modulated saturation spectroscopy respectively while the spectral line width ~ 55 MHz was obtained with CLIBS measurements. The accuracy of the hyperfine coupling constant *A* determined by the Doppler limited method was 3 - 7 MHz and 2 - 5 MHz in case of inter-modulated saturation spectroscopy whereas the accuracy of less than 1 MHz was obtained by the method of CLIBS. The coupling constant *B* is determined with the method of CLIBS only because due to very small value of electric quadrupole moment Q the values of *B* cannot determined with high accuracy.

7.3.2 The Hyperfine Structure of Pr II Spectral Line 5786.17 Å

The spectral line 5786.17 Å shown in Figure 7.8 is the result of the transition from upper level $^{5}\mathrm{I}_{5}^{\circ}$ ($\sigma = 24716.04\mathrm{cm}^{-1}$) to lower level $^{3}\mathrm{I}_{5}^{\circ}$ ($\sigma = 7438.23\ \mathrm{cm}^{-1}$). The figure ‘a’ shows the energy level diagram of the line and the figure ‘b’ shows the hyperfine structure recorded by three different spectroscopic techniques. As mentioned in previous section curve ‘1’, curve ‘2’ and curve ‘1’ are recorded by the Doppler limited, inter-modulated saturation spectroscopy and CLIBS respectively. The Doppler limited measurements were taken at buffer gas pressure of 0.2 mbar and laser power was ~ 220 mW and the saturation spectroscopy was performed at laser power ~ 670 mW at gas pressure of 0.2 mbar. In both cases the strongest LIF signal corresponding to wavelength 4118 Å was recorded and the investigation of the line was made with liquid nitrogen cooled hollow cathode discharge lamp. The CLIBS structure was recorded at laser power of ~ 110 mW. For this spectral line the Doppler limited spectroscopy neither resolved the diagonal nor the off-diagonal hyperfine components. In case of inter-modulated saturation spectroscopy the off-diagonal components are resolved but the diagonal components are not resolved at all and the intensities of off-diagonal components are nearly 70% less than the theoretical predicted values. But all the diagonal as well as off-diagonal hyperfine components

are completely resolved in case of CLIBS measurements. The spectral line width of nearly 650 MHz, 230 MHz and 65 MHz was obtained with Doppler limited spectroscopy, inter-modulated saturation spectroscopy and CLIBS respectively. Again the accuracy of the hyperfine coupling constants were most accurately determined with CLIBS method.

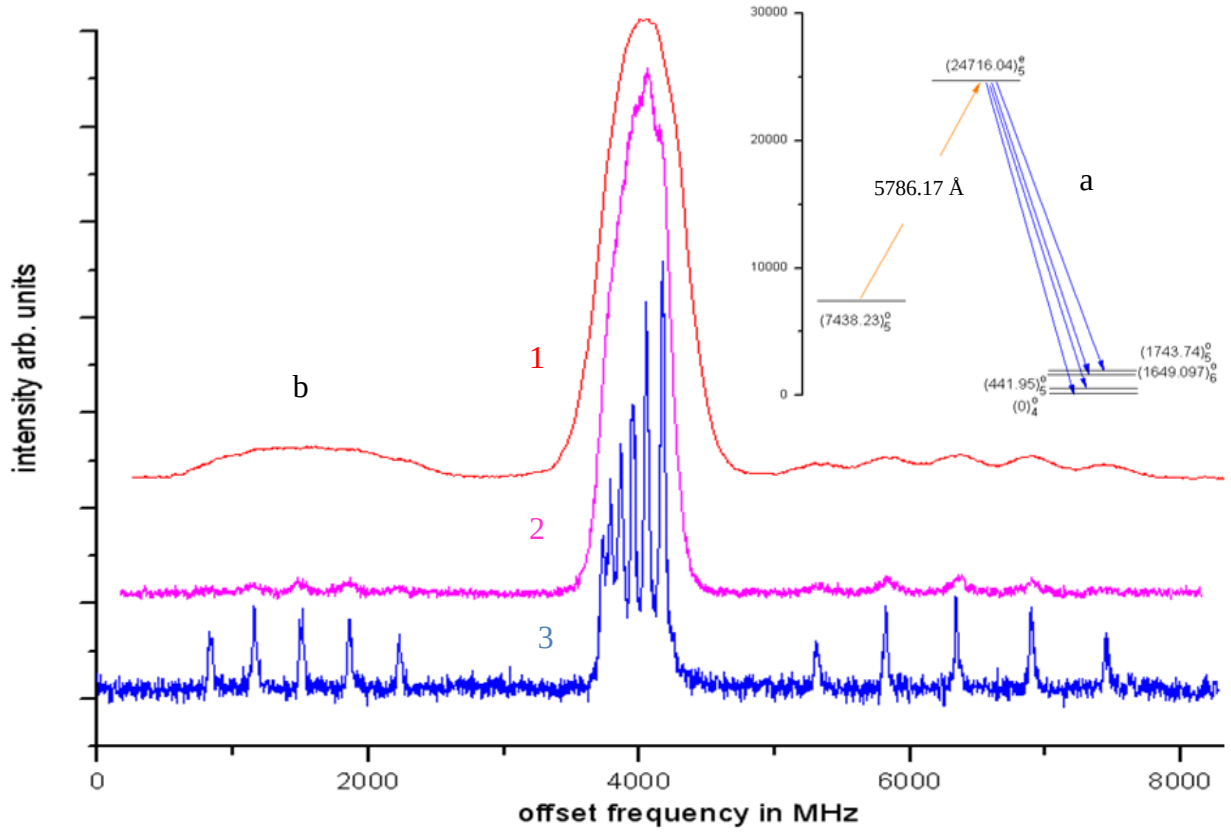

Figure 7.8: * *The Hyperfine Structure of Pr II Spectral Line 5786.17 Å, a) Energy level diagram, b) Comparison of the hyperfine structure recorded by three laser techniques, 1) Doppler limited, 2) Inter-modulated, 3) CLIBS.*

*This line was recorded in co-operation with one of my colleagues and was presented at 75th annual meeting of Deutsche Physical Society (DPG), 13th – 18th of March 2011, Dresden, Germany, POS A-26.58.

Table 7.1: Comparison of hyperfine coupling constants measured by three methods.

Excitation Wavelength λ(air)/Å	Energy of the levels σ /cm^{-1}	Spectroscopic Method Applied					
		Doppler Limited Spectroscopy		Inter-modulation Saturation Spectroscopy		CLIBS	
		A/MHz	B/MHz*	A/MHz	B/MHz*	A/MHz	B/MHz
5815.17	8465.04 25656.69	581(4) 659(7)		578(4) 656(5)		574.5(3) 655.3(4)	5(3) -20(5)
5786.17	7438.23 24716.04	711(6) 738(5)		707(4) 731(3)		704.6(2) 729.8(3)	29(6) 20(4)
5761.26**	8489.87 25842.37	790(4) 668(7)		-		787.7(5) 666.8(6)	0(5) -9(4)
5830.95	8465.04 25610.20	572 (4) 539(7)		574(2) 540(3)		575.0(6) 540.6(7)	2(4) -43(9)
5839.40	8489.87 25610.20	791(6) 543(5)		788(3) 539(5)		787.3(4) 540.1(5)	35(7) -23(8)

* The *B* values were poor in case of Doppler limited and saturation spectroscopy.

**The line intensity was too weak for saturation spectroscopy.

7.4 **Discussions**

In this chapter the inter-modulated laser induced fluorescence spectroscopy has been discussed and the spectroscopic investigations of spectral lines of singly ionized praseodymium have been carried out by three techniques of laser spectroscopy. The first technique applied in this work (Doppler limited laser induced fluorescence spectroscopy) was discussed in detail in chapter 6 section 6.2.1.1 whereas the second technique (inter-modulated laser induced fluorescence spectroscopy) have been discussed and applied in this chapter. A full discussion about the third technique (CLIBS) will be presented theoretically and practically in chapters 8, 9 and 10.

As we have seen from two spectral lines presented in the Figure 7.7 and Figure 7.8 that the spectral line width is largest (~ 650 MHz) in case of Doppler limited spectroscopy and it decreases almost three times (~ 210 MHz) in case of inter-modulated laser induced fluorescence spectroscopy. In both cases the measurements were carried out in the liquid nitrogen cooled hollow cathode discharge lamp. The spectral line widths obtained with CLIBS method are in the range of 40 - 70 MHz and are more than 10 times smaller as compared to the line width obtained with Doppler limited spectroscopy and nearly 5 times smaller than inter-modulated laser induced fluorescence spectroscopy. Table 7.1 reveals that the accuracy of the hyperfine coupling

constants is also much better in case of CLIBS method and the values of the magnetic dipole coupling constant *A* are less than 1 MHz whereas the divergence in the electric quadrupole coupling constant *B* are generally in the range of 1-5 MHz but sometimes due to poor recordings relatively large values are also observed. Generally the *B*-values in case of praseodymium are not determined accurately due to the very small value of the electric quadrupole moment Q (Q = -0.066 for Pr). In Table 7.1 the *B*-values for Doppler limited and saturation spectroscopy are not shown because the poor resolution and the low intensities of the off-diagonal components further increase the scatter in electric quadrupole coupling constant.

The saturation effects also play a role in broadening of the spectral lines and the poor accuracy of the hyperfine coupling constants. In case of saturation spectroscopy the intensities of the off-diagonal components are 40 - 60 % smaller than the theoretically predicted values. The saturation is a nonlinear phenomenon and normally it is more pronounced for diagonal components and less for the off-diagonal components. The saturation spectroscopy is relatively difficult to perform in the sense that very high laser power is required and it is difficult to obtain high laser power in broad region of laser dyes and also it becomes difficult to stabilize the high power laser. The thermal effects also cause the instabilities and the mode hopping is quite frequent which aggravate the spectral signal and the linearity of the laser scanning also suffers. The saturation spectroscopy is quite often used for the stabilization of the laser spectroscopy. The Lamb dips provide a good sharp reference signal for the stabilization of laser on a hyperfine component of a spectral transition. A laser stability of less than 100 kHz is achieved using Lamb dip spectroscopy [176].

Among the three discussed spectroscopic techniques the CLIBS is best suited for the determination of the hyperfine coupling constants and to reduce the Doppler broadening mechanism. The more benefits and the drawbacks of the CLIBS method will be discussed in details in the upcoming chapters.

8 COLLINERAR LASER ION BEAM SPECTROSCOPY (CLIBS)

8.1 Fundamental of CLIBS

Collinear Laser Ion Beam Spectroscopy (CLIBS) is a powerful and precise technique for high-resolution spectroscopy. Other names and abbreviations have also been used in literature to describe this method like Collinear Fast Ion Beam Laser Spectroscopy (CFIBLS) and Fast Ion Beam Collinear Laser Spectroscopy (FIBCLAS), but CLIBS is most widely used among all. The first part of FIBCLAS acronym depicts the basis of the method which is the use of accelerated ion beams and the second part indicates the collinear interaction of laser and ion beam. The ions may be of either atomic or molecular nature and may be neutralized through charge exchange after passing through an alkaline vapor cell to provide an accelerated beam of neutral atoms.

The high resolution and the specific characteristics of the CLIBS method are very useful to investigate the complex structure of rare-earth ions/atoms, unstable molecular systems which are difficult to study and short-lived radio isotopes. The spectral resolution (FWHM) obtained with CLIBS is in the range of 40-70 MHz. In contrast, the Doppler-broadened line has width of ~ 1.0 GHz at an estimated plasma temperature of 1000 K [177]. The high resolution of CLIBS allows to investigate the various parameters of spectroscopic interest such as hyperfine structures, nuclear moments and nuclear spins [178], measuring the radiative lifetime of electronic states [179], isotopic shifts [135], branching ratios and oscillator strengths [149] on stable and radioactive isotopes.

The fundamental parts of CLIBS are described in following discussions.

8.1.1 Principle of CLIBS

The most promising feature of CLIBS is the reduction of Doppler broadening. It is achieved by accelerating the ions to very high velocities (~170 km/s). Generally at room temperature and especially in hot ion sources the spread in the ion velocities is very large and consequently the

Doppler width is very large. But when the ions are accelerated to very high velocities by applying a high potential difference the spread in velocities decreases and the Doppler width is reduced. The working principle of CLIBS can be divided into five steps. In the first step, ions are produced in an ion source, in the second step the ions are accelerated by applying a high acceleration voltage, in the third step a mass separated collimated ion beam is achieved by a magnet, electrostatic lenses and deflection plates, in the fourth step the interaction of the ion beam takes place with laser light collinearly (or anti-collinearly), and in the last step the fluorescence signal is detected.

8.1.2 **Kinematic Compression (Velocity Bunching Effect)**

The basic idea of the velocity-bunching phenomena occurring in a fast beam of ions was introduced by Kaufman [20] and Wing et al. [21] independently, in 1976. The velocity-bunching effect in words of Kaufman is "*the ions having large initial velocity spent less time in the acceleration field and thus gain less velocity than the initially slower ions*". Now the phrase kinematic compression or acceleration cooling is mostly used to describe the narrowing of the velocity spread. Kinematic compression occurs when identical ions with different velocity components are accelerated in one direction by applying a high potential difference and the difference in velocities is reduced in the direction of applied field. The spread in velocity distribution of two ions before and after the application of the acceleration voltage can be calculated.

Consider two ions each of mass *M,* charge *e* and their thermal velocities in ion source are v_1 and v_2, respectively. When these ions are accelerated by a potential difference *U*, their velocities become u_1 and u_2 respectively, and their kinetic energies E_1 and E_2 are given by

$$E_1 = \frac{1}{2} M u_1^2 = \frac{1}{2} M v_1^2 + eU$$

$$E_2 = \frac{1}{2} M u_2^2 = \frac{1}{2} M v_2^2 + eU$$

The difference of the two equations gives

$$\Delta u_o = u_2 - u_1 = \frac{v}{u} \Delta v_o \qquad 8.1$$

where

$$\Delta v_o = v_2 - v_1 ,$$

$$u = \frac{1}{2}(u_2 + u_1)$$

and

$$v = \tfrac{1}{2}(v_2 + v_1) .$$

The kinetic energy of ions in the electric field *U* is given by

$$\frac{1}{2} M u^2 = eU \quad , \text{thus}$$

$$u = \sqrt{\frac{2eU}{M}} . \qquad 8.2$$

Since

$$E_{th} = \tfrac{1}{2} M \vec{v}^2 \qquad \Rightarrow \qquad v = \sqrt{\tfrac{2E_{th}}{M}}$$

The spread in final velocity is given by

$$\Delta u_o = \Delta v_o \sqrt{\frac{E_{th}}{eU}} \qquad 8.3$$

In frequency term,

$$\Delta \vartheta_o = \Delta \vartheta \sqrt{\frac{E_{th}}{eU}}$$

From equation 8.3, we have

$$\Delta u_o = R \Delta v_o \quad \text{or} \quad \Delta \vartheta = R \Delta \vartheta$$

where

$$R = \sqrt{\frac{E_{th}}{eU}} \qquad 8.4$$

and is called as Doppler width reduction factor.

For

$$E_{th} \ll eU \;\Rightarrow\; \Delta u_o \ll \Delta v_o$$

For eU = 20 keV and ΔE_{th} = 0.1 eV, $\Delta u_o = \sqrt{5} \times 10^{-3}\, \Delta v_o$. In other words, it can be stated that the acceleration cooling has decreased the Doppler width by a factor of ~ 250. The fluctuations of the (thermal) kinetic energies as well the fluctuations of the acceleration voltage contribute equally to the energy spread.

The plot of equation 8.2 shows clearly (Figure 8.1) that at higher kinetic energy the spread in velocity distribution is significantly decreased. This reduction of the velocity spread is due to the fact that energies are added instead of velocities. At higher acceleration potential the fluctuations of initial thermal velocity do not contribute too much but any change in acceleration voltage can change the final velocity significantly. That is why the acceleration voltage should have very good stability to take full advantage of acceleration cooling.

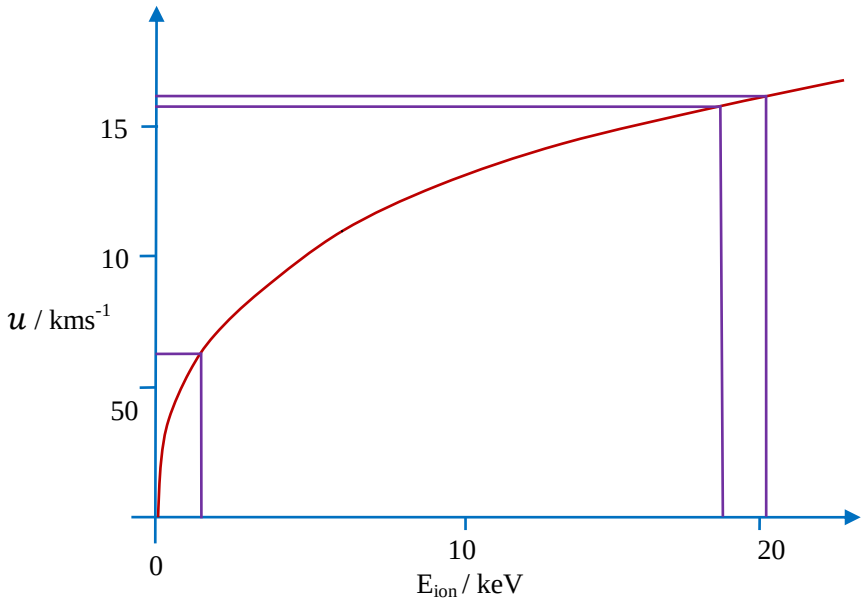

Figure 8.1: Kinematic compression (Acceleration cooling): For same spread of energy the spread in velocity decreases by accelerating the ions.

8.1.3 **Doppler Tuning**

The interaction of laser beam and ion beam take place in an interaction chamber just in front of the light collector and the LIF signal is recorded which gives the hyperfine structure of spectral line being investigated. Usually the tuning is performed by scanning the laser frequency and keeping the ions velocity fixed, but CLIBS offers another way, called Doppler tuning, to record hyperfine structures. In Doppler tuning an accelerating or retarding electrical potential is applied along the beam path and the laser frequency is kept fixed. The rapidly moving ions change their velocity in the region of the applied field and therefore the laser light frequency in the centre of gravity system of the ions changes.

The frequency of the laser radiation in the rest frame of a moving ion is Doppler-shifted relative to the laser frequency υ_L in the laboratory frame of reference, given by

$$\Delta\upsilon_D = \pm\frac{\upsilon_L}{c}\sqrt{\frac{2eU}{M}} \qquad 8.5$$

Where *c*, *e* and *M* are the light velocity, the ion charge and mass, respectively, and *U* is the acceleration voltage. The " $\pm$ " sign is used to indicate whether the laser beam and ion beam are interacting anti-collinearly or collinearly. For anti-collinear interaction as in our case, the + sign is used.

In this work, Doppler tuning has been used for recording hyperfine structure of spectral lines of several lanthanides elements. It has several advantages over the laser scanning system.

- To lock the laser frequency to a fixed value is relatively easy as compared to repeatedly scanning of the laser frequency over a large spectral range without mode hops.
- In Doppler tuning the ion velocity can be tuned locally, repeatedly and consistently with a very high resolution and high degree of precision.

If the excitation would also occur outside the light collector chambers then the metastable states would be depleted and thus not used for the measurements. This always happens when the scanning voltage is around zero Volt. To avoid this problem a minimum post-acceleration (or retarding) voltage equivalent to the FWHM of the structure under investigation should be applied before start of the scanning.

The recording of the hyperfine structure splitting with high precision demands a very high stability of the acceleration voltage and laser frequency or a stabilization mechanism which can simultaneously address any change in both parameters. In this work the laser was locked to one of the hyperfine components of the structure being recorded. This locking scheme is very useful in fast ion beam spectroscopy and can address simultaneously any drift in laser frequency or the acceleration voltage. Details of this locking scheme will be discussed in chapter 9.

8.1.4 **Sensitivity**

In general, the parameters which define the sensitivity of many other types of spectroscopy are also used to determine the sensitivity of CLIBS. The sensitivity is the efficiency with which the fluorescence signal is detected. Although the intrinsic sensitivity of CLIBS is relatively high as compared to other high resolution techniques, such as atomic beam crossed laser beam spectroscopy or saturation spectroscopy, but if optical detection is used it can decrease due to the following reasons:

- Due to the large interaction region (~ 3cm), the collection of fluorescence photons is not very efficient.
- The fluorescence signal is obscured due to stray laser light.

Some of the parameters which generally define the sensitivity are listed below:

i. Probability of interaction between the ion beam and laser light
ii. Intensity of the laser beam
iii. Intensity of the ion beam current
iv. Detection efficiency of the laser induced fluorescence (LIF)

8.1.4.1 Probability of Interaction

The nature of transition determines the interaction probability between the ion and a photon (laser light). For a two-level atom the cross section for the interaction is Lorentzian [180], with a peak value of

$$\sigma(0) = {}^{\lambda^2}/_{2\pi} \qquad 8.6$$

and a full width at half maximum of $1/(2\pi\tau)$, where τ is the life time of the upper state. The available laser beam photon fluxes are sufficient for electrical dipole allowed transitions.

8.1.4.2 Intensity of laser Beam

The peak absorption cross section $\sigma(0)$ for a laser wavelength of 600 nm (16600 cm^{-1}) is given from equation (8.5), $\sigma(0) = 4 \times 10^{-14}$ $m^{2,}$ whereas the atomic diameter is of the order of 10^{-10} m. If the life time $'\tau'$ of the upper state is 10^{-8} s then the atomic line width is 16 MHz. The line width of laser light can be much smaller than the atomic line width and at resonance, a photon flux of 10^{15} mm^{-2} s^{-1}, will excite a single atom in a time comparable to the upper state life time. This photon flux corresponds to laser intensity of only 0.3 mW mm^{-2} [180]. The duration of the interaction is related to the ion velocity. If an atom remains in the resonance field for 10^{-7} s then it absorbs and emits at least five photons. The intensity of laser beam used in our experiment was much higher as compared to this minimum intensity.

8.1.4.3 Ion Beam Current

The intensity of the fluorescence signal is directly related to the intensity of the ion beam and the population of the metastable states. The ion beam current and the population of metastable states depend upon the chemical nature of sample, its purity, isotopic abundance and the design of the ion source. The minimum yields of about 10^5 particles/s is required to detect a signal in classical collinear laser ion beam spectroscopy [181].

We used a Johnson type surface ion source which can populates metastable states up to energy of 14000 cm^{-1}.

8.1.4.4 Detection of Laser Induced Fluorescence (LIF)

The sensitivity of the CLIBS also depends upon the detection of the absorption of light by the ion beam. There are many methods of detection of the absorption of light but monitoring the fluorescence photons is most widely used.

At the final stage of the ion beam, in the interaction chamber, when the resonance conditions of Doppler shifted ion beam and laser frequency are fulfilled, a transition takes place from the lower metastable state to higher excited state. The energy difference of the two states is $h\upsilon = E_2 - E_1$.

The life time of the excited state is very small, in the order of 10^{-8} s, and it decay to some lower states by emitting fluorescence light. The process is shown in the Figure 8.2. The observation of the fluorescence signal gives the pattern of the hyperfine structure.

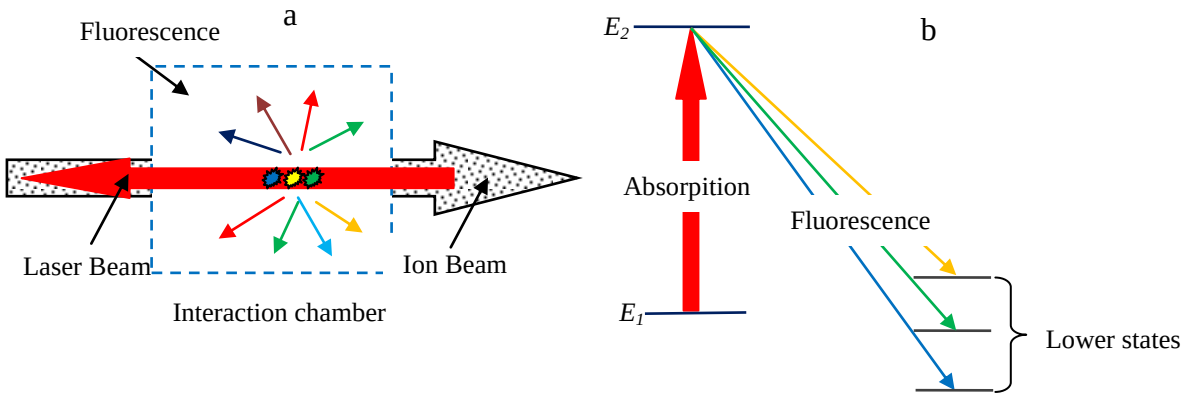

Figure 8.2:a) Laser ion beam interaction . b) A lower level E_1 is excited to higher level E_2 by absorbing resonant laser wavelength and de-excites to lower states by emitting fluorescence.

8.1.5 **The Mass Separator**

Although the mass separator is not one of the basic part of the CLIBS its presence enhances the performance of CLIBS many fold. An electric field or a magnetic field can be used as the mass-separation mechanism and provides a way to separate the impurities and different isotopes. Normally due to the simple design and high mass resolution electromagnetic separation is used in the experiments like CLIBS. The use of a mass separator between ion source and observation region can provides the following advantages:

- It is possible to select species of interest by its charge/mass ratio.
- If the element in the ion source has more than one isotope, it is possible to select a specific isotope.
- The selection of an isotopically pure beam is fairly easy.
- A selected pure isotopic beam gives an undisturbed hyperfine spectrum due to the absence of hyperfine components of other isotopes.
- The background from the unwanted isotopes and impurities can be removed.
- The mass separators offer an opportunity to provide simultaneously a beam under investigation and a second beam for stabilization of the laser frequency or for delivering a

reference frequency. This arrangement can be used to determine the isotopic shifts accurately.

8.1.5.1 Principle of an Electromagnetic Mass Separator

The most common method of separating masses for isotopic measurements in CLIBS is a magnetic sector and it separates different isotopes according to charge to mass ratios. The force *F* acting on a charged particle (ion) passing through the magnetic field *B* is given by

$$F = e(\vec{v} \times \vec{B})$$

Where *e* is the charge of the ion and *v* is the velocity of the ion. In magnetic sector mass separators the trajectories of the charged particles are always perpendicular to the magnetic field, so we have

$$F = evB \qquad 8.7$$

In the presence of this force, the ions will move on a circular orbit (part of circular orbit) in a uniform magnetic field and the centripetal force balances the magnetic force.

Thus we have

$$evB = \frac{Mv^2}{R}$$

as

$$v = \sqrt{\frac{2eU}{M}}$$

Thus we have,

$$R = \frac{1}{B}\sqrt{\frac{2UM}{e}} \qquad 8.8$$

It is obvious from equation 8.7 that the mass passed through the magnet is proportional to the square of the field. It can also be noted that the radius is proportional to the square root of the

mass to charge ratio. So, different isotopes will have different trajectories after passing through the magnet and will be separated.

8.1.5.2 Dispersion and Resolving Power of a Mass Separator

The dispersion (D) for the ion beam with mass M and $M + \Delta M$ is given by

$$D = d\frac{M}{\Delta M} \qquad 8.9$$

where d is the displacement between the M and $M + \Delta M$ in the image plane perpendicular to the beam axis. If the line width of the mass M in the image plane is δM the resolving power (R_p) of a mass separator is given by

$$R_p = \frac{D}{\delta M} = d\ \frac{M}{\Delta M \delta M} \qquad 8.10$$

So high resolution demands high dispersion of the mass separator and the width of the mass line should be small. Higher dispersion can be achieved by increasing the radius of the magnet i.e. by increasing the size of the magnet. The width of the line can be decreased by decreasing the diameter of the beam of ions from the ion source, but this will also decrease the ion current.

8.2 Line Broadening Mechanisms in CLIBS

According to Kaufman [20] the theoretical limit of spectral line width which can be obtained in optical region in CLIBS is less than 10 MHz. But practically the minimum line width which has been recorded by CLIBS is ~ 30 MHz and in most cases the line width lies in the range of 40 - 70 MHz. There are several parameters which limit the ultimately theoretical resolution of CLIBS. Some of the most significant line broadening reasons are discussed in the following paragraphs.

8.2.1 Acceleration Voltage Instability

The acceleration voltage (acceleration cooling) is the basic reason of reduction of Doppler broadening in CLIBS. But at the same time, it is one of the main sources of the relatively large spectral line width. The large spectral line width arises from the instability and noise of the acceleration voltage. The dependence of line broadening on the acceleration voltage change is given by the following relation.

$$\Delta\vartheta = \frac{\vartheta_o}{c}\,\Delta u = \vartheta_o \sqrt{\frac{eU}{2Mc^2}}\,\frac{\Delta U}{U} \qquad 8.11$$

At acceleration voltage of 20 kV, a ripple of 1 V, in the visible laser frequency range can bring a change of ~ 7.5 MHz in the spectral line width in a rare-earth ion beam. Doppler broadening reduces by increasing the acceleration voltage but at the same time the stability of the acceleration voltage decreases which increases the spectral line width again. It becomes harder and harder to stabilize a higher acceleration voltage. Therefore, there is a trade-off between stability and acceleration voltage. Major reduction in line width occurs at modest acceleration potentials.

8.2.2 **Angular Divergence**

The line width also depends upon the angular divergence ($\Delta\vartheta_{\Delta\theta}$) between the laser beam and the ion beam. If the laser beam and the ion beam make a small angle ($\Delta\theta$) with each other, the distribution of the z-component of the velocity distribution in the spectral line width is given by the following relation [20]

$$\Delta\vartheta_{z\Delta\theta} = \frac{v_o u_o}{4cR}\,(\Delta\theta)^2 \qquad 8.12$$

and the spectral line width in direction perpendicular to the laser beam is given by [20]

$$\Delta\vartheta_{y\Delta\theta} = \frac{v_o u_o}{c}\,(\Delta\theta) \qquad 8.13$$

Here $\Delta\theta$ includes all the angles either by ion beam divergence, or by laser beam divergence or due to the laser and ion beam misalignment. Generally the divergence of the laser beam is much smaller as compared to the ion beam divergence.

The typical values of line broadening due to the angular divergence for $\Delta\theta = 0.005$ rad and a laser frequency $\upsilon = 5 \times 10^{14}$ Hz, are $\Delta\vartheta_{z\Delta\theta} = 3.0$ MHz and $\Delta\vartheta_{y\Delta\theta} = 5.5$ MHz

8.2.3 **Time of Flight Broadening**

The time of flight broadening can be calculated by Heisenberg´s uncertainty principle

$$\Delta E \Delta t \geq \hbar$$

If an ion spent time Δt, in the interaction chamber the transit time broadening is given by

$$\Delta E \Delta t = \Delta \vartheta h \Delta t$$

$$\Delta \vartheta = \frac{1}{2\pi \Delta t} \qquad 8.14$$

For an interaction length of ~ 3 cm (in this work) and an ion velocity of 170 kms^{-1} [24], time of flight broadening is $\Delta \vartheta \sim 1$ MHz.

8.2.4 **Recoil Momentum**

Another reason of shift and line broadening is the recoil momentum due to the atoms by the light beam. If on the average *N* photons per atom are absorbed from the beam and are reemitted spontaneously, then the resulting shift is given by [20].

$$\delta \vartheta_R = \frac{Nh}{m \lambda^2}$$

The average rms line width is

$$\Delta \vartheta_R = \frac{\delta \vartheta_R}{\sqrt{3}} \qquad 8.15$$

For $N = M$ (atomic mass number) and in the visible frequency range, $\Delta \vartheta_R \sim 1$ MHz.

Some other important mechanisms which can broaden the line profile are listed below:

- Jittering of laser frequency can add a width of up to 10 MHz to the spectral line.
- Saturation broadening due to high laser power is also a major source of line broadening.
- Ion source energy spread and plasma instabilities in the ion source due to impurities and other isotopes can also cause broadening.
- Collisional broadening due to the interaction of the ion beam with residual gases, at chamber pressure of 10^{-6} mbar, can increase the line width ~ 2 MHz.
- Line broadening can also occur by averaging different recordings if the laser stabilization is not working properly.
- Line broadening is also possible if the ion beam strikes somewhere inside the mass separator giving rise to a spread in the velocity distribution of the ion beam.

- The experimental uncertainties in the acceleration voltage, scanning voltage and laser frequency can also cause some systematical errors in line broadening.

8.2.5 **Total Line Width**

Total line width in a CLIBS experiment is the sum of all types of broadening mechanism discussed and is given by

$$\Delta\vartheta_{Tot} = \sum_{i=0}^{n} \Delta\vartheta_i = \Delta\vartheta_{nat} + \Delta\vartheta + \Delta\vartheta_{\Delta\theta} + + \Delta\vartheta_R \ldots \qquad 8.16$$

If the natural line width of the spectral line is ~ 15 MHz, then approximately total line width is given by

Natural line width	15 MHz
Acceleration voltage instability	10 MHz
Laser frequency jittering	14 MHz
Angular divergence	7 MHz
Collisional broadening	2 MHz
Time of flight broadening	1 MHz
Recoil Momentum	1 MHz
Resultant line width (~)	50 MHz

In the above calculation of line broadening, only approximately values of different broadening effects are taken. The line widths observed in this work are in the range of 40 – 70 MHz. The experimental values of line widths are generally in good agreement with theoretically predicted values. But sometimes exceptions occur due to large saturation effects at high laser power and poor stability of ion source.

Generally the line widths observed in this work are larger than the measurements by Hühnermann et al [182], in which the line widths are ~ 30 MHz. The relatively large line widths are due to the larger diameter of the extracting hole of the ion source (~ 2 mm) as compared to the diameter of the ion source (~ 0.7 mm) used by Hühnermann.

8.3 **A Summary of Advantages of CLIBS**

CLIBS has several advantages over conventional laser spectroscopic methods. Some of the advantages of CLIBS are listed below.

- In a fast ion beam the Doppler-width is reduced due to the kinematic compression (kinematic cooling) and a resolution of few megahertz can be obtained at optical frequencies [20].
- The collinear (anti-collinear) geometry allows relatively long laser-ion interaction time.
- The geometrical layout of the system can also be used for pumping experiments and preparation of particular states prior to the observation region [183].
- Usually the tuning is performed by scanning the laser frequency and keeping the ions velocity fixed, but CLIBS offers an opportunity for Doppler tuning.
- In Doppler tuning, the ion velocity can be scanned locally, repeatedly and consistently with a very high resolution and high degree of precision.
- The proper choice of electrical potentials provides a wide range of tunability.
- To lock laser on a fixed frequency is relatively easy as compared to repeatedly scanning the laser frequency over a large spectral range without mode hops.
- The mass separator unambiguously makes possible to select species of interest by its charge/mass ratio (unknown samples and their composition can also be determined).
- Due to the mass separator, selection of isotopically pure beam is fairly easy.
- This technique also allows the online studies of short-lived radio-isotopes [184].
- Due to collision free environment (vacuum of typically 10^{-6} mbar and beam density of the order of 10^{6} cm^{-3}) short lived excited states may persist long enough to be observed.
- The experimental setup can easily be modified for radiative lifetime measurements by the laser-beam method and for branching ratios, which gives accurate oscillator strength [32].

8.4 **Applications of CLIBS**

Since the first successful application of CLIBS in metastable xenon ions [23], this technique has gained much attention in the field of high resolution spectroscopy. Several groups around the world applied this technique for the study of hf structure [183, 185-187], measuring nuclear moments [30, 188-189] and nuclear spin [178, 190], measuring radiative lifetime of electronic

states [32, 179, 191], isotopic shift [192-194], branching fraction and oscillator strength [195-198]. This high resolution technique has been applied to short-lived radioactive isotopes having life time in the range of milliseconds [199], photo-fragmentation spectroscopy of molecular ion beam [200] and laser photo-detachment spectroscopy [201]. CLIBS has also been extensively used for several elements e.g. La II [29, 38, 72-73] , Pr II [36, 73, 202-203] , Ba II [178, 204] , Sm II [177, 189, 205-206] , Eu II [34-35, 207-208], Pm II [184], Xe II [209-210], Ce II [211], Mn II [212], Th II [197], Cs II [213].

The resolution of Collinear laser-rf-double-resonance spectroscopy (RF-CLIBS) is of the order of few kHz (factor of 10^3 more as compared to classical CLIBS) and with this resolution it is possible to study small effects like broadening and light shifts of the levels caused by virtual optical transitions [214]. RF-CLIBS had been applied on various elements like ^{235}U [215], ^{135,137}Ba [216] and ^{167}Er [217].

Nuclear properties of the exotic high-spin isomer $^{178}Hf^{m2}$ had been studied by collinear laser spectroscopy [218] and the quadrupole moment, isomer shift as well as a precise value of the magnetic dipole moment had been determined. Recently lowlying isomer in ^{229}Th has been investigated at Jyvaskyla IGISOL (Ion Guide Isotope Separator On-Line) facility by collinear laser ion beam spectroscopy [219]. High-resolution laser spectroscopy on the negative osmium ion has been performed by U. Warring et al [220]. The group has applied first time a combination of laser excitation and electric-field detachment to negative atomic ions, which resulted in an enhancement of the excited-state detection efficiency by at least two orders of magnitude. Applying this method, a measurement of the bound-bound electric-dipole transition frequency in $^{192}Os^-$ was performed using collinear spectroscopy with a narrow-bandwidth cw laser. This investigation resulted in more than 100 times better precision in transitions frequency.

9 THE EXPERIMATAL SETUP OF CLIBS (MARS-II)

The Marburg mass separator MARS-II was installed at the University of Marburg Germany and was brought to Graz University of Technology in 2002. In the period 1976 - 1996 a lot of work concerning the hyperfine structure and isotopic shift of various elements such as xenon, barium samarium, promethium, lanthanum, europium etc was already done in Marburg. MARS-II had contributed to more than 60 journal publications and nearly 15 people had completed their PhD work on this machine. The system MARS-II was reinstalled and readjusted at Institute of Experimental Physics, University of Technology Graz and now is fully functional for last couple of years and is being used for the Doppler-reduced spectroscopic investigations. The new results produced with this machine are quite satisfactory and in most of the cases the accuracy of the results is better than that of the published results. Some of the experimentally determined of spectroscopic constants were already presented in various international conferences and journal publications. In near future some more results are expected, based on the recent investigations of the hyperfine spectral lines measurements of different elements. A schematic diagram of MARS-II is represented in Figure 9.1. Some of the important components of the MARS-II will be described in detail in the following sections.

9.1 Description of the Mass Separator MARS-II

The isotope separator MARS-II was designed and developed in 1970 by W. Kornal and G. Krömer. The ions are generated in an ion source and are accelerated up to approximately 170 km/s by applying a high acceleration potential, ~ 20 kV. After passing through an 80° sector magnet a mass separated ion beam is obtained. The ionic beam of the selected isotope is guided into the interaction chamber through a set of deflection plates. A collinear and anti-parallel interaction of the laser beam and the ion beam takes place in the interaction chamber. If the Doppler shifted laser frequency is in resonance with the optical transition of the spectral line, an excitation from a lower level to an upper level takes place. The fluorescence signal generated

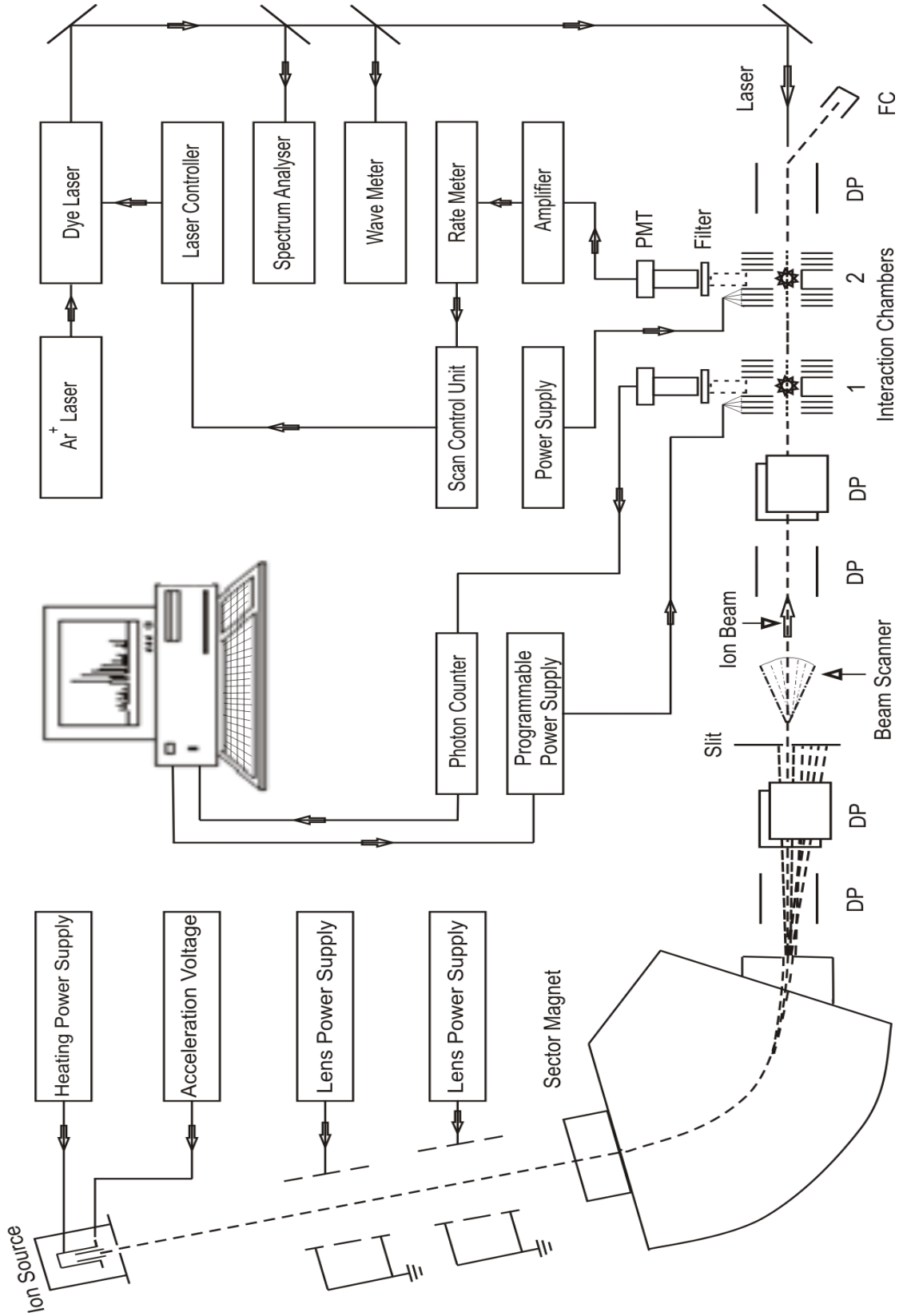

Figure 9.1: Schematic diagram of experimental setup for CLIBS, MARS-II .
FC: Faraday cup, DP: deflection plates, PMT: photomultiplier tube

from the decay of the upper level to some lower level is recorded with the help of a photomultiplier tube (PMT).

The original MARS-II system consisted of two ion beam lines (for two different isotopes), thus interaction of two isotopes with laser light can be observed simultaneously. One beam could be chosen as a reference beam. After the beam scanner beams are deflected by an angle of ~ 42˚ in opposite directions to enter into the two interaction tubes. This large angle deflection of the ion beam resulted in a lower number of ions in the interaction chambers available for the experiments. In order to avoid this large defection and thus to improve the ion beam current one of the channel tube (left channel) was removed. Now the ion beam is deflected by an angle of about 9˚ into the interaction tube. With this new configuration the numbers of ions reaching the end of the interaction tube were increased nearly 4 times as compared to the previous setup and resulted in improvement of the LIF signals. Of course, one looses in this way the possibility to investigate two isotopes and to use one isotope for reference for isotope shift measurement. However, initially our main interest was devoted to Pr II, which has only one stable isotope, the change was useful.

9.1.1 **Ion Source**

For production of positive ions, a Johnson type surface ion source is used [221]. An ion source of this type is shown in Figure 9.2. In the first step both the oven and the ionizer are heated by applying ohmic heating. The temperature of the ionizer must be high enough to dissociate the molecules of the specimen under investigation first into neutral atoms and then to ionize them. Initially, the vapors of the specimen are produced in the oven (Tantalum-cup) followed by adsorption on the heated surface of the ionizer to get ionized. The material of the ionizer is selected in such a way that it should have higher electron negativity than that of the sample. A strong acceleration potential ~ 20 kV pushes the ions away from the ion source immediately after production of ions. The accelerated ions can attain a velocity of nearly 170 km/s [24].

A suitable ionizer should have following characteristics:

- The electron negativity of ionizer must be higher than that of the sample material.
- It should not be reactive with sample material and with air.
- The stability at high temperatures must exist.

- The ionizer must be refractory.
- The ionizer should be free from impurities.

In this work the hyperfine structure of four different elements Nd II, La II, Pr II and Ba II spectral lines were investigated but here, for production of positive ions, only one element (Nd) will be discussed. The production of ions for the other two elements and ion source conditions are almost similar but the heating power used is far less than Nd.

A few milligrams of natural neodymium (Nd) in form of very fine metallic grains is used in the ion source for the productions of the Nd^{+} beam. The Nd sample is filled in the Tantalum (Ta) cup and a Ta heating tube was used as an ionizer. Various materials and different dimensions of heating cups and ionizers were tried to produce a stable and high ion beam current of Nd. After a number of experiments and careful observations it was realized that the best results are possible for the ionizer thickness 0.025 mm, length L1 = 45 mm and inner diameter of Ta tube ≤ 2 mm, and the specification of Ta cup were, L2 = 15 mm, outer diameter was 5 mm, the cavity of inner diameter (w) $1.5 \leq w \leq 2$ mm and depth (d) = 5 mm, while the aperture of extraction electrode is 5 mm.

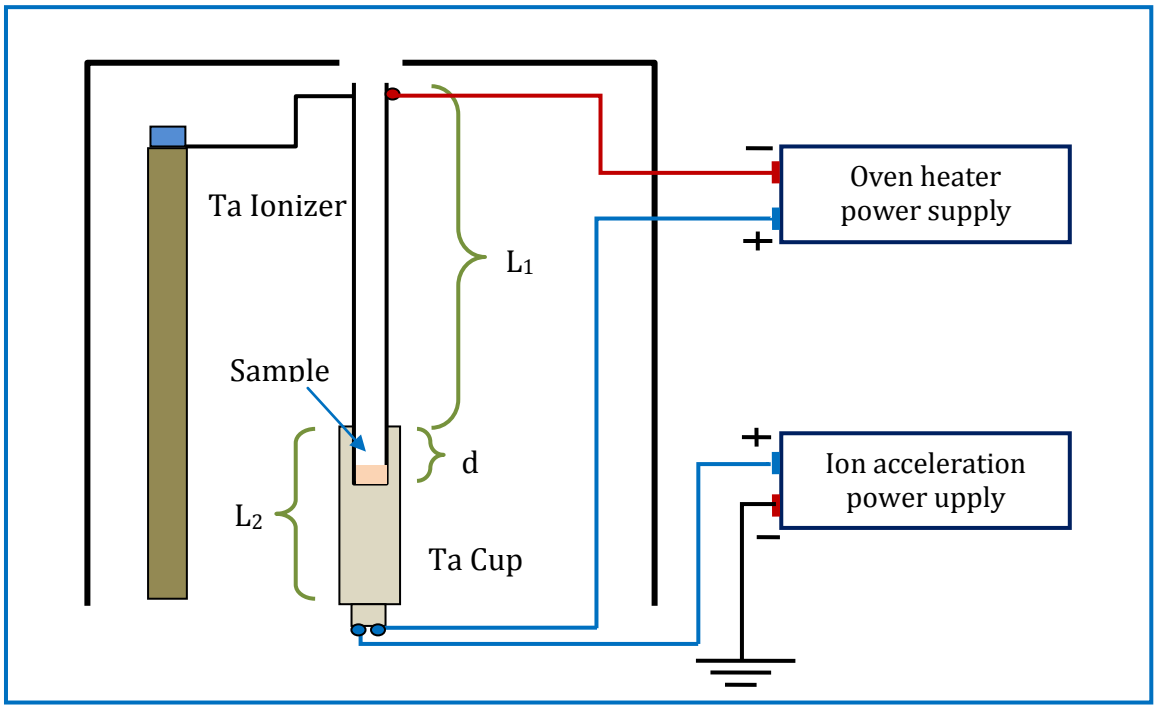

Figure 9.2: Surface ion source for positive ions.

It is also observed that for high production rate of ions and better ion beam stability, whenever the ion source is filled with a fresh sample, it should be heated for nearly one hour at heating power of about 150 - 200 Watt under high vacuum conditions (~10^{-6} mbar) of the mass separator. After this the ion source and mass separator is switched off and the ion source is let to be cooled down to room temperature. Normally it takes 3 - 4 hours to reach thermal equilibrium to room temperature. All this exercise is possibly helpful in removing impurities/oxides by the process of vaporization and the remaining material inside the Ta cup is most probably pure neodymium. When the ion source is heated again an ion current of 10 - 15 nA for mass separated $^{143}Nd^{+}$ can be maintained for 1- 2 hours with heating power of 300-350 Watt. The ion beam current is measured with a Faraday cup after the interaction chambers. The number of ions decreases with time, so to increase the ion beam intensity, the heating power is further increased. But at the heating power of about 410 – 440 Watt, the Ta heating tube breaks up most likely due to melting and the oven is not working anymore. For further experiments, again a new heating tube is installed and fresh neodymium is filled in the oven.

9.1.2 **Electrostatic Lens System**

Two electrostatic lens systems are installed at the region between the ion source and the magnet. One lens controls the ion beam in horizontal direction (Z-lens) while the other lens is used for vertical control (Y-lens) of the ion beam. The design of electrostatic lens system used here was suggested by G. N. Plass in 1942 [222] and it offers minimum spherical aberration. A plot of potential distribution for such a lens is given in Figure 9.3.

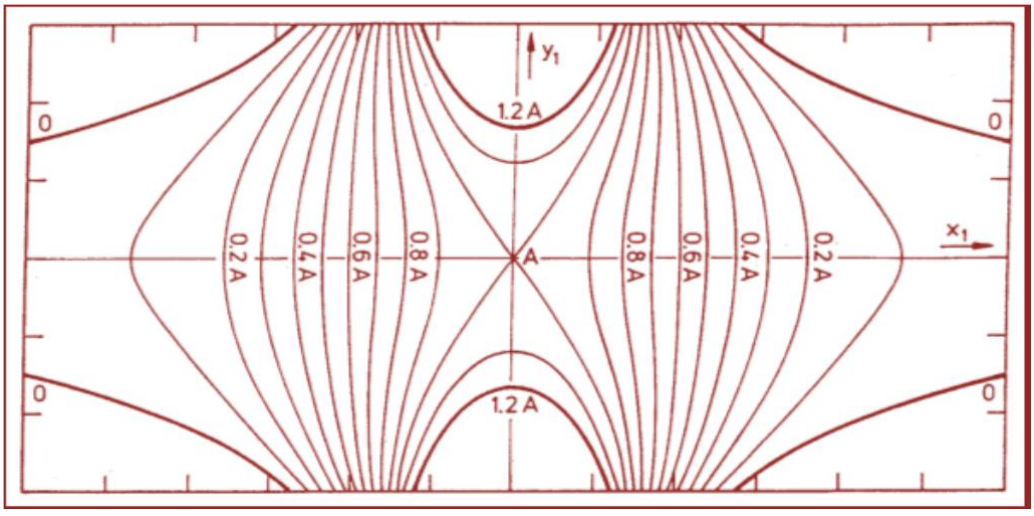

Figure 9.3: Sketch of equipotential field of an electrostatic lens having minimum spherical aberration. A represents potential at the center of the lens[223].

Lens electrodes are made of metal which is resistive to oxidation, stable against corrosion and most importantly it produces minimum secondary electrons. Aluminum is the best suited metal for such purposes.

The acceleration potential and voltage applied to focus the ion beam are directly related to each other. For an ion beam of $^{143}Nd^{+}$ and acceleration potential of ~ 20 kV, 11 -13 kV for the z-lens and 1- 3 kV for the y-lens are used for the optimal focusing of the ion beam.

9.1.3 **The Magnet**

The sector magnet used in mass separator MARS-II was developed by W. Kornal and G. Krömer. This electromagnet is quite big in size and its total weight is ~ 4000 kg, average radius of curvature is 80 cm and the angle of deflection of the central beam is 80˚. The nominal resolving power and the dispersion of the isotope separator are approximately 3000 and 1200, respectively [223]. Some important features of this sector magnet are given in Table 9.1 [223]. The operation of ion optical system of the mass separator is described in Figure 9.5.

Table 9.1: Selected parameters of the sector magnet.

Description	**Value**	**Notation**
Radius of curvature	80 cm	R
Angle of deflection	80°	Φ
Entrance angle	0°	ε_1
Exit Angle	34.8°	ε_2
Radius of curvature of the field boundary at the entrance	50 cm	r_1
Radius of curvature of the field boundary at the exit	- 41 cm	r_2
Distance between the field entrance boundary and the ion source	120 cm (1.5 R)	I_1
Distance between the field exit boundary and the image	143 cm (1.79 R)	I_2
Pole pieces separation (width× height)	16 cm × 6 cm	g

There are four packets of coils in the magnet. Each packet further consists of ten coils and each small coil has 56 windings. Approximately 3 mm thick wire is used in these windings. The complete circuit diagram of the coils is given in Figure 9.4. A stabilized power supply (Transistor-Netzgerät TN 60 - 24000) of 100 V and 80 A is used which can produce magnetic

field lines up to 6600 Gauss. For cooling purposes, a special set up of copper plates surrounded by copper pipes is designed between the magnetic coil packets. The copper plates are cooled by circulating cool water through the copper pipes.

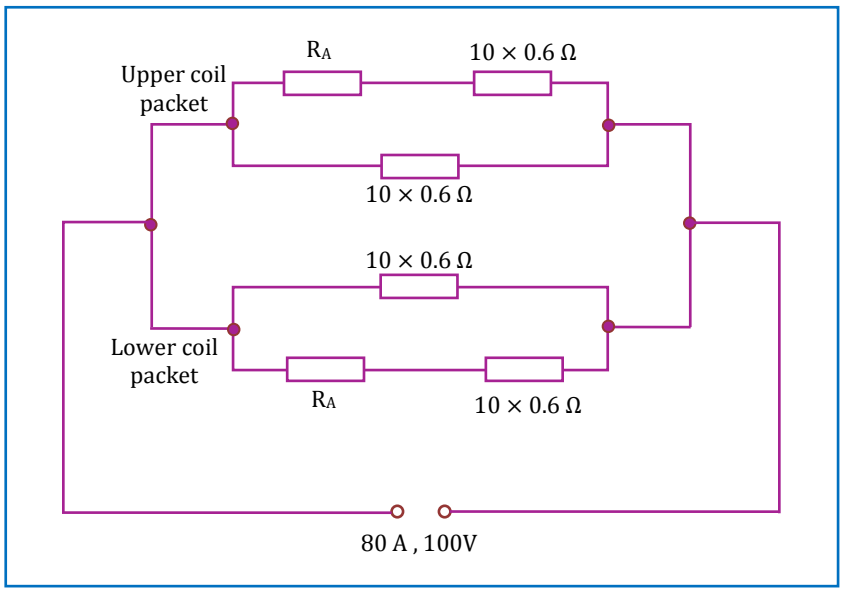

Figure 9.4: The circuit diagram of the winding of the sector magnet. The compensating resistance R_A (R_A=0.50Ω, 200 Watt) is same for the upper and lower coil packets [223].

A fringing free and homogenous magnetic field was essentially required for obtaining the high resolving power. In order to minimize the effect of fringing field the entrance and the exit of the magnet were made circular and the curvature radii were calculated by applying the Hintenberger conditions [224]. The specification of the pole pieces of a convex profile with a radius of curvature of 47.8 cm at entrance and a concave profile with a radius of curvature 42.5 cm at the exit are used. The pole pieces of width 37 cm, thickness 6.7 cm, with segment angle 67˚ and radius of curvature 78.5 cm used between the vacuum chamber and the magnetic yoke that extends over full length of the magnet. Moreover, for attenuation of the fringing field, extra magnetic shields were mounted at the entrance and exit edges of the pole pieces. The pole pieces are independent and separated from the magnetic yokes by two air gaps, each of 2 mm wide. In order to maintain the better homogeneity of the magnetic field, this gap must be changed accordingly. A precisely calculated wax sheet with different thickness of iron powder was placed in between the pole pieces and magnetic yokes in order to maintain the variation of the thickness of the air gap. This phenomenon of investigations of fringing field and homogeneity of the magnet is expressed in more details by Th. Win at al [223]. The variations observed in the

magnetic field are: 0.001% in the range of -3 ≥ z ≥ +3 cm in the median plane and 0.002% in the range of -5.5 ≥ y ≥ +5.5 cm.

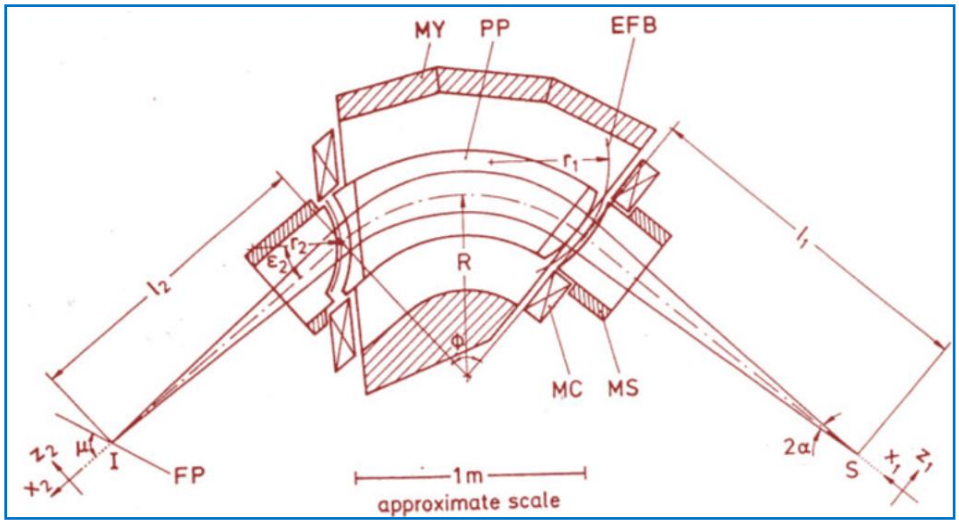

Figure 9.5: Schematic of the ion optics of the mass separator. S:Ion source, FEB: Effective field boundary, PP: Pole piece, MY: Magnetic yolk, MS: Magnetic shield, MC: Magnetic coil, I is the image and FP is the focal plane (the remaining notations are described in table 9.1)[223]

9.1.4 **Interaction Chamber**

There are two identical interaction chambers (interaction chamber 1 and interaction chamber 2) in MARS-II where the laser and ion beams interactions takes place collinearly. Hyperfine structures are recorded in the interaction chamber 1 and the interaction chamber 2 is used to lock the laser frequency to one of the hyperfine components under investigation. The side and top view of a four stage interaction chamber is drawn in Figure 9.6.

A post acceleration scanning voltage (Doppler tuning) in the range of 0 - 3500 V (full power supply range) applied across the interaction chamber can tune the Doppler shift (in the lab-system) up to 25 GHz. The potential inside the interaction chambers is more uniform as compared to the potential near to the entering and exit holes. This non-uniformity in potential can disturb the symmetric line profile of the recorded hyperfine structures. To avoid this asymmetric behavior additional electrodes were introduced as potential dividers in the interaction chambers. The design of the interaction chambers also helps to have laser and ion beam interaction (in resonance conditions) just in front of the photomultipliers tubes (PMTs). If the excitation also occurs outside the light collector chambers then the metastable states are depleted and thus not used for the measurements. This always happens when the scanning voltage is around zero volts.

A minimum voltage equivalent to the line width (FWHM) of the spectral line being investigated should be applied before starting the Doppler scanning.

The large interaction region (~ 30 mm) helps to have a better LIF signal intensity as compared to transverse laser atomic beam spectroscopy in which the interaction region is limited to the diameter of the atomic beam. In order to collect the maximum fluorescence signal the inner walls of the interaction chamber are covered with a high reflecting aluminum foil. The laser induced fluorescence (LIF) signal is transported through plexiglass rods to the PMTs. To suppress the background light from the ion beam and stray laser light Schott BG-12 glass filters are used. Finally, the LIF signal is detected by a head-on photomultiplier tube (Photonis XP2020).

A second interaction chamber just similar to first one is used for the stabilization of the laser frequency to one of the hyperfine components. This laser frequency locking technique will be discussed in section 9.2.4.

Principally the Doppler tuning can be performed with accelerating and retarding potentials. But if deceleration voltage is used then the collinearity of the ion beam in the interaction chamber regions is much more critical as compared to use acceleration voltage. Slowing down the ion velocity can also deviate the ion beam from its rectilinear path and the chance of a collision between the ion beam and the inner walls of the interaction chamber increases with increasing retarding voltage. The background signal increases rapidly when the retarding voltage (positive potential) is increased beyond 2 kV. On the other hand when acceleration voltage (negative potential) is used for Doppler tuning then a further increase in the ions velocity do not change their rectilinear path and the ion beam do not strike inside the interaction chamber.

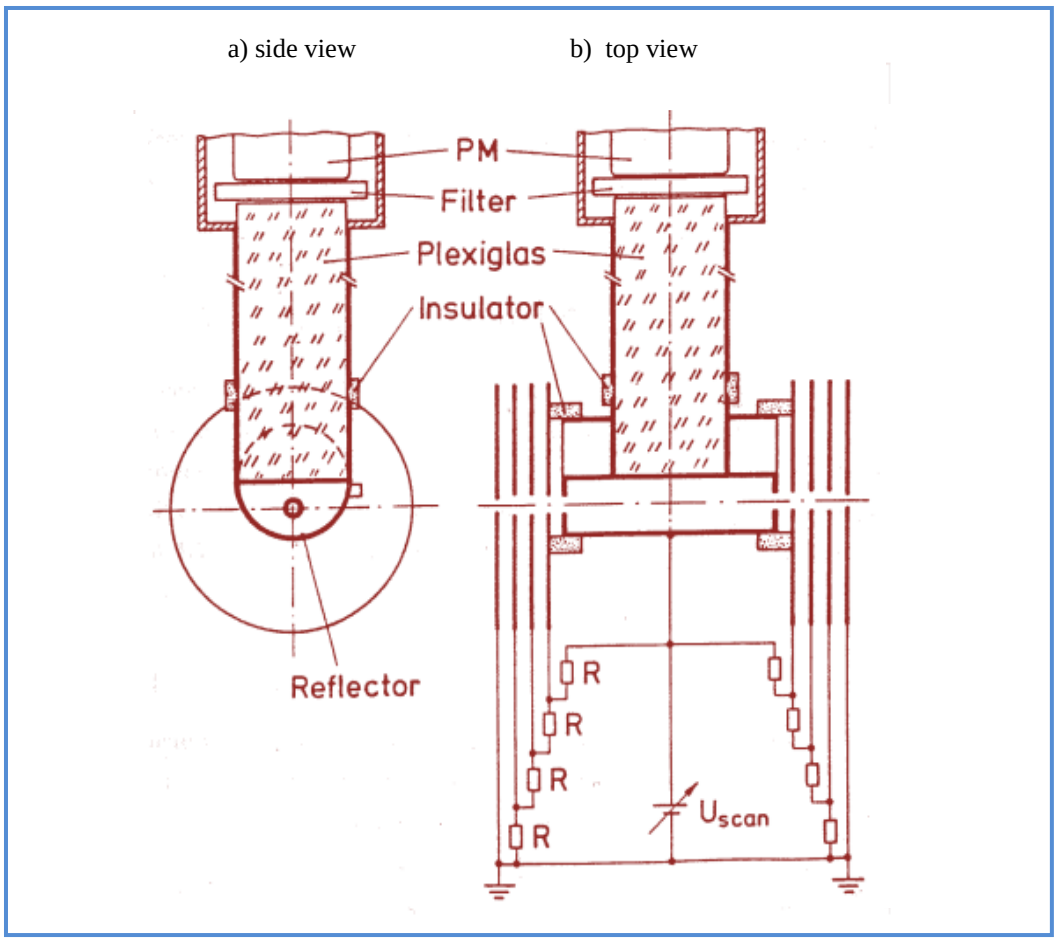

Figure 9.6: The interaction chamber installed in MAR-II. (a) side view (b) top view, R=1MΩ

9.1.5 **Vacuum System of MARS-II**

The MARS-II is a very huge system in respect of volume and length. Its volume is roughly in the range of 4 - 5 m^3 and length more than 5 meters. To maintain the whole system on high vacuum (~ 10^{-6} mbar) is not a very easy task and it needs many sophisticated vacuum pumps and good understanding of high vacuum technology. The high vacuum is necessary in the experiments like CLIBS. Some of reasons are stated below:

- The presence of the high vacuum helps to avoid collisional quenching and collision induced fluorescence.
- High vacuum is also necessary to obtain a focused and collinear ion beam.
- It is also necessary to maintain the initial metastable states (populated in the ion source) of ions.

The enclosed outer housing of MARS-II systems is made from solid stainless steel sheets of thickness 2 – 3 cm. The stainless steel is used because its mechanical strength is very high and degassing from this material is very low. Also stainless steel is easy to mould in desired shapes and friendly for welding. Generally viton O-rings are used between the vacuum flanges and valves to integrate different parts and accessories of the system.

A detailed schematic diagram of the vacuum system of MARS-II is presented in Figure 9.7. The abbreviations used in this diagram are: R1… Rotary pumps, V1…Vacuum valves, S1… pneumatically controlled vacuum valves, LNT….Liquid nitrogen traps, TK-FR…Turbo Klein (small turbo molecular pump), TG…Turbo Groß (big turbo molecular pump), SI…Ion pump, Cyl…Cylinders, and mm1…, 1A…etc. = used for different pressure heads.

There are five major sections of the vacuum system of MARS-II: Ion source, electrostatic lenses chamber, magnet chamber, ion collector chamber, and a vacuum tube where the interaction chambers are located. Whenever needed, by using pneumatically controlled vacuum valves each section can be isolated from others. The valve S4 can be operated manually or automatically. In automatic mode, this valve can turn off itself if the pressure in the interaction region (vacuum tube) reaches 10^{-1} mbar; therefore the rest of the vacuum system is maintained on high vacuum. The flow signal of cooling water of some turbo molecular pumps (TK and TG) also control valve S4 and closes it if the flow of cooling water stops during operation. Also the vacuum valve S1 and the flow of cooling water of the big turbo-molecular pump (TG-IS) both are synchronized in the ion source section. The vacuum valve S5 is installed between the lenses chamber and the ion source. The ion source chamber is opened frequently in order to fill the oven to introduce a fresh sample for investigation. Therefore by closing valve S5 the ion source is separated from the rest of the mass separator. Now it is easy to evacuate the relatively small volume of the ion source as compared to the whole mass separator. The volume of the ion source section is more than 100 time smaller than the volume of the whole MARS-II. An integrated portable unit of a rotary pump and turbo molecular pump is used to create a fore-vacuum in an isolated vacuum chamber.

The vacuum stages can be classified into two broad ranges, fore vacuum and fine vacuum. The fore-vacuum system consists of a small turbo molecular pump TK-FR and a rotary pump R1. Another rotary pump R2 operates as a backup system if there is any malfunctioning of R1. Two big rotary pumps R3 and R4 are attached with the fore-vacuum line. These two pumps are placed

in another room (room K32) and are connected to the MARS-II through copper pipes. These two big rotary pumps are operated only when the whole system has to be evacuated from atmospheric pressure and can bring the pressure down to 10^{-2} mbar in half an hour.

In fine vacuum system there are three turbo molecular pumps: TK, TG and TGIS. These pumps are backed by fore-vacuum system. The abbreviation used here and detailed features of all the vacuum pumps are listed in Table 9.2.

Fore Vacuum:

In order to create a vacuum environment especially from atmospheric pressure in MARS-II, the vacuum pumps and vacuum valves are turned ON and OFF according to procedure given below: When the vacuum valves S1, S2, S4 and S5 and vacuum valves V10, V21, V3 and V1 are opened, only than the big rotary pumps R3 and R4 are switched ON. When the pressure inside the system is decreased to ~ 10^{-1} mbar, the small turbo pump TK-FR should be turned ON. Now close the valves V1, V3, V7 and V8 and turn OFF the rotary pumps R3 and R4 and also open the valves V2 and V4. When TK-FR reaches to its normal operation (green light is on) open the valves V6, V9 and V10. Now the air inside the mass separator is evacuated into the cylinders Cyl1, Cyl2 and Cyl3. A Leybold-Heraeus gauge mm5 (Model: Thermovac TM201 S2), is installed to measure the pressure in the cylinders. A pressure limit with P1 > P2 is fed into gauge mm5, a voltage signal related to P1 and P2 is sent to the electromagnetic valve V5 and the rotary pump R1. The pressure comparative relation of P1 and P2 controls the ON/OFF operation of rotary pump R1. When the pressure in the cylinders is equivalent to P1, the valve V5 is opened automatically and the rotary pump R1 is turned ON and evacuation of the three cylinders starts. The rotary pump R1 is stopped and V5 is closed automatically when the pressure at mm5 reaches P2. A computer interfaced with electromagnetic valve V5, stores the OPEN/CLOSE timings of V5. The leak rate of the system can be estimated from the OPEN/CLOSE data of valve V5.

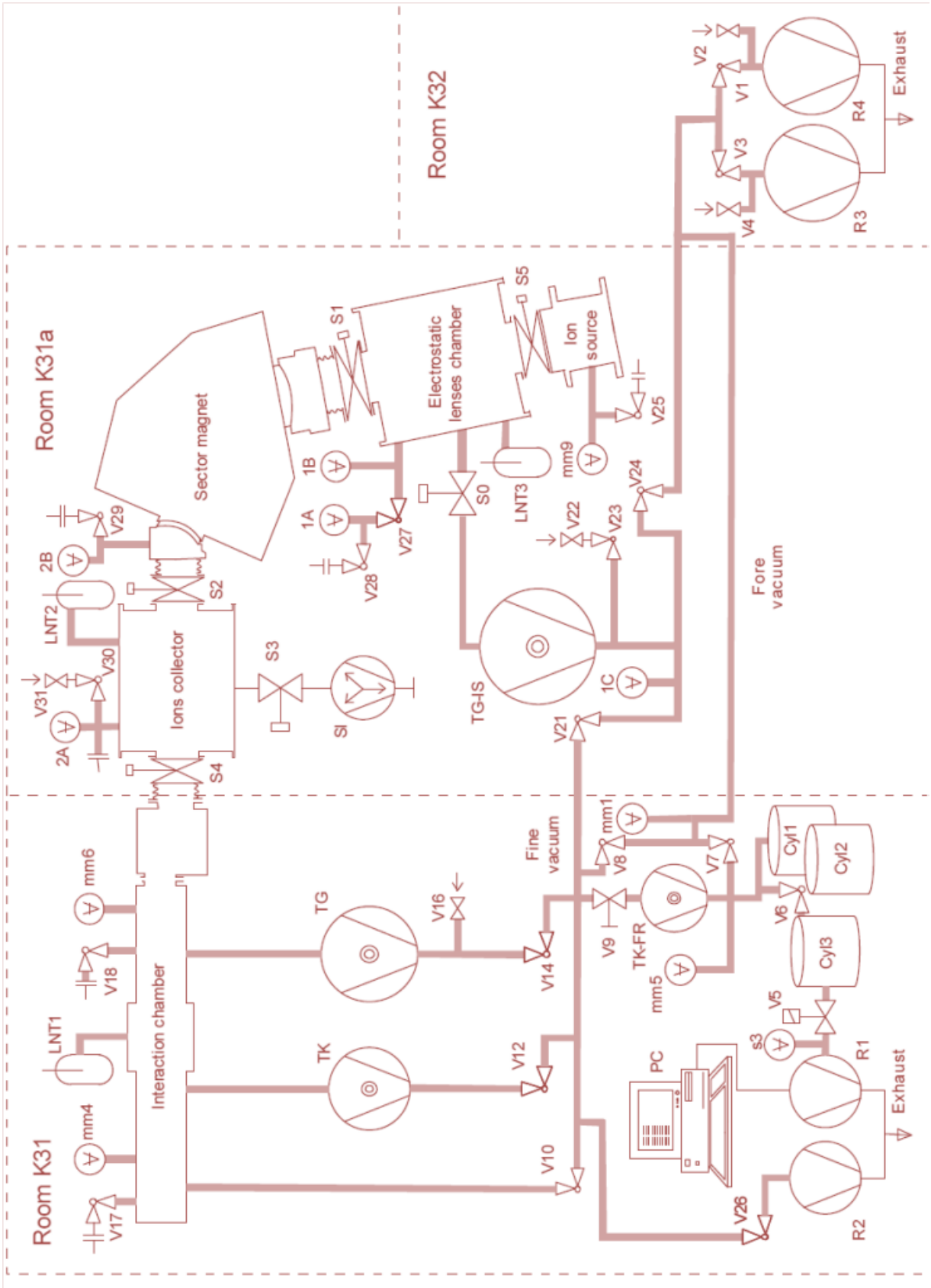

Figure 9.7: A layout of the vacuum system of the MARS-II. (for explanation and labels see section 9.1.5)[162].

Table 9.2: Specifications of the pumps used in the vacuum system of the MARS-II

Pump name/model	Power supply	Pumping power	Vacuum region
R1: Pfeiffer Balzers Model: DUO 008 B	AC 220 V, 50Hz	8 m^3/h	Fore vacuum
R2: Pfeiffer Balzers Model: DUO 2.5	AC 220 V, 50Hz	2.5 m^3/h	Fore vacuum
R3: Balzers Model: D12	AC 220 V, 50Hz	12 m^3/h	Fore vacuum
R4: Balzers Model: DUO 25	AC 220 V, 50Hz	28 m^3/h	Fore vacuum
TK-FR: Turbo molecular Model: ATW 398043 MDP 5011	Adixen ACT 100	7.5 l/s	Fore vacuum
TK: Leybold-Heraeus Model: Turbovav 150	Leybold-Heraeus Turbotronik NT 120	115 l/s	Fine vacuum
TG: Leybold-Heraeus Model: Turbovav 450	Leybold-Heraeus NT 450	450 l/s	Fine vacuum
TGIS: Leybold-Heraeus Model: Turbovav 1500	Leybold-Heraeus NT 1500	1500 l/s	Fine vacuum

Fine vacuum:

When the fore-vacuum system has evacuated the mass separator down to the range of 10^{-2} mbar, the turbo pumps TK and TG are turned ON, open the valves V12 and V14 and closed valve V10. Within half an hour of normal operation these pumps can reduce the pressure inside the mass separator in the range of 10^{-5} mbar. Now the big pump, TG-IS is turned ON and when it reaches its normal speed the valve S0 is opened. If there is no leakage in the system and all the pumps and valves are working properly then within one hour the whole system should reach in the range of 5×10^{-6} mbar. The pressure can be decreased up to 1×10^{-6} mbar by filling three liquid nitrogen traps (LNT) with liquid nitrogen.

When the experiment is finished turn OFF the turbo molecular pumps and close the valves V12, V14 and S0, open the valve V10 , the pumps TK-FR and R1 keep the system on fore-vacuum.

The vacuum pump S1 is out of order and has never been used during the operation of MARS-II here in Technical University Graz. That is why the valve S3 always remains closed. It is also necessary to mention here that majority of the vacuum pumps used in mass separator are water cooled. So before starting the vacuum pumps the water cooling system should be turned ON otherwise the pumps will not start at all.

In order to check the vacuum inside the MARS-II, several pressure heads are installed at different places of the mass separator. To measure the pressure near the interaction chamber and in ion source two vacuum gauges mm6 (Balzers TPG 251) and mm9 are used respectively. Pressure heads 2A and 2B are used to measure the pressure in the ion collector chamber, whereas 1A and 2B measure the pressure in the electrostatic lenses chamber. To measure the pressure in fore-vacuum region pressure gauges mm1, s3, mm5 and 1C are installed.

9.1.6 **Electronics System of MARS-II**

The electronic system of MARS-II is show in Figure 9.8. Several deflection plates are installed on different places in the mass separator. The vertical direction of the ion beam is adjusted with Z-lens and the deflection plates 1V and 2VR while the Y-lens and the deflection plates 1T, YK, 2UR and 3UR are used for adjustment of ion beam in horizontal direction. For the initial basic alignment of the ion beam the ion source and focusing chamber are mounted on moveable ports. The Faraday cups 1FR….4FR and the plates 1B and AK (mounted on the vacuum feed through) are used to measure ion beam current. To observe the shape of the mass spectrum of ion beam a beam scanner is installed in the ion collector chamber and 4-quadrent detectors, 14QR and 24QR are placed in the interaction tube to examine the path of ion beam. Two adjustable orifices 1ZB and 2ZB are used for proper narrow ion beam selection.

The preparation of the mass separator for experiment and the procedure to align the ion beam is given in following discussion:

When the pressure inside the mass separator is ~ 2×10^{-6} mbar turn ON the magnetic field and acceleration voltage and adjust the their values for selected element according to the relation given in graph (Figure 9.9). The rough values of Z-lens (10 - 13 kV) and Y-lens (0 -3 kV) are also applied for crud shape of ion beam. Switch ON all the other power supplies and modules (except ion source) i.e. used for alignment, detection and measurement of the ion beam. Now turn on the oven power supplies and increase the heating gradually. Measure the ion current at 1ZB, insert the plate1B in the lenses chamber and maximize the ion current on this plate by adjusting the position of orifice 1ZB. Remove 1B from the path of the ion beam and let the beam pass through the electrostatic lenses and the magnet, a mass spectrum of the ion beam should be visible on beam scanner. Insert the plate AK in the path of the ion beam and adjust the height of beam through the electrostatic lenses and the stage of electrostatic lenses chamber such that the

ion beam passes through centre of 1V. Remove the plate AK from the path of the ion beam. Now a further optimization in beam shape and position can be made by monitoring the mass spectrum on beam scanner and adjusting with it with acceleration voltage, magnetic field and electrostatic lenses. Make adjustments in the deflection potentials 1V, 1T YK; 2VR and 2UR so that the ion beam passes through the center of 14QR. The beam current on different places can be measured by inserting Faraday cups 1FR, 2FR, and 3FR in the beam path. A well collimated ion beam after passing through interaction chambers and 24QR falls on the Brewster window. To avoid the deposition of ions on the Brewster window a proper deflection potential (3URR/3URL) is applied to direct the ion beam towards Faraday cup 4FR. The 4-quadrent detectors 14QR/24QR and the orifice 2ZB are adjusted collinearly to obtain maximum ion beam current measured at 4FR.

All the deflection plates and other modules are insulated from the outer casing of mass separator and are grounded properly to avoid undesirable potentials. The specification of electronics modules are listed in table 9.3.

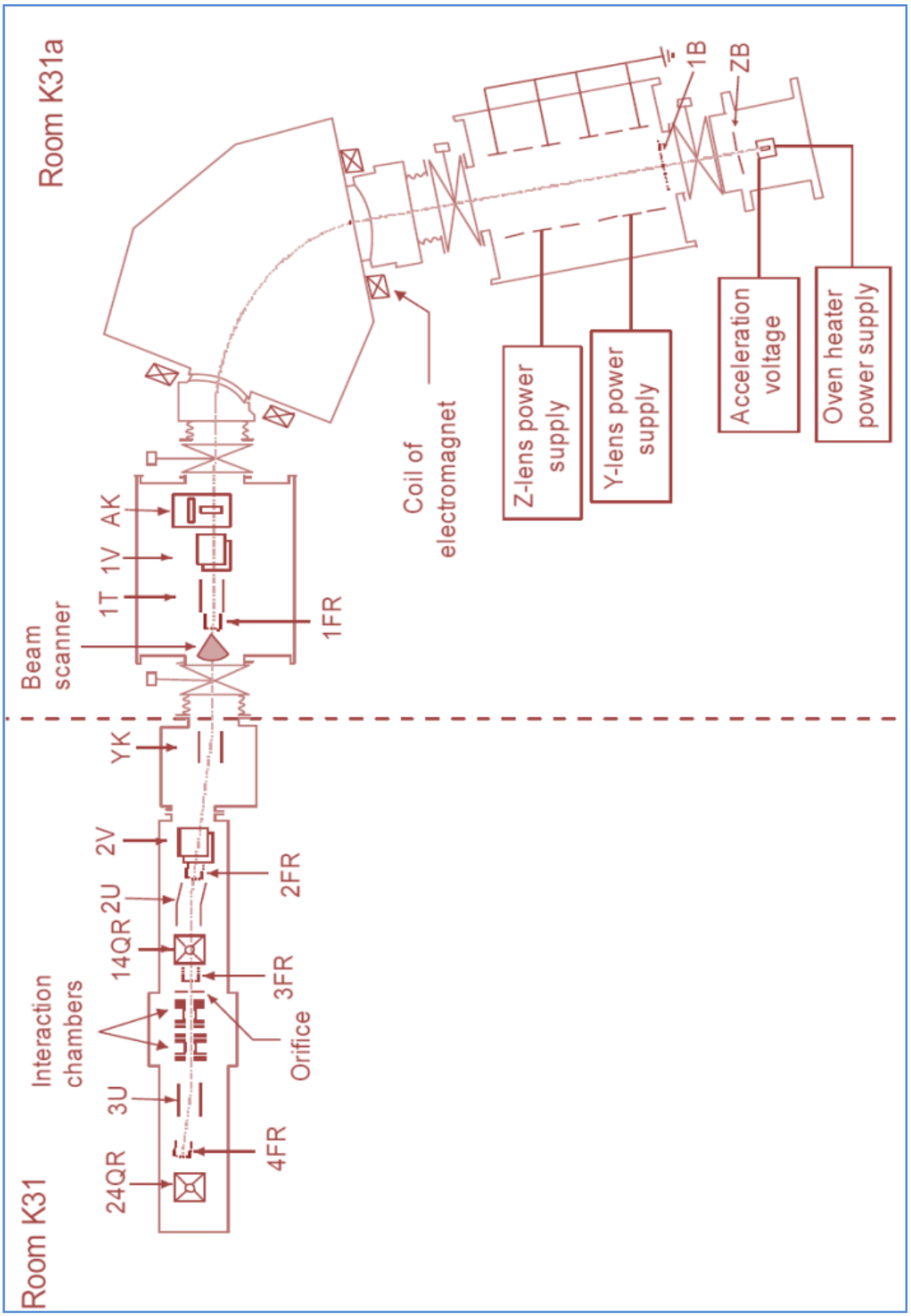

Figure 9.8: Schematic of the electronic system of the MARS-II (for description seen section 9.1.6)[162].

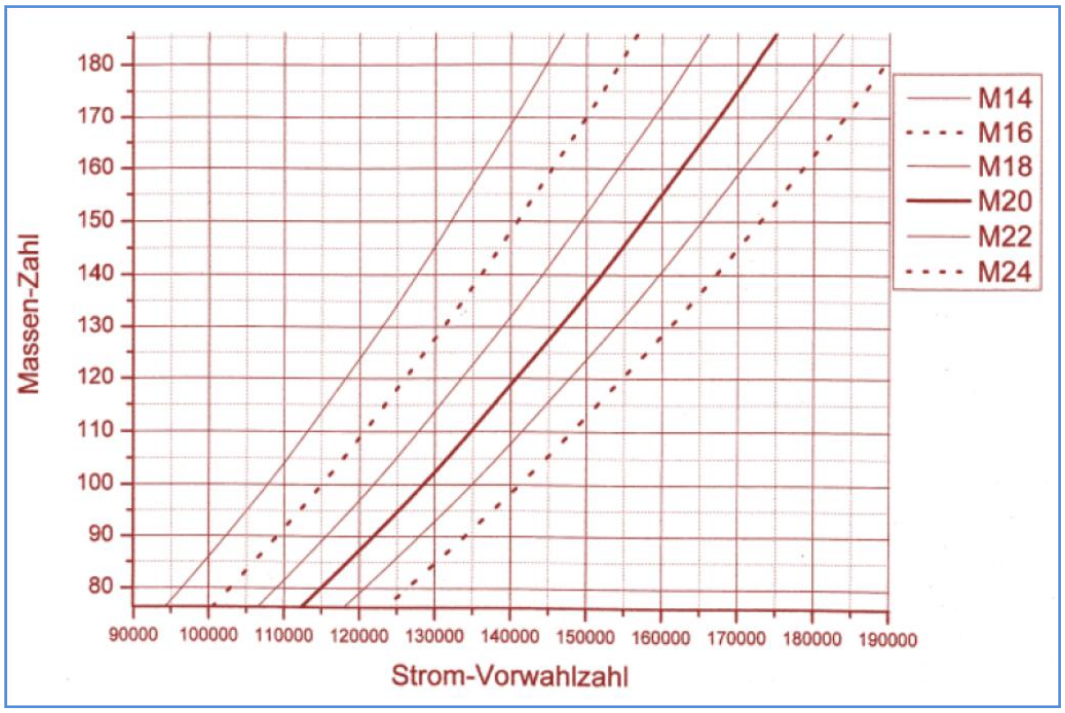

Figure 9.9: The mass number (Massen-Zahl) versus the current code number (Strom-Vorwahlzhl) of the electromagnetic. The lines M14….M24 correspond to the acceleration voltage in kV.

Table 9.3: Important electronic devices used for the alignment of the ion beam in MARS-II

Electronic Module	**Specification/Model**
Electromagnetic- Power supply	Heinzinger: Transistor-Netzgerät TN 60-24000 (100 V, 80 A)
Oven heater- Power supply	Manson SPS 9400
Acceleration-Power supply	HCN 140M - 35000
Z-lens -Power supply	HCN 140M - 20000
Y-lens -Power supply	HCN 140M - 20000
8 Channel potential dividers -Power supply	Wenzel-Electronik: HV N1130
Beam scanner	Sinusgenerator: SIG-02 (manufactured at Marburg University)
Monitor to observe mass spectrum	Hewlett Packard: 143 A Oscilloscope
4 Quadrant detectors	MON-03 (manufactured at Marburg University)
Ion current measurment	High speed PICOAMPERMETER: 417

9.2 Optical instruments

9.2.1 Lasers

A single mode ring dye laser (Coherent 699-21) of bandwidth less than 1 MHz is used in CLIBS experiments to provide excitation light source. A multi line visible spectrum (MLVS) Ar ion laser (Coherent INNOVA 200) is used as the pumping source for ring dye laser. The output power of the ring dye laser is measured by a Coherent power meter (model: Fieldmate). In this work, two dyes Rhodamine 6G and Sulforhodamine B (Kiton red) are used to cover the desired wavelength range. A water cooled Coherent pump (model: 591 utility model) is used to circulate the dyes through the jet of the ring dye laser.

9.2.2 Optical System

The optical arrangements of the experimental setup of MARS-II are described in detail in Figure 9.10. The laser beam from the output coupler (OPC) of the ring dye is divided into two parts, a weaker part (10%) and stronger part (90%, when it falls on beam splitter BS1. The weaker part of the laser beam is further splitted into two parts. One part of the splitted beam which goes to the spectrum analyzer (Spectra Physics, Model 470, free spectral range of 2 GHz) and is used for mode structure analysis and the second part which goes to the wavemeter which is used to measure the wavelength of the dye laser.

The stronger part of laser beam (90%) is shifted to the height of the ion beam with the help of mirror M1, beam shifter 1 and beam shifter 2 and is guided towards the interaction chamber through the mirrors M3 and M4 and Brewster window (as shown in Figure 9.10). The beam splitter 1 (Pellin–Broca-Prism) is a kind of spectral aperture and allows only the dye laser (yellow or red) to pass and the green light of the Ar+ pump laser is directed to a side. In other words the beam shifter prevents the light from the Ar^+ laser to reach the interaction chamber which helps to suppress the background light from Ar^+ laser. Two pin holes PH1 and PH2 defines the path (horizontally and vertically) of the laser beam. A focusing lens (focal length 1.5 m) is used to focus the laser beam in front of the light collectors. After passing through the interaction chambers the laser beam is reflected out of the interaction tube by mirror M5. The mechanical mount of the mirror M5 is properly grounded to avoid any deformation of the electric field lines.

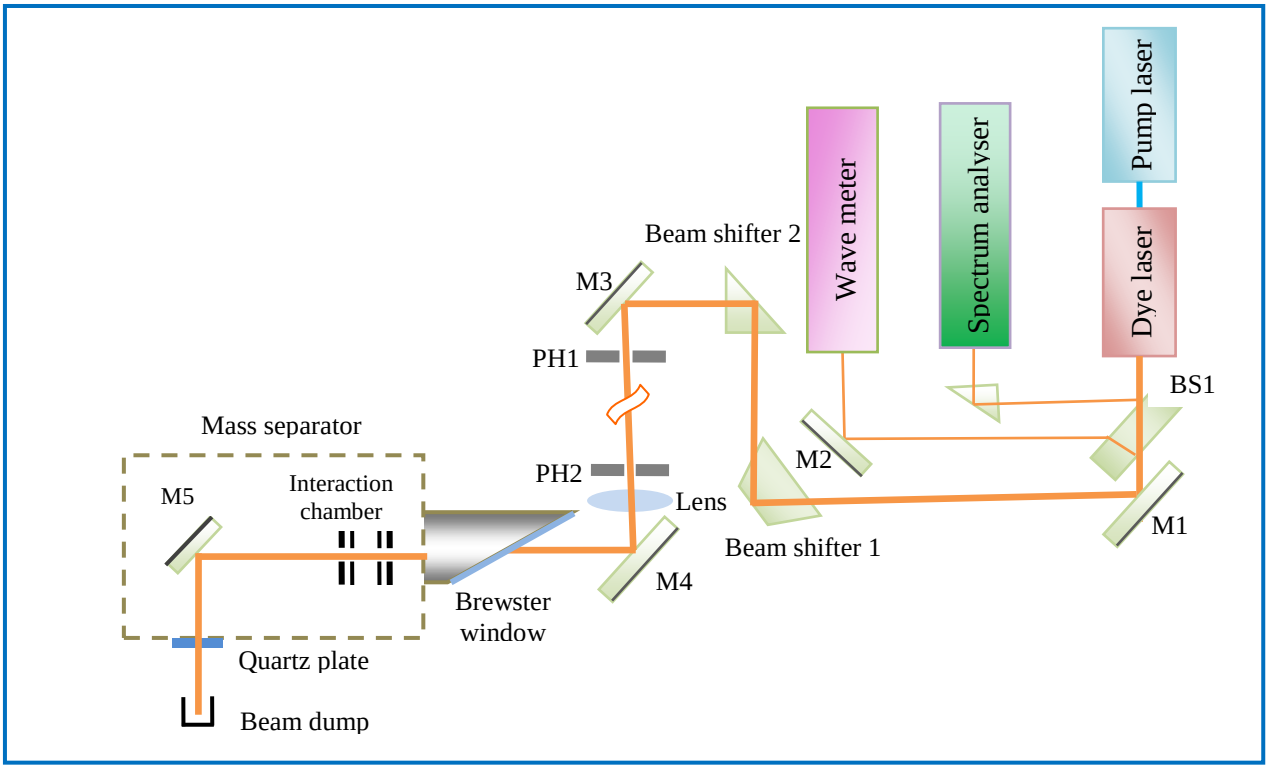

Figure 9.10: A layout of the optical system of the MARS-II. M: Mirror, BS: Beam splitter, PH: Pin hole.

9.2.3 **Wave Meter**

The optical layout of the wavemeter used for measurement of the dye laser frequency is shown in Figure 9.11. This wavemeter is based on a double Michelson interferometer and it measures the unknown wavelength in comparison to a known wavelength. When the wavemeter is perfectly aligned a readjusted light beam from He-Ne laser (the reference beam) and another beam from the dye laser (frequency to be measured) traversed the same path in the wavemeter. The working principle of the wavemeter is illustrated below:

The beam splitter BS1 divides the He-Ne laser beam into two parts. One part of the laser beam after transmitting through the beam splitter BS1 is reflected by beam splitter BS2 onto a photodiode PH1. The second part of the laser beam is reflected by the beam splitter BS1 towards a moveable triple prism. This beam after back reflection from triple prism when reaches at beam splitter BS2, a path difference between the two part of the He-Ne laser beam is introduced. The triple prism is moved back and forth with the help of an electromagnetic coil over a length of 12 cm. This oscillatory motion of triple prism causes a change in interference pattern on the photodiode PH1and the photodiode current increase and decrease following the interference

conditions. The dye laser beam also follows the same procedure but starting from beam splitter BS2 and ending at photodiode PH2.

The signals from the photodiodes are amplified, transformed to TTL pulses and are counted. The photodiode PH3, installed at region between BS2 and triple prism monitors the oscillatory motion of the triple prism. When the triple prism crosses the photodiode PH3 it sent a signal to the PH1 to start counting the pulses from interference of He-Ne laser. The counting cycle is stopped when the PH1 reaches 158023 pulses [225]. This number 15802.3 cm^{-1} is the wave number of the He-Ne laser. The wavelength of the dye laser in terms of the wave number (cm^{-1}) is giving by:

$$\sigma_{\text{dye laser}} = [(\text{number of pulses counted by photodiode PH2}) \times 0.1] \pm 0.1$$

The electronic unit "Wavemeter Controller WMC-01" performs the necessary calculations and displays the result on the screen. A push button on front panel of this electronic unit is used to mark the required laser frequency (in wave number) and the difference between actual wave number of the dye laser and the marked one is displayed on the electronic unit.

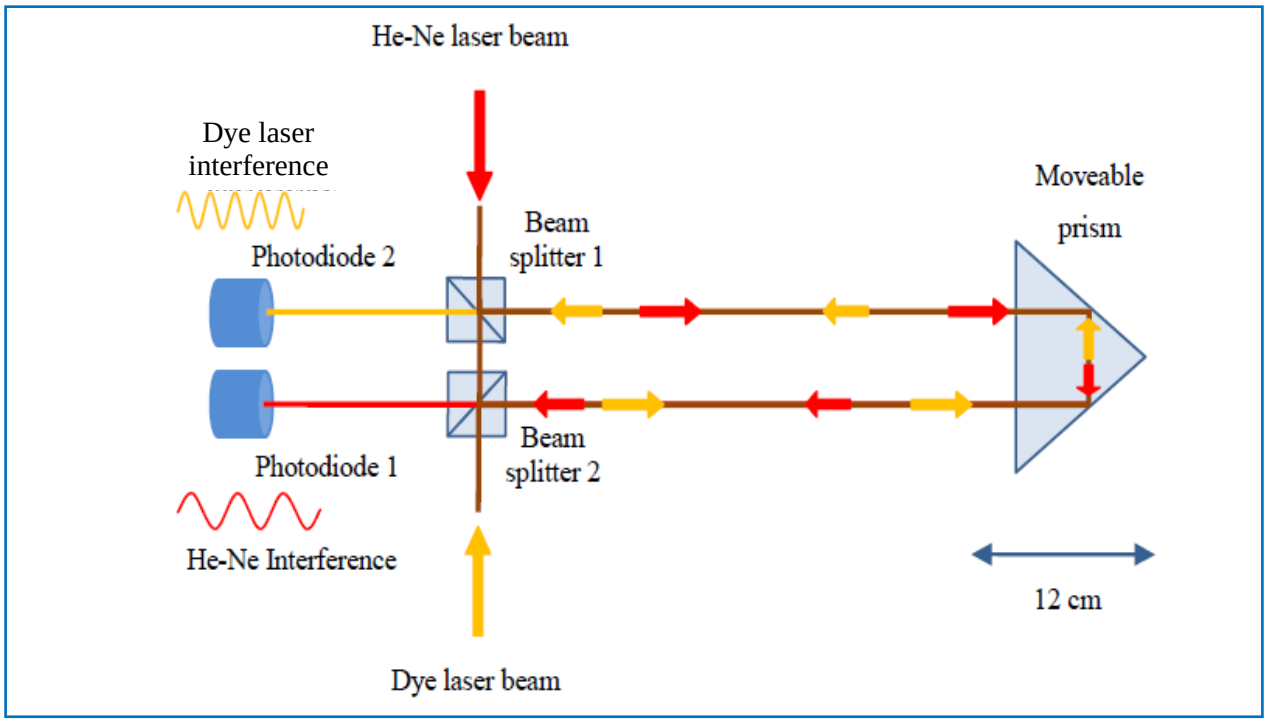

Figure 9.11: Layout of the double Michelson interferometer [162].

9.2.4 **Laser Frequency Stabilization**

As already discussed, in the present experimental setup of CLIBS the laser frequency is locked to the one of the hyperfine components of the ionic structure under investigation. This stabilization scheme was introduced by Hühnermann et al [182] and is based on the differential measurements of resonance conditions of ion velocity and laser frequency. This kind of stabilization technique is very suitable for fast ion beam laser experiments because it can simultaneously compensate any drift in the laser frequency as well as fluctuations in acceleration voltage and it minimizes the need for high stability of the acceleration voltage. As far as the laser frequency is locked to one of the hyperfine components several scans of the same structure can be averaged and the signal to noise ratio of poor recordings can be improved. This locking scheme is discussed below:

When the Doppler shifted ions velocity and laser frequency are in resonance by applying a particular post acceleration voltage U_o in the interaction chamber 1, a transition takes place and fluorescence light is detected. When the post acceleration voltage (U_{pa}) applied in interaction chamber 2 is such that $U_{pa} = U_o$, resonance conditions are fulfilled and fluorescence light is detected in the interaction chamber 2 as well and PMT produces maximum pulse rate. Now a square voltage with peak to peak amplitude equal to the line width of the hyperfine component (e.g. 6 V corresponding to ~ 50 MHz) is used to modulate the post-acceleration voltage. The modulation frequency used in this work is ~ 2 kHz. As shown in Figure 9.12 that the count rate (N1, N2) is same i.e. $\Delta N = N2 - N1 = 0$, for first one-half modulation period and for the next one-half modulation period. If $\Delta N \neq 0$, then a proper phase of the square wave is adjusted for $\Delta N = 0$ and this reference signal provided to a "forward-backward counter". If the resonance conditions of acceleration voltage U_o and laser frequency are changed (due to the fluctuations in acceleration voltage or due to the drift in laser frequency) then $\Delta N \neq 0$ (doted curve in figure 9.14). A difference in counts (N1 - N2) is converted into a DC voltage by a digital analog converter and corresponding signal is sent to the laser control unit. The laser control unit makes an adjustment according to the DC voltage and brings back the laser frequency into resonance again. The modulation of the post acceleration voltage, forward-backward counting and the conversion of difference in photon counts into DC voltage signal, is performed by a scan control unit (Scan u. Regeleinheit SRE-01 Gerät Nr. 01/03).

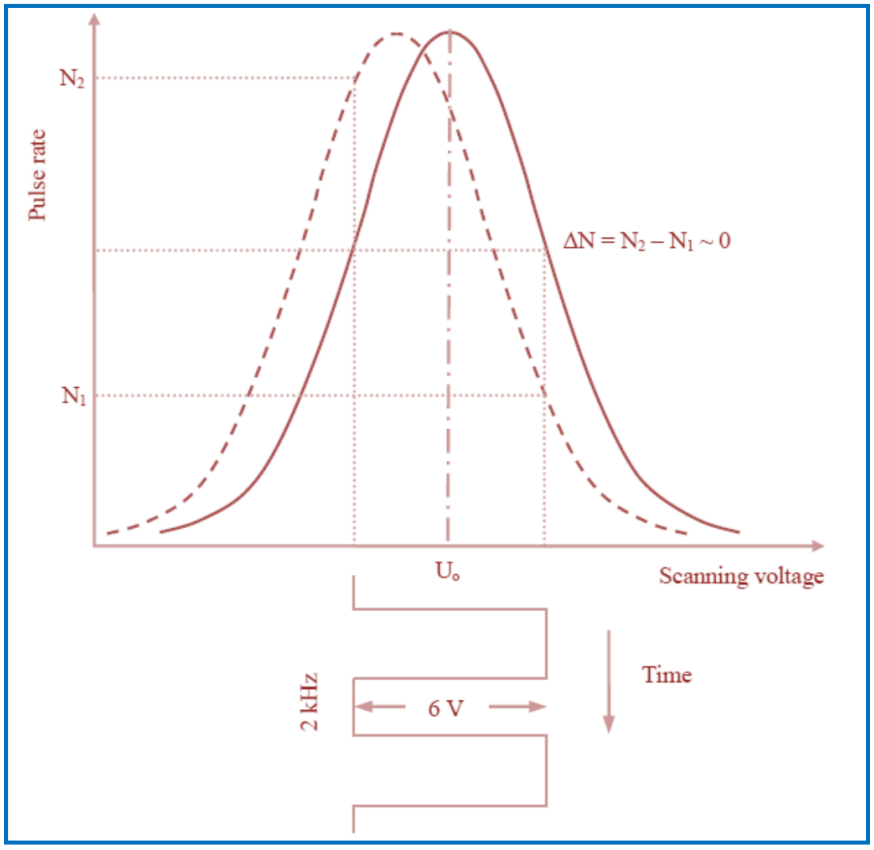

Figure 9.12: The laser frequency stabilization on a hyperfine component. The solid curve represents resonance of laser frequency with the hyperfine component at post acceleration voltage U_o and $\Delta N = 0$. The dashed curve represents a small change in voltage and gives different count rate i.e. $\Delta N \neq 0$.

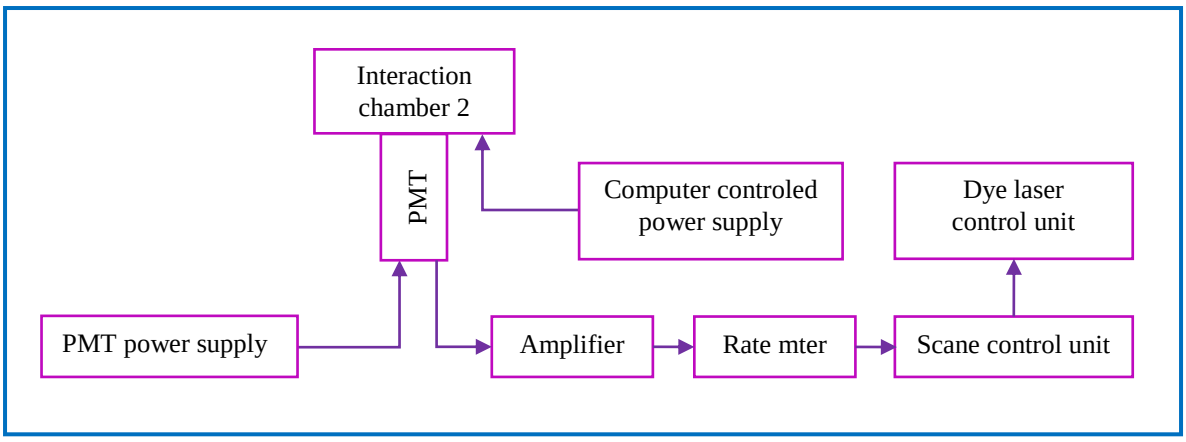

Figure 9.13: Circuit diagram of the laser frequency stabilization system.

The specifications of different electronic modules used for the laser frequency stabilization are given in Table 9.4.

Table 9.4: Electronic module for the laser frequency stabilization in the MARS-II

Electronic Module	**Specification/Model**
Photomultiplier tube (PMT)	Photonis: Dead on type: XP2020
PMT power supply	HCN: 35 M-3500: ± 3500 V, 10 mA
Photon counter	SSR Ins., Model: 1120 Amplifier-Discriminator
Rate meter	Wenzel-Elektronik: N-R-107
Scanning power supply	HCN: 35 M-3500: ± 3500 V, 10mA
Programmable power supply	TTi THURLBY THUNDER INSTRUMENTS Model: QPX1200
Scan control unit	Scan U. Regeleinheit: SRE-01 Gerät Nr. 01/03 (manufactured at Marburg University)

9.3 Computer Programs used for Recordings and Analysis

For recording and analysis of the hyperfine structure different computer programs are used. For the interfacing of the photon counter (Stanford Research System Inc. RS400) and the programmable power supply (TTi QPX 1200) with a computer, a computer program developed in lab view is used. This program is used to record the hyperfine structure in digital form in a computer. A program called "data viewer" developed by Prof. L. Windholz is used to view the recorded hyperfine structure. For the linearization of the recorded data points a computer program developed in "visual basic" is employed. As discussed in section 9.2.4 the laser frequency is locked to one of the components of the hyperfine structure under investigation and this helps to average many recordings of the same hyperfine structure to increase the signal to noise ratio. For the averaging of multiple files the commercially available software "Origin 8.5" is used. The line width and the hyperfine coupling constants are determined using a fit program called "Fitter" (discussed in section 7.2.3).

9.3.1 Interfacing of Programmable Power Supply and Photon Counter with a Computer

For recording the hyperfine structure the Doppler tuning is performed through a programmable high voltage power supply (HCN: 35 M-3500: ± 3500 V, 10mA) which is controlled by another computer controlled programmable power supply (TTi QPX1200: 0-10 V). Thus 0-10 V of QPX1200 corresponds to 0-3500 V of HCN: 35 M-3500 power supply and a scan of ~ 30 GHz is

possible across the interaction chambers. A photon counter (Stanford Research System Inc. RS400) is incorporated to count the current pulses from a head on photomultiplier tube (Photonis: XP2020). The power supply QPX1200 and the photon counter are interfaced with a computer using RS232 serial port by a computer program "Scan (SR400QPX1200)". The front panel of this program is shown in Figure 9.14. On front panel the parameters like start and stop voltage, number of scans, current scan, scan rate, step size and sequence are can be adjusted. The plot of the hyperfine structure is recorded scanning voltage versus photons counts. The execution of the program, the block diagram and the flow chart are given in appendix.

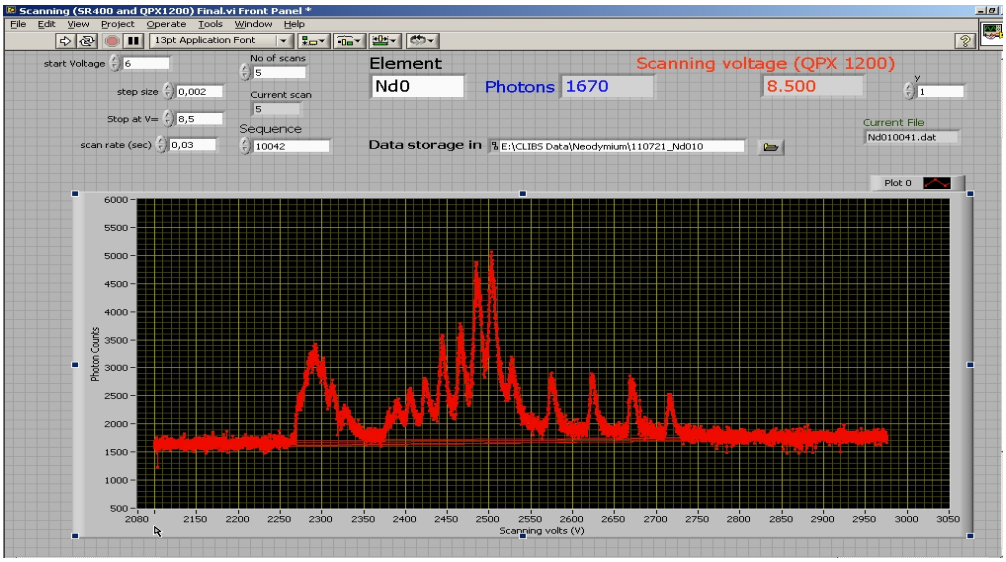

Figure 9.14: The front panel of the program "Scan (SR400QPX1200).The graph shows five recording of a ^{143}Nd II spectral line and all the hyperfine components are completely overlapped.

9.3.2 **The Data Viewer**

The software "data viewer" is employed for the graphical depiction of the hyperfine structure and for the correction of the background. For this program a specific format of 4 entries, separated by double space is essential i.e. for 4 measurable quantities.

X(space)(space)Y (space) (space)A(space) (space) B(space) (space)

Here X is the independent variable (i.e. scanning voltage) Y is the dependent variable (i.e. recoded intensity) and C and D are constants numbers.

For correction of background a linear or a spline function can be used and once maximum 50 data points can be selected to minimize the irregular background effect. An example is displayed in Figure 9.15 .

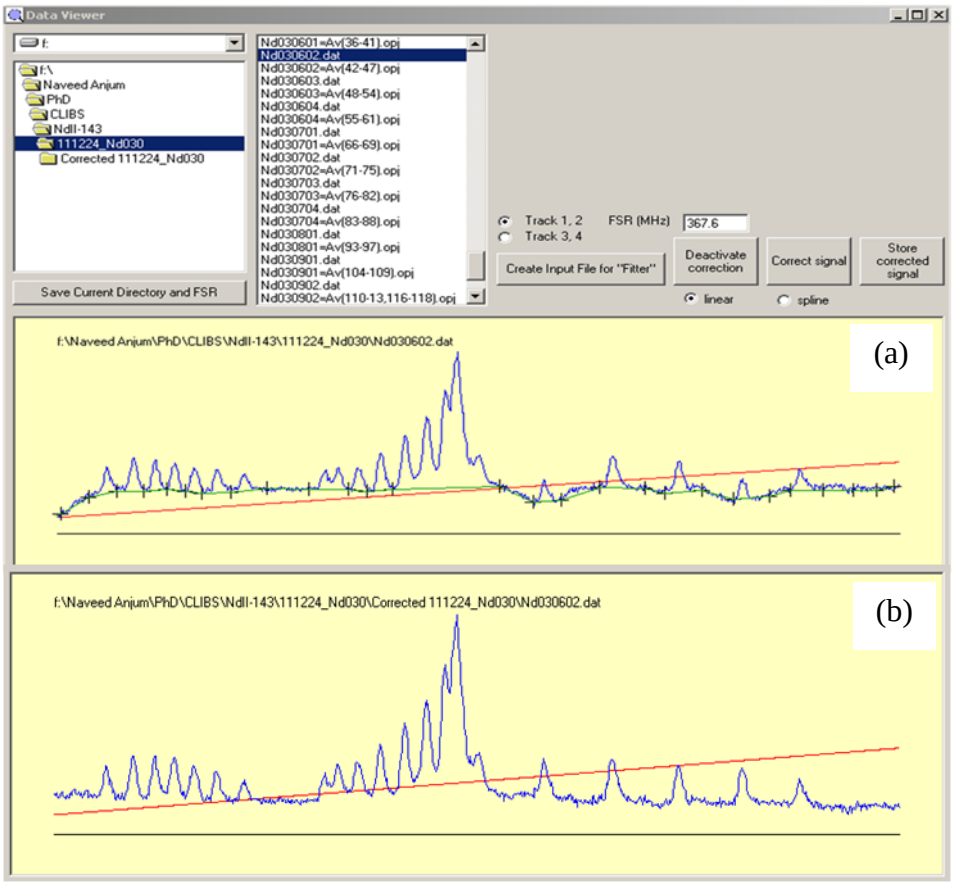

Figure 9.15:(a) A recording of a hyperfine structure with irregular background. (b) Same recording after background correction.

9.3.3 **Linearization Program "NdLinRel"**

The scanning is performed with equal voltage steps. According to equation 8.5 the frequency and the acceleration voltage are not linearly related. As discussed in section 7.2.3 for the fitting the rapid convergence to the best values is achieved if the data points are linear in frequency scale. The program "NdLinRel" is used for the linearization of the recorded data. The relation given in equation 9.1 [226] is used for the linearization and the relativistic effects are also taken into account.

$$\upsilon = \upsilon_L \ (1+\beta)/\sqrt{1-\beta^2}\,. \qquad 9.1$$

where

$$\beta = {}^{\upsilon}/_{c} = \sqrt{1-(1+b)^{-2}} \quad \text{and } b = \frac{eU}{mc^2}\,.$$

Here *U* is the acceleration voltage, *e* is the charge, *m* is the rest mass of the ion and *c* is the velocity of light in vacuum.

In the linearization process the new values 'X' of the independent variable (x-values) are calculated with an equal difference (sz) between the old values. At a specific point X_p, the new value of the Y_p (y-values) is calculated from the experimentally recorded x and y values by the addition of the weighted y-values within the range ± sz. The weights are greater for the points which are closer to X_p and vice versa. If 'ds' represents the weights, the values of Y_p at pint X_p can be determined applying the relation given below.

$$Y_p = \frac{\sum(y_i)(ds_i)}{\sum(ds_i)} \quad . \qquad \forall\, ds < sz \tag{9.2}$$

where

$$ds_i = \frac{sz - |Xp - x_i|}{sz} \quad . \tag{9.3}$$

The linearization is possible only if

$$sz \geq \max_{i=1\ to\ n} |x_i - x_{i-1}| \quad . \tag{9.4}$$

where n represents the total number of data points.

The algorithm and flow chart of the program "NdLinRel" is given in appendix.

9.4 **The Measurement of the Hyperfine Structure**

In this research work the hyperfine structures of spectral lines of ^{137}Ba II, ^{141}Pr II, ^{139}La II ^{143}Nd II and ^{145}Nd II have been investigated by the method of CLIBS. A beam of singly ionized ions is produced in a Johnson type surface ion source [221], filled with few milligrams of natural metal of the respective element. The ion beam is accelerated by 20 kV potential difference, shaped by an electrostatic lens system and mass-separated by an 80° magnet. An isotopically pure ion beam current of 10 - 20 nA is obtained. The ion beam passes through two interaction chambers where it is superposed with a counter propagating laser beam. The beam current is measured by a Faraday cup 4FR at the far end of mass-separator. The chamber pressure is kept in the range of 10^{-6} mbar.

9.4.1 **Recording of the Hyperfine Structure**

The laser frequency is adjusted with help of wavemeter to the Doppler shifted ($\Delta\sigma \approx$ -9.5 to -8.5 cm^{-1}, depending upon the element and the laser wavelength) centre of the gravity of the spectral transition under investigation. A voltage scan of 0 - 3.5 kV is carried out in the interaction chamber 1 and if the Doppler shifted laser transition frequency and the frequency of the ions are in resonance, the ions absorb light and the reemitted fluorescence light is led to photomultipliers tubes. Usually within the range of ± 0.5 cm^{-1} (measured on wavemeter) the resonance occurs and the fluorescence signal is observed.

The fluorescence signal is optimized by adjusting the ion beam and laser frequency. For locking the laser frequency on one of the hyperfine component the fluorescence signal is searched and optimized in the interaction chamber 2. As discussed in section 9.2.4 the laser frequency is locked to one of the components of the hyperfine structure under investigation. When the laser is locked on the hyperfine component, the hyperfine structure is recorded in interaction chamber 1 by applying the post-acceleration voltage. For the scanning of the post-acceleration voltage and for the recording of the hyperfine structure the program "Scan(SR400-QPX1200)" is used. A voltage step size of 0.002 V (or 0.003 V) on the programmable power supply TTi QPX1200 corresponds to the (0.002 ×3.5) = 0.7 V which is ~ 5.25 MHz in terms of frequency. The counting period is set to 0.003 seconds. The program "Scan(SR400-QPX1200)" store the data from the photon counter and the scanning voltage power supply (TTi QPX 1200) in a computer. Several recoding are made for hyperfine structure of one spectral line. To improve the signal to noise ratio 5-8 files are averaged to make one data file and at least 3 data files are used to calculate the statistical deviation of the hyperfine coupling constants of a hyperfine structure.

A layout of the scanning mechanism and recording of the hyperfine structure is shown in Figure 9.16 and the specifications of the electronic modules are given in Table 9.5.

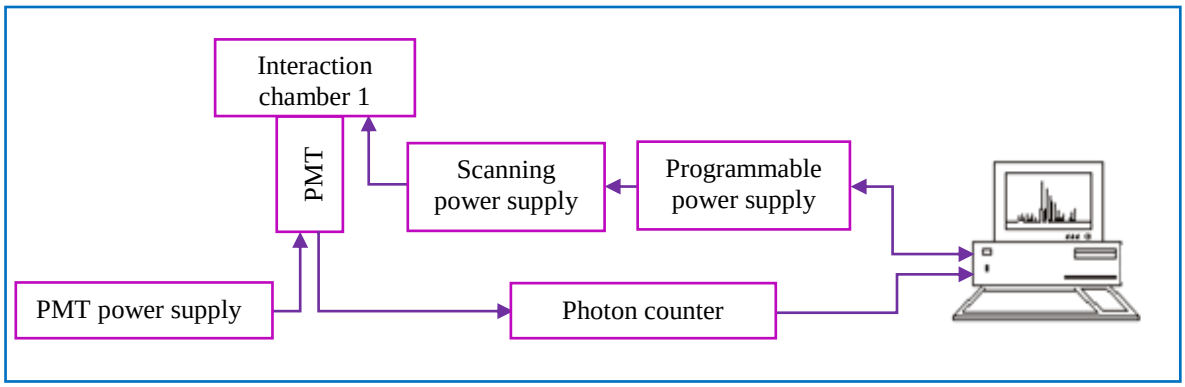

Figure 9.16: A layout of the scanning mechanism and recording of the hyperfine structure.

Table 9.5: Electronic module for the scanning and recording of the hyperfine structure.

Electronic Module	**Specification**
Photomultiplier tube (PMT)	Photonis: Head on type: XP2020 ,V = 2000V
Power supply for PMT	Heinzinger: Transisitor-Netzgerät HN 10-2000
Photon counter	Stanford Research System Inc. SR400
High voltage programmable power supply	HCN: 35 M-3500: ± 3500 V, 10mA
Computer controlled power supply	TTi QPX 1200: 60V, 50A

9.4.2 **Data Analysiss**

The recorded data files are viewed through the "data viewer" software. Good quality data files (in terms of signal to noise ratio, stabilization of laser frequency to hyperfine components and stability of ion source) are selected and if necessary the background irregularities are removed. To improve the signal to noise ratio 5-8 data files are averaged to make one data file using the software "Origin 8.5". The averaged files are linearized in frequency scale with sz (step size) = 6 MHz or 8 MHz depending upon scanning voltage step size. The linearized data files are curve fitted using "Fitter Program" to determine the magnetic dipole coupling constants A and electric quadrupole coupling constants B of the levels involved in the transitions.

9.5 **Lab Pictures**

For a realistic view some pictures of the experiment setup are added. The picture 1 and 2 are two different views of the ion source and electrostatic lens section. Picture 3 is of the 80° sector magnet and picture 4 shows two interaction chambers for the recording of the hyperfine structure and laser frequency stabilization. The two interaction tubes are shown in picture 5 and the complete laser set up is shown in picture 6.

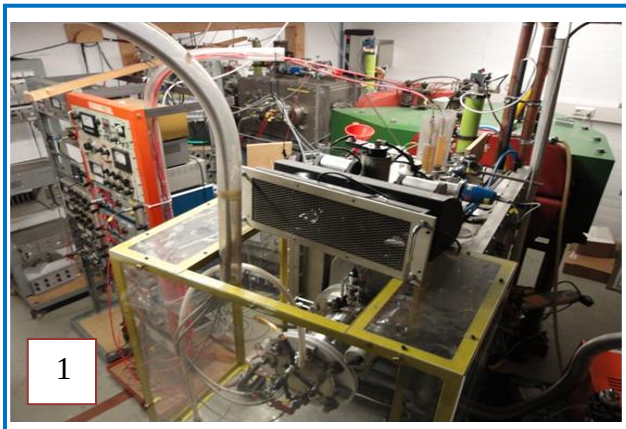

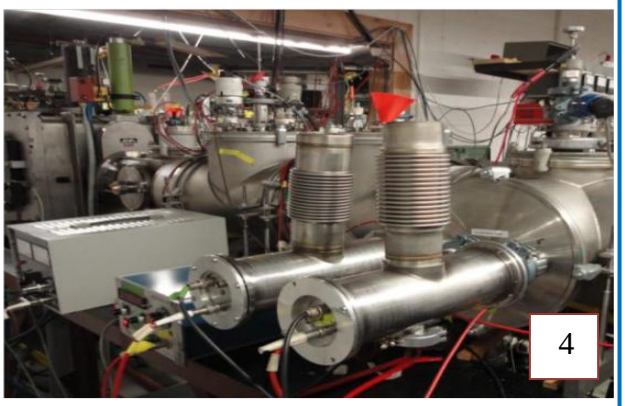

10 RESULTS AND DISCUSSION

The first part of the experimental investigations carried out in this work, concerning the study of the hyperfine structure of singly ionized praseodymium (Pr II) and the comparison of three different techniques of the laser spectroscopy, was presented in chapter 7. The second part is concerned with the readjustment and the control-check of the Marburg mass separator MARS-II, as it was shifted from the University of Marburg, Germany, to Graz University of Technology in 2002. The control-check is performed using a well known spectral line 5853.67 Å of the odd isotope of barium-137 (^{137}Ba II). In the third part the hyperfine structure of spectral lines of lanthanum (La II) is investigated. The fourth part is devoted to the investigation of the hyperfine structure of lines of two odd isotopes of singly ionized neodymium (^{143}Nd II and ^{145}Nd II) and the determination of the ratios of magnetic dipole constants, i.e A_{143}/A_{145}, and electric quadrupole constants B_{143}/B_{145} of the two odd isotopes of neodymium. The last three parts of this research project are discussed here. The high resolution technique of collinear laser ion beam spectroscopy (CLIBS) was used.

10.1 The Control-Check of MARS-II Using 5853.67 Å Spectral Line of ^{137}Ba II

The chemical element barium belongs to the group 2 of the periodic table and is the fifth element of this group. It has two electrons in its valence shell and its atomic number is Z = 56. Barium has six naturally occurring stable isotopes ^{132}Ba, ^{134}Ba, ^{135}Ba, ^{136}Ba, ^{137}Ba, and ^{138}Ba and one very long-lived radioisotope ^{130}Ba with a half life of ~ 2.2×10^{21} years. The natural abundance of ^{138}Ba is 71.7 % and for ^{137}Ba is 11.2 % and for all remaining isotopes the natural abundance is even less. The two odd isotopes have nuclear spin quantum number I = 3/2 while for the five even isotopes the nuclear spin quantum number is zero. A fine structure levels splits into a hyperfine structure only if the nuclear spin quantum number is non-zero. The electronic configuration of natural and singly ionized barium i.e. Ba I and Ba II are [Xe]$6s^2$ and [Xe]$6s^1$, respectively. Where Xe is a xenon core and has the configuration $1s^2\,2s^2\,2p^6\,3s^2\,3p^6\,3d^{10}\,4s^2 4p^6\,4d^{10}\,5s^2\,5p^6$.

The control-check of the mass separator MARS-II is performed using 5853.67 Å spectral line of ^{137}Ba II. Barium nitrate, $Ba(NO_3)_2$ in form of powder is used in the Johnson type surface ion source [221] for the production of an ion beam of ^{137}Ba. The melting point of the $Ba(NO_3)_2$ is low (592 °C) which helps to operate the ion source for an extended period of time at moderate heating power of nearly 200 Watt. The ion beam is accelerated by applying 20 kV potential difference, shaped by an electrostatic lens system and mass separated by an 80° magnet. After passing through several deflecting plates an isotopically pure and stable ^{137}Ba ion beam current of ~ 1 nA is achieved (measured behind the interaction chambers). The mass separated spectrum of barium observed at the beam scanner is shown in figure 10.1.

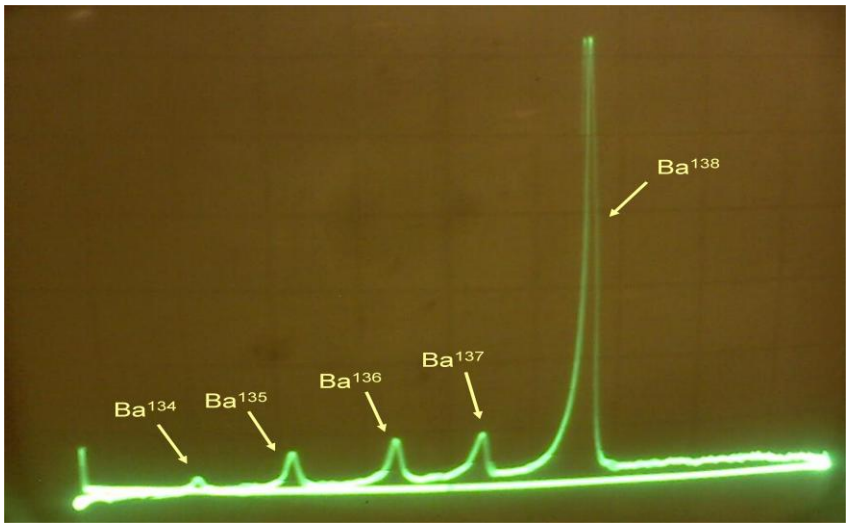

Figure 10.1: The mass separated spectrum of barium observed at the beam scanner.
The natural abundance of the isotopes can be estimated from the intensities of the peaks.

For the spectral transition $5d\ ^2D_{3/2} \rightarrow 6p\ ^2P°_{3/2}$, the metastable even-parity lower level ($\sigma = 4873.85\ cm^{-1}$) is excited to the odd-parity level ($\sigma = 21952.42\ cm^{-1}$) by absorbing the laser wavelength λ = 5853.67 Å. The level energies and wavelength values are taken from reference [227]. The LIF signal λ = 4554 Å is emitted when the upper level decays to the ground state ($6s\ ^2S_{1/2}$) as shown in figure 10.2. To compensate the Doppler shift ($\Delta\sigma \approx 9.6\ cm^{-1}$) for ^{137}Ba at acceleration potential of 20 kV the laser frequency is tuned to 17068.81 cm^{-1} and to tune the absorption frequency, voltage is applied to the interaction chambers which further accelerates the ions and subsequently changes the Doppler shift. To examine the entire hyperfine structure the post acceleration voltage is scanned over 200 V with a step size of 0.7 V (~5.3 MHz). The simulated and recorded structure is shown in figure 10.3(a) 10.3(b) respectively.

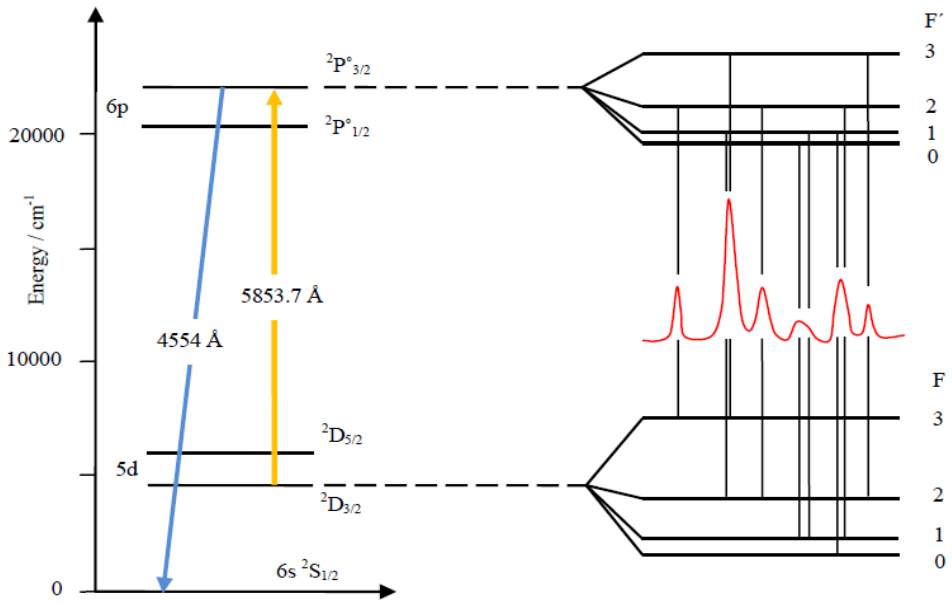

Figure 10.2:The energy level scheme and hyperfine structure of the ^{137}Ba II transition 5d $^2D_{3/2}$ → 6p $^2P°_{3/2}$ [162].

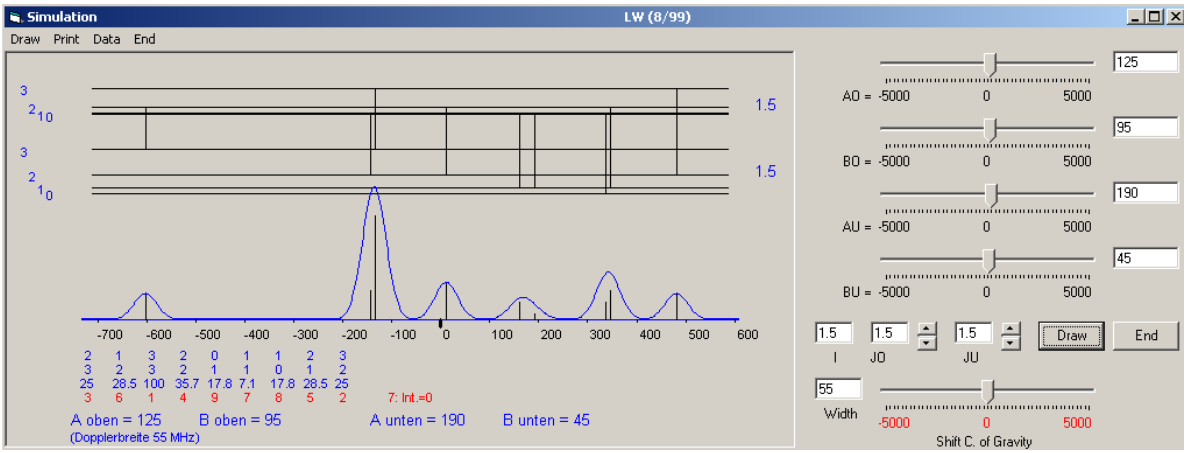

Figure 10.3: The simulated hyperfine structure of the ^{137}Ba II transition 5d $^2D_{3/2}$ → 6p $^2P°_{3/2}$.

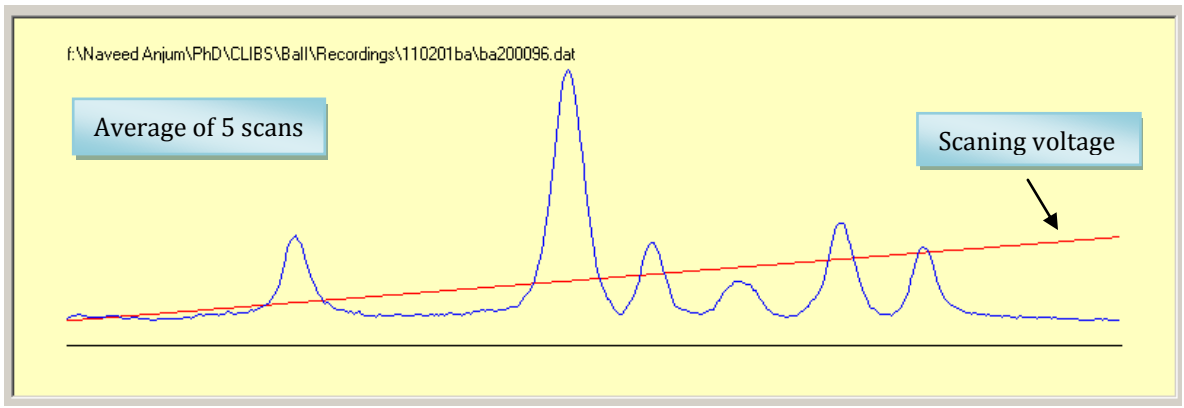

Figure 10.4: The recorded hyperfine structure of the ^{137}Ba II transition 5d $^2D_{3/2}$ → 6p $^2P°_{3/2}$.

For the transition under investigation the values of the total angular momentum quantum number J for both combing levels and the nuclear spin quantum number of I of ^{137}Ba are J = 3/2 , and I=3/2. According to the transition rules total 9 hyperfine components are possible for this spectral line. But in the recorded structure apparently only 6 peaks are visible. But a careful observation reveals that the remaining three components are also present but are strongly overlapped with other components. Three diagonal components belong to the $\Delta F = \Delta J = 0$ transition, three off-diagonal components to $\Delta F = +1$ and three off-diagonal components to $\Delta F = -1$. A fitter program [175] based on the least square method is used for curve fitting and to determine the hyperfine coupling constants of the combing levels. The best curve fitting of the spectral line is obtained when a mixed line profile (80% Gaussian and 20% Lorentzian) is used. The best fit situation of the recorded structure is shown in figure 10.5. A spectral line width of nearly 55 MHz is obtained for this transition. Our preliminary results were presented at 60th annual meeting of the Austrian Physical Society (OPG) 6 -10 Sep, 2010 Salzburg, Austria. For the preliminary investigations the dye laser was locked on the transmission peak of a confocal Fabry-Perot interferometer (free spectral range 150 MHz) but in the present work the laser is locked to one of the hyperfine components of the structure under investigation (the locking technique is discussed in chapter 9). This locking technique is exceptionally suitable for the accelerated ion beam experiments because it can simultaneously compensate any drift in the laser frequency as well as fluctuations in the acceleration voltage. This locking scheme enabled us to more accurately determine the hyperfine coupling constants and reduction of the Doppler broadening. The improved results of magnetic dipole constants A and electric quadrupole constant B are compared with theoretical results as well as with old measurements performed on MARS-II in Marburg and other literature values in table 10.1.

Table 10.1: Comparison of hyperfine structure of ^{137}Ba II transition $5d\ ^2D_{3/2} \rightarrow 6p\ ^2P°_{3/2}$

Measurement Method	A_{lower}	B_{lower}	A_{upper}	B_{upper}	Reference
CLIBS	190.1(5)	44.3(18)	126.5(5)	93.8(20)	This work
Theoretical	189.92	46.23	128.27	92.87	[228]
CLIBS	191.1(6)	46.8(20)	126.2(8)	95.8(15)	[24]
*CLIBS	189.7288(7)	44.5408(17)	127.1(6)	89.7(15)	[229]

*CLIBS applied with radio frequency spectroscopy.

The comparison of results reveal that the investigations carried out in this work are in excellent agreement with literature values, therefore it is concluded that the experimental setup of the MARS-II is working accurately and can be used for the spectroscopic investigation of the spectral lines of other elements.

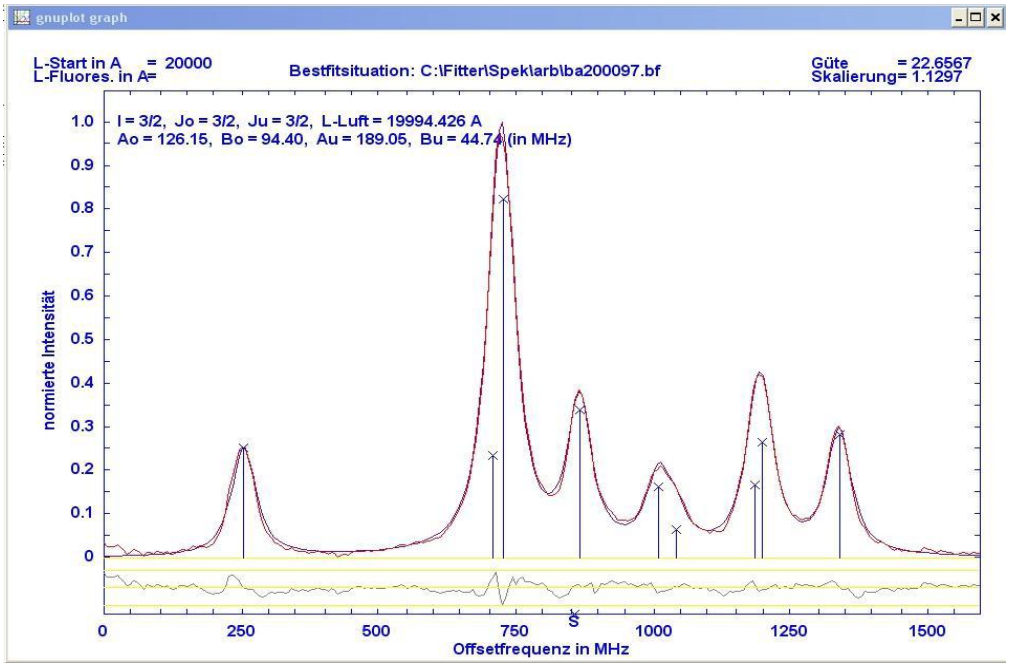

Figure 10.5: The best fit structure of the ^{137}Ba for transition $5d\ ^2D_{3/2} \rightarrow 6p\ ^2P°_{3/2}$.

Note: The control-check of MARS-II was carried out together with one of my colleagues.

10.2 Investigations of Hyperfine Structure of ^{139}La II Spectral Lines

Lanthanum (La) has two natural isotopes, a stable isotope ^{139}La and a radioactive isotope ^{138}La. The natural abundance of ^{139}La is 99.91% and that of ^{138}La is 0.01%. As the natural abundance of ^{138}La is extremely small so it cannot be observed here. The experimental investigations of the hyperfine structure of the spectral lines of the singly ionized odd isotope of lanthanum (^{139}La II) are presented in this section. In this part of work 10 spectral lines of ^{139}La II were investigated using the method of CLIBS. These investigations led us to determine the magnetic dipole coupling constant *A* and electric quadrupole coupling constants *B* of 12 fine structure energy levels. Out of these are 7 odd-parity upper levels and 5 are even-parity lower levels. The investigated spectral lines are given in Table 10.2 and the hyperfine coupling constants are compared with literature values and are summarized in Table 10.3 and Table 10.4. The recoded spectral line widths are in the range of 45 – 70 MHz.

Due to an odd number of protons Z = 57, the nuclear spin of all the isotopes of lanthanum is non-zero i.e. for ^{139}La, I = 7/2 and ^{138}La, I = 5. The presence of three electrons which can be excited causes the atomic spectra of La to be complex. In case of ^{139}La most of the spectral lines are well separated and can be recorded without the influence of the hyperfine components of neighboring spectral lines but occasionally the center of gravity of two or more spectral transition may lie very close to each other or even can overlap. In the second case the intensities of the overlapped hyperfine components are added but the hyperfine structures can be analyzed using the multi-lines fitting option in the fit program.

The hyperfine structures of few well separated single spectral lines are discussed in section 10.2.1 and the recording of the hyperfine structure of overlapping lines are presented section 10.2.2.

10.2.1.1 Hyperfine Structure of ^{139}La II Spectral Line 6126.07 Å

The recorded hyperfine structure of the ^{139}La II spectral line 6126.07 Å is shown in the Figure 10.6. In this transition ions in the lower level even-parity metastable state $\sigma = 10094.86\ \text{cm}^{-1}$ are excited to the odd-parity upper level $\sigma = 26414.01\ \text{cm}^{-1}$ and the transition takes place from J_u (J-value for lower level) = 2 to J_o (J-value for upper level) = 2. As the spin quantum number I for ^{139}La is 7/2 i.e. $I > J$, thus according to the transition rules there are 13 possible hyperfine components for this transition. The diagonal (stronger) components belongs to $\Delta J = \Delta F = 0$ and off-diagonal (weaker) components to $\Delta F = \pm 1$. In this transition all the components are clearly resolved except one diagonal component ($\Delta F = 0$) and one off-diagonal component ($\Delta F = -1$) are overlapped. The metastable level $\sigma = 10094.86\ \text{cm}^{-1}$ involved in this transition is the highest energy lower level that has been investigated for ^{139}La II during this work. The hyperfine structure level configuration of the spectral line 6126.07 Å is shown in Figure 10.7 and best fit situation is shown in Figure 10.8.

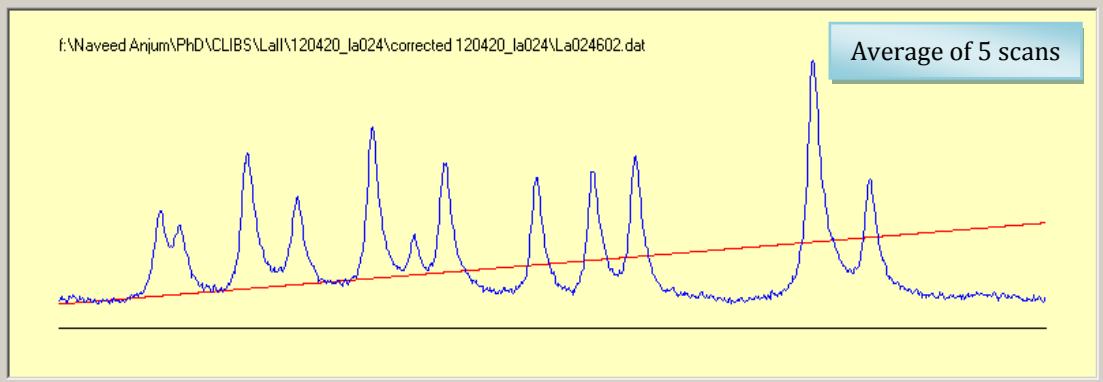

Figure 10.6: Experimentally recorded hyperfine structure of the spectral line 6126.07 Å.

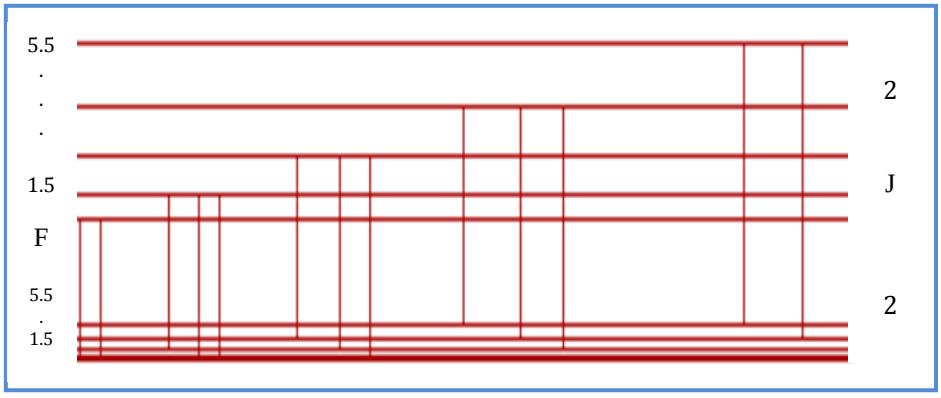

Figure 10.7: The hyperfine structure level configuration of the spectral line 6126.07 Å ().
$5d^2a\ ^1G_2 \rightarrow 5d6p\ x\ ^3F_2{}^0$

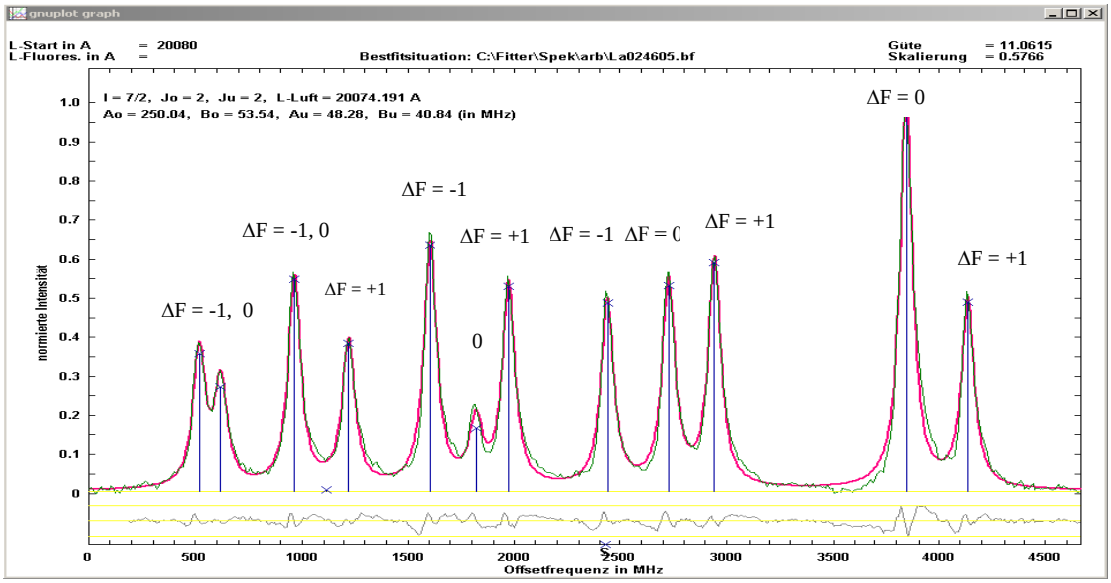

Figure 10.8: Best fit situation of the spectral line 6126.07 Å ($\sigma = 10094.86 \rightarrow 26414.01\ \mathrm{cm}^{-1}$).

10.2.1.2 Hyperfine Structure of ^{139}La II Spectral Line 5863.69 Å

The hyperfine structure of the ^{139}La II spectral line 5863.69 Å recorded through the method of CLIBS is shown in the Figure 10.9. In this transition ions in the even-parity lower level metastable state $5d^2$ a $^1G_4$ ($\sigma = 7473.31\ \mathrm{cm}^{-1}$) are excited to the odd-parity upper level 4f 5d y $^1F°_3$ ($\sigma = 24522.70\ \mathrm{cm}^{-1}$). This transition takes place from J_o = 3 to J_u = 4 and $I > J$, thus according to the transition rules there are 20 possible hyperfine components for this transition. A set of 7 hyperfine components belongs to diagonal transitions ($\Delta J = \Delta F$ = -1) and 7 off-diagonal hyperfine components for ΔF = 0 and 6 off-diagonal hyperfine components for ΔF = +1. All the diagonal components and most of the off-diagonal components are clearly resolved except 2 hyperfine components belonging to ΔF = 0 and ΔF = +1 are not separated. At the extreme right side of the structure (higher frequency side) the intensity of one of ΔF = +1 component is very low. The hyperfine structure level configuration and the best fit situation of the spectral line 5863.69 Å are shown in Figure 10.10 and Figure 10.11, respectively.

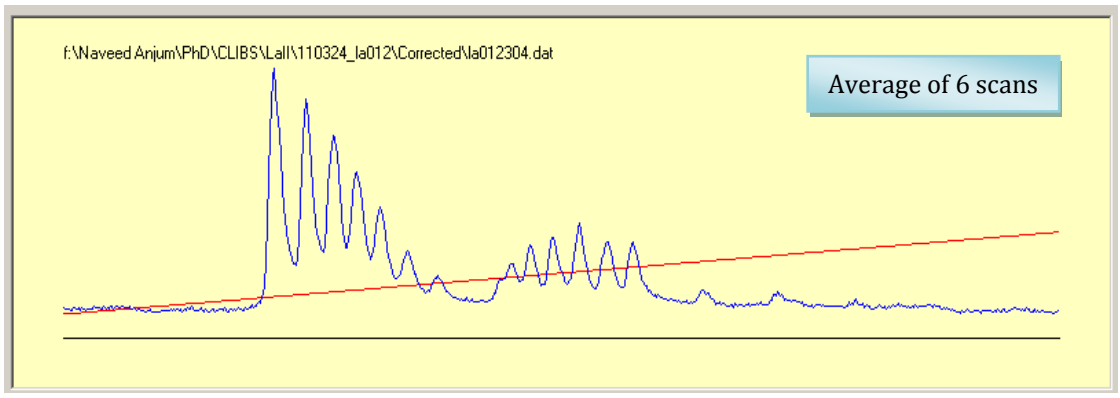

Figure 10.9: Experimentally recorded hyperfine structure of the spectral line 5863.69 Å.

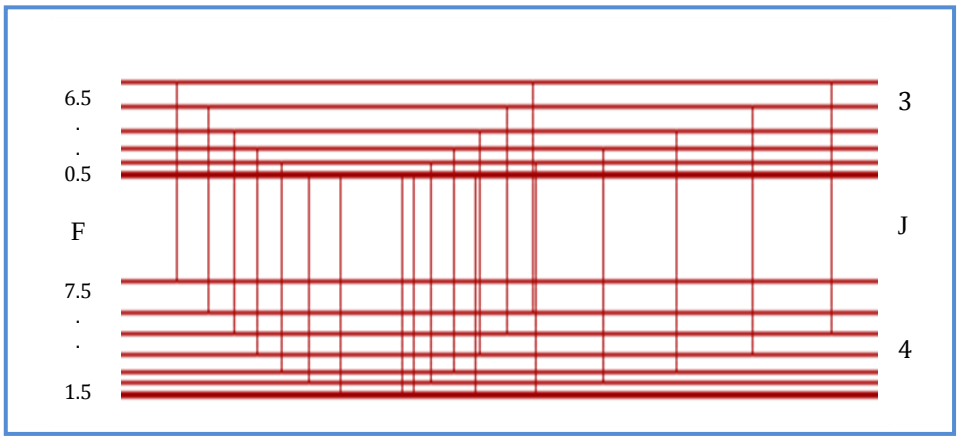

Figure 10.10: The hyperfine structure level configuration of the spectral line 5863.69 Å.
$5d^2a\,^1G_4 \rightarrow 4f\,5dy\,^1F^\circ_3$

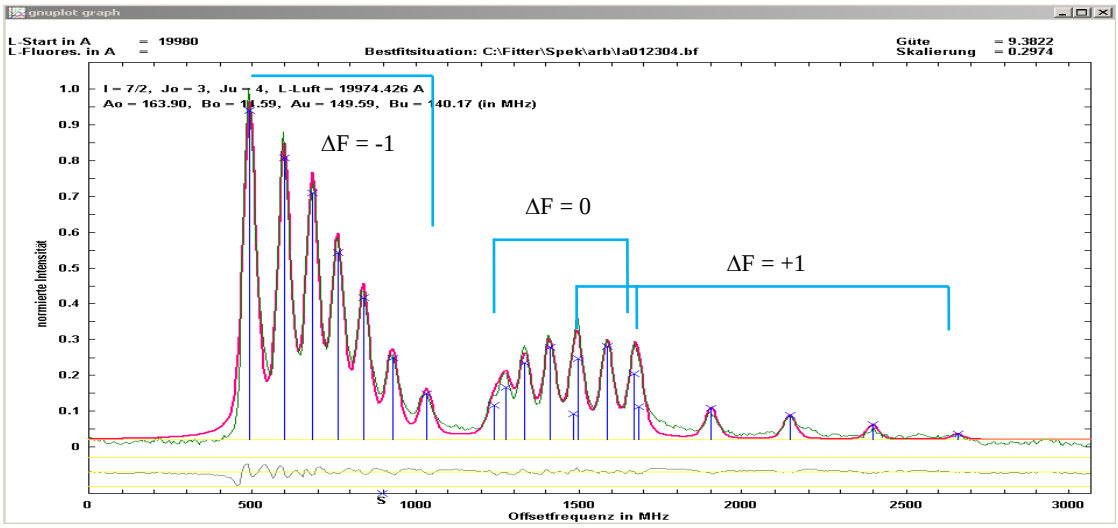

Figure 10.11: Best fit situation of the spectral line 5863.69 Å ($\sigma = 7473.31 \rightarrow 24522.70\ cm^{-1}$).

10.2.1.3 Hyperfine Structure of ^{139}La II Spectral Line 6100.37 Å

A hyperfine structure of the spectral line 6100.37 Å is shown in the Figure10.12. In this transition the even-parity lower level metastable state $5d^2\ a^3P_1$ ($\sigma = 5718.12\ cm^{-1}$) is excited by laser absorption to the odd-parity upper level 4f 5d z $^3D°_2$ ($\sigma = 22106.02\ cm^{-1}$). Here $J_o = 2$, $J_u = 1$ and $I > J$, thus total 9 hyperfine components are possible and 3 diagonal components belongs to $\Delta J = \Delta F = +1$ and 3 off-diagonal components belongs to each of $\Delta F = 0$ and $\Delta F = -1$. All diagonal as well off-diagonal components are clearly resolved. A set of 3 components starting from the extreme right side (higher frequency side) is the highest intensity component belonging to $\Delta F = +1$, next component (towards decreasing frequency) is $\Delta F = 0$ and the next one is $\Delta F = -1$. A similar pattern continues for 2nd and 3rd set but the intensities are decreasing for $\Delta F = +1$ and increasing for $\Delta F = 0$ and $\Delta F = -1$. The hyperfine structure level configuration and the best fit situation of the spectral line 6100.37 Å are shown in Figure 10.13and Figure 10.14, respectively.

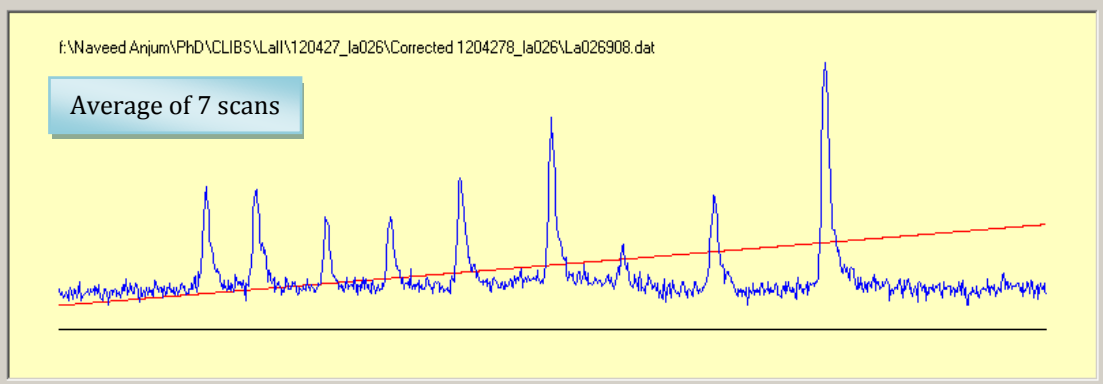

Figure10.12: Experimentally recorded hyperfine structure of the spectral line 6100.37 Å.

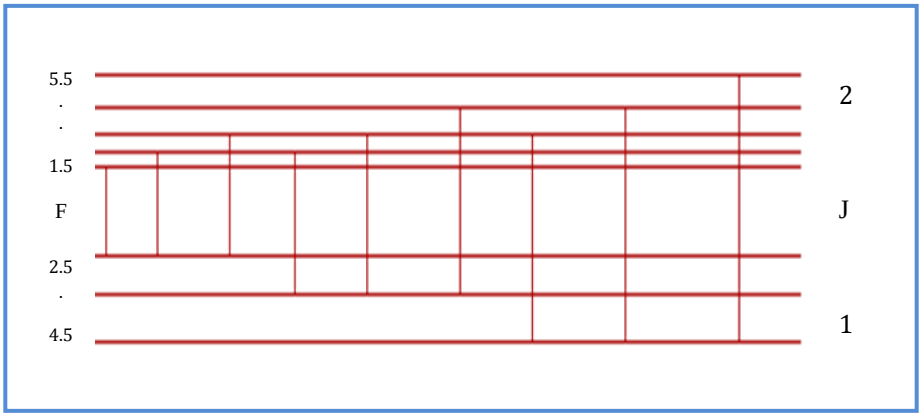

Figure 10.13: The hyperfine structure level configuration of the spectral line 6100.37 Å.
$5d^2\ a^3P_1 \rightarrow\ 4f\ 5d\ z\ ^3D°_2$

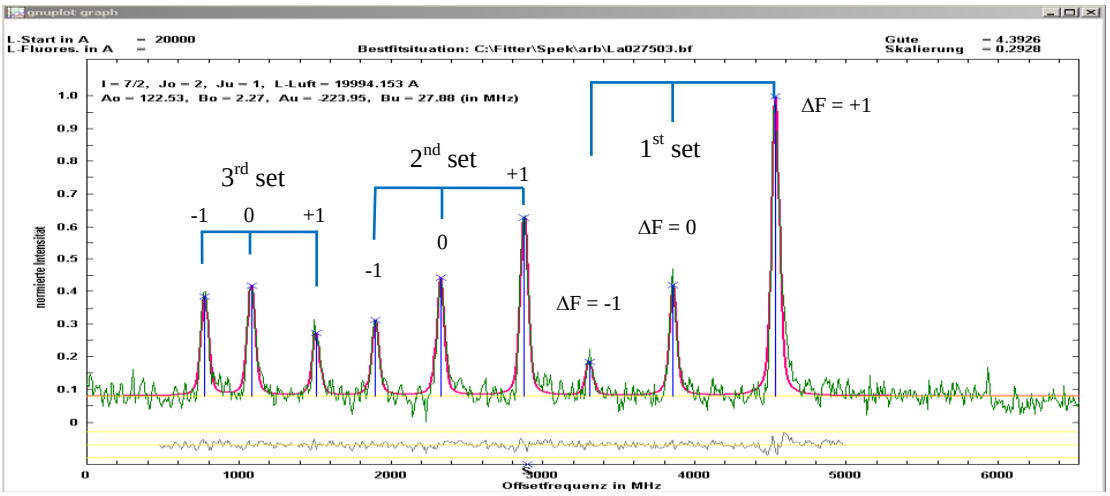

Figure 10.14: Best fit situation of the spectral line 6100.37 Å ($\sigma = 5718.12 \rightarrow 22106.02\ cm^{-1}$).

10.2.1.4 Hyperfine Structure of ^{139}La II Spectral Line 6174.17 Å

The experimentally recorded hyperfine structure of the spectral line 6174.17 Å is shown in Figure 10.15. This spectral line is a result of a transition from the even-parity lower level metastable state $5d^2$ a $^3P_0$ ($\sigma = 5249.70\ cm^{-1}$) to the odd-parity upper level 4f 5d z $^3D°_1$ ($\sigma = 21441.73\ cm^{-1}$). In this transition J_o = 1 to J_u = 0 and thus it has only 3 hyperfine components. One components belongs to each ΔF = +1, ΔF = 0 and ΔF = -1 transitions starting from highest to lowest frequency, respectively. As only 3 components exists so all the components are clearly resolved and are well separated. The metastable level $\sigma = 5249.70\ cm^{-1}$ involved in this transition is the lowest energy lower level that has been investigated for ^{139}La II during this work. This is also the only one and first spectral line for all elements (Pr II, ^{139}La II, ^{143}Na II, ^{145}Na II and ^{137}Ba II) investigated by our group using CLIBS method in which the lower level involved in the transition has *J*-value zero. The hyperfine structure level configuration and the best fit situation of the spectral line 6174.17 Å are shown in Figure 10.17 and Figure 10.17, respectively.

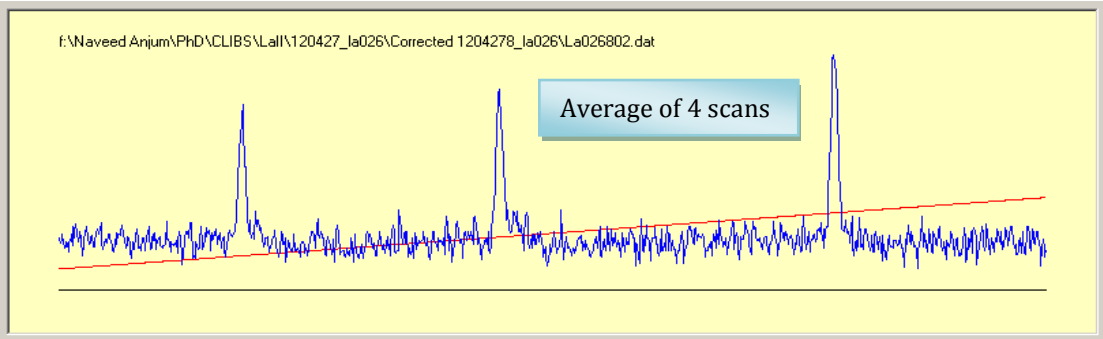

Figure 10.15: Experimentally recorded hyperfine structure of the spectral line 6174.17 Å.

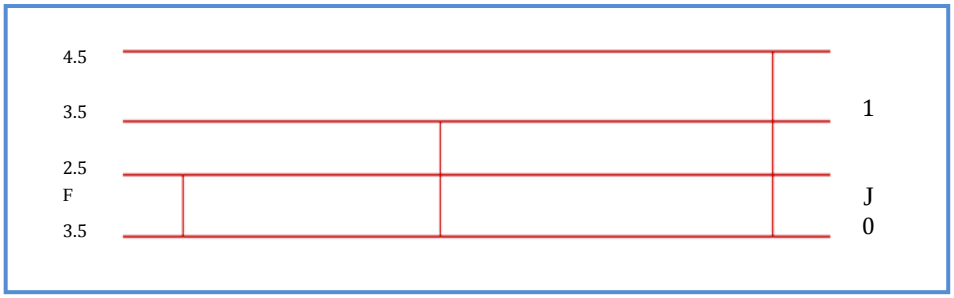

Figure 10.16: The hyperfine structure level configuration of the spectral line 6174.17 Å.
$5d^2\ a\ ^3P_0 \rightarrow 4f\ 5d\ z\ ^3D°_1$

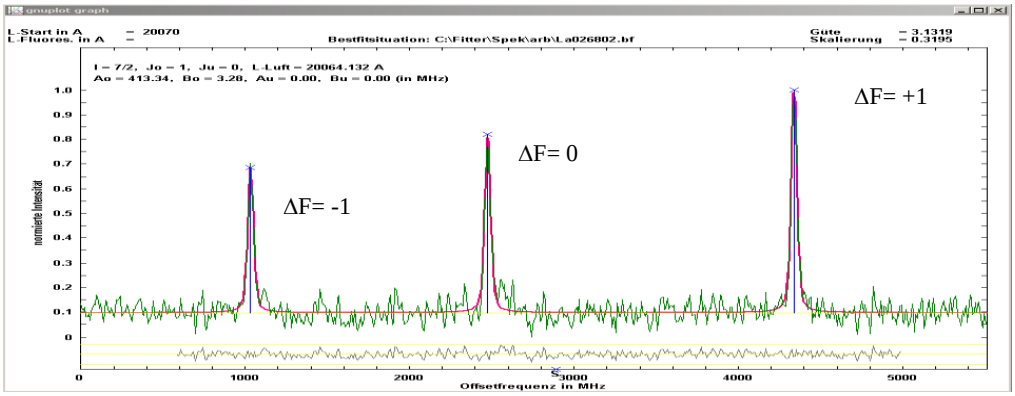

Figure 10.17: Best fit situation of the spectral line 6174.17 Å ($\sigma = 5249.70 \rightarrow 21441.73\ cm^{-1}$).

10.2.2 A Blend of Two Hyperfine Structures of ^{139}La II Spectra Lines in the Wavelength Region 6296.06 Å

A blend situation of two hyperfine structures of ^{139}La II recorded in a single scan in the wavelength region 6296.06 Å is shown in Figure 10.18. The structure on the lower frequency side (structure-1) is a result of a transition from the even-parity lower metastable state 5d6s b^1D_2 ($\sigma = 10094.86\ cm^{-1}$) to the odd-parity metastable state 5d6p $y^3D°_1$ ($\sigma = 25973.37\ cm^{-1}$) and

the structure on the higher frequency side (structure-2) is excited from the even-parity metastable state $5d^2\ a^3P_2$ ($\sigma = 6227.42\ cm^{-1}$) to the odd-parity upper metastable state $4f5d\ z^3D°_1$ ($\sigma = 22106.02\ cm^{-1}$). The center of gravity (cg) of two structures involved in these transitions are ~ 0.12 cm^{-1} apart and most of the hyperfine components of both structures are well resolved except at the center where the two structures are overlapped. The transition probability of structure-1 is higher than that of structure-2 and is obvious from the intensities of the spectral lines. All 9 hyperfine components of structure-1 are clearly resolved and are distributed in 3 sets and each set contains one component for each transitions i.e. $\Delta F = +1$, $\Delta F = 0$ and $\Delta F = -1$ (from higher to lower frequency). All the 13 components of structure-2 are also resolved but only 10 of them are visible in the recorded and fitted structure. The remaining 3 components are buried under the 1st set of components of structure-1. Due to this overlapping of the hyperfine components the structures are called as blended structures. These structures are analyzed using two lines fitting in the fitter program. Such closely spaced structures are very useful for the accurate determination of difference of centre of gravities (Δcg) of the structures involved. The hyperfine structure level configuration and the best fit situation of the blend structure in the wavelength region 6296.06 Å are shown in Figure 10.19 and Figure 10.20, respectively.

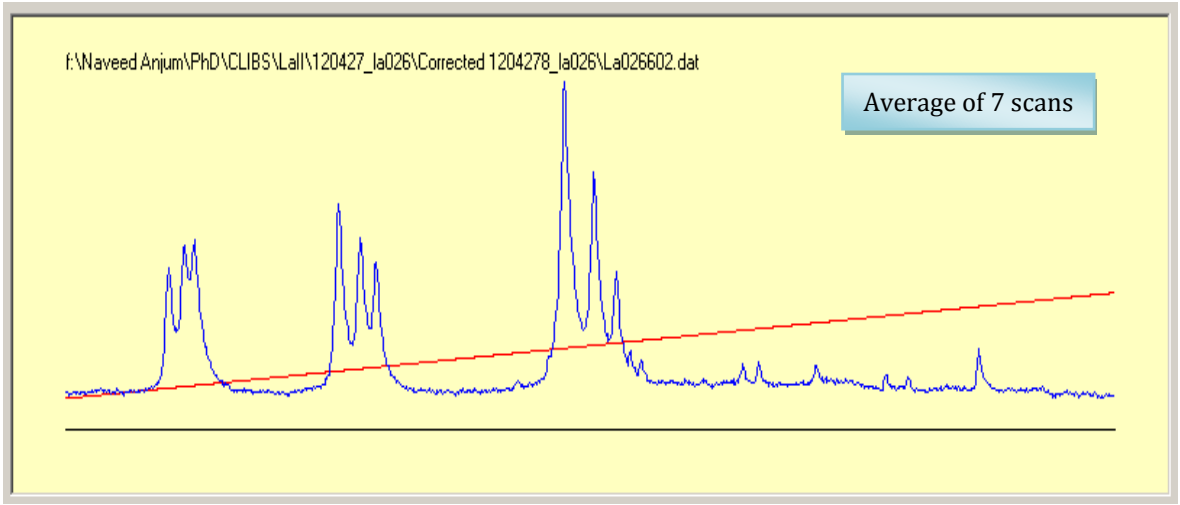

Figure 10.18: Experimentally recorded blend structure of the ^{139}La II in wavelength region 6296.06 Å.

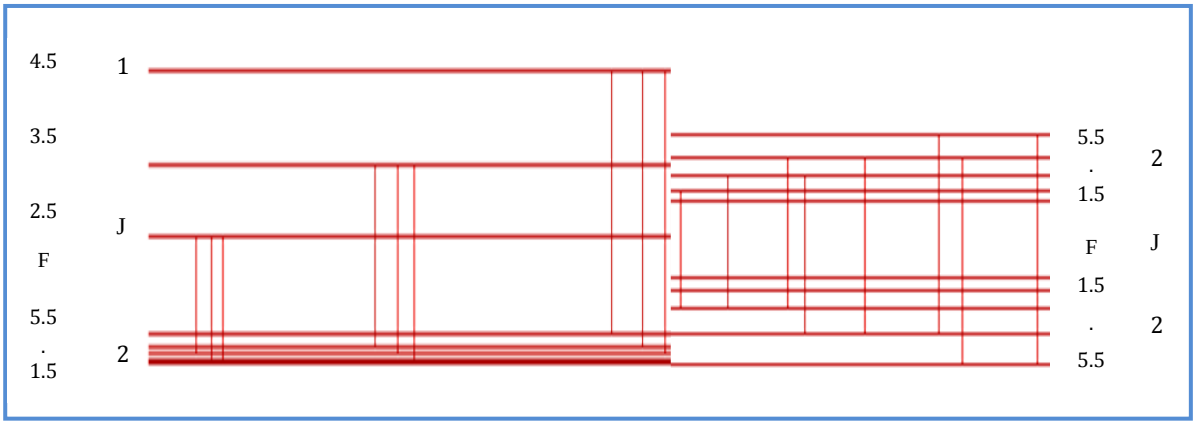

Figure 10.19: The hyperfine structure level configuration of a blend in wavelength region 6296.06 Å.

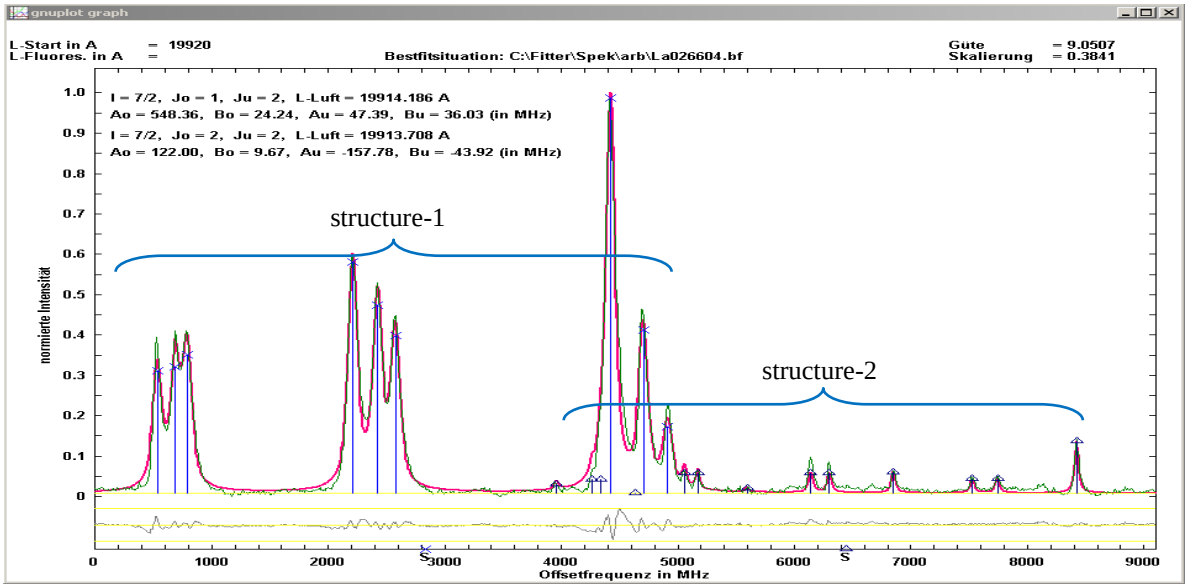

Figure 10.20: Best fit situation of blend structure of the ^{139}La II in wavelength region 6296.06 Å.

10.3 **Investigations of Hyperfine Structure of Spectral Lines of Two Odd Isotopes of Neodymium**

Neodymium (Nd) is a mixture of five naturally occurring stable isotopes, ^{142}Nd, ^{143}Nd, ^{145}Nd, ^{146}Nd and ^{148}Nd and two radioisotopes, ^{144}Nd and ^{150}Nd. The natural abundance of naturally occurring isotopes according to increasing mass is 27.2%, 12.2%, 8.3% , 17.2% and 5.7% while the abundance of two radioisotopes is 23.8% and 5.6%, respectively [52]. Up to now thirty- three radioisotopes of neodymium have been characterized. The half-life of the two naturally occurring radioisotopes are 2.29×10^{15} years for ^{144}Nd and for ^{150}Nd 7×10^{18} years. The half-lives of all the

remaining radioactive isotopes are less than 11 days and the majority of them have half-lives less than 70 seconds.

The ground state configuration of Nd II it is (Xe) $4f^3(^5I_4)\ 4f^4\,6s\ ^6I_{7/2}$ where Xe is the xenon core. Due to even number of protons Z = 60 only two odd isotopes (^{143}Nd and ^{145}Nd) have nuclear spin quantum number I = 7/2 while for the five even isotopes the nuclear spin quantum number is zero. Therefore hyperfine splitting of only odd isotopes i.e. ^{143}Na and ^{145}Na exists. The presence of six electrons in valence shell which can take part in interactions, due to open 4*f* shell configuration and occurrence of seven stable isotopes the spectrum of neodymium is tremendously complex with very large number of lines. The low natural abundance of ^{143}Nd and ^{145}Nd forced us to use high heating power (~ 400 Watt) of the ion source which not only unstabilized the ions beam but also decreased the working time of ion source from more than 5 hours to less than 1 hour before melting/breaking of the ionizer tube in ion source. For the investigation of Nd spectral lines nearly 150 times the ionizer tube in ion source was changed and a new filling of the ion source was made. It takes at least 7-8 hours for one preparation of the ion source. An extra slit just before beam scanner was inserted in MARS-II to get rid of traces of adjacent even isotopes. An isotopically pure ion beam current of only 10-20 nA was obtained for ^{143}Nd II and 8-12 nA for ^{145}Nd II. Due to the very small number of ions available for the experiment only high intensity spectral lines are investigated.

The experimental investigations of the hyperfine structure of the spectral line of singly ionized neodymium-143 (^{143}Nd II) are presented in this section. In this part of work 87 spectral lines of ^{143}Nd II are investigated using the method of CLIBS. These investigations led us to determine the magnetic dipole coupling constant *A* and electric quadrupole coupling constants *B* of 82 fine structure energy levels of ^{143}Nd II which resulted in 54 odd-parity upper levels and 28 even-parity lower levels. Like ^{139}La II few blend structures of ^{143}Nd II are also investigated during these measurements. The recoded spectral line widths are in the range of 45 – 75 MHz.

Few selected single line and multiline spectral lines of 143Nd II are discussed in section 10.3.1 and are summarized in Table 10.5 For 145Nd II few investigated spectral lines are presented in section 10.3.2 and are given in Table 10.8. The hyperfine coupling constants are compared with the literature values (wherever available) and for 143Nd II are summarized in Table 10.6an Table 10.7 and for 145Nd II in Table 10.9 and Table 10.10.

10.3.1.1 Hyperfine Structure of ^{143}Nd II Spectral Line 5706.20 Å

A selected hyperfine structure of the ^{143}Nd II at laser wavelength λ_{air} = 5706.20 Å is shown in Figure 10.21. In this hyperfine structure the ions being in the even-parity metastable state $4f^4(^5I)$ 5d $^6I_{7/2}$ ($\sigma = 7524.74\ cm^{-1}$) are excited to the odd-parity state $4f^4$ (^5I) 6p $^6I^\circ_{7/2}$ ($\sigma = 25044.68\ cm^{-1}$). Here I and J are equal to 7/2, thus the total hyperfine components for this structure are 21. In this transition the seven diagonal components with $\Delta F = 0$ are the prominent ones and most of them are clearly resolved. At the extreme left of the structure (lower frequency side) apparently only 4 out of 7 hyperfine components belonging to transitions ΔF = +1 are visible. But a more careful observation reveals that the other three components are also present but are strongly overlapped. In this part of the hyperfine pattern the component 7 – 6 (F_{upper} - F_{lower}) is well resolved while the components 6 – 5 and 1 – 0, 5 – 4 and 2 – 1, 4 – 3 and 3 – 2 are almost overlapped. The other group of hyperfine components belonging to ΔF = -1 appears on the right side of the main diagonal hyperfine components. Four hyperfine components are clearly resolved while the remaining 3 components are coincident with 3 strong hyperfine components having ΔF = 0.

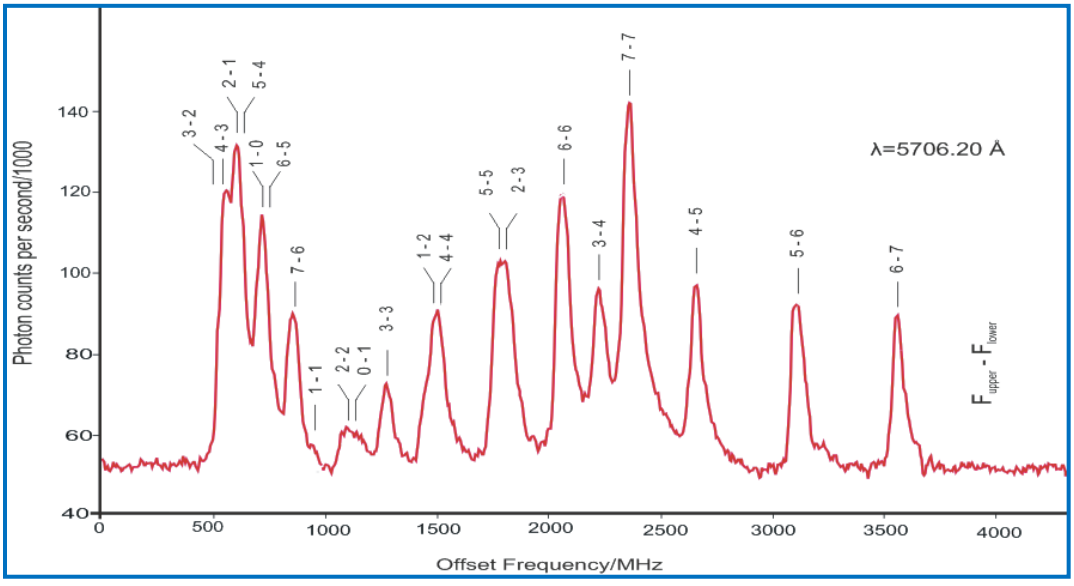

Figure 10.21: Hyperfine structure of the ^{143}Nd II excited from even-parity metastable state $4f^4(^5I)$ 5d $^6I_{7/2}$ ($\sigma = 7524.74\ cm^{-1}$) to the odd-parity state $4f^4$ (^5I) 6p $^6I^\circ_{7/2}$ ($\sigma = 25044.68\ cm^{-1}$)

Experimentally recorded hyperfine structure of the spectral line 5706.20 Å is given in Figure 10.22 and the best fit situation is given in Figure 10.23.

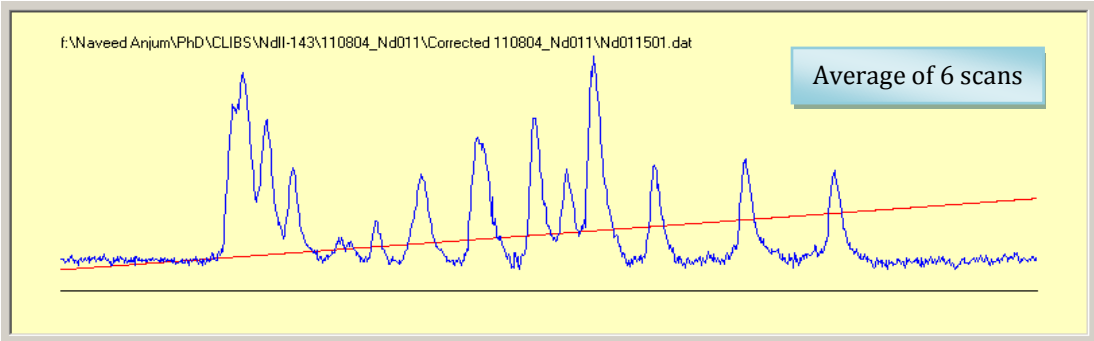

Figure 10.22: Experimentally recorded hyperfine structure of the spectral line 5706.20 Å.

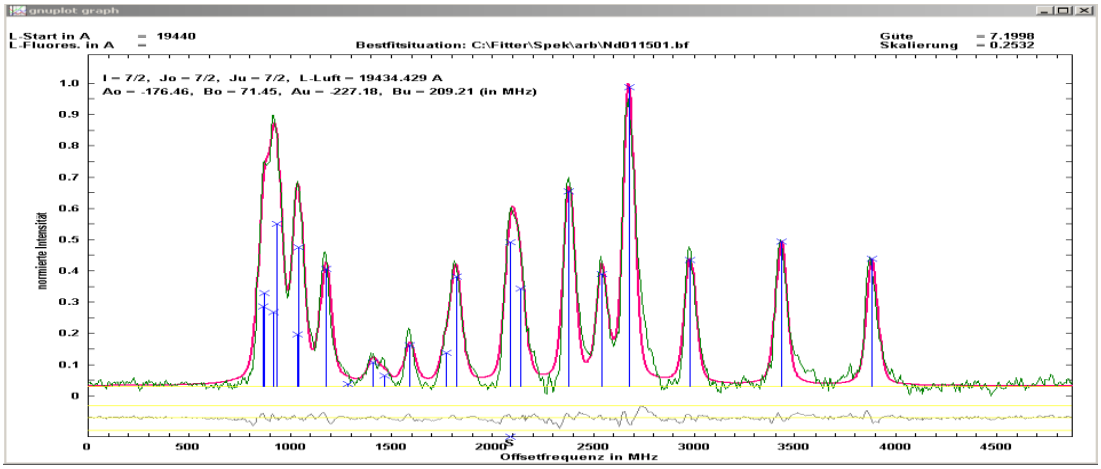

Figure 10.23: Best fit situation of the spectral line 5706.20 Å (σ = 7524.74 → 25044.68 cm^{-1}).

10.3.1.2 Hyperfine Structure of ^{143}Nd II Spectral Line 5823.91 Å

The hyperfine structure of the spectral line 5823.91 Å is shown in Figure 10.24. This hyperfine structure belongs to an excitation from the metastable lower level $4f^4$ (^{5}I) 5d $^6K_{9/2}$ (σ = 6005.27 cm^{-1}) to the odd-parity upper level $X^{\circ}_{9/2}$ (σ = 23171.11 cm^{-1}). The symbol "X" used for the level designation indicates that term symbol is unknown. Here the configuration and multiplicity of the upper level are unknown, however, its *J*-value is known. According to the transition rules this structure has altogether 22 hyperfine components, 2 out of the 8 diagonal hyperfine components ($\Delta F = \Delta J = 0$) are present on the two extreme sides of the structure. One of the off-diagonal hyperfine component for transition 7 – 8 (ΔF = -1) is adjacent to diagonal hyperfine component for transition 8 – 8 (ΔF = 0) and one off-diagonal hyperfine component for transition 2 – 1 (ΔF = +1) is adjacent to diagonal hyperfine component for transition 1 – 1 (ΔF = 0). The remaining 18 hyperfine components are distributed in 6 groups such that each diagonal hyperfine component is surrounded by two off-diagonal hyperfine components belonging to the

one of off-diagonal components (ΔF = ±1). This is the only second known transition (up to now) in which the involved upper level ($\sigma = 23171.11$ cm^{-1}) has a positive value of magnetic dipole interaction constant *A*. In all other even or odd levels, except the odd-parity level $X^{\circ}_{11/2}$ ($\sigma = 25561.19$ cm^{-1} [33], the *A*-values are always negative for ^{143}Nd II. The experimentally recorded hyperfine structure is shown in Figure 10.25 and the best fit situation is given in Figure 10.26.

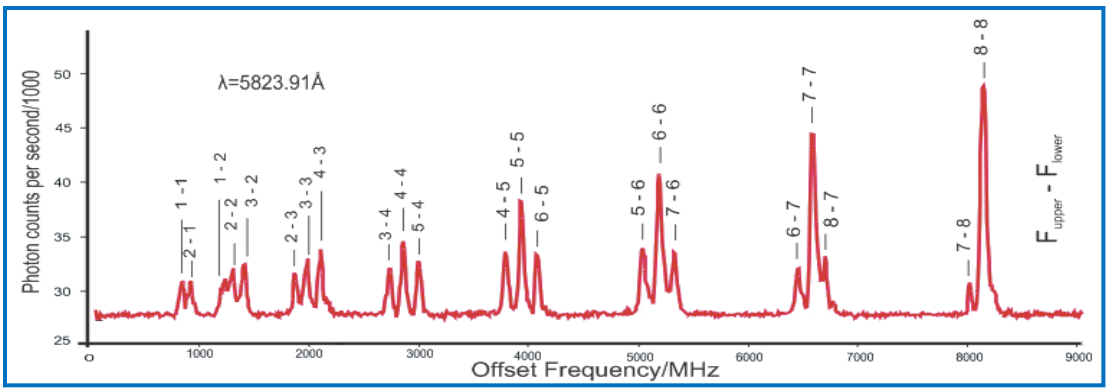

Figure 10.24: Hyperfine structure of the ^{143}Nd II excited from even-parity metastable state $4f^4(^5I)\ 5d\ ^6K_{9/2}$ (σ = 6005.27 cm^{-1}) to the odd-parity state $X^{\circ}_{7/2}$ (σ = 23171.11 cm^{-1})

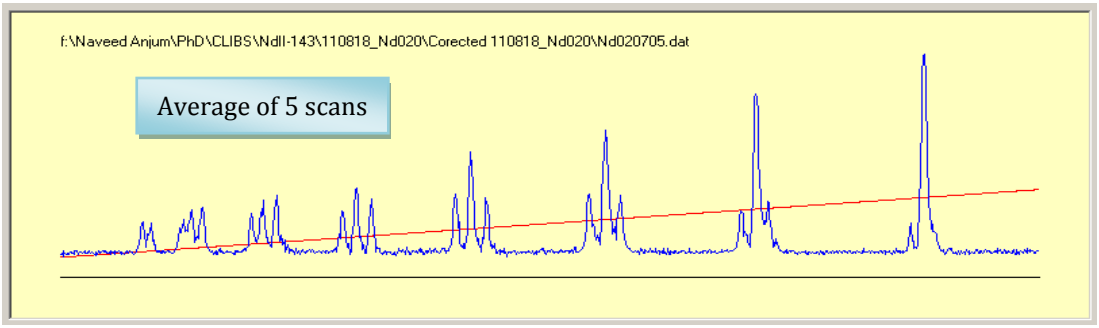

Figure 10.25: Experimentally recorded hyperfine structure of the spectral line 5823.91 Å.

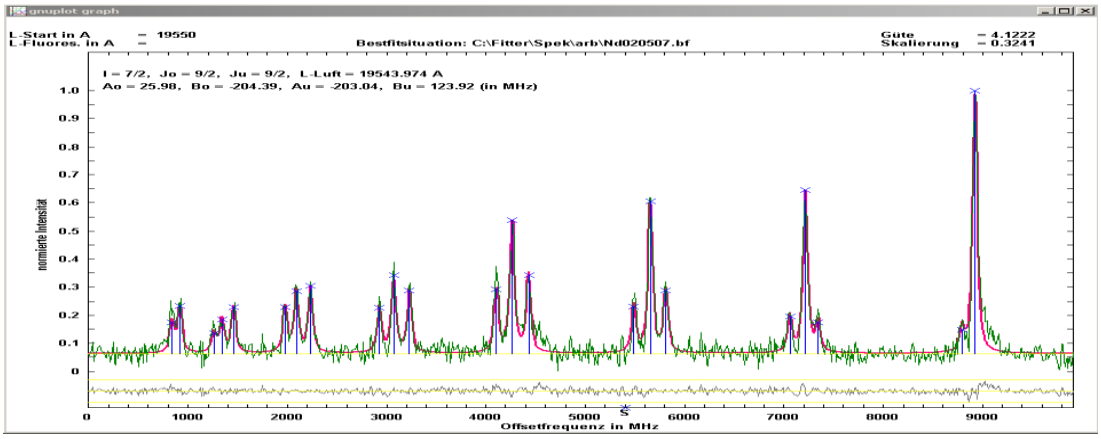

Figure 10.26: Best fit situation of the spectral line 5823.91 Å ($\sigma = 6005.27 \rightarrow 23171.11 cm^{-1}$).

10.3.1.3 Hyperfine Structure of ^{143}Nd II Spectral Line 5825.86 Å

The hyperfine structure of the ^{143}Nd II spectral line 5825.86 Å recorded through the method of CLIBS is shown in Figure 10.27. In this transition ions in the even-parity lower level metastable state $4f^4(^5I)5d\,^6G_{3/2}$ ($\sigma = 8716.46\ cm^{-1}$) are excited to the odd-parity upper level $4f^4(^5I)6p\,^6H°_{5/2}$ ($\sigma = 25876.56\ cm^{-1}$). In this transition J_u = 3/2 to J_o = 5/2 and $I > J$, thus according to the transition rules there are 12 possible hyperfine components for this transition which are clearly resolved and are distributed in 4 groups and each group contains 3 hyperfine components. The 1st component (from highest to lower frequency side) belongs to ΔF = -1 transition the 2nd to ΔF = 0 and the 3rd component belongs to ΔF = +1 transition. This pattern is also followed in the group 2, 3 and 4. The lower level involved in this transition has the lowest value of the angular momentum (J =3/2) for all the investigated transitions of Nd. The hyperfine structure level configuration and the best fit situation of the spectral line 5825.86 Å are shown in Figure 10.28 and Figure 10.29, respectively.

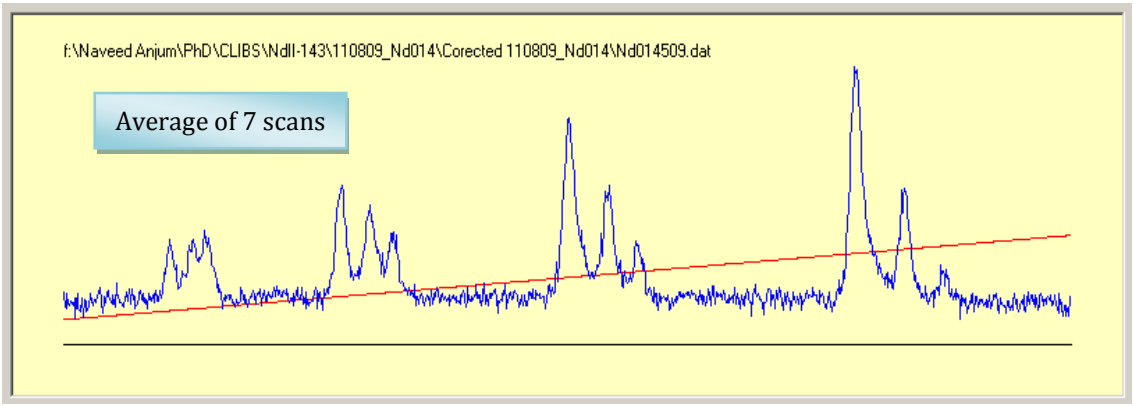

Figure 10.27: Experimentally recorded hyperfine structure of the spectral line 5825.86 Å.

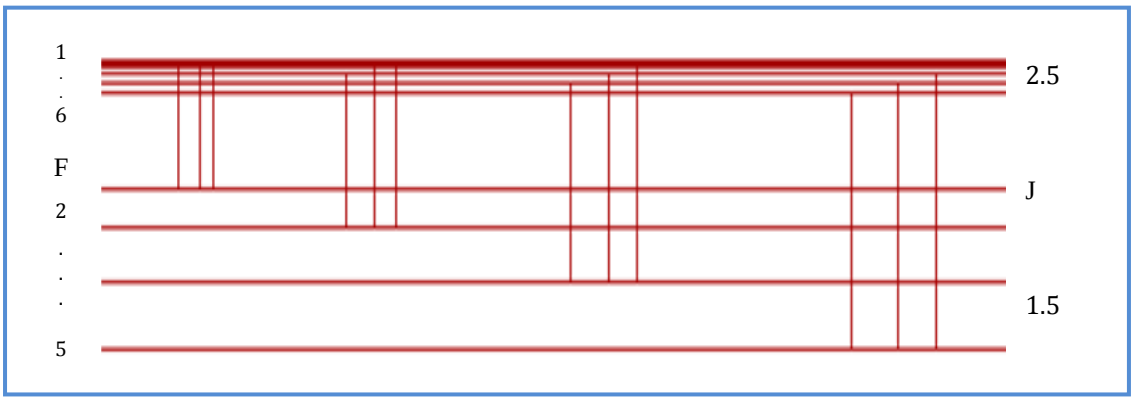

Figure 10.28: The hyperfine structure level configuration of the spectral line 5825.86 Å.
$4f^4(^5I)5d\,^6G_{3/2} \rightarrow 4f^4(^5I)6p\,^6H°_{5/2}$

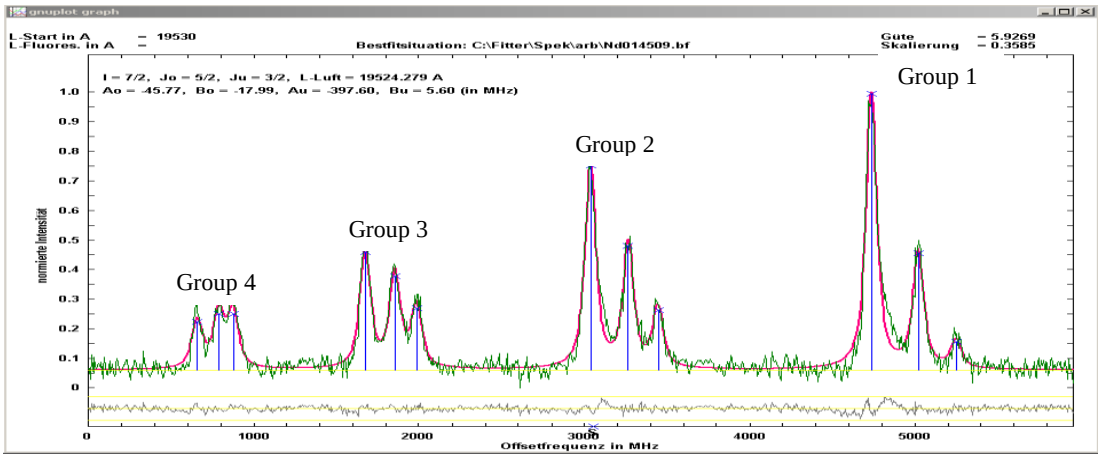

Figure 10.29: Best fit situation of the spectral line 5825.86 Å ($\sigma = 8716.46 \rightarrow 25876.56 cm^{-1}$).

10.3.1.4 Hyperfine Structure of ^{143}Nd II Spectral Line 6284.72 Å

The hyperfine structures of the spectral line 6284.72 Å is shown in Figure 10.30. For this transition the ions being in the even-parity metastable state 4f $^4(^5F)$ 6s $^4F_{9/2}$ ($\sigma = 13971.62$ cm^{-1}) are excited to the odd-parity state $\sigma = 29878.83$ cm^{-1}. In this transition for the upper level the configuration and term values are unknown but *J*-value is known (7/2). In this transition the upper level has the maximum energy value of all the investigated transitions of the Nd whereas the lower level has the maximum energy value of all the investigated transitions of all elements (Ba, Pr, La and Nd) with the method of CLIBS in our group. A well resolved and prominent group of diagonal components ($\Delta J = \Delta F = -1$) is located on the higher frequency side. A poorly resolved group of the off-diagonal components ($\Delta F = 0$) lies in the center of the structure whereas the last group ($\Delta F = +1$) which should be on the lower frequency side is hidden in noise and is not visible in recording. The hyperfine structure level configuration and the best fit situation of the spectral line 6284.72 Å are shown in Figure 10.31 and Figure 10.32, respectively.

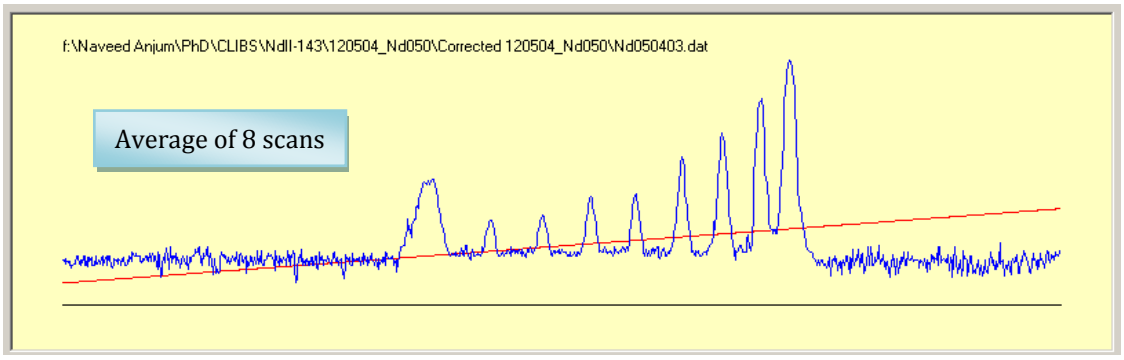

Figure 10.30: Experimentally recorded hyperfine structure of the spectral line 6284.72 Å.

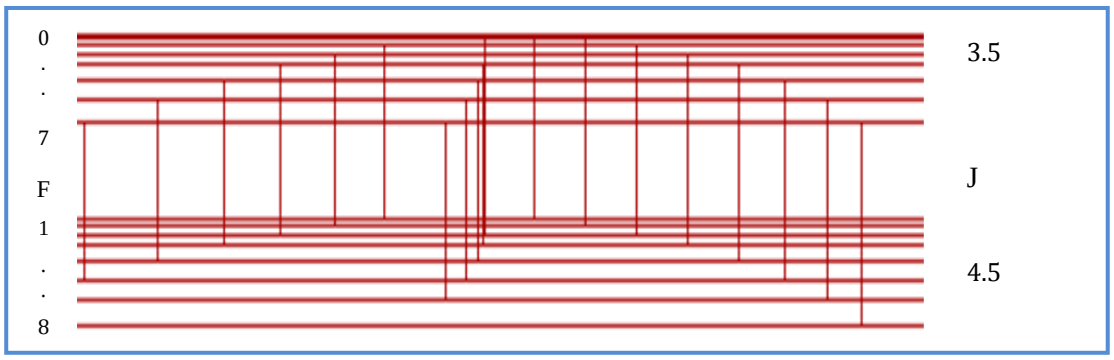

Figure 10.31: The hyperfine structure level configuration of the spectral line 6284.72 Å.

$4f^4(^5F)\ 6s\ ^4F_{9/2} \rightarrow X°_{7/2}$

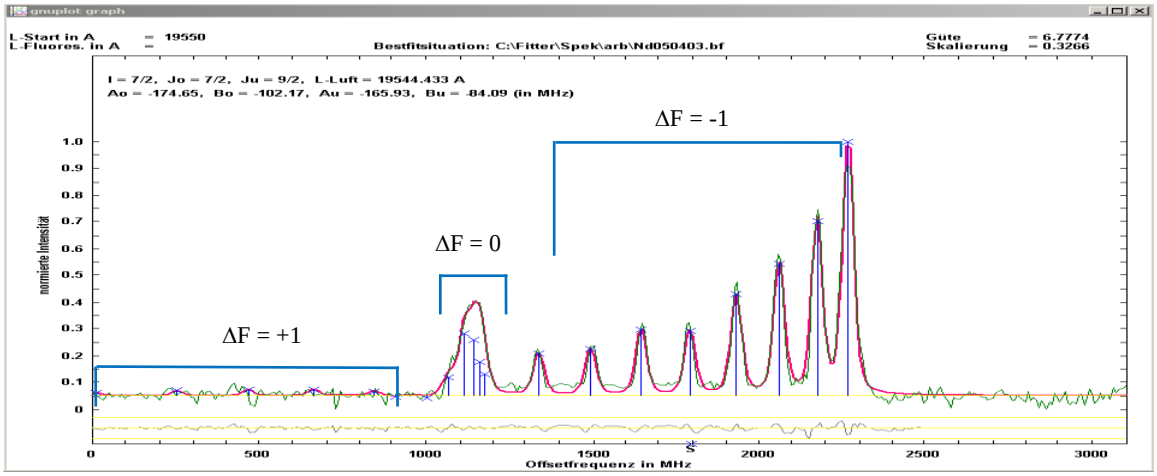

Figure 10.32: Best fit situation of the spectral line 6284.72 Å (σ = 13971.62 → 29878.83cm^{-1}).

10.3.1.5 Hyperfine Structure of ^{143}Nd II Spectral Line 6031.27 Å

The hyperfine structure of the spectral line 6031.27 Å is shown in Figure 10.33. In this transition the ions in the even-parity metastable state $4f^4(^5I)5d\ ^6I_{13/2}$ ($\sigma = 10337.10\ cm^{-1}$) are excited to the odd-parity level $4f^4(^5I)6p\ ^6K°_{15/2}$($\sigma = 26912.77\ cm^{-1}$). According to the transition rules there are 21 possible hyperfine components for this transition. The orbital angular momentums involved in this transition have very large values and J_o = 15/2 up to now is the largest value for the Nd during CLIBS investigation of this work. The 8 diagonal components corresponding to ΔF = +1 are the most prominent one and 3 off-diagonal components corresponding to ΔF = 0 are also visible on the higher frequency side of the structure but 4 remaining components are overlapped with the diagonal components. The off-diagonal components belonging to ΔF = -1 lie on the higher frequency side but are very weak and are not visible in recording. The hyperfine structure level configuration and the best fit situation of the spectral line 6031.27 Å are shown in Figure 10.34 and Figure 10.35, respectively.

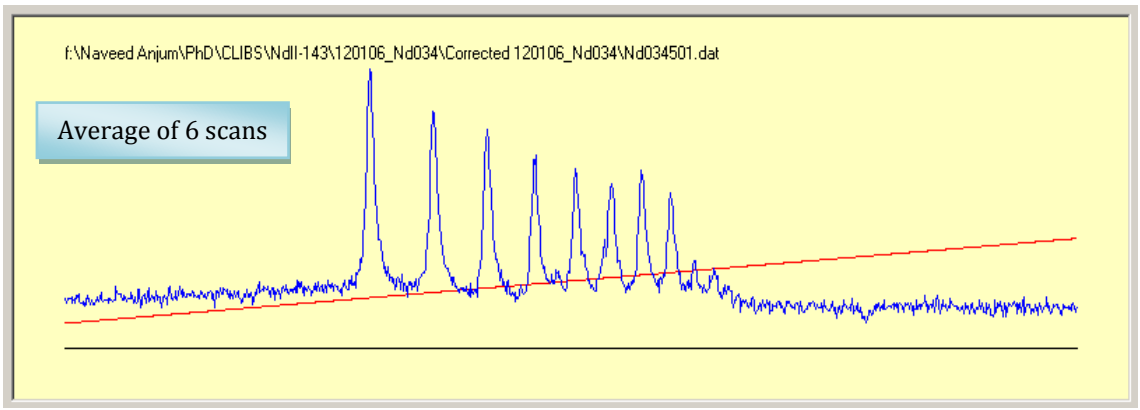

Figure 10.33: Experimentally recorded hyperfine structure of the spectral line 6031.27 Å.

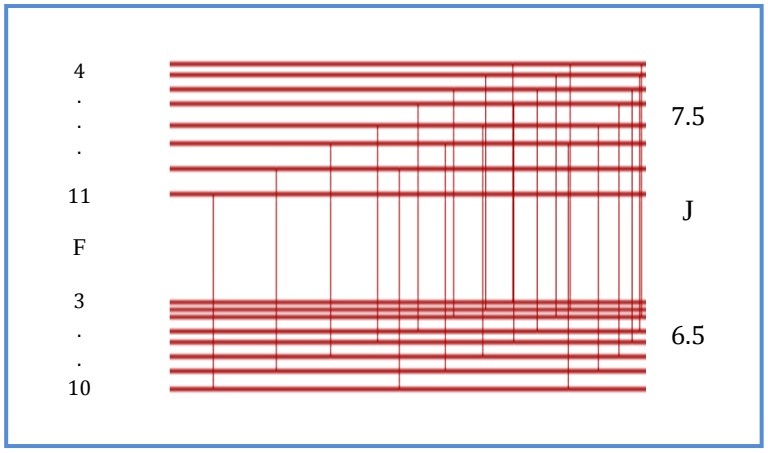

Figure 10.34: The hyperfine structure level configuration of the spectral line 6031.27 Å.
$4f^4(^5I)5d\ ^6I_{13/2} \rightarrow 4f^4(^5I)6p\ ^6K°_{15/2}$

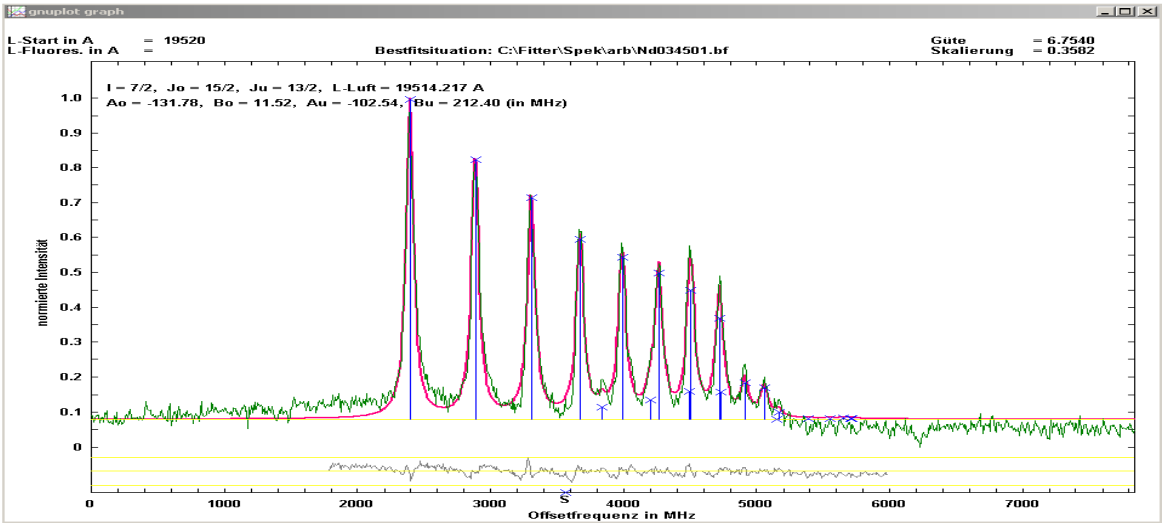

Figure 10.35: Best fit situation of the spectral line 6031.27 Å ($\sigma = 8716.46 \rightarrow 25876.56 cm^{-1}$).

10.3.1.6 Hyperfine Structure of ^{143}Nd II Spectral Line 6170.48 Å

The hyperfine structure of the spectral line 6170.48 Å is shown in Figure 10.36. In this transition the ions in the even-parity metastable state $4f^4(^5I)5d\ ^6H_{5/2}$ ($\sigma = 9674.84\ cm^{-1}$) are excited to the odd-parity level $4f^4(^5I)6p\ ^6H°_{5/2}$ ($\sigma = 25876.56\ cm^{-1}$). In this transition $J < I$ for both levels and have altogether 16 hyperfine components. The 6 diagonal components correspond to ($\Delta J = \Delta F = 0$) and their intensities decreases from higher to lower frequency. The off-diagonal components which correspond to $\Delta F = -1$ are relatively on the higher frequency side of the diagonal components whereas the off-diagonal components corresponding to $\Delta F = +1$ are on lower frequency side of the diagonal components. All the components are well resolved. The line width recorded for this structure is 64 MHz. The hyperfine structure level configuration and the best fit situation of the spectral line 6284.72 Å are shown in Figure 10.37 and Figure 10.38, respectively.

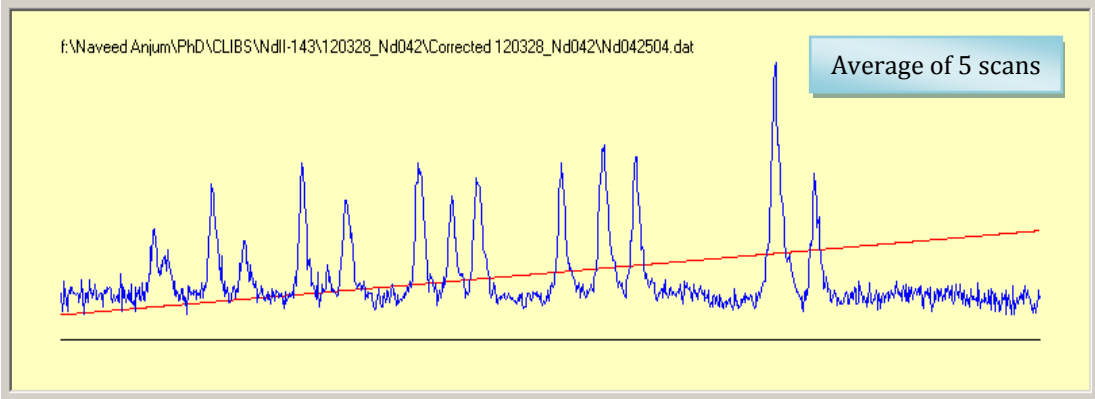

Figure 10.36: Experimentally recorded hyperfine structure of the spectral line 6170.48 Å.

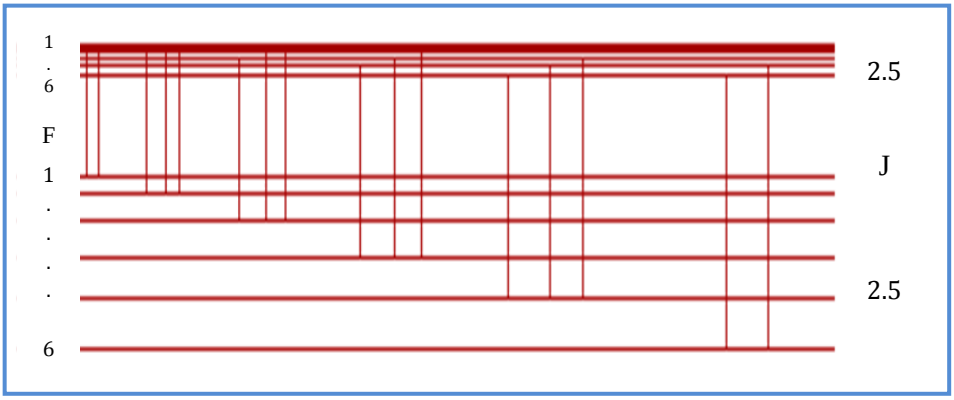

Figure 10.37: The hyperfine structure level configuration of the spectral line 6170.48 Å.
$4f^4(^5I)5d\ ^6H_{5/2} \rightarrow 4f^4(^5I)6p\ ^6H°_{5/2}$

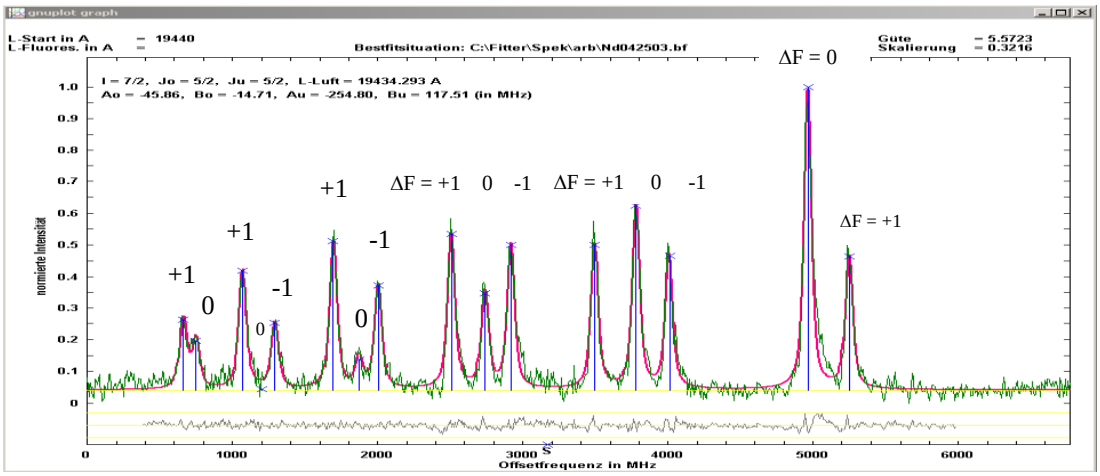

Figure 10.38: Best fit situation of the spectral line 6170.48 Å ($\sigma = 8716.46 \rightarrow 25876.56 cm^{-1}$).

10.3.1.7 Hyperfine Structure of ^{143}Nd II Spectral Line 6263.20 Å

The experimentally recoded hyperfine structure of the spectral line 6263.20 Å is shown in Figure 10.39. In this transition the ions in the even-parity metastable state $4f^4(^5I)5d\ ^6H_{13/2}$ ($\sigma = 13298.89\ cm^{-1}$) are excited to the odd-parity level $4f^4(^5I)6p\ ^4H°_{15/2}$ ($\sigma = 29260.74\ cm^{-1}$). In this transition high *J*-values are involved and 21 hyperfine components exist for this structure. The 8 diagonal components belong to $\Delta F = +1$, 7 off-diagonal components belong to $\Delta F = 0$ and 6 off-diagonal components belong to $\Delta F = -1$. The diagonal components are distributed over entire structure and are clearly resolved and their intensity decreases with increasing frequency. The 7 off-diagonal components corresponding to $\Delta F = 0$ are also visible but have much lower intensities as compared to the diagonal components while the off-diagonal components corresponding to $\Delta F = -1$ are not visible. The recorded spectral width for this line is 55 MHz. The hyperfine structure level configuration and the best fit situation of the spectral line 6263.20 Å are shown in Figure 10.40 and Figure 10.41, respectively.

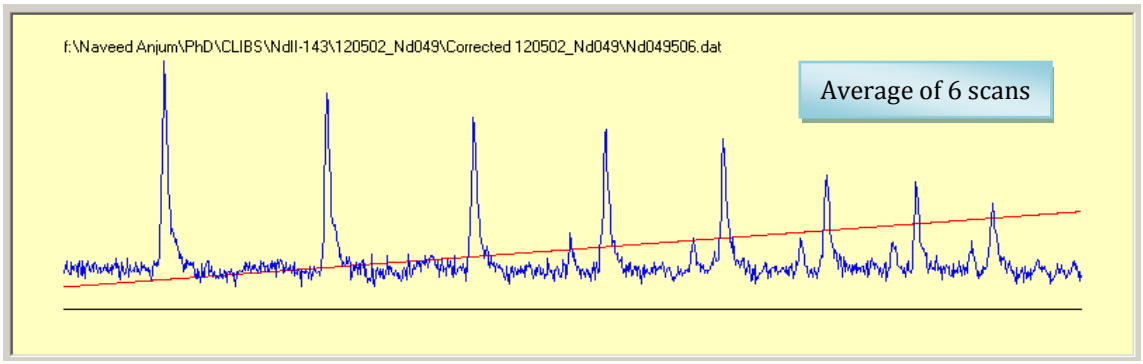

Figure 10.39: Experimentally recorded hyperfine structure of the spectral line 6263.20 Å.

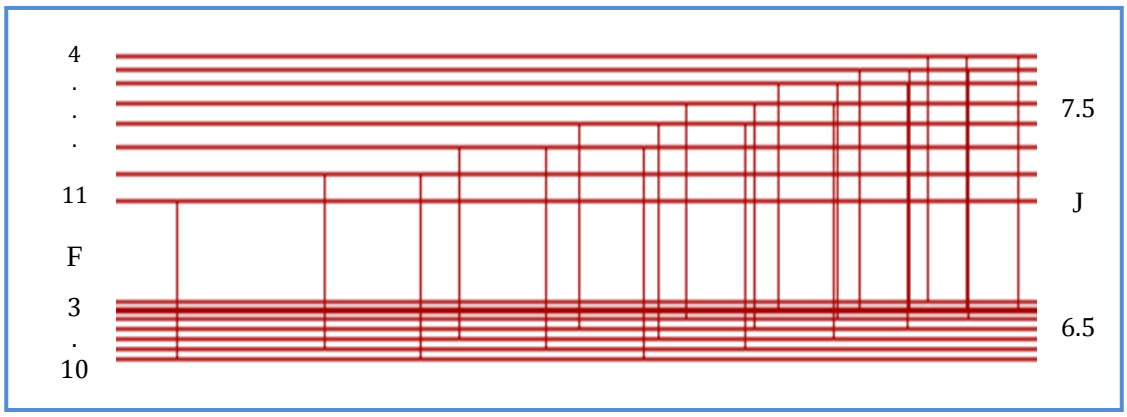

Figure 10.40: The hyperfine structure level configuration of the spectral line 6263.20 Å.
$4f^4(^5I)5d\ ^6H_{13/} \rightarrow 4f^4(^5I)6p\ ^4H°_{15/2}$

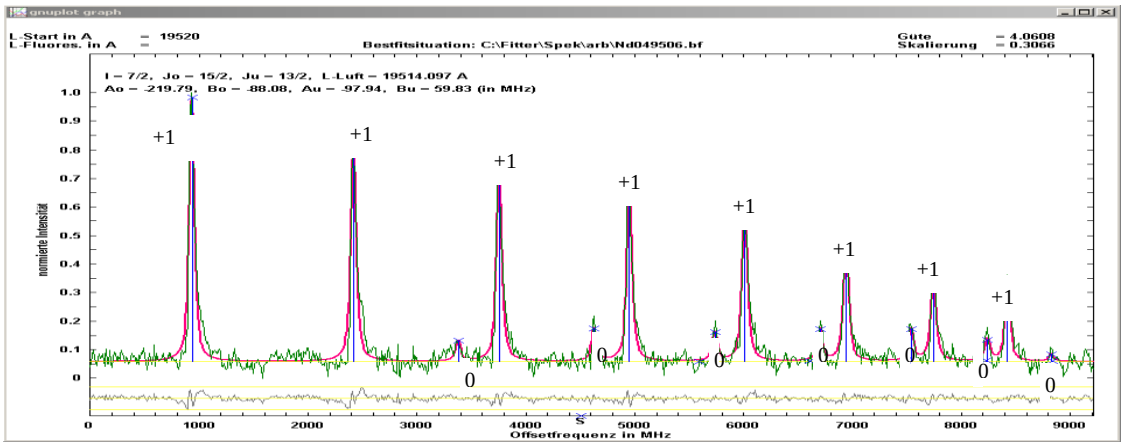

Figure 10.41: Best fit situation of the spectral line 6263.20 Å ($\sigma = 13298.89 \rightarrow 29260.74 cm^{-1}$).

10.3.1.8 A Blend of Two Hyperfine Structures of ^{143}Nd II Spectral Lines in the Wavelength Region 6358.38 Å

A blend situation of two hyperfine structures of the ^{143}Nd II recorded in a single scan in the wavelength region 6358.38 Å is shown in Figure 10.42 . The structure on the lower frequency side (structure-1) is a result of a transition from the even-parity lower metastable state $4f^4(^5I)5d\ ^6G_{11/2}$ ($\sigma = 12021.35\ cm^{-1}$) to the odd-parity metastable state $4f^4(^5I)6p\ ^6I°_{13/2}$ ($\sigma = 27744.20\ cm^{-1}$) and the structure on high frequency side (structure-2) is excited from the even-parity metastable state $4f^4(^5I)5d\ ^6I_{11/2}$ ($\sigma = 9357.91\ cm^{-1}$) to the odd-parity upper metastable state $X°_{11/2}$ ($\sigma = 22106.02\ cm^{-1}$). The configuration and term values of odd-parity level is unknown and only *J*-value is known. The center of gravity (cg) of two structures involved in these transitions are ~ 0.11 cm^{-1} apart and structure-1 altogether have 21 hyperfine components

and structure-2 have 22 hyperfine components. For structure-1, 8 diagonal hyperfine components ($\Delta J = \Delta F$ = +1) are prominent one and decrease in intensity from lower to higher frequency side. The off-diagonal components corresponding to ΔF = 0 are mostly superimposed with the diagonal components while the off-diagonal components corresponding to ΔF = -1 are very weak and are buried in noise. For structure-2, the diagonal hyperfine components ($\Delta J = \Delta F$ = 0) lie in the middle of the structure and one set of the off-diagonal components corresponding to ΔF = -1 is present on the higher frequency side and second set of the off-diagonal components corresponding to ΔF = +1 is present on the lower frequency side of the structure-2. These structures are analyzed using two lines fitting in the fitter program. The spectral line width for structure-1 is 48 MHz and 40 MHz for structure-2. The hyperfine structure level configuration and best fit situation of blend structures in wavelength region 6358.38 are shown in Figure 10.43 and Figure 10.44, respectively.

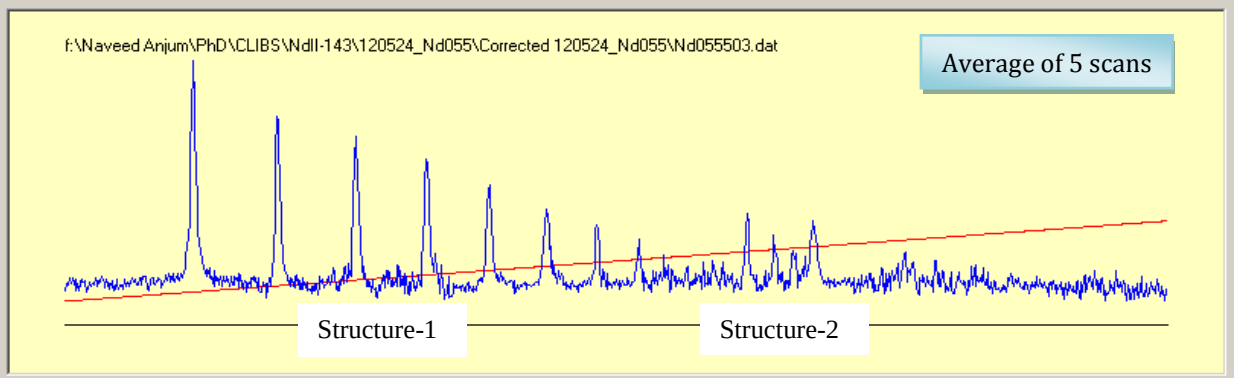

Figure 10.42: Experimentally recorded blend structure of the ^{143}Nd II in wavelength region 6358.38 Å.

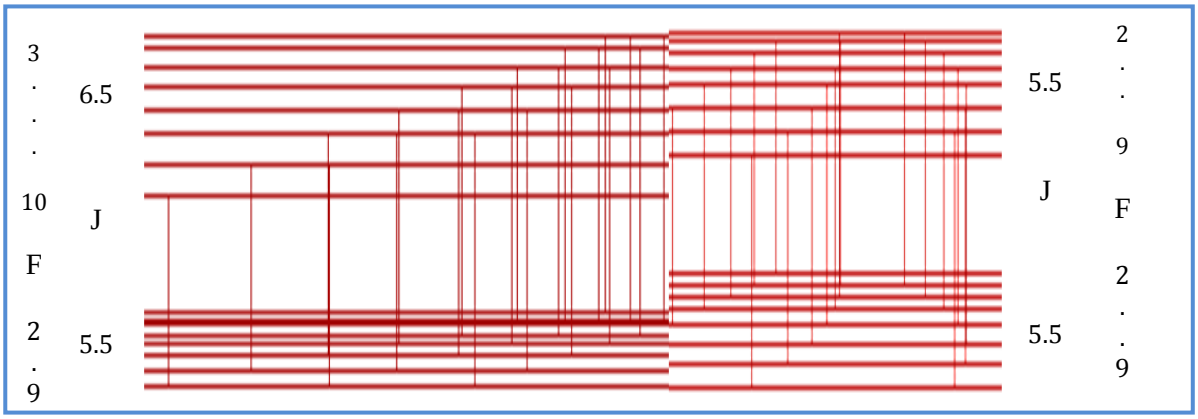

Figure 10.43: The hyperfine structures level configuration of a blend in wavelength region 6358.38 Å. $4f^4(^5I)5d\,^6G_{11/2} \rightarrow 4f^4(^5I)6p\,^6I°_{13/2}$ and $4f^4(^5I)5d\,^6I_{11/2} \rightarrow X°_{11/2}$

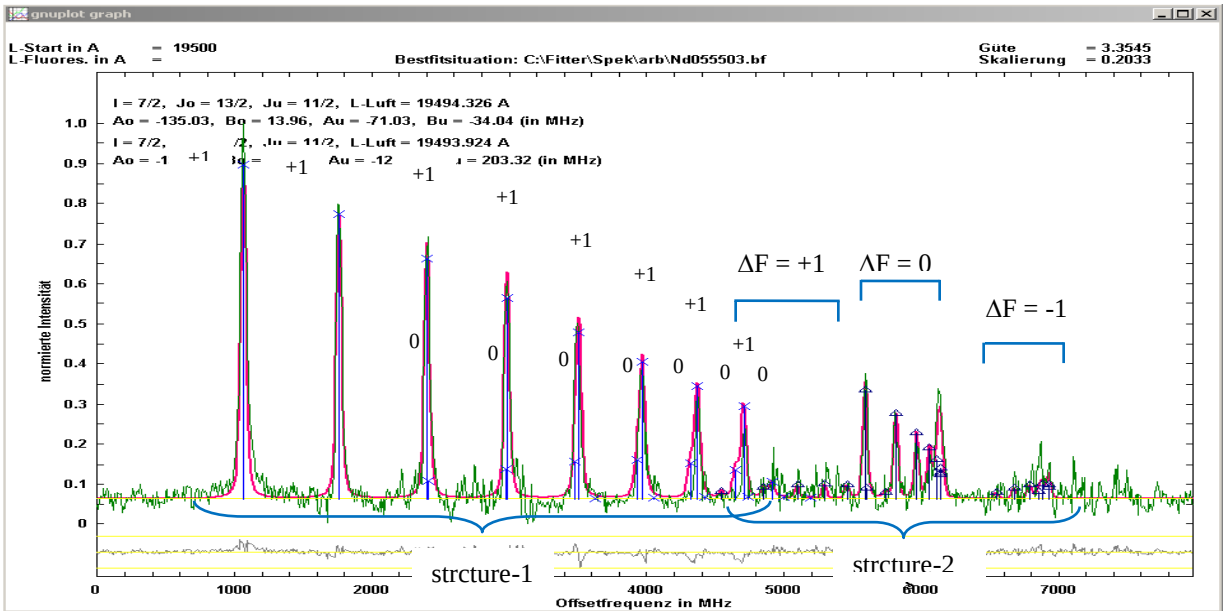

Figure 10.44: Best fit situation of blend structure of the ^{143}Nd II in wavelength region 6358.38 Å.

10.3.2 **Investigations of Hyperfine Structure of ^{145}Nd II Spectral Lines**

The nuclear spin quantum number *'I'* of ^{143}Nd and ^{145}Nd is '7/2' but the magnetic dipole moment of ^{143}Nd is μ_I = -1.065(5) while for ^{145}Nd is μ_I = -0.656(4) and the electric quadrupole moment of ^{143}Nd is Q = -0.63(6) barn while for ^{145}Nd is Q = -0.33(3) barn [107]. Therefore the magnetic dipole coupling constant *A* and electric quadrupole coupling constant *B* are changed according to the ratios of magnetic dipole moments and electric quadrupole moments of the two isotopes respectively.

The experimental investigations of the hyperfine structure of the spectral line of singly ionized neodymium-145 (^{145}Nd II) are presented in this section. As the natural abundance of the ^{145}Nd is just 8.3% consequently the numbers of ions available for the experiments are very low (8-12 nA) even at the maximum heating power of the ion source. Therefore only the spectral lines of very high intensities are investigated for ^{145}Nd II. In this part of the work 35 spectral lines are investigated which resulted in 48 fine structure energy levels. Out of these are 18 even-parity lower levels and 30 are the odd-parity upper levels. The hyperfine structure of few selected spectral lines of ^{145}Nd II is discussed in the following examples.

10.3.2.1 Hyperfine Structure of ^{145}Nd II Spectral Line 6298.41 Å

A selected, one of the most intense spectral line of ^{145}Nd II at wavelength λ_{air} = 6298.41 Å is shown in Figure 10.45. In this hyperfine structure the ions being in the even-parity metastable state $4f^4(^5I)\ 5d\ ^6I_{7/2}$ ($\sigma = 7524.74\ cm^{-1}$) are excited to the odd-parity state $^6K^{\circ}_{7/2}$ ($\sigma = 23397.38 cm^{-1}$). Here the configuration of the upper levels is missing but the term value is known. The 7 diagonal components ($\Delta J = \Delta F = 0$) are the most prominent and are stretched out in middle of the structure and most of them are clearly resolved. At the extreme left of the structure (lower frequency side) apparently only 5 out of 7 hyperfine components belonging to the transitions ΔF = +1 are visible. But a more careful observation reveals that the other 2 components are also present but are overlapped with the diagonal components. The other group of the hyperfine components belonging to ΔF = -1 appears on the right side of the main diagonal hyperfine components. Five hyperfine components are clearly resolved while the remaining 2 components (on higher frequency side) are not resolved. The recorded spectral width for this spectral line is 50 MHz. The hyperfine structure level configuration and the best fit situation of the spectral line 6298.41 Å are shown in Figure 10.46 and Figure 10.47, respectively. The diagonal and the off-diagonal groups are also marked in the best fit structure.

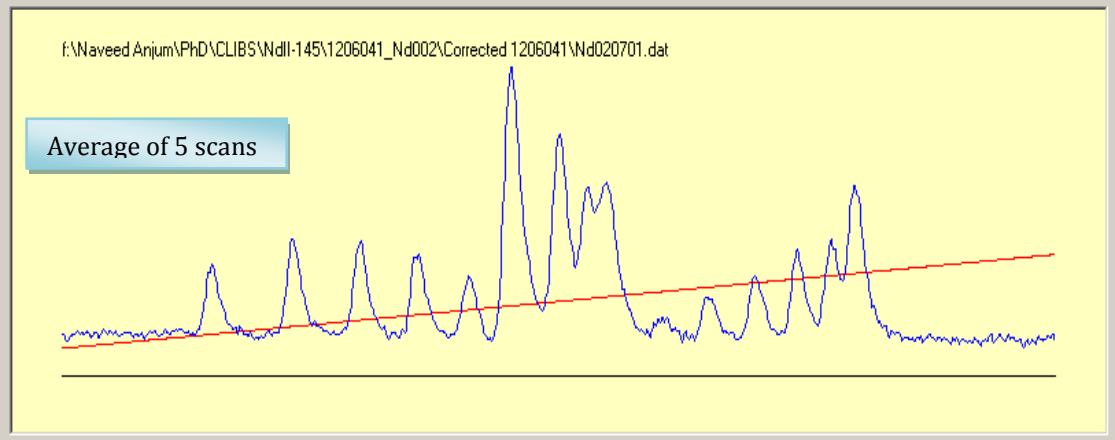

Figure 10.45: Experimentally recorded hyperfine structure of the spectral line 6298.41 Å.

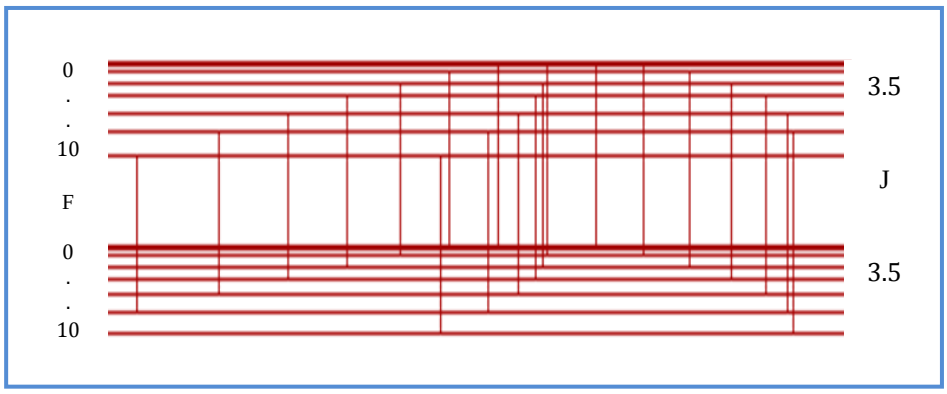

Figure 10.46: The hyperfine structure level configuration of the spectral line 6298.41 Å.
$4f^4(^5I)\ 5d\ ^6I_{7/2} \rightarrow {}^6K^{\circ}_{7/2}$

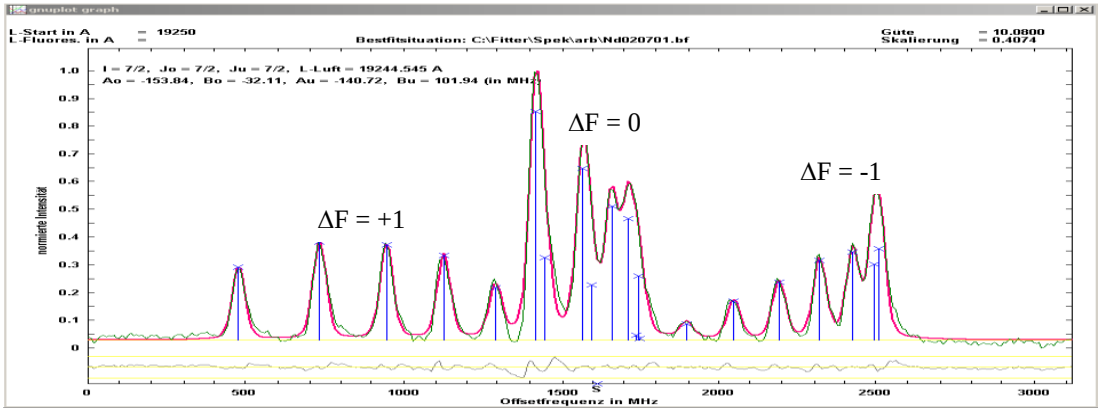

Figure 10.47: Best fit situation of the spectral line 6298.41 Å ($\sigma = 7524.74 \rightarrow 23397.38\ cm^{-1}$).

10.3.2.2 Hyperfine Structure of ^{145}Nd II Spectral Line 6133.95 Å

The investigated hyperfine structure of the spectral line 6133.95 Å is shown in Figure 10.39. In this transition the ions in the even-parity metastable state $4f^4\ (^5I)5d\ ^6K_{11/2}$ ($\sigma = 6931.80\ cm^{-1}$) are excited to the odd-parity level $4f^4\ (^5I)6p\ ^6K^{\circ}_{9/2}$ ($\sigma = 23229.99\ cm^{-1}$). According to the transition rules 21 hyperfine components exist for this structure. The 8 diagonal components ($\Delta J = \Delta F = -1$) are on the higher frequency side of the structure but are not completely resolved. The 7 off-diagonal components ($\Delta F = 0$) which lie on the lower frequency side are also not resolved completely whereas the 6 off-diagonal components ($\Delta F = +1$) are very weak and just two of them are visible. The recorded spectral width for this spectral line is 49 MHz. The hyperfine structure level configuration and the best fit situation of the spectral line 6133.95 Å are shown in Figure 10.49 and Figure 10.50, respectively.

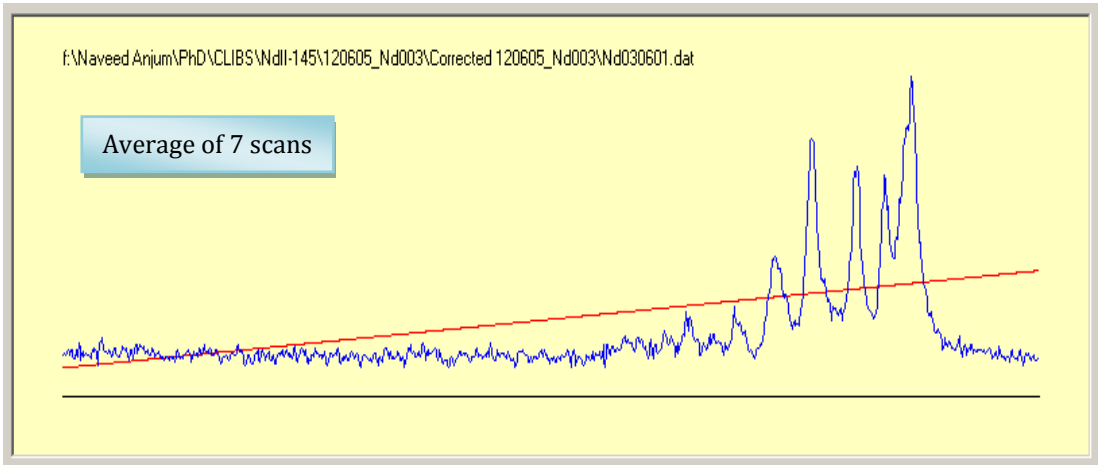

Figure 10.48: Experimentally recorded hyperfine structure of the spectral line 6133.95 Å.

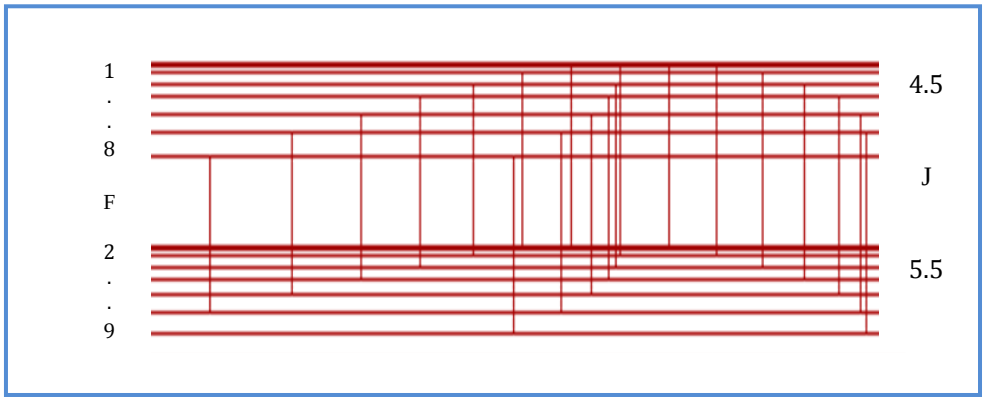

Figure 10.49: The hyperfine structure level configuration of the spectral line 6133.95 Å.
$4f^4(^5I)5d\ ^6K_{11/2} \rightarrow 4f^4(^5I)6p\ ^6K°_{9/2}$

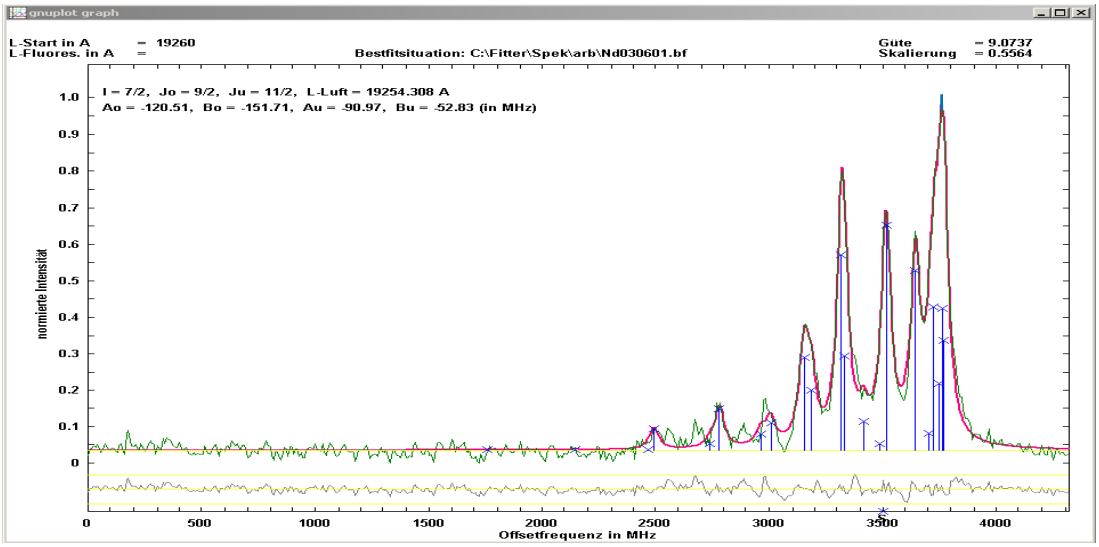

Figure 10.50: Best fit situation of the spectral line 6133.95 Å ($\sigma = 6931.80 \rightarrow 23229.99\ cm^{-1}$).

10.3.2.3 Hyperfine Structure of ^{145}Nd II Spectral Line 6302.66 Å

The experimentally recorded hyperfine structure of the spectral line 6302.66 Å is shown in Figure 10.51. In this transition the ions in the even-parity metastable state $4f^4(^5I)5d\ ^6G_{13/2}$ (σ = 12334.22 cm^{-1}) are excited to the odd-parity level σ = 23229.99 cm^{-1}. The configuration and term value of the upper level is unknown but *J*-value (13/2) is known. In this structure relatively higher *J*-values (13/2) are involved and the hyperfine pattern follows the typical hyperfine structure for $\Delta J = \Delta F = 0$ transition. In this type of structure the diagonal components lie in the middle of the structure and one set of the off-diagonal components lie on one side whereas the other set of the off-diagonal components lie on the other side of the diagonal components. Here the diagonal components are well resolved but the off-diagonal components (ΔF = -1) are strongly overlapped in one large peak. The other set of off-diagonal components (ΔF = +1) is very weak and most of the components are not visible due to very low ion current. The line width for this spectral line is 52 MHz. The hyperfine structure level configuration and the best fit situation of the spectral line 6302.66 Å are shown in Figure 10.52 and Figure 10.53, respectively.

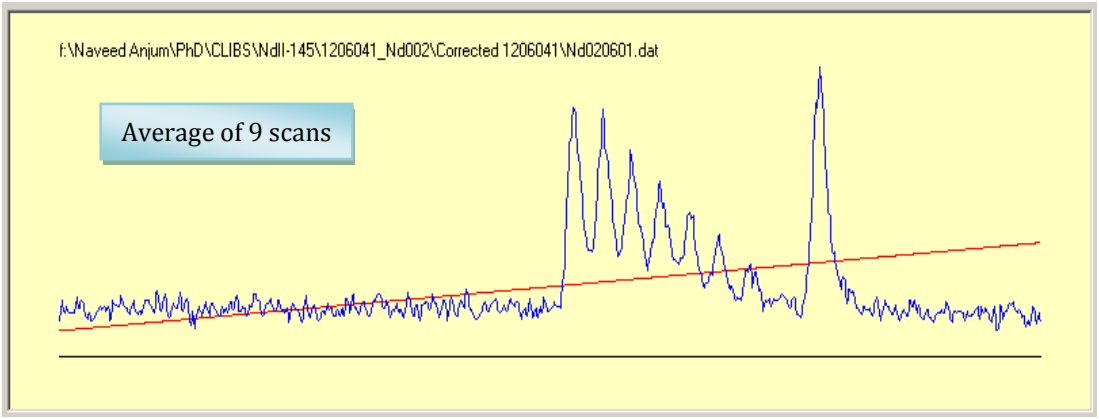

Figure 10.51: Experimentally recorded hyperfine structure of the spectral line 6302.66 Å.

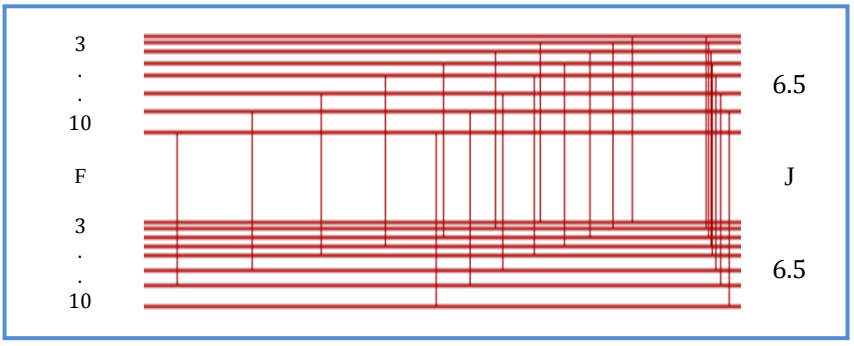

Figure 10.52: The hyperfine structure level configuration of the spectral line 6302.66 Å.
$4f^4(^5I)5d\ ^6G_{13/2} \rightarrow X°_{13/2}$

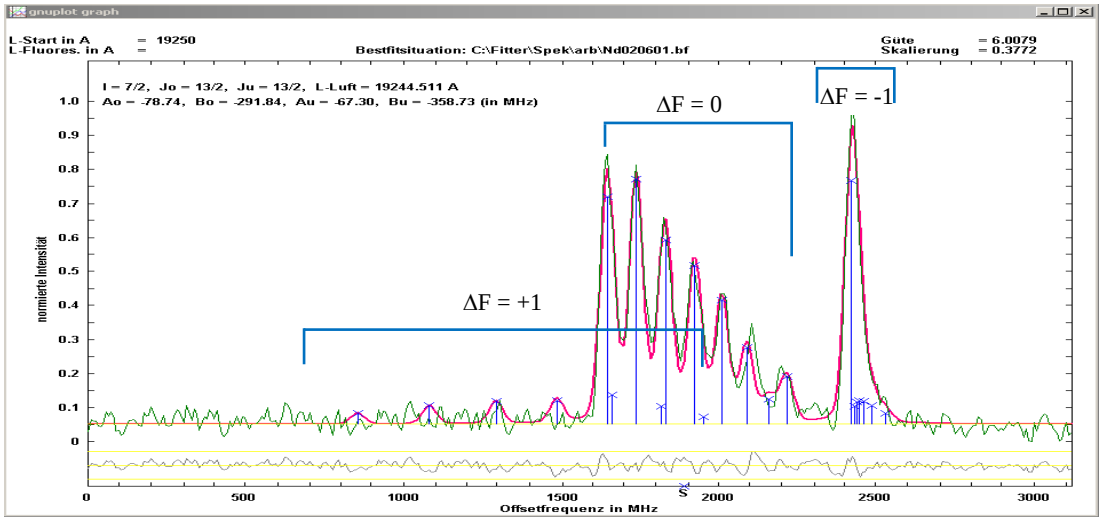

Figure 10.53: Best fit situation of the spectral line 6302.66 Å ($\sigma = 12334.22 \rightarrow 23229.99\ cm^{-1}$).

Table 10.2: Spectral lines investigated for ^{139}La II using CLIBS.

S. No.	Wavelength (air) λ/Å	Lower Level		Upper Level	
		J	Energy / cm^{-1}	J	Energy / cm^{-1}
1	5703.31	1	5718.12	2	23246.92
2	5769.06	2	10094.86	1	27423.91
3	5863.69	4	7473.31	3	24522.69
4	6100.37	1	5718.12	2	22106.02
5	6126.07	2	10094.86	2	26414.01
6	6129.56	2	6227.42	3	22537.30
7	6174.17	0	5249.70	1	21441.73
8	6296.04	2	6227.42	1	22106.02
9	6296.08	2	10094.86	1	25973.37
10	6358.10	1	5718.12	1	21441.73

Table 10.3: Measured hyperfine constants of even parity fine energy levels of ^{139}La II. The results are compared (wherever available) with the results of C. Höhle [29] and Ma Hong-Liang [73].

Level Energy /cm^{-1}	J	Parity	λ/Å Comment [Ref]	Combining Level			A/MHz	B/MHz
				Energy/cm^{-1}	J	Parity		
5249.70	0	even	6174.17	21441.73	1	odd	0.00	0.00
5718.12	1	even	5703.31	23246.92	2	odd	-223.72 (42)	23.8 (11)
5718.12	1	even	6358.10	21441.73	1	odd	-223.94 (13)	26.4 (19)
5718.12	1	even	6100.37	22106.02	2	odd	-223.99 (14)	26.2 (17)
			Mean				**-223. 89 (14)**	**25.4 (13)**
			[29]				-224.45 (20)	25.8 (9)
			[73]				-227.2 (16)	35.0 (100)
6227.42	2	even	6129.56	22537.30	3	odd	-157.28 (18)	-43.9 (16)
6227.42	2	even	6296.04	22106.02	1	odd	-157.53 (23)	-43.3 (25)
			Mean				**-157.41 (17)**	**-43.6 (21)**
			[29]				-158.2 (4)	-45.0 (110)
7473.31	4	even	5863.69	24522.69	3	odd	149.56 (18)	141.4 (66)
			[29]				149.96 (18)	151.7 (54)
			[73]				148.1 (12)	156.3 (24)
10094.86	2	even	5769.06	27423.91	1	odd	48.01 (37)	40.5 (19)
10094.86	2	even	6126.07	26414.01	2	odd	48.16 (13)	38.7 (15)
10094.86	2	even	6296.08	25973.37	1	odd	47.97 (33)	37.8 (17)
			Mean				**48.05 (12)**	**39.1 (15)**
			[29]				48.27 (30)	40.8 (30)
			[73]				48.8 (6)	43.1 (45)

Table 10.4: Measured hyperfine constants of even parity fine energy levels of ^{139}La II. The results are compared (wherever available) with the results of C. Höhle [29] and Ma Hong-Liang [73].

Level Energy /cm^{-1}	J	Parity	λ/Å Comment [Ref]	Combining Level			A/MHz	B/MHz
				Energy/cm^{-1}	J	Parity		
21441.73	1	odd	6174.17	5249.70	0	even	413.22 (11)	3.4 (11)
21441.73	1	odd	6358.10	5718.12	1	even	413.28 (14)	3.3 (11)
			Mean				**413.25 (8)**	**3.4 (9)**
22106.02	2	odd	6100.37	5718.12	1	even	122.30 (20)	4.2 (12)
22106.02	1	odd	6296.04	6227.42	2	even	122.25 (18)	7.2 (34)
			Mean				**122.28 (12)**	**5.7 (21)**
22537.30	3	odd	6129.56	6227.42	2	even	97.98 (10)	-23.5 (33)
23246.92	2	odd	5703.31	5718.12	1	even	34.51 (27)	12.2 (28)
			[29]				34.45 (27)	11.4 (12)
			[73]				34.9 (12)	14.2 (45)
24522.69	3	odd	5863.69	7473.31	4	even	163.84 (27)	15.9 (29)
			[29]				164.17 (21)	20.4 (48)
			[73]				162.0 (21)	22.3 (42)
25973.37	1	odd	6296.08	10094.86	2	even	548.06 (28)	25.4 (11)
26414.01	2	odd	6126.07	10094.86	2	even	250.10 (10)	52.8 (12)
			[73]				251.0 (18)	48.1 (24)
27423.91	1	odd	5769.06	10094.86	2	even	889.49 (25)	-16.7 (12)
			[73]				886.9 (15)	-18.9 (48)

Table 10.5: Spectral lines investigated for ^{143}Nd II using CLIBS.

S. No	Wavelength (air) λ/Å	Even Level		Odd Level	
		J	Energy / cm^{-1}	J	Energy / cm^{-1}
1	5702.24	9/2	6005.27	9/2	23537.39
2	5706.20	7/2	7524.74	7/2	25044.68
3	5708.27	11/2	6931.80	11/2	24445.39
4	5726.82	9/2	8420.32	9/2	25877.18
5	5744.12	9/2	6005.27	9/2	23409.54
6	5748.14	9/2	6005.27	7/2	23397.38
7	5748.54	7/2	9908.65	7/2	27299.54
8	5761.69	9/2	8420.32	9/2	25771.53
9	5770.49	3/2	8716.46	5/2	26041.21
10	5783.67	15/2	9042.74	13/2	26328.01
11	5804.00	9/2	6005.27	9/2	23229.99
12	5811.57	11/2	6931.80	11/2	24134.10
13	5823.91	9/2	6005.27	9/2	23171.11
14	5825.86	3/2	8716.46	5/2	25876.56
15	6031.27	13/2	10337.10	15/2	26912.77
16	6048.44	7/2	7524.74	9/2	24053.35
17	6051.86	11/2	9357.91	9/2	25877.18
18	6065.64	15/2	9042.74	13/2	25524.48
19	6067.11	11/2	6931.80	9/2	23409.54
20	6077.21	9/2	6005.27	9/2	22455.62
21	6086.96	13/2	10337.10	11/2	26759.24
22	6087.50	9/2	8420.32	11/2	24842.88
23	6104.41	9/2	8420.32	9/2	24797.39
24	6108.19	11/2	10942.01	13/2	27308.94
25	6108.40	5/2	9674.84	5/2	26041.21
26	6113.46	9/2	6005.27	9/2	22358.08
27	6126.33	7/2	9908.65*	9/2	26227.11
28	6133.95	11/2	6931.80	9/2	23229.99
29	6156.60	15/2	11373.47	15/2	27611.72
30	6170.48	5/2	9674.84	5/2	25876.56

S. No	Wavelength (air) λ/Å	Even Level		Odd Level	
		J	Energy / cm^{-1}	J	Energy / cm^{-1}
31	6170.79	13/2	11580.86*	11/2	27781.77
32	6174.63	7/2	9198.39	9/2	25389.22
33	6177.22	13/2	7950.07	11/2	24134.10
34	6183.89	11/2	9357.91	13/2	25524.48
35	6202.73	5/2	8796.38	7/2	24913.86
36	6206.14	9/2	10883.26	11/2	26991.89
37	6210.66	7/2	9198.39	7/2	25295.29
38	6243.34	7/2	7524.74	9/2	23537.39
39	6248.27	9/2	9877.17	9/2	25877.18
40	6250.43	11/2	9357.91	11/2	25352.38
41	6251.82	13/2	10337.10	13/2	26328.01
42	6258.80	11/2	12887.08	11/2	28860.16
43	6263.20	13/2	13298.89	15/2	29260.74
44	6271.73	7/2	9198.39	7/2	25138.56
45	6272.76	13/2	11580.86	11/2	27518.40
46	6273.57	15/2	11373.47	13/2	27308.94
47	6284.72	9/2	13971.62	7/2	29878.83
48	6287.20	9/2	8420.32	9/2	24321.26
49	6293.59	7/2	7524.74	9/2	23409.54
50	6298.01	13/2	10337.10	13/2	26210.75
51	6298.41	7/2	7524.74	7/2	23397.38
52	6300.94	9/2	6005.27	7/2	21871.52
53	6302.66	13/2	12334.22	13/2	28196.16
54	6310.19	11/2	9357.91	11/2	25200.91
55	6319.62	15/2	12906.58	13/2	28725.93
56	6319.73	11/2	10942.01	11/2	26759.24
57	6338.83	13/2	11580.86	11/2	27352.28
58	6341.38	11/2	6931.80	11/2	22696.88
59	6341.54	13/2	13597.86	15/2	29362.53
60	6346.31	5/2	10887.25	7/2	26640.09

S. No	Wavelength (air) λ/Å	Even Level		Odd Level	
		J	Energy / cm^{-1}	J	Energy / cm^{-1}
61	6354.74	11/2	6931.80	9/2	22663.73
62	6358.36	11/2	9357.91	11/2	25080.88
63	6358.41	11/2	12021.35	13/2	27744.20
64	6361.40	7/2	9198.39	7/2	24913.86
65	6361.42	9/2	11709.60	9/2	27425.02
66	6362.01	7/2	10666.78	9/2	26380.73
67	6362.08	9/2	8420.32	11/2	24134.10
68	6365.54	7/2	7524.74	9/2	23229.99
69	6366.74	7/2	10666.78*	7/2	26369.06
70	6378.62	7/2	7524.74	7/2	23197.79
71	6382.06	13/2	11580.86	11/2	27245.45
72	6385.14	11/2	9357.91	11/2	25014.93
73	6385.19	15/2	12906.58	13/2	28563.48
74**	6389.49	11/2		13/2	
75**	6349.88	15/2		19/2	
76**	6331.44	13/2		13/2	
77**	6328.65	11/2		13/2	
78**	6279.69	11/2		13/2	
79**	6260.83	7/2		5/2	
80**	6232.17	13/2		13/2	
81**	6180.97	3/2		5/2	
82**	6113.82	15/2		13/2	
83**	5823.17	15/2		13/2	
84**	5766.95	7/2		7/2	
85**	5744.36	13/2		15/2	
86**	6374.15	9/2		11/2	
87**	6379.18	5/2		7/2	

*Hyperfine constants of lower level were fixed.

** Weak recording and not used for the calculation of the hyperfine constants.

Table 10.6: Measured hyperfine constants of even parity fine energy levels of ^{143}Nd II. The results are compared (wherever available) with the results of Maoscheng [99].

Level Energy /cm^{-1}	J	Parity	λ/Å Comment [Ref]	Combining Level			A/MHz	B/MHz
				Energy/cm^{-1}	J	Parity		
6005.27	9/2	even	5702.24	23537.39	9/2	odd	-203.18 (8)	130.3 (19)
6005.27			5744.12	23409.54	9/2	odd	-203.19 (6)	131.1 (19)
6005.27			5748.14	23397.38	7/2	odd	-203.09 (7)	128.5 (35)
6005.27			5804.00	23229.99	9/2	odd	-203.02 (5)	131.2 (24)
6005.27			5823.91	23171.11	9/2	odd	-203.16 (10)	116.9 (78)
6005.27			6077.21	22455.62	9/2	odd	-203.10 (5)	122.1 (15)
6005.27			6113.46	22358.08	9/2	odd	-203.19 (12)	127.4 (46)
6005.27			6300.94	21871.52	7/2	odd	-203.11 (14)	124.3 (22)
			Mean				**-203.13 (18)**	**126.8 (54)**
			[99]				-200.2 (10)	116.2 (50)
6931.80	11/2	even	5708.27	24445.39	11/2	odd	-150.73 (11)	121.6 (26)
6931.80			5811.57	24134.10	11/2	odd	-150.65 (7)	118.8 (39)
6931.80			6067.11	23409.54	9/2	odd	-150.73 (10)	112.6 (95)
6931.80			6133.95	23229.99	9/2	odd	-150.00 (45)	121.7 (29)
6931.80			6341.38	22696.88	11/2	odd	-150.71 (11)	124.2 (39)
6931.80			6354.74	22663.73	9/2	odd	-150.66 (17)	119.8 (10)
			Mean				**-150.58 (29)**	**119.8 (40)**
			[99]				-150.8 (4)	54.5 (26)
7524.74	7/2	even	5706.20	25044.68	7/2	odd	-227.28 (9)	204.6 (44)
7524.74			6048.44	24053.35	9/2	odd	-227.27 (13)	204.2 (43)
7524.74			6243.34	23537.39	9/2	odd	-227.34 (10)	201.1 (21)
7524.74			6293.59	23409.54	9/2	odd	-227.62 (9)	201.4 (51)
7524.74			6298.41	23397.38	7/2	odd	-227.18 (17)	199.9 (21)
7524.74			6365.54	23229.99	9/2	odd	-227.30 (29)	205.4 (24)
7524.74			6378.62	23197.79	7/2	odd	-227.09 (17)	211.1 (11)
			Mean				**-227.30 (17)**	**203.6 (44)**
7950.07	13/2	even	6177.22	24134.10	11/2	odd	-119.50 (20)	106.9 (24)
8420.32			5726.82	25877.18	9/2	odd	-162.02 (12)	199.5 (21)
8420.32	9/2	even	5761.69	25771.53	9/2	odd	-162.02 (5)	197.9 (50)
8420.32			6087.50	24842.88	11/2	odd	-161.68 (15)	199.9 (27)
8420.32			6104.41	24797.39	9/2	odd	-161.65 (14)	200.7 (69)
8420.32			6287.20	24321.26	9/2	odd	-161.56 (5)	195.8 (31)
8420.32			6362.08	24134.10	11/2	odd	-161.56 (2)	192.9 (11)
			Mean				**-161.75 (22)**	**197.8 (29)**

Level Energy /cm^{-1}	J	Parity	λ/Å Comment [Ref]	Combining Level			A/MHz	B/MHz
				Energy/cm^{-1}	J	Parity		
8716.46	3/2	even	5770.49	26041.21	5/2	odd	-397.67 (33)	7.7 (14)
8716.46			5825.86	25876.56	5/2	odd	-397.56 (6)	3.7 (21)
			Mean				**-397.62 (10)**	**5.7 (28)**
			[99]				-394.3 (5)	5.1 (48)
8796.38	5/2	even	6202.73	24913.86	7/2	odd	-195.73 (10)	-8.1 (34)
9042.74	15/2	even	5783.67	26328.01	13/2	odd	-102.08 (41)	238.9 (139)
9042.74			6065.64	25524.48	13/2	odd	-101.03 (2)	233.3 (58)
			Mean				**-101.56 (74)**	**236.1 (40)**
9198.39	7/2	even	6174.63	25389.22	9/2	odd	-144.86 (31)	107.4 (41)
9198.39			6210.66	25295.29	7/2	odd	-144.81 (29)	101.0 (60)
9198.39			6271.73	25138.56	7/2	odd	-144.93 (16)	109.3 (39)
9198.39			6361.40	24913.86	7/2	odd	-144.45 (12)	107.1 (33)
			Mean				**-144.82 (21)**	**106.2 (36)**
9357.91	11/2	even	6051.86	25877.18	9/2	odd	-124.04 (6)	201.5 (22)
9357.91			6183.89	25524.48	13/2	odd	-124.05 (9)	203.3 (29)
9357.91			6250.43	25352.38	11/2	odd	-124.06 (9)	196.3 (22)
9357.91			6310.19	25200.91	11/2	odd	-123.83 (10)	201.6 (45)
9357.91			6358.36	25080.88	11/2	odd	-123.83 (29)	202.6 (33)
9357.91			6385.14	25014.93	11/2	odd	-123.82 (29)	191.7 (167)
			Mean				**-123.94 (12)**	**199.5 (46)**
9674.84	5/2	even	6108.40	26041.21	5/2	odd	-254.22 (4)	117.8 (21)
9674.84			6170.48	25876.56	5/2	odd	-254.75 (11)	116.4 (48)
			Mean				**-254.48 (37)**	**117. 2(30)**
9877.17	9/2	even	6248.27	25877.18	9/2	odd	-112.63 (13)	136.9 (39)
9908.65	7/2	even	5748.54	27299.54	7/2	odd	-227.03 (42)	198.3 (49)
9908.65			6126.33	26227.11	9/2	odd	-226.78 (18)	206.8 (44)
			Mean				**-226.90 (17)**	**202.5 (61)**
10337.10	13/2	even	6031.27	26912.77	15/2	odd	-102.50 (4)	217.1 (43)
10337.10			6086.96	26759.24	11/2	odd	-102.73 (24)	212.7 (58)
10337.10			6251.82	26328.01	13/2	odd	-102.80 (19)	210.3 (43)
10337.10			6298.01	26210.75	13/2	odd	-102.49 (5)	213.9 (32)
			Mean				**-102.63 (16)**	**213.5 (29)**
10666.78	7/2	even	6362.01	26380.73	9/2	odd	-77.49 (26)	110.3 (28)
10666.78			6366.74	26369.06	7/2	odd	-76.58 (15)	112.0 (25)
			Mean				**-77.03 (65)**	**101.2 (12)**
10883.26	9/2	even	6206.14	26991.89	11/2	odd	-122.40 (19)	62.9 (47)
10887.25	5/2	even	6346.31	26640.09	7/2	odd	-274.77 (41)	44.2 (10)

Level Energy /cm^{-1}	J	Parity	λ/Å Comment [Ref]	Combining Level			A/MHz	B/MHz
				Energy/cm^{-1}	J	Parity		
10942.01	11/2	even	6108.19	27308.94	13/2	odd	-96.36 (27)	133.2 (52)
10942.01			6319.73	26759.24	11/2	odd	-96.48 (20)	134.7 (55)
			Mean				**-96.42 (19)**	**134.0 (26)**
11373.47	15/2	even	6156.60	27611.72	15/2	odd	-90.84 (11)	225.3 (23)
11373.47			6273.57	27308.94	13/2	odd	-91.06 (18)	221.4 (40)
			Mean				**-90.95 (15)**	**223.4 (28)**
11580.86	13/2	even	6170.79	27781.77	11/2	odd	-117.67 (15)	295.0 (50)
11580.86			6272.76	27518.40	11/2	odd	-118.65 (29)	299.5 (225)
11580.86			6338.83	27352.28	11/2	odd	-117.84 (49)	316.1 (102)
11580.86			6382.06	27245.45	11/2	odd	-117.90 (14)	296.0 (57)
			Mean				**-118.01 (44)**	**301.7 (99)**
11709.60	9/2	even	6361.42	27425.02	9/2	odd	-140.98 (49)	162.1 (39)
12021.35	11/2	even	6358.41	27744.20	13/2	odd	-70.95 (21)	-31.1 (42)
12334.22	13/2	even	6302.66	28196.16	13/2	odd	-86.73 (14)	-47.1 (22)
12887.08	11/2	even	6258.80	28860.16	11/2	odd	-132.13 (26)	-113.2 (76)
12906.58	15/2	even	6319.62	28725.93	13/2	odd	-79.80 (30)	-191.2 (66)
12906.58			6385.14	28563.48	13/2	odd	-79.96 (44)	-179.3 (101)
			Mean				**-79.88 (12)**	**-185.3 (84)**
13298.89	13/2	even	6263.20	29260.74	15/2	odd	-97.66 (24)	65.8 (57)
13597.86	13/2	even	6341.54	29362.53	15/2	odd	-97.11 (4)	389.1 (74)
13971.62	9/2	even	6284.72	29878.83	7/2	odd	-166.29 (34)	-66.5 (153)

Table 10.7: Measured hyperfine constants of odd parity fine energy levels of ^{143}Nd II. The results are compared (wherever available) with the results of Rosner [33] and Maoscheng [99].

Level Energy /cm^{-1}	J	Parity	λ/Å Comment [Ref]	Combining Level			A/MHz	B/MHz
				J	Parity	Energy/cm^{-1}		
21871.52	7/2	odd	6300.94	9/2	even	6005.27	-217.82 (20)	39.2 (48)
22358.08	9/2	odd	6113.46	9/2	even	6005.27	-162.31 (6)	-76.4 (27)
			[33]				-164.90 (77)	-114 (20)
22455.62	9/2	odd	6077.21	9/2	even	6005.27	-187.31 (12)	-77.3 (7)
			[33]				-188.9	-73.4 (74)
22663.73	9/2	odd	6354.74	11/2	even	6931.80	-166.43 (26)	3.5 (15)
			[33]				-169.80 (78)	266 (20)
22696.88	11/2	odd	6341.38	11/2	even	6931.80	-153.17 (14)	136.0 (30)
			[33]				-152.64 (76)	167 (20)
23171.11	9/2	odd	5823.91	9/2	even	6005.27	25.79 (17)	-208.4 (72)
			[33]				26.89 (76)	-244 (21)
23197.79	7/2	odd	6378.62	7/2	even	7524.74	-248.04 (23)	5.7 (19)
23229.99	9/2	odd	5804.00	9/2	even	6005.27	-198.22 (9)	-99.8 (25)
23229.99	9/2	odd	6133.95	11/2	even	6931.80	-198.26 (25)	-120.3 (17)
23229.99	9/2	odd	6365.54	7/2	even	7524.74	-198.41 (25)	-103.1 (35)
			Mean				**-198.30 (15)**	**-107.7 (20)**
			[33]				-199.03 (86)	-101.2 (56)
			[99]				-197.2 (7)	-106.1 (94)
23397.38	7/2	odd	5748.14	9/2	even	6005.27	-248.14 (10)	-67.8 (38)
23397.38	7/2	odd	9298.41	7/2	even	7524.74	-248.17 (16)	-66.1 (40)
			Mean				**-248. 15 (12)**	**-66.9 (12)**
23409.54	9/2	odd	5744.12	9/2	even	6005.27	-142.22 (9)	-7.6 (58)
23409.54	9/2	odd	6067.11	11/2	even	6931.80	-142.60 (13)	-5.4 (23)
23409.54	9/2	odd	6293.59	7/2	even	7524.74	-142.14 (16)	-6.0 (27)
			Mean				**-142.32 (25)**	**-6.3 (12)**
			[33]				-142.86 (73)	14.4 (93)
23537.39	9/2	odd	5702.24	9/2	even	6005.27	-180.13 (14)	-50.3 (21)
23537.39	9/2	odd	6243.34	7/2	even	7524.74	-180.17 (11)	-59.1 (39)
			Mean				**-180.15 (10)**	**-54.7 (62)**
			[33]				-180.37 (44)	-48.0 (96)
			[99]				-175.5 (11)	-57.9 (104)
24053.35	9/2	odd	6048.44	7/2	even	7524.74	-89.58 (13)	51.0 (43)
			[33]				-89.49 (58)	66 (15)
24134.10	11/2	odd	5811.57	11/2	even	6931.80	-147.88 (16)	8.7 (25)

Level Energy /cm^{-1}	J	Parity	λ/Å Comment [Ref]	Combining Level			A/MHz	B/MHz
				J	Parity	Energy/cm^{-1}		
24134.10	11/2	odd	6177.22	13/2	even	7950.07	-147.43 (12)	6.7 (15)
24134.10	11/2	odd	6362.08	9/2	even	8420.32	-147.61 (5)	15.1 (10)
			Mean				**-147.64 (22)**	**10.1 (44)**
			[33]				-147.80 (36)	11.8 (95)
			[99]				-148.0 (16)	46.6 (92)
24321.26	9/2	odd	6287.20	9/2	even	8420.32	-163.76 (7)	-141.5 (39)
			[33]				-162.93 (69)	-111 (26)
			[99]				-163.2 (8)	-180. (42)
24445.39	11/2	odd	5708.27	11/2	even	6931.80	-134.23 (9)	-116.5 (61)
			[33]				-134.44 (39)	-126 (12)
			[99]				-134.7 (7)	-211.3 (46)
24797.39	9/2	odd	6104.41	9/2	even	8420.32	-18.27 (19)	82.0 (47)
24842.88	11/2	odd	6087.50	9/2	even	8420.32	-109.11 (9)	-9.2 (25)
			[33]				-108.78 (34)	-3 (12)
24913.86	7/2	odd	6202.73	5/2	even	8796.38	-84.35 (5)	63.0 (44)
24913.86	7/2	odd	6361.40	7/2	even	9198.39	-84.47 (14)	71.0 (33)
			Mean				**-84.41 (12)**	**67.0 (56)**
			[33]				-85.15 (62)	77 (25)
25014.93	11/2	odd	6385.14	11/2	even	9357.91	-124.34 (53)	137.5 (327)
25044.68	7/2	odd	5706.20	7/2	even	7524.74	-176.50 (10)	72.2 (14)
25080.88	11/2	odd	6358.36	11/2	even	9357.91	-138.01 (27)	-73.1 (35)
			[33]				-138.18 (42)	-121 (23)
25138.56	7/2	odd	6271.73	7/2	even	9198.39	-86.33 (9)	65.2 (26)
			[33]				-86.89 (62)	57 (25)
25200.91	11/2	odd	6310.19	11/2	even	9357.91	-165.67 (12)	51.4 (33)
			[33]				-165.47 (82)	28 (20)
25295.29	7/2	odd	6210.66	7/2	even	9198.39	-106.45 (12)	35.3 (48)
			[33]				-106.84 (65)	34 (25)
25352.38	11/2	odd	6250.43	11/2	even	9357.91	-48.28 (6)	-37.9 (44)
			[33]				-50.49 (45)	-80 (45)
25389.22	9/2	odd	6174.63	7/2	even	9198.39	-191.70 (25)	35.2 (21)
			[33]				-193.9 (14)	111 (22)
25524.48	13/2	odd	6065.64	15/2	even	9042.74	-145.46 (11)	79.6 (56)
25524.48	13/2	odd	6183.89	11/2	even	9357.91	-145.18 (22)	48.9 (154)
			Mean				**-145.32 (20)**	**64.2 (217)**
			[33]				-144.94 (70)	44 (25)

Level Energy /cm^{-1}	J	Parity	λ/Å Comment [Ref]	Combining Level			A/MHz	B/MHz
				J	Parity	Energy/cm^{-1}		
25771.53	9/2	odd	5761.69	9/2	even	8420.32	-162.04 (4)	56.02 (36)
25876.56	5/2	odd	5825.86	3/2	even	8716.46	-45.98 (36)	-20.3 (24)
25876.56	5/2	odd	6170.48	5/2	even	9674.84	-45.89 (29)	-15.7 (27)
			Mean				**-45.94 (6)**	**-18.0 (33)**
			[99]				-45.5 (10)	-22.1 (76)
25877.18	9/2	odd	5726.82	9/2	even	8420.32	-195.99 (9)	157.5 (25)
25877.18	9/2	odd	6051.86	11/2	even	9357.91	-195.78 (7)	147.4 (10)
25877.18	9/2	odd	6248.27	9/2	even	9877.17	-195.87 (9)	156.0 (21)
			Mean				**-195.88 (11)**	**153.6 (55)**
			[33]				-195.97 (77)	102 (25)
26041.21	5/2	odd	5770.49	3/2	even	8716.46	-70.72 (19)	-2.5 (42)
26041.21	5/2	odd	6108.40	5/2	even	9674.84	-70.44 (16)	1.8 (24)
			Mean				**-70.58 (19)**	**-0.4 (30)**
			[99]				-70.3 (4)	-6.3 (54)
26210.75	13/2	odd	6298.01	13/2	even	10337.10	-115.78 (6)	-62.0 (48)
			[33]				-114.71 (71)	-73 (20)
26227.11	9/2	odd	6126.33	7/2	even	9908.65	-153.09 (18)	136.7 (35)
26328.01	13/2	odd	5783.67	15/2	even	9042.74	-217.30 (21)	59.7 (150)
26328.01	13/2	odd	6251.82	13/2	even	10337.10	-217.40 (27)	56.3 (25)
			Mean				**-217.35 (11)**	**58.0 (24)**
			[33]				-217.54 (79)	63 (25)
26369.06	7/2	odd	6366.74	7/2	even	10666.78	-153.36 (14)	227.7 (46)
26380.73	9/2	odd	6362.01	7/2	even	10666.78	-106.03 (19)	132.7 (39)
26640.09	7/2	odd	6346.31	5/2	even	10887.25	-107.46 (32)	14.8 (14)
26759.24	11/2	odd	6086.96	13/2	even	10337.10	-182.20 (19)	55.8 (46)
26759.24	11/2	odd	6319.73	11/2	even	10942.01	-181.72 (14)	58.2 (51)
			Mean				**-181.96 (34)**	**57.1 (17)**
			[33]				-181.51(75)	35 (25)
26912.77	15/2	odd	6031.27	13/2	even	10337.10	-131.80 (8)	6.7 (52)
			[33]				-132.02 (85)	-77 (73)
26991.89	11/2	odd	6206.14	9/2	even	10883.26	-215.17 (11)	118.1 (41)
27245.45	11/2	odd	6382.06	15/2	even	11580.86	-115.49 (21)	281.4 (123)
27299.54	7/2	odd	5748.54	7/2	even	9908.65	-84.51 (7)	67.1 (19)
27308.94	13/2	odd	6108.19	11/2	even	10942.01	-167.06 (14)	-12.3 (53)
27308.94	13/2	odd	6273.57	15/2	even	11373.47	-167.34 (18)	-12.1 (26)

Level Energy /cm^{-1}	J	Parity	λ/Å Comment [Ref]	Combining Level			A/MHz	B/MHz
				J	Parity	Energy/cm^{-1}		
			Mean				**-167.20 (20)**	**-12.2 (18)**
27352.28	11/2	odd	6338.83	15/2	even	11580.86	-134.82 (60)	365.0 (348)
27425.02	9/2	odd	6361.42	9/2	even	11709.60	-246.89 (29)	-13.7 (27)
27518.40	11/2	odd	6272.76	15/2	even	11580.86	-107.53 (25)	338.7 (303)
27611.72	15/2	odd	6156.60	15/2	even	11373.47	-139.88 (12)	-189.9 (109)
			[33]				-139.61 (69)	-244 (25)
27744.20	13/2	odd	6358.41	11/2	even	12021.35	-134.97 (18)	17.0 (44)
27781.77	11/2	odd	6170.79	15/2	even	11580.86	-56.74 (16)	235.2 (55)
28196.16	13/2	odd	6302.66	13/2	even	12334.22	-105.31 (10)	59.2 (23)
			[33]				-105.16 (65)	-90 (25)
28563.48	13/2	odd	6385.14	15/2	even	12906.58	-90.85 (15)	-43.3 (132)
28725.93	13/2	odd	6319.62	15/2	even	12906.58	-90.68 (33)	-68.5 (91)
28860.16	11/2	odd	6258.80	11/2	even	12887.08	-76.75 (12)	-210.8 (22)
29260.74	15/2	odd	6263.20	13/2	even	13298.89	-219.74 (17)	-89.3 (40)
29362.53	15/2	odd	6341.54	13/2	even	13597.86	-166.38 (10)	309.7 (37)
29878.83	7/2	odd	6284.72	9/2	even	13971.62	-175.03 (37)	-99.9 (23)

Table 10.8: Spectral lines investigated for ^{145}Nd II using CLIBS.

S. No	Wavelength (air) λ/Å	Even Level		Odd Level	
		Energy / cm^{-1}	J	Energy / cm^{-1}	J
1	6051.86	9357.91	11/2	25877.18	9/2
2	6065.64	9042.74	15/2	25524.48	13/2
3	6067.11	6931.80	11/2	23409.54	9/2
4	6077.21	6005.27	9/2	22455.62	9/2
5	6086.96	10337.10	13/2	26759.24	11/2
6	6087.50	8420.32	9/2	24842.88	11/2
7	6104.41	8420.32	9/2	24797.39	9/2
8	6108.19	10942.01	11/2	27308.94	13/2
9	6108.40	9674.84	5/2	26041.21	5/2
10	6126.33	9908.65	7/2	26227.11	9/2
11	6133.95	6931.80	11/2	23229.99	9/2
12	6156.60	11373.47	15/2	27611.72	15/2
13	6170.48	9674.84	5/2	25876.56	5/2
14	6170.79	1158.86	13/2	27781.77	11/2
15	6174.63	9198.39	7/2	25389.22	9/2
16	6183.89	9357.91	11/2	25524.48	13/2
17	6202.73	8796.38	5/2	24913.86	7/2
18	6210.66	9198.39	7/2	25295.29	7/2
19	6243.34	7524.74	7/2	23537.39	9/2
20	6248.27	9877.17	9/2	25877.18	9/2
21	6250.43	9357.91	11/2	25352.38	11/2
22	6273.57	11373.47	15/2	27308.94	13/2
23	6287.20	8420.32	9/2	24321.26	9/2
24	6289.41	7524.74	7/2	23397.38	9/2

S. No	Wavelength (air) λ/Å	Even Level		Odd Level	
		Energy / cm^{-1}	J	Energy / cm^{-1}	J
25	6298.01	10337.10	13/2	26210.75	13/2
26	6302.66	12334.22	13/2	28196.16	13/2
27	6319.62	12906.58	15/2	28725.93	13/2
28	6319.73	10942.01	11/2	26759.24	11/2
29	6338.83	1158.86	13/2	27352.28	11/2
30	6341.38	6931.80	11/2	22696.88	11/2
31	6341.54	13597.86	11/2	29362.53	15/2
32	6354.74	6931.80	11/2	22663.73	9/2
33	6365.54	7524.74	7/2	23229.99	9/2
34	6382.06	1158.86	13/2	27245.45	11/2
35	6382.08	8420.32	9/2	24134.10	11/2

Table 10.9: Measured hyperfine constants of even parity fine energy levels of ^{145}Nd II. The results are compared (wherever available) with the results of Maoscheng [99].

Level Energy /cm^{-1}	J	Parity	λ/Å Comment [Ref]	Combining Level			A/MHz	B/MHz
				Energy/cm^{-1}	J	Parity		
6005.27	9/2	even	6077.21	22455.62	9/2	odd	-126.23 (15)	81.6 (66)
			[99]				-124.1(10)	66.7 (105)
6931.80	11/2	even	6067.11	23409.54	9/2	odd	-93.89 (63)	58.3 (59)
6931.80	11/2	even	6133.95	23229.99	9/2	odd	-92.80 (20)	53.0 (30)
6931.80	11/2	even	6341.38	22696.88	11/2	odd	-92.32 (31)	35.7 (37)
6931.80	11/2	even	6354.74	22663.73	9/2	odd	-93.69 (41)	70.3 (15)
			Mean				**-93.17 (74)**	**54.3 (144)**
			[99]				**-93.5 (11)**	**28.1 (15)**
7524.74	7/2	even	6243.34	23537.39	9/2	odd	-140.18 (42)	103.6 (37)
7524.74	7/2	even	6289.41	23397.38	9/2	odd	-140.77 (12)	100.9 (14)
7524.74	7/2	even	6365.54	23229.99	9/2	odd	-140.60 (19)	112.0 (70)
			Mean				**-140.52 (30)**	**105.5 (58)**
8420.32	9/2	even	6087.50	24842.88	11/2	odd	-100.16 (71)	103.7 (11)
8420.32	9/2	even	6104.41	24797.39	9/2	odd	-100.07 (23)	100.0 (40)
8420.32	9/2	even	6287.20	24321.26	9/2	odd	-99.91 (13)	88.5 (16)
8420.32	9/2	even	6382.08	24134.10	11/2	odd	-98.28 (32)	112.8 (12)
			Mean				**-99.60 (89)**	**101.2 (99)**
8796.38	5/2	even	6202.73	24913.86	7/2	odd	-121.79 (49)	-0.1 (79)
9198.39	7/2	even	6174.63	25389.22	9/2	odd	-89.69 (58)	53.1 (30)
9198.39	7/2	even	6210.66	25295.29	7/2	odd	-90.69 (17)	55.7 (24)
			Mean				**-90.19 (71)**	**54.4 (19)**
9674.84	5/2	even	6108.40	26041.21	5/2	odd	-158.79 (17)	63.7 (13)
9674.84	5/2	even	6170.48	25876.56	5/2	odd	-158.55 (26)	57.2 (11)
			Mean				**-158.67 (18)**	**60.4 (46)**
9877.17	9/2	even	6248.27	25877.18	9/2	odd	-69.60 (20)	67.5 (54)
9908.65	7/2	even	6126.33	26227.11	9/2	odd	-140.80 (20)	103.3 (31)

Level Energy /cm^{-1}	J	Parity	λ/Å Comment [Ref]	Combining Level			A/MHz	B/MHz
				Energy/cm^{-1}	J	Parity		
9357.91	11/2	even	6051.86	25877.18	9/2	odd	-76.27 (31)	89.5 (81)
9357.91	11/2	even	6183.89	25524.48	13/2	odd	-76.13 (13)	97.1 (141)
9357.91	11/2	even	6250.43	25352.38	11/2	odd	-76.71 (37)	98.9 (62)
			Mean				**-76.64 (33)**	**99.5 (103)**
9042.74	15/2	even	6065.64	25524.48	13/2	odd	-62.14 (59)	114.5 (92)
10337.10	13/2	even	6086.96	26759.24	11/2	odd	-64.14 (39)	110.5 (33)
10337.10	13/2	even	6298.01	26210.75	13/2	odd	-64.15 (17)	111.6 (37)
			Mean				**-64.15 (19)**	**111.1 (15)**
10942.01	11/2	even	6108.19	27308.94	13/2	odd	-60.41 (30)	74.1 (31)
10942.01	11/2	even	6319.73	26759.24	11/2	odd	-59.29 (18)	74.4 (52)
			Mean				**-59.85 (80)**	**74.2 (14)**
11373.47	15/2	even	6156.60	27611.72	15/2	odd	-56.99 (19)	107.5 (58)
11373.47	15/2	even	6273.57	27308.94	13/2	odd	-57.68 (28)	121.0 (15)
			Mean				**-56.99 (49)**	**114.2 (96)**
1158.86	13/2	even	6170.79	27781.77	11/2	odd	-73.51 (20)	160.0 (50)
1158.86	13/2	even	6338.83	27352.28	11/2	odd	-73.13 (29)	164.1 (56)
1158.86	13/2	even	6382.06	27245.45	11/2	odd	-72.85 (32)	166.3 (102)
			Mean				**-73.17 (33)**	**163.9 (45)**
12334.22	13/2	even	6302.66	28196.16	13/2	odd	-62.24 (43)	-239.2 (681)
12906.58	15/2	even	6319.62	28725.93	13/2	odd	-49.82 (49)	-103.6 (46)
13597.86	11/2	even	6341.54	29362.53	15/2	odd	-60.44 (31)	200.3 (25)

Table 10.10: Measured hyperfine constants of odd parity fine energy levels of ^{145}Nd II. The results are compared (wherever available) with the results of Maoscheng [99].

Level Energy /cm^{-1}	J	Parity	λ/Å Comment [Ref]	Combining Level			A/MHz	B/MHz
				Energy/cm^{-1}	J	Parity		
22455.62	9/2	odd	6077.21	6005.27	9/2	even	-116.07 (16)	-32.7 (84)
22663.73	9/2	odd	6354.74	6931.80	11/2	even	-103.70 (47)	-19.7 (30)
22696.88	11/2	odd	6341.38	6931.80	11/2	even	-94.12 (39)	80.0 (51)
23229.99	9/2	odd	6133.95	6931.80	11/2	even	-122.85 (21)	-57.5 (60)
23229.99	9/2	odd	6365.54	7524.74	7/2	even	-122.75 (17)	-58.8 (69)
			Mean				**-122.80 (19)**	**-58.16 (65)**
			[99]				-121.1 (12)	-52.0 (91)
23397.38	9/2	odd	6289.41	7524.74	7/2	even	-153.83 (15)	-34.3 (25)
23409.54	9/2	odd	6067.11	6931.80	11/2	even	-88.84 (76)	-4.6 (17)
23537.39	9/2	odd	6243.34	7524.74	7/2	even	-111.00 (31)	-42.3 (38)
			[99]				-109.8 (14)	-31.4 (57)
24134.10	11/2	odd	6382.08	8420.32	9/2	even	-90.33 (35)	9.8 (15)
							-91.95 (270)	23.1 (83)
24321.26	9/2	odd	6287.20	8420.32	9/2	even	-101.67 (11)	-78.1 (13)
			[99]				-100.9 (16)	-103.1 (31)
24797.39	9/2	odd	6104.41	8420.32	9/2	even	-11.54 (26)	38.1 (78)
24842.88	11/2	odd	6087.50	8420.32	9/2	even	-67.60 (57)	-9.6 (27)
24913.86	7/2	odd	6202.73	8796.38	5/2	even	-52.60 (40)	34.6 (62)
25295.29	7/2	odd	6210.66	9198.39	7/2	even	-67.17 (13)	33.2 (45)
25352.38	11/2	odd	6250.43	9357.91	11/2	even	-29.87 (32)	-20.9 (21)
25389.22	9/2	odd	6174.63	9198.39	7/2	even	-118.82 (51)	17.5 (24)
25524.48	13/2	odd	6183.89	9357.91	11/2	even	--89.80 (21)	34.7 (49)
25524.48	13/2	odd	6065.64	9042.74	15/2	even	-89.77 (68)	44.5 (69)
			Mean				**-89.78 (12)**	**39.6 (70)**
25876.56	5/2	odd	6170.48	9674.84	5/2	even	-28.83 (12)	-14.5 (16)
			[99]				-28.3 (4)	-9.7 (32)
25877.18	9/2	odd	6248.27	9877.17	9/2	even	-120.99 (24)	77.1 (65)
25877.18	9/2	odd	6051.86	9357.91	11/2	even	-120.46 (45)	73.0 (19)
			Mean				**-120.73 (37)**	**75.1 (29)**

Level Energy /cm^{-1}	J	Parity	λ/Å Comment [Ref]	Combining Level			A/MHz	B/MHz
				Energy/cm^{-1}	J	Parity		
26041.21	5/2	odd	6108.40	9674.84	5/2	even	-44.05 (13)	-1.4 (22)
26210.75	13/2	odd	6298.01	10337.10	13/2	even	-72.36 (17)	-29.2 (54)
26227.11	9/2	odd	6126.33	9908.65	7/2	even	-94.89 (27)	59.3 (56)
26759.24	11/2	odd	6086.96	10337.10	13/2	even	-113.43 (44)	30.7 (21)
26759.24	11/2	odd	6319.73	10942.01	11/2	even	-111.92 (12)	36.7 (35)
			Mean				**-112.68 (107)**	**30.7 (42)**
27245.45	11/2	odd	6382.06	1158.86	13/2	even	-71.33 (28)	149.5 (50)
27308.94	13/2	odd	6108.19	10942.01	11/2	even	-104.28 (24)	1.3 (18)
27308.94	13/2	odd	6273.57	11373.47	15/2	even	-105.13 (25)	0.7 (40)
			Mean				**-104.71 (60)**	**1.0 (5)**
27352.28	11/2	odd	6338.83	1158.86	13/2	even	-84.25 (32)	247.3 (186)
27611.72	15/2	odd	6156.60	11373.47	15/2	even	-87.49 (17)	-105.6 (33)
27781.77	11/2	odd	6170.79	1158.86	13/2	even	-35.77 (30)	123.5 (58)
28196.16	13/2	odd	6302.66	12334.22	13/2	even	-73.83 (42)	-166.0 (450)
28725.93	13/2	odd	6319.62	12906.58	15/2	even	-57.22 (14)	-34.6 (41)
29362.53	15/2	odd	6341.54	13597.86	11/2	even	-103.44 (28)	170.9 (71)

10.4 **DISCUSSION**

In this chapter the experimental investigations of the hyperfine structure of the spectral lines of the singly ionized odd isotopes of barium (^{137}Ba II), lanthanum (^{139}La II) and neodymium (^{143}Nd II and ^{145}Nd II) have been discussed. These investigations are carried out on the experimental set up of MARS-II, using the high resolution spectroscopic technique of collinear laser ion beam spectroscopy. To investigate the hyperfine structure the magnetic dipole coupling constants *A* and the electric quadrupole coupling constants *B* of the fine structure energy levels have been determined and the results are compared with the literature values.

The hyperfine structure of the well known spectral line $5d\ ^2D_{3/2} \rightarrow 6p\ ^2P°_{3/2}$ (λ = 5853.67 Å) of the ^{137}Ba II is investigated for the control-check of the MARS-II and to test out the stabilities of the magnetic field of the 80° sector magnet and high voltages involved in the experiment. The newly incorporated laser frequency locking system in which the laser frequency is locked on the frequency of one of the components of the hyperfine structure under investigation was also checked. Our results for the investigation of ^{137}Ba II presented in Table 10.1 show an excellent agreement with theoretical as well as experimental investigations.

The hyperfine structure constants *A* and *B* of fine structure levels are determined from the experimentally recorded structure by solving equation 4.13, using the method of least-squares. To improve the signal to noise ratio, minimum 5 similar recordings were averaged to form a single data file and to compute statistical averages and statistical errors for a particular transition, minimum 3 such data files are used. The preliminary values of *A* and *B* for the fit program were estimated with the help of a simulation program which takes as input *I* and *J* values of the combing levels. A mixed line profile (20% Gaussian and 80% Lorentzian) yielded the best fitting of the recorded structure. The observed spectral line width (FWHM) is of the order of 40 – 75 MHz but generally it is not constant across a single structure because of the power broadening variation which is due to the variation in oscillator strengths for different hyperfine components [177]. Normally the diagonal components ($\Delta J = \Delta F$) are broadened due to optical pumping while the off-diagonal components ($\Delta J = \Delta F \pm 1$) are not. The intensity of the hyperfine components is also affected by the optical pumping and it is more pronounced for the diagonal components as compared to the off-diagonal components. Despite the fact that the experientially recorded spectral line width is several times less than the line width in a strongly cooled hollow cathode

discharge lamp even than it is much larger as compared to the natural line width. A detail discussion about the line broadening in CLIBS is presented in chapter 8. The major reasons are fluctuations in the acceleration voltage, the ion source energy spread caused by collisions with impurities and other isotopes. The laser power broadening, jittering and divergence of laser beam and the inadequate collinearity of laser- and ion beam can be other reasons of line broadening. The averaging of different recordings can also cause line broadening if the laser frequency stabilization is not working accurately. The systematic errors can also come into play due the experimental uncertainties in the acceleration voltage and scanning voltage.

Occasionally a minor asymmetricity was observed in the lines profiles of the spectral lines under investigation, particularly for ^{143}Nd II and ^{145}Nd II spectral lines. The asymmetric line profile could be due to the striking of a small fraction of the ion beam with entrance aperture of the interaction chamber or scattering of the ion beam from a slit inserted just before beam scanner to get rid of traces of adjacent even isotopes of Nd. Poor collinearity of laser- and ion beam in the interaction chamber can also cause asymmetry in line profile. The symmetricity of the line shape can be improved by inserting the ion beam into the interaction chamber on a slightly different path but it reduces the number of ions available for the experiment. As the natural abundance of ^{143}Nd and ^{145}Nd is just 12.2% and 8.3%, respectively thus the isotopically pure ion beam current for these isotopes useful for the experiments is very small. So the ion bean current was preferred over the asymmetricity of the line profile and also in the fitting of the hyperfine structure this asymmetricity was ignored. The blend structures of maximum two spectral lines were recorded together in a single scan and these structures were analyzed using two lines fitting in the fit program.

The experimentally determined and the literature values (wherever available) of the magnetic dipole coupling constant *A* and electric quadrupole coupling constant *B* of the spectral lines of ^{139}La II, ^{143}Nd II and ^{145}Nd II are given in tabulated form at the end of this chapter (before discussion section). The values of the coupling constants *A* are not only consistent when a level is investigated at different transitions but are also in agreement with the literature values and mostly their accuracy is significantly improved. Although *B*-values are somewhat inadequately determined, our results depict a much confined statistical deviation. Generally a small value of the electric quadrupole moment results in the relative large scatter in the *B*-values.

The metastable even-parity level $\sigma = 10094.86\ \text{cm}^{-1}$ is the highest energy lower level and metastable even-parity level $\sigma = 5249.70\ \text{cm}^{-1}$ is the lowest energy lower level that has been investigated for ^{139}La II during this work. The energy level $\sigma = 5249.70\ \text{cm}^{-1}$ is also the only one level for all elements (Pr II, ^{139}La II, ^{143}Na II, ^{145}Na II and ^{137}Ba II) investigated in our group using CLIBS method which has zero *J*-value. The highest and the lowest energy metastable upper levels for ^{139}La II investigated during this study are $\sigma = 27423.91\ \text{cm}^{-1}$ and $\sigma = 21441.73\ \text{cm}^{-1}$, respectively. For both ^{143}Na II and ^{145}Na II the highest and the lowest energy upper levels which were excited during this work are $\sigma = 29878.83\ \text{cm}^{-1}$ and $\sigma = 21871.52\ \text{cm}^{-1}$, respectively, while the highest and the lowest energy lower levels are $\sigma = 13971.62\ \text{cm}^{-1}$ and $\sigma = 6005.27\ \text{cm}^{-1}$, respectively. The even-parity metastable lower level $\sigma = 13971.62\ \text{cm}^{-1}$ has the maximum energy value of all the investigated levels for all the elements (Ba, Pr, La and Nd) with the method of CLIBS in our group. The odd-parity upper energy level $\sigma = 23171.11\ \text{cm}^{-1}$ is the only one energy level for ^{143}Nd II and ^{145}Nd II investigated so far in our group which has a positive value of magnetic dipole interaction constant *A*. In all other known energy levels either even or odd, except the odd-parity energy level $\sigma = 25561.19\ \text{cm}^{-1}$ excited by Rosner et al [33], the *A*-values are always negative for Nd II.

Using the hyperfine coupling contents of ^{143}Nd II and ^{145}Nd II the hyperfine anomaly is also calculated. Theoretically the ratios A_{143}/A_{145} should be equal to the ratios of the nuclear magnetic moments i.e. $(\mu_{143}/I_{143})\Big/(\mu_{143}/I_{143})$ with typically 1% hyperfine anomaly [230]. As the nuclear spin quantum number *I* for ^{143}Nd and ^{145}Nd is equal ($I_{143} = I_{145} = 7/2$) therefore μ_{143}/μ_{145} is equal to A_{143}/A_{145} and similarly B_{143}/B_{145} is equal to the ratio of the nuclear electric quadrupole moments i.e. Q_{143}/Q_{145}. The hyperfine anomaly have been determined most accurately by atomic beam magnetic resonance [125], electron paramagnetic resonance [231] and electron nuclear double resonance methods [232]. The weighted averages from these results as determined by Rosner [33] are μ_{143}/μ_{145} = 1.60884 (2) and Q_{143}/Q_{145} = 1.919 (33). The hyperfine anomaly calculated from our results is A_{143}/A_{145} = 1.607 (11) and B_{143}/B_{145} = 1.882(27). Although the CLIBS technique is not suitable for such investigations our results are generally in agreement with literature results with some exceptions. For weak lines in some cases the *B*-values and rarely the *A*-values were fixed with values known from other transitions to calculate A_{143}/A_{145} and B_{143}/B_{145}.

11 CONCLUSIONS

In this research work the hyperfine structure of spectral lines of ^{137}Ba II and three lanthanides elements; ^{141}Pr II, ^{139}La II, ^{143}Nd II, and ^{145}Nd II, were investigated. The magnetic dipole constants *A* and the electric quadrupole constants *B* of the involved levels were determined with high accuracy and the data were compared with other published results.

The hyperfine structures of some spectral lines of ^{141}Pr II was investigated using three different laser spectroscopic techniques: Doppler limited LIF spectroscopy, inter-modulated saturation spectroscopy and CLIBS. The spectral line width was the largest (600 -700 MHz) in case of LIF spectroscopy and it decreased almost three times (200-250 MHz) in case of inter-modulated laser induced fluorescence spectroscopy. The spectral line widths obtained with CLIBS method were in the range of 40 - 70 MHz and were more than 10 times smaller as compared to the line width obtained with Doppler limited spectroscopy and nearly 5 times smaller than inter-modulated laser induced fluorescence spectroscopy. The saturation spectroscopy is relatively difficult to perform in the sense that high laser power is required and it is difficult to obtain high laser power in a broad region of laser dyes. The accuracy of the hyperfine coupling constants was much better in case of the CLIBS method and the values of the magnetic dipole coupling constant *A* were determined with an accuracy of less than 1 MHz, whereas the statistical deviation in the electric quadrupole coupling constants *B* were generally in the range of 1-5 MHz. The comparison of the three spectroscopic methods revealed that CLIBS is the much superior technique to reduce the Doppler broadening and for the accurate determination of hyperfine coupling constants. On the other hand, CLIBS is restricted to the investigation of transitions where metastable low-lying energy levels are involved and the complexity of the experimental setup makes the CLIBS studies difficult to perform.

During the CLIBS measurements a minor asymmetric line profile occasionally observed especially at spectral lines of ^{143}Nd II and ^{145}Nd II, was ignored. The asymmetric line profile could be due to the striking of a small fraction of the ion beam with the entrance aperture of the interaction chamber or cutting of a small fraction of the ion beam from a slit inserted just before the beam scanner to get rid of traces of adjacent even isotopes of Nd. Poor collinearity of

laser- and ion beam in the interaction chamber can also cause asymmetry in line profile. The symmetry of the line shape can be improved by inserting the ion beam into the interaction chamber on a slightly different path but that will reduces the number of ions available for the experiment. As the ion beam current for these isotopes useful for the experiments is very small, the ion beam current was preferred over the asymmetricity of the line profile and also in the fitting of the hyperfine structure this asymmetricity was ignored.

During this research project altogether 149 fine structure energy levels were investigated by laser excitation of 137 spectral lines. Various levels were investigated for the first time and the coupling constants of numerous levels were improved. Blend structures (the hyperfine structures of closely spaced spectral lines) were recorded together in a single scan and these structures were analyzed using two lines fitting in the fit program. The experimental investigation of the spectral lines revealed that the magnetic dipole coupling constant *A* and electric quadrupole coupling constant *B* of the involved levels were not only consistent when a level was investigated at different transitions but were also in agreement with the literature values and mostly their accuracy is significantly improved. Although *B*-values were somewhat inadequately determined, our results depict a narrow statistical deviation. Generally a small value of the electric quadrupole moment results in the relative large scatter in the *B*-values.

The ratios of the magnetic dipole constants for ^{143}Nd II and ^{145}Nd II i.e. A_{143}/A_{145}, generally showed a hyperfine anomaly in good agreement with literature values but occasionally it violates whereas the ratios of the electric quadrupole constants B_{143}/B_{145} depicted a relatively large variation.

The highest energy upper level which was excited during this work belongs to ^{143}Nd II and has energy $\sigma = 29878.83\ \text{cm}^{-1}$. The odd-parity upper energy level $\sigma = 23171.11\ \text{cm}^{-1}$ is the only one energy level for ^{143}Nd II and ^{145}Nd II investigated so far in our group which has a positive value of magnetic dipole interaction constant *A*. In all other known energy levels, either even or odd, except the odd-parity energy level $\sigma = 25561.19\ \text{cm}^{-1}$ investigated by Rosner et al [33], the *A*-values are always negative for Nd II. The metastable even-parity levels $\sigma = 13971.62\ \text{cm}^{-1}$ and $\sigma = 5249.70\ \text{cm}^{-1}$ are the highest and the lowest energies lower levels, respectively that were investigated in this work. The level $\sigma = 13971.62\ \text{cm}^{-1}$ belongs to ^{143}Nd II and the level $\sigma = 5249.70\ \text{cm}^{-1}$ belongs to ^{139}La II. The even-parity lower level $\sigma = 13971.62\ \text{cm}^{-1}$ has the

maximum energy value and the energy level $\sigma = 5249.70\ \mathrm{cm}^{-1}$ is the only one level which has a zero *J*-value, for of all the investigated levels for all the elements (Ba, Pr, La and Nd) with the method of CLIBS in our group. The maximum and the minimum energy limit on the lower levels is caused by the ion source of MARS-II and the combination of stray laser light suppressing filter (BG-12) and the photomultiplier tube (PMT XP2020), respectively. Simply by changing the filter and PMT combination many other levels of Pr, La and Nd can be investigated. Using enriched ^{143}Nd or ^{145}Nd instead of natural Nd in the ion source a large number of spectral lines can be investigated without changing any other components of the present experimental setup.

We hope this work will be helpful in the studies of the lanthanides in astrophysics and will reduce the uncertainties in the analysis of Doppler shift, speed of stars, elemental and isotopic abundances in stellar spectra. It will also be a strong motivation for supplementary experiments and will be an important foundation for advance theoretical studies.

APPENDIX

Algorithm of the program "Scan(SR400QPX1200)"[162].

1) The communication port, COM1 is assigned to the power supply and port COM2 is assigned to the photon counter.
2) The program reads the entries from the front panel. For example scan start voltage "V1", scan stop voltage, step size "DELTAV1", destination folder to save the recorded files etc.
3) The photon counter is reset and the parameters like, dwell time "dt = 0", period counts "NP".

   are fixed.
4) Then a loop starts in which the scanning is carried out. The photons are counted for a counting period (this value is manually fed in the photon counter; therefore before starting the scanning these values must be confirmed). In the scanning loop, a delay corresponding to the counting time is introduced.
5) The displays of the power supply (voltage value; x-axis) and photon counter (photon counts; y-axis) are read.
6) A data file is created in the destination folder; the photon counts are saved in column 1, the scanning voltage is saved in column 2. In columns 3 and 4 constant values for example 100 and 150 are stored, respectively. The entries in columns are separated by a double space. This format of data entries is the prerequisite of the data viewer. The file is created for the first measurement; for next measurements, the data points are stored in next rows of this file. A new file is created for a new scan.
7) The recorded data point is displayed in the digital form as well as in the graphical form on the front panel.
8) The scanning voltage is increased by a step size (sz). The rise time of the high voltage scanning power supply is about 15 msec therefore a delay of 0.02 sec is also introduced, so that the counting starts when the voltage is stable at its new value.
9) Steps from 4-8 are repeated until the stop voltage is reached or the program is forcibly stopped.
10) If more than one scans is required, the QPX1200 is set to the start voltage again. A delay of 2 seconds is provided before the start of each additional scan so that the high voltage power supply becomes stable at start voltage. Steps from 2 to 9 are repeated.

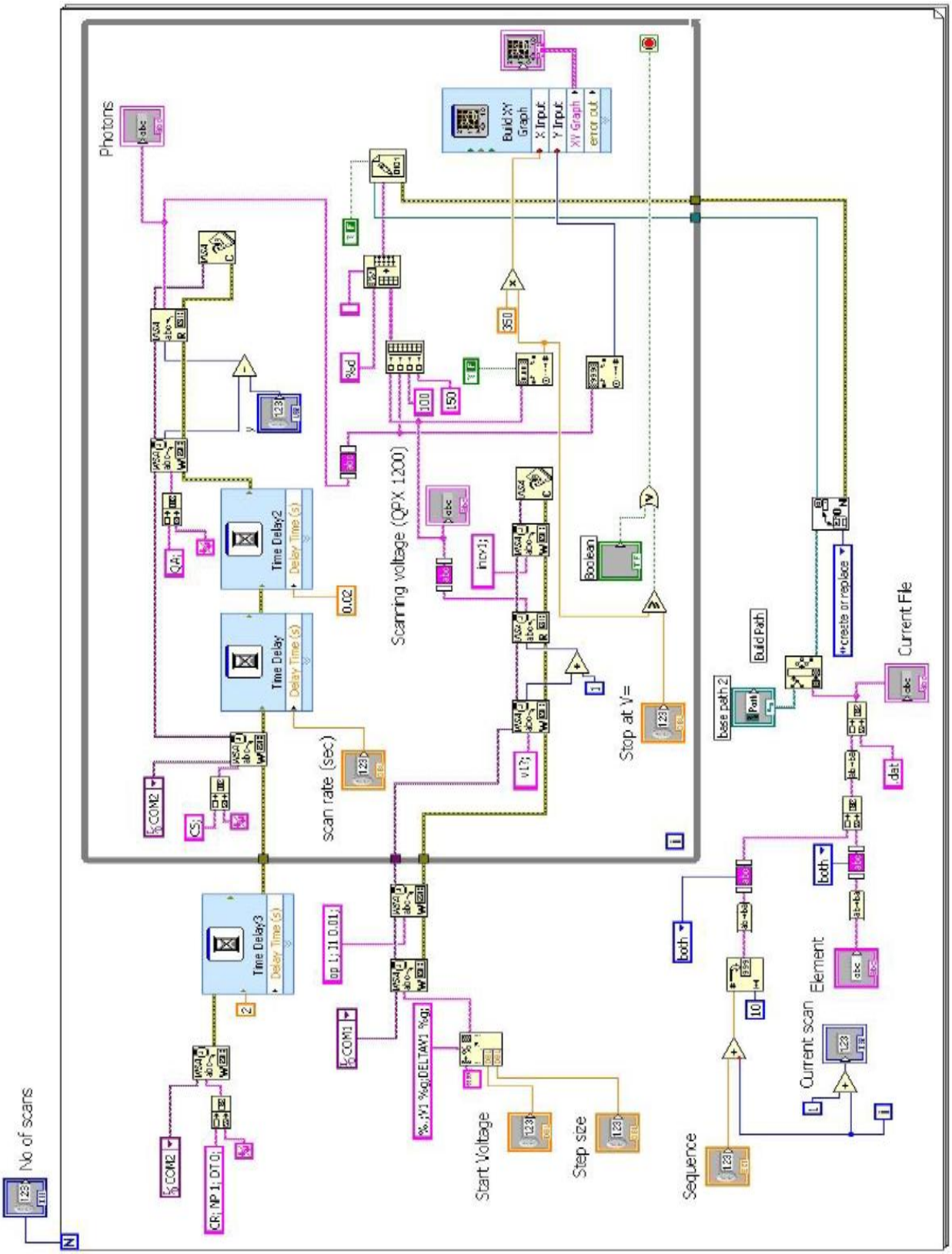

Figure 11.1: The block diagram of the program "Scan(SR400QPX1200)" [162].

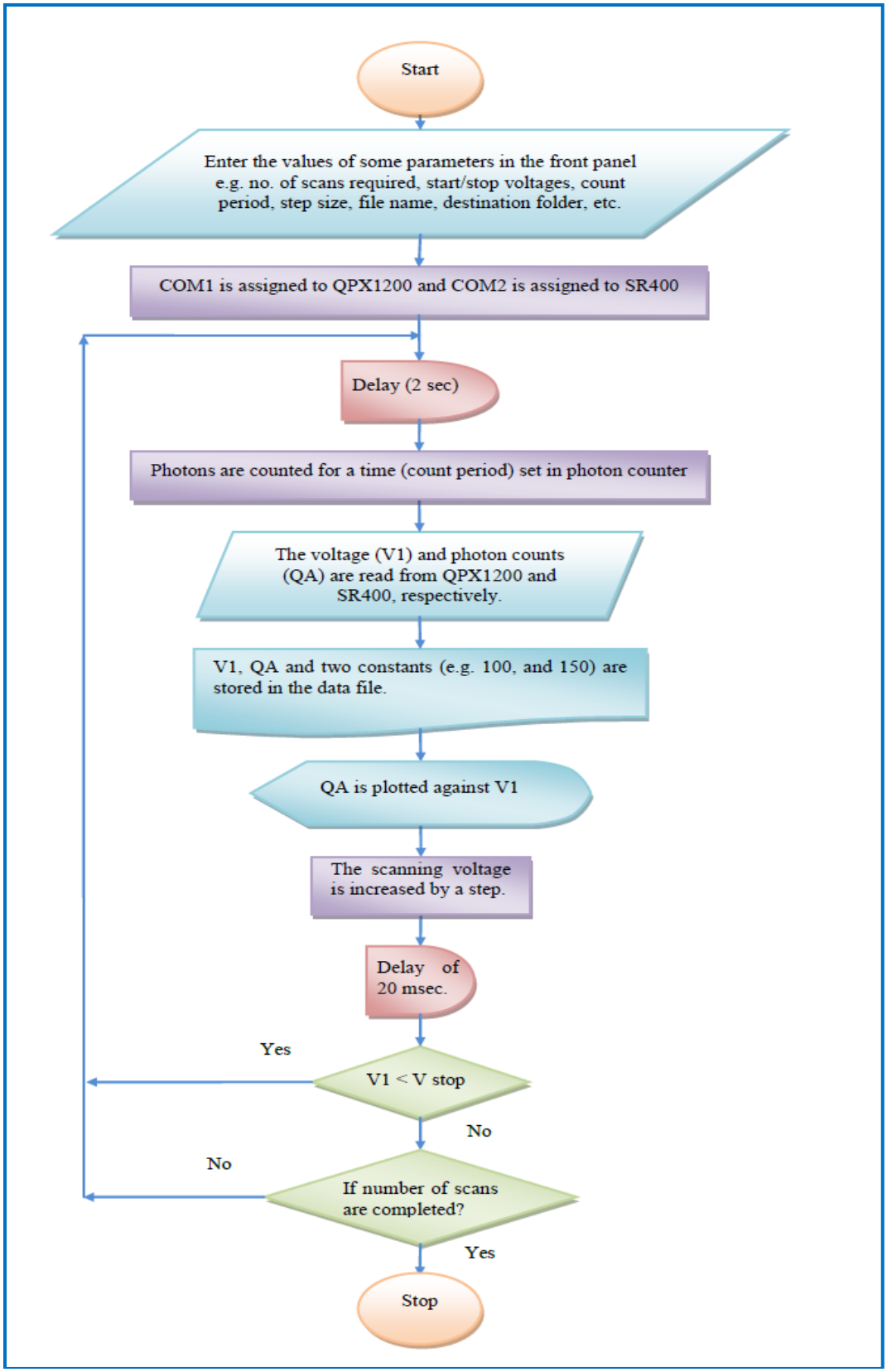

Figure 11.2: The flow chart of the program "Scan(SR400QPX1200)" [162].

Algorithm of the Program "NdLinRel" [162].

1) A data file is selected and input parameters, like acceleration voltage, wave number, and acceleration voltage and step size are inserted.
2) The data points X1 (voltages) and T (intensities) are extracted from the data file and the frequency points (X5) are determined applying equation 9.1.
3) For a = 1 to bb (total number of points), a linear frequency scale is produced using linx(a) = a * sz.
4) For i = 1 to bb, the linear frequency points are compared with the recorded data points i.e. ds(i) = linx(a) - X5(i).
5) The weights for all the points which lie within the ± sz (step size) of the linear frequency point are determined by ds1(i) = [sz-|ds(i)|] / sz.
6) The weighted intensity of the ith point is calculated by T1(i) = T(i)*ds1(i)
7) Total weights ds2(i) = and total intensities T2(i) = are calculated.
8) New intensity at linear frequency point is determined by T2/ds2.
9) Steps 5 - 10 are repeated for next data point.
10) The calculated intensities are stored in a "LIN" file.
11) Some parameters are stored in a "PAR" file.

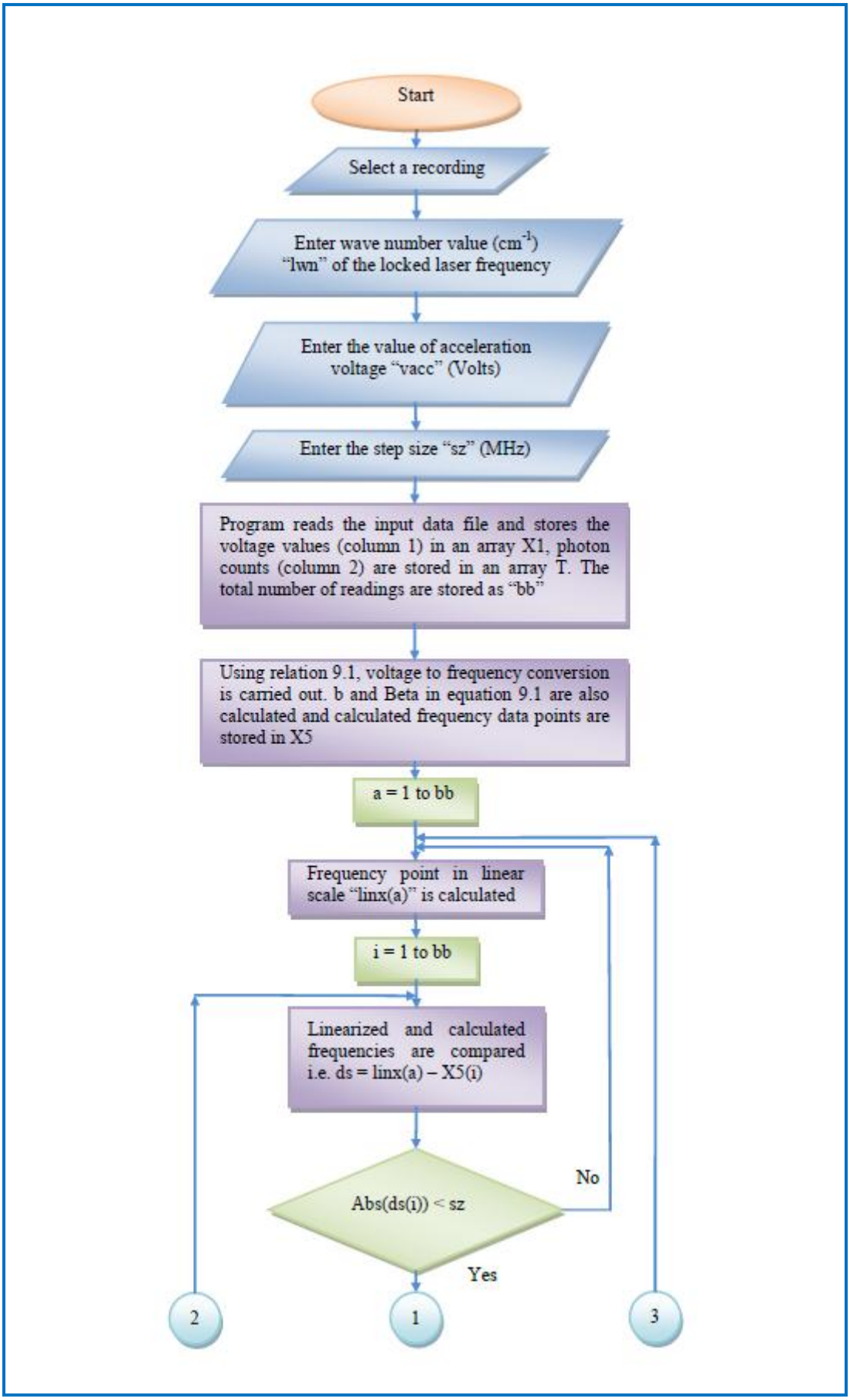
Start
Select a recording
Enter wave number value (cm-1) "lwn" of the locked laser frequency
Enter the value of acceleration voltage "vacc" (Volts)
Enter the step size "sz" (MHz)
Program reads the input data file and stores the voltage values (column 1) in an array X1, photon counts (column 2) are stored in an array T. The total number of readings are stored as "bb"
Using relation 9.1, voltage to frequency conversion is carried out. b and Beta in equation 9.1 are also calculated and calculated frequency data points are stored in X5
a = 1 to bb
Frequency point in linear scale "linx(a)" is calculated
i = 1 to bb
Linearized and calculated frequencies are compared i.e. ds = linx(a) – X5(i)
Abs(ds(i)) < sz
No
Yes
2
1
3

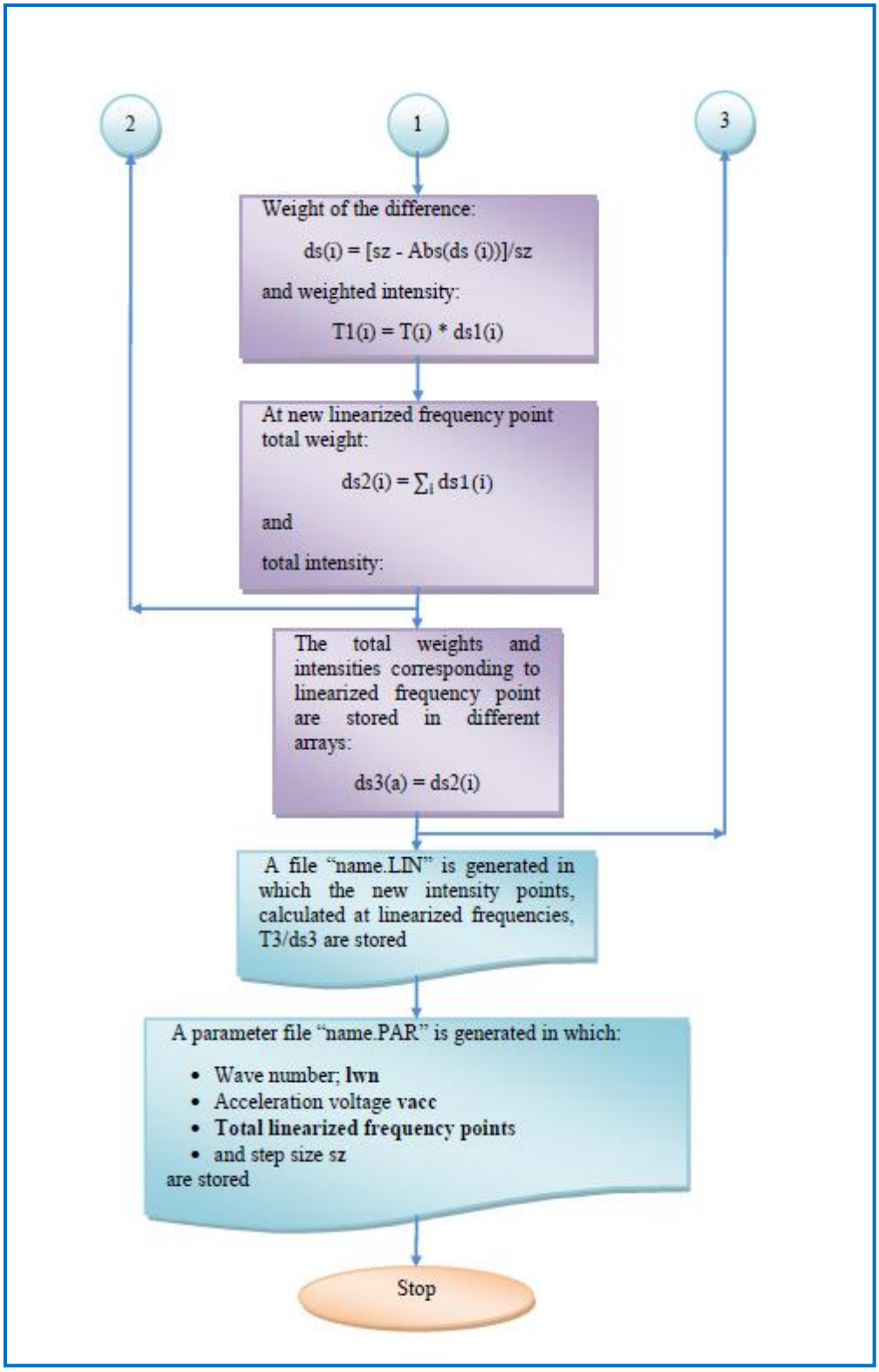

Figure 11.3: The flow chart of the linearization software "NdLinRel"[162].

BIBLIOGRAPHY

Literature Consulted

- White H. E., Introduction to Atomic Spectra, McGraw-Hill Ltd. (1934).
- Wolfgang Demtröder, Atoms, Molecules and Photons, Springer-Verlag Berlin Heidelberg (2006).
- Condon E. U. and Shortly G. H., The Theory of Atomic Spectra, Cambridge University Press, 1959.
- G. K. Woodgate., Elementary Atomic Structure, Oxford University Press Oxford, 2nd edition 1980.
- Kuhn H. G., Atomic Spectra, Academic Press, New York (1962).
- Thorne, A. P., Spectrophysics, Chapman & Hall, London 2nd edition, (1974).
- Martin W C, Zalubas R and Hagan L., 1978 Atomic Energy Levels - The Rare Earth Elements National Bureau of Standards, NSRDS-NBS 60, Washington, DC.
- Radiant Dyes, CW-Ring Dye Laser Operation and Maintenance Manual Wermelskirchen, Germany.
- Demtröder, W., Laser Spectrscopy Basic Concepts and Instrumentation. 3rd edition., Berlin Heidelberg New York: Springer-Verlag, 2002.
- Demtröder, W., Laser Spectroscopy, Springer (1982).
- Sune Svanberg, Atomic and Molecular Spectroscopy, Basic aspects and Practical applications Spring-Verlag, (1991).
- Wolfgang Demtröder, Laser Spectroscopy Basic Concepts and Instrumentation, Third Edition Springer (2002).
- Lide, David R., CRC Handbook of Chemistry and Physics, 83rd edition, CRC Press: Boca Raton, FL, 2002.
- William T. Silvast, Laser Fundamentals, 2nd edition, Cambridge University press (2004).

REFERENCES

1. Newton, I., Phil. Trans. Ray. Soc. London, 1672. **5**: p. 3075.
2. Wollaston, W.H., Phil. Trans. Roy. Soc. London, 1802. **11**: p. 365.
3. Fraunhofer, J., Ann. Phys., 1817. **26**: p. 264.
4. Holtzelw, H.F., Robinson, W.R, *General Chemistry*. 8th ed. 1988, Massachusetts
5. Svanberg, S., *Atomic and Molecular Spectroscopy: Basic Aspects and Practical Applications*. Springer Series on Atoms and Plasmas, ed. G. Ecker. Vol. 6. 1991, Springer-Verlag.
6. A. Mooradian, T.J., P. Stokseth, *Tunable Lasers and Applications*,. Vol. 3. 1976, Springer-Verlag.
7. Nesbitt, D.J. and S.R. Leone, *Laser-initiated chemical chain reactions.* The Journal of Chemical Physics, 1980. **72**(3): p. 1722-1732.
8. Khundkar, L.R. and A.H. Zewail, *Ultrafast Molecular Reaction Dynamics in Real-Time: Progress Over a Decade.* Annual Review of Physical Chemistry, 1990. **41**(1): p. 15-60.
9. Yaroslavsky, A.N., et al., *Influence of the Scattering Phase Function Approximation on the Optical Properties of Blood Determined from the Integrating Sphere Measurements.* Journal of Biomedical Optics, 1999. **4**(1): p. 47-53.
10. Demtröder, W., *Laser Spectrscopy Basic Concepts and Instrumentation*. third ed. 2002, Springer-Verlag
11. Plucke , J., Ann. der Phys., 1858. **103**(88).
12. Wein, W., Verhanal. Physik Ges., 1898. **17**.
13. Thomson, J.J., *Rays of Positive Electricity and Their Applications to Chamical Analysis*. 1913, London: Longmans Green.
14. Cox, S.G., et al., *High-resolution spectroscopy of ion beams.* Measurement Science and Technology, 1999. **10**(9): p. R101.
15. Maiman, T.H., *Stimulated Optical Radiation in Ruby*. Nature, 1960. **187**(4736): p. 493-494.
16. Hall, J.L., E.J. Robinson, and L.M. Branscomb, *Laser Double-Quantum Photodetachment of I^{-}.* Physical Review Letters, 1965. **14**(25): p. 1013-1016.
17. Lineberger, W.C. and B.W. Woodward, *High Resolution Photodetachment of S^{-} Near Threshold.* Physical Review Letters, 1970. **25**(7): p. 424-427.
18. Andrä, H.J., A. Gaupp, and W. Wittmann, *New Method for Precision Lifetime Measurements by Laser Excitation of Fast-Moving Atoms.* Physical Review Letters, 1973. **31**(8): p. 501-504.
19. Andrä, H.J., *Quantum beats and laser excitation is fast beam spectroscopy*, ed. E.W.W.A.W. G. Putlitz. 1975, New York: Plenum

20. S.L, K., *High-resolution laser spectroscopy in fast beams.* Optics Communications, 1976. **17**(3): p. 309-312.
21. Wing, W.H., et al., *Observation of the Infrared Spectrum of the Hydrogen Molecular Ion HD^{+}.* Physical Review Letters, 1976. **36**(25): p. 1488-1491.
22. Dufay, M., et al., *High-Resolution Studies in Ion Beams with Laser-Induced Resonances.* Physical Review Letters, 1976. **37**(25): p. 1678-1681.
23. Meier, T., H. Hühnermann, and H. Wagner, *High-resolution spectroscopy on a fast beam of metastable xenon ions.* Optics Communications, 1977. **20**(3): p. 397-400.
24. Höhle, C., et al., *High resolution spectroscopy of the transition 5d2D3/2→6p2P{3/2/0} in a fast Ba+ ion beam.* Zeitschrift für Physik A Hadrons and Nuclei, 1978. **284**: p. 261-265.
25. Rosner, S.D., R.A. Holt, and T.D. Gaily, *Measurement of the Zero-Field Hyperfine Structure of a Single Vibration-Rotation Level of Na_{2} by a Laser-Fluorescence Molecular-Beam-Resonance Technique.* Physical Review Letters, 1975. **35**(12): p. 785-789.
26. Ertmer, W. and B. Hofer, *Zero-field hyperfine structure measurements of the metastable states 3 d2 4 s4F3/2, 9/2 of45Sc using laser-fluorescence atomic-beam-magnetic-resonance technique.* Zeitschrift für Physik A Atoms and Nuclei, 1976. **276**(1): p. 9-14.
27. Mansour, N.B., et al., *Laser-rf double-resonance measurements of the hyperfine structure in Sc ii.* Physical Review A, 1989. **39**(11): p. 5762-5767.
28. Höhle, C., H. Hühnermann, and M. Elbel, *Observation of ΔF=±2 transitions in the hyperfine structure of ^{139}La II 5 d^2 ^{3}F 4→5 d4 f^3 F^{04}.* Zeitschrift für Physik A Hadrons and Nuclei, 1980. **295**: p. 1-5.
29. Höhle, C., H. Hühnermann, and H. Wagner, *Measurements of the hyperfine structure constants of La II using the high-resolution spectroscopy on collinear laser-ion-beams.* Zeitschrift für Physik A Hadrons and Nuclei, 1982. **304**(4): p. 279-283.
30. Dörschel, K., et al., *Nuclear moments and isotope shifts of europium isotopes by hyperfine structure investigations with collinear laser — Ion beam spectroscopy.* Zeitschrift für Physik A Hadrons and Nuclei, 1983. **312**(3): p. 269-270.
31. Rosner, S.D., et al., *A Study of theX2Σ+andA2Π States of SiO+Using Fast-Ion-Beam Laser Spectroscopy.* Journal of Molecular Spectroscopy, 1998. **189**: p. 83-94.
32. Scholl, T.J., et al., *Measurement of radiative lifetimes in Sm II.* Canadian Journal of Physics, 2002. **80**(12): p. 1621-1629.
33. Rosner, S.D., et al., *Measurement of hyperfine structure and isotope shifts in NdII.* Canadian Journal of Physics, 2005. **83**: p. 841-854.
34. Villemoes, P., et al., *Hyperfine structure measurements of 151,153Eu II with fast ion beam-laser spectroscopy.* Physics Letters A, 1992. **162**: p. 178-181.

35. Villemoes, P. and M. Wang, *Hyperfine structure of the 4 f 7 (8 S 0) 6 s 7 S {3/0} level in151,153Eu II by fast ion beam — laser spectroscopy.* Zeitschrift fur Physik D Atoms Molecules Clusters, 1994. **30**: p. 19-22.
36. Iimura, H., et al., *Measurement of Hyperfine Structure of the 4f35d 5G-4f36p 5H in PrII by Collinear Laser-Ion-Beam Spectroscopy.* Journal of the Physical Society of Japan, 1990. **59**: p. 4208.
37. Chen, M., et al., *Hyperfine Structure Measurements of NdII Using the Collinear Laser-Ion-Beams Spectroscopy.* Journal of the Physical Society of Japan, 1999. **68**: p. 2934.
38. Maosheng, L., et al., *Hyperfine Structure Measurements in the Lines 576.91 nm, 597.11 nm and 612.61 nm of La II.* Physica Scripta, 2000. **61**(4): p. 449.
39. Li, M., et al., *Measurement of hyperfine structure in the lines 578.77 nm and 587.04 nm of PrII.* Hyperfine Interactions, 2000. **128**: p. 417-422.
40. Otto, R., et al., *Hyperfine structure investigations and identification of new energy levels in the ionic spectrum of 147 Pm.* Journal of Physics B: Atomic, Molecular and Optical Physics, 1995. **28**(16): p. 3615.
41. Derkatch, A., et al., *Experimental and theoretical investigation of radiative decay rates of metastable levels in La II.* Physical Review A, 2002. **65**(6): p. 062508.
42. Hale, G.E., *The Astrophysical Journal.* The Astrophysical Journal, 1895. **1**: p. 80-84.
43. Fowler, A., *Some problems of astronomy (IV Solar and stellar photospheres).* The Observatory, 1913. **36**: p. 182-185.
44. Pinciuc, C.M., et al., *Measurement of radiative lifetimes in Nd II.* Canadian Journal of Physics, 2001. **79**(9): p. 1159-1167.
45. Wahlgren, G.M., *The Lanthanide Elements in Stellar and Laboratory Spectra.* Physica Scripta, 2002. **2002**(T100): p. 22.
46. Biémont, E. and P. Quinet, *Recent Advances in the Study of Lanthanide Atoms and Ions.* Physica Scripta, 2003. **2003**(T105): p. 38.
47. Rosner, S.D., et al., *Measurement of hyperfine structure and isotope shifts in Nd II.* Canadian Journal of Physics, 2005. **83**(8): p. 841-854.
48. Curry, J.J., E.A. Den Hartog, and J.E. Lawler, *Radiative lifetimes of Dy I and Dy II.* J. Opt. Soc. Am. B, 1997. **14**(11): p. 2788-2799.
49. Blagoev, K.B. and V.A. Komarovskii, *Lifetimes of Levels of Neutral and Singly Ionized Lanthanide Atoms.* Atomic Data and Nuclear Data Tables, 1994. **56**(1): p. 1-40.
50. Abt, A., *Hyperfine Structure in the Solar Spectrum.* The Astrophysical Journal, 1952. **115**: p. 199.
51. Booth, A.J. and D.E. Blackwell, *The effect of hyperfine structure on stellar abundance analysis.* Monthly Notices of the Royal Astronomical Society, 1983. **204**: p. 777-781.

52. Audi, G., et al., *The Nubase evaluation of nuclear and decay properties.* Nuclear Physics A, 2003. **729**(1): p. 3-128.
53. Sansonetti, J.E. and W.C. Martin, *Handbook of Basic Atomic Spectroscopic Data.* Journal of Physical and Chemical Reference Data, 2005. **34**(4): p. 1559-2259.
54. Cooper, C.M., et al., *A new large area lanthanum hexaboride plasma source.* Review of Scientific Instruments, 2010. **81**(8): p. 083503-8.
55. Schell, G., et al., *Electronic structure and superconductivity in metal hexaborides.* Physical Review B, 1982. **25**(3): p. 1589-1599.
56. Harrington, J.A., *Infrared Fibers and Their Applications*. Vol. PM135. 2004: SPIE Press Book. 312.
57. Rybar, S., Phys. Zeit, 1911. **12**: p. 889.
58. Popow, S., Ann. d. Physik, 1914. **45**: p. 147.
59. Paulson, E., Ann. d. Physik, 1914. **45**: p. 1203.
60. King, A.S. and E. Carter, *The Electric-Furnace Spectra of Yttrium, Zirconium, and Lanthanum.* The Astrophysical Journal, 1927. **65**: p. 86.
61. Meggers, W.F., *THE STRUCTURE OF THE LA II SPECTRUM.* J. Opt. Soc. Am., 1927. **14**(3): p. 191-204.
62. Meggers, W.F. and K. Burns, *HYPERFINE STRUCTURES OF LANTHANUM LINES.* J. Opt. Soc. Am., 1927. **14**(6): p. 449-453.
63. Anderson, O.E., *The Nuclear Magnetic Moment of Lanthanum.* Physical Review, 1934. **46**(6): p. 473-476.
64. Ting, Y., *Hyperfine Structure and Quadrupole Moment of Lanthanum-139.* Physical Review, 1957. **108**(2): p. 295-304.
65. Ben Ahmed, Z., C. Bauche-Arnoult, and J.F. Wyart, *Energy levels and hyperfine structures in the (5d + 6s)3 configurations of La I.* Physica, 1974. **77**(1): p. 148-158.
66. Fischer, W., et al., *Optical determination of the quadrupole moment of 138La.* Physics Letters B, 1972. **40**(1): p. 87-88.
67. Childs, W.J. and L.S. Goodman, *Complete resolution of hyperfine structure in the close doublet ?5930.6 of 139La by laser-atomic-beam spectroscopy.* J. Opt. Soc. Am., 1977. **67**(9): p. 1230-1234.
68. Childs, W.J. and L.S. Goodman, *Hyperfine structure of excited, odd-parity levels in 139La by laser?atomic-beam fluorescence.* J. Opt. Soc. Am., 1978. **68**(10): p. 1348-1350.
69. Höhle, C., H. Hühnermann, and H. Wagner, *Measurements of the hyperfine structure constants of all the 5 d ^{2} and 5 d6 s levels in ^{139}La II using the high-resolution spectroscopy on collinear laser-ion-beams.* Zeitschrift für Physik A Hadrons and Nuclei, 1982. **304**: p. 279-283.

70. Childs, W.J. and U. Nielsen, *Hyperfine structure of the (5d+6s)^{3} configuration of ^{139}i: New measurements and ab initio multiconfigurational Dirac-Fock calculations.* Physical Review A, 1988. **37**(1): p. 6-15.
71. Caiyan, L., et al., *Studies on the hyperfine structure of La I in a hollow-cathode discharge tube.* Journal of Physics D: Applied Physics, 1990. **23**(10): p. 1327.
72. Li, G.-W., et al., *Hyperfine Structure Measurement of LaII by Collinear Fast Ion-Beam-Laser Spectroscopy.* Japanese Journal of Applied Physics, 2001. **40**: p. 2508.
73. Ma, H.-L., *Hyperfine structure of singly ionized lanthanum and praseodymium.* Chinese Physics, 2002. **11**: p. 905-909.
74. Schef, P., et al., *Precise hyperfine structure measurements of La II utilizing the laser and rf double resonance technique.* Physica Scripta, 2006. **73**(2): p. 217.
75. Furmann, B., D. Stefanska, and J. Dembczynski, *Hyperfine structure analysis odd configurations levels in neutral lanthanum: I. Experimental.* Physica Scripta, 2007. **76**(3): p. 264.
76. Furmann, B., et al., *Hyperfine structure in La II even configuration levels.* Journal of Physics B Atomic Molecular Physics, 2008. **41**: p. 5002.
77. Furmann, B., et al., *Hyperfine structure in La II odd configuration levels.* Journal of Physics B Atomic Molecular Physics, 2008. **41**: p. 5004.
78. Furmann, B., D. Stefańska, and J. Dembczyński, *Experimental investigations of the hyperfine structure in neutral La: I. Odd parity levels.* Journal of Physics B: Atomic, Molecular and Optical Physics, 2009. **42**(17): p. 175005.
79. Furmann, B., D. Stefańska, and J. Dembczyński, *Experimental investigations of the hyperfine structure in neutral La: II. Even parity levels.* Journal of Physics B: Atomic, Molecular and Optical Physics, 2010. **43**(1): p. 015001.
80. Dembczyński, J., et al., *Critical analysis of the methods of interpretation in the hyperfine structure of free atoms and ions: case of the model space (5d+6s) 3 of the lanthanum atom.* Journal of Physics B: Atomic, Molecular and Optical Physics, 2010. **43**(6): p. 065001.
81. Nighat, Y., et al., *Investigation of the hyperfine structure of lanthanum lines by a laser-induced fluorescence technique.* Journal of Physics B: Atomic, Molecular and Optical Physics, 2010. **43**(12): p. 125001.
82. Anjum, N., Akhtar, N., Hühnermann,H., Windholz, L., *High resolution spectroscopic study of La II by using collinear laser ion beam spectroscopy,* in *EGAS 43 (Congress of the European Group on Atomic Systems)*. 2011: Fribourg Switzerland
83. Güzelçimen, F., et al., *New energy levels and hyperfine structure measurements of neutral lanthanum by laser-induced fluorescence spectroscopy.* Journal of Physics B: Atomic, Molecular and Optical Physics, 2012. **45**(13): p. 135005.

84. Rokhlin, L.L., *Magnesium Alloys Containing Rare-Earth Metals: Structure and Properties*. 2003: Taylor & Francis.

85. King, A.S., *Temperature Classification of the Stronger Lines of Cerium and Praseodymium.* Astrophysical Journal, 1928. **68**( ): p. 194.

86. White, H.E., *Hyperfine Structure in Singly Ionized Praseodymium.* Physical Review, 1929. **34**(11): p. 1397.

87. Rosen, N., G.R. Harrison., and J.R.J. McNally, *Zeeman Effect Data and Preliminary Classification of the Spark Spectrum of Praseodymium—Pr II.* Physical Review, 1941. **60**(10): p. 722.

88. Baker, J.M. and B. Bleaney, *Hyperfine Structure of Praseodymium.* Proceedings of the Physical Society. Section A, 1955. **68**(10): p. 936.

89. Amado, Y.C., et al., *Hyperfine Structure of Praseodymium-142.* Physical Review, 1962. **126**(3): p. 1004.

90. Reader, J. and J. Sugar, *Nuclear Magnetic Moment of Pr^{141} from Hyperfine structure of Pr II.* Phys. Rev., 1965. **137**: p. B 784.

91. Wyart, J.F., *Progrès Récents dans l'Interprétation des Configurations $4f^N$ (5 d + 6 s) des Lanthanides II. Etude Paramétrique des Configurations.* Phys. Scr., 1974. **9**(6): p. 325.

92. Ginibre, A. 1988, Universite de Paris-sud,: Paris.

93. Ginibre, A., *Fine and hyperfine structures of singly ionized praseodymium: I. energy levels, hyperfine structures and Zeeman effect, classified lines.* Physica Scripta, 1989. **39**(6): p. 694.

94. Ginibre, A., *Fine and hyperfine structures of singly ionised praseodymium: II. parametric interpretation of fine and hyperfine structures for the even levels of singly ionised praseodymium.* Physica Scripta, 1989. **39**(6): p. 710.

95. Childs, W.J. and L.S. Goodman, Phys. Rev., 1981. **24**(3): p. 1342.

96. Macfarlane, R.M., D.P. Burum, and R.M. Shelby, *New Determination of the Nuclear Magnetic Moment of ^{141}Pr.* Physical Review Letters, 1982. **49**(9): p. 636.

97. Imura, H., et al., *Measurement of Hyperfine Structure of the $4f^3 5d\,^5G$-$4f^3 6p\,^5H$ in PrII by Collinear Laser-Ion-Beam Spectroscopy.* J. Phys. Soc. Jpn., 1990. **59** p. 4208-4210

98. Kuwamoto, T., et al., J. Phys. Soc. Japan, 1996. **65**(10): p. 3180.

99. Maosheng, L., et al., *Hyperfine-structure measurements in 141Pr II and 143,145Nd II by collinear laser-ion-beam spectroscopy.* Physical Review A, 2000. **62**: p. 52504.

100. Rivest, R.C., et al., *Laser spectroscopic measurements of hyperfine structure in Pr II.* Can. J. Phys., 2002. **80**: p. 557.

101. Furmann, B., et al., Eur. Phys. J., 2001. **D 17**(3): p. 275.

102. Li, R., et al., *Oscillator strength measurements in Pr II with the fast-ion-beam laser-induced-fluorescence technique.* Physica Scripta, 2007. **76**: p. 577-592.
103. Oppel, S.G., et al., *Active laser frequency stabilization using neutral praseodymium (Pr).* Applied Physics B: Lasers and Optics, 2010. **101**(1): p. 33-44.
104. Anjum, N., Akhtar, N., Hühnermann,H., Windholz, L; *Measurements of hyperfine structure constants of Pr II by using high resolution collinear laser ion beam spectroscopy*, in *60th ÖPG Coference (Austrtian Physical Society)*. 2010: University of Salzburg Austria.
105. Gamper, B., *Investigation of the hyperfine structure of Pr I and Pr II lines based on highly resolved Fourier transform spectra.* Journal of Physics B: Atomic, Molecular and Optical Physics, 2011. **44**(4): p. 045003.
106. Akhtar, N. and L. Windholz, *Improved energy levels and wavelengths of Pr II from a high-resolution Fourier transform spectrum.* Journal of Physics B: Atomic, Molecular and Optical Physics, 2012. **45**(9): p. 095001.
107. Raghavan, P., *Table of nuclear moments.* Atomic Data and Nuclear Data Tables, 1989. **42**(2): p. 189-291.
108. Cowley, C.R. and G. Mathys, *Line identifications and preliminary abundances from the red spectrum of HD 101065 (Przybylski's star).* Astronomy and Astrophysics, 1998. **339**: p. 165-169.
109. Lyubimkov, L.S., T.M. Rachkovskaya, and S.I. Rostopchin, *Chemical composition of the components of the binary Am star β Aur.* Astronomy Reports, 1996. **40**: p. 802-811.
110. Dolk, L., et al., *The presence of Nd and Pr in HgMn stars.* A&A, 2002. **385**(1): p. 111-130.
111. Butcher, H.R., *Thorium in G-dwarf stars as a chronometer for the Galaxy.* Nature, 1987. **328**(6126): p. 127-131.
112. Lawler, J.E., W. Whaling, and N. Grevesse, *Contamination of the Th II line and the age of the Galaxy.* Nature, 1990. **346**(6285): p. 635-637.
113. Norman, M.J., et al., *Multipass Reconfiguration of the HELEN Nd:Glass Laser at the Atomic Weapons Establishment.* Appl. Opt., 2002. **41**(18): p. 3497-3505.
114. King, A.S., Astrophys. J., 1933. **78**(9).
115. VandeVliet, H. J. 1939: Amsterdam.
116. Albertson, W.E., G.R. Harrison, and J.R. McNally, Jr., *First Spark Spectrum of Neodymium—Preliminary Classification and Zeeman Effect Data.* Physical Review, 1942. **61**(3-4): p. 167-174.
117. Klinkenberg, P.F.A., *The isotope effect in the spectrum of Nd i.* Physica, 1945. **11**: p. 327-338.
118. Schuurmans, P., *On the spectra of neodymium and uranium.* Physica, 1946. **11**(5): p. 419-425.
119. Bleaney, B. and H.E.D. Scovil, *Nuclear Spins of Neodymium 143 and 145.* Proceedings of the Physical Society. Section A, 1950. **63**(12): p. 1369.

120. Murakawa, K. and J.S. Ross, *Hyperfine Structure of Sm^{149}, Sm^{147}, Nd^{145}, and Nd^{143}.* Physical Review, 1951. **82**(6): p. 967-968.
121. Bleaney, B., H.E.D. Scovil, and R.S. Trenam, *The Paramagnetic Resonance Spectra of Gadolinium and Neodymium Ethyl Sulphates.* Proceedings of the Royal Society of London. Series A. Mathematical and Physical Sciences, 1954. **223**(1152): p. 15-29.
122. Halford, D., C.A. Hutchison, Jr., and P.M. Llewellyn, *Electron Nuclear Double Resonance of Neodymium.* Physical Review, 1958. **110**(1): p. 284-286.
123. Nöldeke, G., *Isotopieverschiebung im Nd II-Spektrum.* Zeitschrift fur Physik, 1955. **143**: p. 274-284.
124. Hassan, G.E.M.A. and P.F.A. Klinkenberg, *The atomic spectrum of neodymium: II. Classification of lines, zeeman effect and isotope shift of Nd I.* Physica, 1963. **29**(11): p. 1133-IN1.
125. Spalding, I.J., *The Hyperfine Structure and Nuclear Moments of 143 Nd and 145 Nd.* Proceedings of the Physical Society, 1963. **81**(1): p. 156.
126. Blaise, J., et al., *Present State of the Analysis of Nd I and Nd II.* J. Opt. Soc. Am., 1971. **61**(10): p. 1335-1342.
127. Childs, W.J. and L.S. Goodman, *Hyperfine-Structure Constants and g_{J} Values of ^{5}I_{4,5,6,7,8} Atomic States of ^{143,145}Nd.* Physical Review A, 1972. **6**(5): p. 1772-1786.
128. Childs, W.J., *Hyperfine structure of high-L states in ^{143,145}i by atomic-beam laser-rf double resonance.* Physical Review A, 1991. **44**(1): p. 760-763.
129. van Leeuwen, K.A.H., et al., *High resolution measurements of hyperfine structure and isotope shifts in 9 spectral lines of Nd I.* Zeitschrift für Physik A Hadrons and Nuclei, 1981. **301**(2): p. 95-99.
130. Blaise, J., Ann. Physique, 1958. **3**: p. 1019.
131. Wyart, J.F., PhD Thesis 1968, Universityof Paris.
132. Morillion, C., *Etude des spectres d'émission du Samarium, du Néodyme et de l'Uranium entre 2,3 et 4,1 μm avec un spectromètre à grilles.* Spectrochimica Acta, 1970. **25**: p. 513-538.
133. Ahmad, S.A. and G.D. Saksena, *Isotope shifts in the energy levels of the singly ionized neodymium atom.* Spectrochimica Acta Part B: Atomic Spectroscopy, 1981. **36**(10): p. 943-950.
134. Nakhate, S.G., S.M. Afzal, and S.A. Ahmad, *Term isotope shift of high lying odd and even energy levels of Nd II.* Zeitschrift für Physik D Atoms, Molecules and Clusters, 1997. **42**(2): p. 71-76.
135. Fuquan, L., et al., *Optical isotope shifts in the 5702-Å line of Nd ii by collinear fast-beam-laser spectroscopy.* Physical Review A, 1991. **44**: p. 1843-1847.
136. Hongliang, M., et al., *Optical isotope shifts of Nd II ? by collinear fast-ion-beam laser spectroscopy.* Journal of Physics B Atomic Molecular Physics, 1997. **30**: p. 3355-3360.

137. Hong-liang, M., et al., *Changes in Mean Square Nuclear Charge Radii of Nd II from Optical Isotope Shifts by Collinear Fast-Ion-Beam Laser Spectroscopy.* Chinese Physics Letters, 1998. **15**(3): p. 178.

138. Ma, H.-L., *Measurement of hyperfine structure and isotope shifts in the 580.56nm line of 142-145,146,148,150Nd+*. Chinese Physics, 2005. **14**: p. 511-515.

139. Macfarlane, R.M., R.S. Meltzer, and B.Z. Malkin, *Optical measurement of the isotope shifts and hyperfine and superhyperfine interactions of Nd in the solid state.* Physical Review B, 1998. **58**(9): p. 5692-5700.

140. Andersen, T., et al., *Lifetimes of some excited states in the rare earths: La ii, Ce ii, Pr ii, Nd ii, Sm ii, Yb i, Yb ii, and Lu ii.* Solar Physics, 1975. **44**(2): p. 257-267.

141. Marek, J. and H.J. Stahnke, *Radiative lifetimes of optical levels of neutral erbium, gadolinium and neodymium.* Zeitschrift für Physik A Hadrons and Nuclei, 1980. **298**(2): p. 81-82.

142. Gorshkov, V.N., et al., *Lifetimes of excited levels of Nd I and Nd II - oscillator strengths of the spectral lines of Nd I.* Journal Name: Astrophysics (Engl. Transl.); (United States); Journal Volume: 17; Other Information: Translated from Astrofizika; 17: 799-806(Oct-Dec 1981), 1982: p. Medium: X; Size: Pages: 437-441.

143. Ward, L., et al., *Radiative Lifetimes in Nd II and the Solar Neodymium Abundance.* Physica Scripta, 1984. **29**(6): p. 551.

144. Ward, L., et al., *Accurate Experimental Lifetimes of Excited Levels in Nd II.* Physica Scripta, 1985. **31**(3): p. 161.

145. LU Fuquan, W.S., SHI Wei, SHI Peixiong, YANG Jianjun, SONG Linggen, TANG Jiayong, YANG Fujia, *lifetime measurement for the (23537)°_{9/2} level of ndii using the collinear ion beam-laser interaction.* Chin. Phys. Lett., 1989. **6**(4): p. 161-164.

146. Wei, S., et al., *Lifetime measurement of the T=23 537 cm^{-1}, J=9/2 odd-parity level in Nd ii using time-resolved collinear fast-beam laser spectroscopy.* Physical Review A, 1991. **43**(3): p. 1451-1454.

147. Scholl, T.J., et al., *Measurement of radiative lifetimes in Pr II and Nd II.* Canadian Journal of Physics, 2002. **80**(7): p. 713-722.

148. Hartog, E.A.D., et al., *Improved Laboratory Transition Probabilities for Nd II and Application to the Neodymium Abundances of the Sun and Three Metal-poor Stars.* The Astrophysical Journal Supplement Series, 2003. **148**(2): p. 543.

149. Li, R., et al., *Fast-ion-beam laser-induced-fluorescence measurements of branching fractions and oscillator strengths in Nd II.* Canadian Journal of Physics, 2007. **85**: p. 1343-1379.

150. Anjum, N., Akhtar, N., Hühnermann,H., Windholz, L.; *Experimental Investigations of the Hyperfine Structure of $^{143}Nd^{+}$ Spectral Lines Using Collinear Laser Ion Beam Spectroscopy*. To be published, 2012.
151. Demtröder, W., *Atoms, Molecules and Photons*. An Introduction to Atomic-, Molecular-and Quantum-Physics. 2005, Springer-Verlag.
152. Russell, H.N. and F.A. Saunders, *New Regularities in the Spectra of the Alkaline Earths.* The Astrophysical Journal, 1925. **61**: p. 38.
153. Hühnermann, H., *Hyperfine structure in stellar spectral lines: a little nothing, a help, or a troublemaker?* Physica Scripta, 1993. **1993**(T47): p. 70.
154. Pauli, W., *Zur Frage der theoretischen Deutung der Satelliten einiger Spektrallinien und ihrer Beeinflussung durch magnetische Felder.* Naturwissenschaften, 1924. **12**(37): p. 741-743.
155. Murakawa, K., *Anomalies in the Fine Structure of the First Spark Spectrum of Iodine.* Nature, 1936. **137**: p. 1030.
156. Schüler, H. and T. Schmidt, *über Abweichungen des Atomkerns von der Kugelsymmetrie.* Zeitschrift für Physik A Hadrons and Nuclei, 1935. **94**(7): p. 457-468.
157. Duarte, F.J., *Tunable Laser Optics*. 2003, New York: Elsevier Academic.
158. Svanberg, S., *Atomic and Molecular Spectroscopy (Basic Aspects and Practical Applications)*. Atoms+Plasmas, ed. P.D.G. Ecker. Vol. 8. 1990, Berlin, Heidelberg, New Yark: Springer-Verlag. 405.
159. Sorokin, P.P. and J.R. Lankard, *Stimulated Emission Observed from an Organic Dye, Chloro-aluminum Phthalocyanine.* IBM Journal of Research and Development, 1966. **10**(2): p. 162-163.
160. Schafer, F.P., W. Schmidt, and J. Volze, *ORGANIC DYE SOLUTION LASER.* Applied Physics Letters, 1966. **9**(8): p. 306-309.
161. *Operating and Maitenance Manual* R.d.C.-R.D. Laser, Editor. 1990.
162. Akhtar, N., *PhD Thesis* 2012, Technical University Graz.
163. Siddiqui, I.A., PhD Thesis 2010,Technical University Graz.
164. Penning, F.M., Physica, 1928. **8**: p. 137.
165. C.Travis, J., *Analytical Optogalvanic Spectroscopy in Flames*, ed. A.N.C. S. Marticllucci. 1985: Plenum New Yark.
166. Masaki, T., Y. Adachi, and C. Hirose, *Application of Optogalvanic Spectroscopy to the Measurement of Pressure Broadening and Shift in the Negative Glow Region of an Ar Hollow Cathode Discharge.* Appl. Spectrosc., 1988. **42**(1): p. 54-56.
167. Rao, G., J. Govindarajan, and M. Reddy, *Optogalvanic spectroscopy of sputtered atoms.* Hyperfine Interactions, 1987. **38**(1): p. 539-552.
168. Vidal, C.R., *Optogalvanic double-resonance spectroscopy.* Opt. Lett., 1980. **5**(4): p. 158-159.

169. Göppert-Mayer, M., *Über Elementarakte mit zwei Quantensprüngen.* Annalen der Physik, 1931. **401**(3): p. 273-294.
170. Kaiser, W. and C.G.B. Garrett, *Two-Photon Excitation in CaF_{2}: Eu^{2+}.* Physical Review Letters, 1961. **7**(6): p. 229-231.
171. Bennett, W.R., Jr., *Hole Burning Effects in a He-Ne Optical Maser.* Physical Review, 1962. **126**(2): p. 580-593.
172. Feldmann, D., *Opto-galvanic spectroscopy of some molecules in discharges: NH2, NO2, H2 and N2.* Optics Communications, 1979. **29**(1): p. 67-72.
173. Behrens, H.-O. and G. Guthöhrlein, H., *High resolution optogalvanic spectroscopy as a useful tool in the determination of atomic hyperfine parameters and isotopic shifts.* J. Phys. Colloques, 1983. **44**(C7): p. C7-149-C7-168.
174. Behrens, H.-O., G. Guthöhrlein, H., and A. Kasper, *Optical-optical double resonance experiments with gallium and indium atoms via optogalvanic detection.* J. Phys. Colloques, 1983. **44**(C7): p. C7-239-C7-250.
175. Quiering, T., Diploma Thesis 1984, Universitat der Bundeswehr: Hamburg.
176. Tsai, C.-C., et al., *CO2 laser frequency stabilization using the radio-frequency optogalvanic Lamb dip.* Appl. Opt., 1991. **30**(27): p. 3842-3845.
177. Young, L., et al., *Hyperfine structure of 147,149Sm ii by collinear laser-ion-beam spectroscopy.* Physical Review A, 1987. **36**: p. 2148-2154.
178. Mueller, A.C., et al., *Spins, moments and charge radii of barium isotopes in the range 122-146Ba determined by collinear fast-beam laser spectroscopy.* Nuclear Physics A, 1983. **403**: p. 234-262.
179. Poulsen, O., et al., *Spectroscopy of the uranium ion using collinear fast-beam-cw-dye-laser modulation spectroscopy: Transition energies and excited-state lifetimes.* Physical Review A, 1981. **24**: p. 2523-2531.
180. Billowes, J. and P. Campbell, *High-resolution laser spectroscopy for the study of nuclear sizes and shapes.* Journal of Physics G: Nuclear and Particle Physics, 1995. **21**(6): p. 707.
181. Silverans, R.E., P. Lievens, and L. Vermeeren, *A sensitive measuring scheme in colunear fast-ion-beam laser spectroscopy: The optical pumping, state-selective neutralization and particle detection sequence.* Nuclear Instruments and Methods in Physics Research B, 1987. **26**: p. 591-597.
182. Hühnermann, H., et al., *A simple and effective stabilization system for collinear laser ion-beam spectroscopy at mass separators.* Nuclear Instruments and Methods in Physics Research B, 1987. **26**: p. 435-439.
183. Young, L., et al., *Hyperfine structure of ^{147},149Sm ii by collinear laser–ion-beam spectroscopy.* Physical Review A, 1987. **36**(5): p. 2148-2154.

184. Alkhazov, G.D., et al., *Hyperfine structure and isotope shift investigations of 145Pm and 147Pm.* Journal of Physics B Atomic Molecular Physics, 1992. **25**: p. 571-576.
185. Höhle, C., H. Hühnermann, and M. Elbel, Zeitschrift für Physik A Hadrons and Nuclei, 1980. **295**(1): p. 1-5.
186. Nielsen, U., et al., *235U II hyperfine structures measured by collinear fast-beam-laser and radio-frequency-laser double-resonance spectroscopy.* J. Opt. Soc. Am. B, 1984. **1**(2): p. 284-292.
187. Eberz, J., et al., Zeitschrift für Physik A Hadrons and Nuclei, 1986. **323**(1): p. 119-123.
188. Neugart, R., et al., *Nuclear moments and charge radii of rare-earth isotopes studied by collinear fast-beam laser spectroscopy.* Hyperfine Interactions, 1983. **15**: p. 181-185.
189. Dörschel, K., et al., *Hyperfine structure investigations in Sm II by collinear laser spectroscopy and nuclear moments of¹⁵¹Sm.* Zeitschrift für Physik A Hadrons and Nuclei, 1981. **302**(4): p. 359-360.
190. Bendali, N., et al., *Two methods for nuclear spin determination in collinear laser spectroscopy : classical r.f. magnetic resonance and observation of the Larmor precession.* J. Phys. France, 1984. **45**(3): p. 421-427.
191. Kronfeldt, H.D., et al., *Hyperfinestructure and lifetime of the Mn I levels with laser- atomic-beam-spectroscopy.* Zeitschrift für Physik A Hadrons and Nuclei, 1985. **322**(2): p. 349-350.
192. Alkhazov, G.D., et al., *Hyperfine structure and isotope shift investigations of 145 Pm and 147 Pm.* Journal of Physics B: Atomic, Molecular and Optical Physics, 1992. **25**(2): p. 571.
193. Ishida, Y., et al., *Isotope shifts of optical transitions in Ce II by collinear laser - ion-beam spectroscopy*. Journal of Physics B: Atomic, Molecular and Optical Physics, 1997. **30**(11): p. 2569.
194. Iimura, H., et al., *Nuclear moments and isotope shifts of 135 La , 137 La , and 138 La by collinear laser spectroscopy.* Physical Review C, 2003. **68**: p. 54328.
195. Li, R., et al., *Fast-ion-beam laser-induced-fluorescence measurements of branching fractions and oscillator strengths in Nd II.* Canadian Journal of Physics, 2007. **85**(12): p. 1343-1379.
196. Holt, R.A., et al., *Fast-ion-beam laser-fluorescence measurements of oscillator strengths in the lanthanides.* Physica Scripta, 2009. **2009**(T134): p. 014012.
197. Simonsen, H., et al., *Lifetime measurements and absolute oscillator strengths for single ionized thorium (Th II).* Physica Scripta, 1988. **38**: p. 370-373.
198. Sharikova, A., et al., *Oscillator strengths in lanthanide ions: Sm II*, in *APS Division of Atomic, Molecular and Optical Physics Meeting Abstracts*. 2003. p. 1165.
199. Höhle, C., et al., *Nuclear moments and optical isotope shift of radioactive 133Ba.* Physics Letters B, 1976. **62**(4): p. 390-392.

200. Huber, B.A., et al., *Laser--ion coaxial beams spectrometer.* Review of Scientific Instruments, 1977. **48**(10): p. 1306-1313.
201. Neumark, D., *High resolution photodetachment sduties of molecular nagative ions*, ed. J.P. Maier. 1989, Amsterdam: Elsevier.
202. Hongliang, M., et al., *Hyperfine structure in the 576 nm line of Pr II by collinear fast-ion-beam laser spectroscopy.* Journal of Physics B Atomic Molecular Physics, 1999. **32**: p. 1345-1349.
203. Rivest, R.C., et al., *Laser spectroscopic measurements of hyperfine structure in Pr II.* Canadian Journal of Physics. **80**(5): p. 557-562.
204. Silverans, R.E., et al., *Collinear fast beam-laser spectroscopy on 5 d 2 D 3/2, 5/2 barium ions.* Zeitschrift für Physik A Hadrons and Nuclei, 1980. **295**: p. 311-314.
205. Beiersdorf, S., et al., *J-dependence of optical isotope shifts in Sm II.* Journal of Physics G Nuclear Physics, 1995. **21**: p. 215-228.
206. Rehse, S.J., et al., *Fast-ion-beam laser-induced-fluorescence measurements of spontaneous-emission branching ratios and oscillator strengths in SmII.* Canadian Journal of Physics, 2006. **84**: p. 723-771.
207. Sen, A., et al., *Measurement and analysis of isotope shifts in ^{151,153}Eu^{+} from hyperfine spectra.* Physical Review A, 1990. **42**(5): p. 2573-2577.
208. Ma, H.-l. and F.-j. Yang, *Measurement of hyperfine coupling constants of the excited states 4f7(8S07/2)6p3/2(7/2, 3/2) in 151,153Eu+.* Chinese Physics, 2001. **10**: p. 512-515.
209. Hühnermann, H., H. Valentin, and H. Wagner, *Nuclear moments and optical isotope shift of133Xe.* Zeitschrift für Physik A Hadrons and Nuclei, 1978. **285**: p. 229-230.
210. Broström, L., et al., *Hyperfine-structure measurements in Xe ii.* Physical Review A, 1996. **53**(1): p. 109-112.
211. Ishida, Y., et al., *Isotope shifts of optical transitions in Ce II by collinear laser - ion-beam spectroscopy.* Journal of Physics B Atomic Molecular Physics, 1997. **30**: p. 2569-2579.
212. Holt, R.A., T.J. Scholl, and S.D. Rosner, *Measurements of hyperfine structure in MN II.* Monthly Notices of the Royal Astronomical Society, 1999. **306**: p. 107-111.
213. Schinzler, B., et al., *Collinear laser spectroscopy of neutron-rich Cs isotopes at an on-line mass separator.* Physics Letters B, 1978. **79**: p. 209-212.
214. Cohen-Tannoudji, C., Ann. Phys. Fr., 1962. **7**: p. 423.
215. Nielsen, U., et al., *Collinear Laser-rf Double-Resonance Spectroscopy: 235U II Hyperfine Structure.* Physical Review Letters, 1983. **51**: p. 1749-1752.
216. Borghs, G., et al., *Light-shift deviations observed in collinear laser-rf double-resonance spectroscopy.* Physical Review A, 1985. **31**: p. 1434-1439.

217. Nielsen, U., et al., *Hyperfine structure of 4f126s and 4f125d Configurations in 167Er II Measured by Collinear Fast-Beam Laser and Radio-Frequency Laser Double-Resonance Spectroscopy.* Physica Scripta, 1986. **34**: p. 776-787.
218. Boos, N., et al., *Nuclear properties of the exotic high-spin isomer ^{178}Hf^{m2} from collinear laser spectroscopy.* Physical Review Letters, 1994. **72**(17): p. 2689-2692.
219. Tordoff, B., et al., *Investigation of the low-lying isomer in 229Th by collinear laser spectroscopy.* Hyperfine Interactions, 2006. **171**: p. 197-201.
220. Warring, U., et al., *High-Resolution Laser Spectroscopy on the Negative Osmium Ion.* Physical Review Letters, 2009. **102**(4): p. 043001.
221. Johnson, P.G., A. Bolson, and C.M. Henderson, *A high temperature ion source for isotope separators.* Nuclear Instruments and Methods, 1973. **106**(1): p. 83-87.
222. Plass, G.N., *Electrostatic Electron Lenses with a Minimum of Spherical Aberration.* Journal of Applied Physics, 1942. **13**(1): p. 49-55.
223. Win, T. , *Operating the Mass Separator, Ion Production and a Technique for the enhancement of the Signal to Background Ratio*, Phlillips Universität Marburg / Lahn, 1993.
224. Hintenberger, H., Z. Naturforschung 1951. **275**(6a).
225. Alkhazo, G.D. 1984, Leningard Nuclear Physics Institute Preprints.
226. Kowalska, M., et al., *Laser and β-NMR spectroscopy on neutron-rich magnesium isotopes.* The European Physical Journal A - Hadrons and Nuclei, 2005. **25**(0): p. 193-197.
227. Larkins, R.P.a.P., *Optical Emission Lines of the Elements*. 2000: John Wiley & Sons.
228. Sahoo, B.K., et al., *Theoretical studies of the 6s^{2}S_{1/2}→5d^{2}D_{3/2} parity-nonconserving transition amplitude in Ba^{+} and associated properties.* Physical Review A, 2007. **75**(3): p. 032507.
229. Van Hove, M., et al., Zeitschrift für Physik A Hadrons and Nuclei, 1985. **321**(2): p. 215-219.
230. G.H.Woodgate, *Elementary Atomic Structure*. 2nd ed. 1980, Oxford: Oxford University Press.
231. Erickson, L.E., *Electron-Paramagnetic-Resonance Absorption by Trivalent Neodymium Ions in Single Crystals of Lanthanum Trichloride and Lanthanum Ethyl Sulphate in Zero Magnetic Field.* Physical Review, 1966. **143**(1): p. 295-303.
232. Halford, D., *Electron-Nuclear Double Resonance, Nuclear Moments, and ⟨r^{-3}⟩ of Neodymium-143 (III) and Neodymium-145 (III) in Lanthanum Trichloride.* Physical Review, 1962. **127**(6): p. 1940-1948.